Biophysical modeling of mesenchymal cell motility and its constitutive relations

vorgelegt von
M. Sc.
Behnam Amiri

an der Fakultät II – Mathematik und Naturwissenschaften
der Technischen Universität Berlin
zur Erlangung des akademischen Grades
Doktor der Naturwissenschaften

Dr. rer. nat.

genehmigte Dissertation

Promotionsausschuss:

Vorsitzender: Prof. Dr. Michael Lehmann

Gutachter: Prof. Dr. Carsten Beta

Gutachter: Prof. Dr. Martin Falcke

Gutachter: Prof. Dr. Holger Stark

Tag der wissenschaftlichen Aussprache: 22.11.2022

Berlin 2023

Declaration of Authorship

I, Behnam Amiri, declare that this thesis titled, 'Biophysical modeling of mesenchymal cell motility and its constitutive relations' and the work presented in it are my own. I confirm that:

- This work was done wholly or mainly while in candidature for a research degree at this University.
- Where any part of this thesis has previously been submitted for a degree or any other qualification at this University or any other institution, this has been clearly stated.
- Where I have consulted the published work of others, this is always clearly attributed.
- Where I have quoted from the work of others, the source is always given. With the exception of such quotations, this thesis is entirely my own work.
- I have acknowledged all main sources of help.
- Where the thesis is based on work done by myself jointly with others, I have made clear exactly what was done by others and what I have contributed myself.

Signed: _____

Date: _____

Abstract

Motility is a fundamental feature of eukaryotic cells maintained across different organisms over millions of years of evolution. Cell motility is critical in many biological processes, including embryonic development, immune response, and wound healing. Errors in the motility mechanisms can have serious consequences, such as the metastatic spread of cancer cells. Cell motility is a very complex phenomenon with numerous molecular components. Although many of these components and basic processes are well characterized, there is a need to integrate this wealth of data and conceptualize the fundamental mechanisms that shape motility behavior. The motility properties vary dramatically between different cell types in different conditions. Nevertheless, some properties and relations seem to be universal, as they have been observed in many cell types and conditions. Studying these universal constitutive relations is the first step toward understanding the fundamental mechanisms of motility. In this thesis, we start by developing two analysis tools that can integrate the experimental data obtained from imaging the cell cytoskeleton and edge morphodynamics. We demonstrated the potential of the analysis workflows to quantitatively characterize the impact of specific molecules on the architecture of the cytoskeleton and the cell morphodynamics. Following the introduction of the analysis tools, we introduced a biophysical model to understand the underlying mechanisms that give rise to the constitutive relations in cell motility. The biphasic adhesion-velocity relation is the first universal observation in cells we studied. We used our experimental data on the MDA-MB-231 cells that were restricted to 1-dimensional motion by Fibronectin coating micro-lanes and introduced a model to obtain a quantitative understanding of how the effect of adhesion on the forces pushing the front and resisting motion at the back leads to the biphasic adhesion-velocity relation. Our model reproduces the measured adhesion-velocity relation in 4 different cell types. The model suggests that the polymerization force at the leading edge, which drives the retrograde flow, is also the force pushing the front. Drag forces along the cell length resist motion. All the forces promoting and resisting motion are velocity-dependent and controlled by adhesion. We find that cells exhibit adhesion-dependent intrinsic length. Our model suggests an elastic force mediates the interaction between cell front and back. We extended our model to include the well-established clutch mechanism. Based on our experimental evidence, a back protrusion is also added to the model. The extended model reproduced coexisting dynamic states of cells. The mechanical competition of protrusions introduced in our model could explain another universal observation in cell motility, the USCP law. Our mechanism suggests retrograde flow speed be the primary determinant of the stability of a protrusion. The proposed mechanical system can explain three universal experimental observations, the biphasic adhesion-velocity relation, the coexistence of oscillatory and steady morphodynamics, and the UCSP law. The main components of the model required to explain those relations are the noisy clutch mechanism, the interaction of back and front protrusions through elastic mechanical force, and the integrin signaling, which determines the

parameters of the mechanical system. The universality of the components of our model explains the universality of the experimentally observed relations.

Acknowledgements

I thank Max Delbrück Center (MDC−Berlin) institution for financial supports.

I thank Prof. Dr. Joachim O. Rädler, Dr. Christoph Schreiber, Johannes Heyn, Dr. Georgi Dimchev, Prof. Dr. Klemens Rottner, Prof. Dr. Florian Schur, Dr. Setareh Dolati, and the members of the mathematical physiology group for the helpful discussions and their contributions to this work.

I thank my supervisor Prof. Dr. Martin Falcke for his invaluable patience and feedback. This work would not have been possible without his support.

I also thank my co-supervisor Prof. Dr. Harald Engel.

I thank my thesis committee; Prof. Dr. Michael Lehmann for serving as chairperson and Prof. Dr. Holger Stark, Prof. Dr. Carsten Beta, and Prof. Martin Falcke for evaluating my work.

Lastly, I thank my family and friends, whose supports kept my motivation high during this journey.

Contents

List of Figures

List of Tables

Chapter 1

Introduction

The ability to migrate is a fundamental property of all animal cells. Cell motility refers to the process of cell migration from one place to another. This ability is crucial for a range of processes, including migration of cells in development, tumor metastasis, wound healing, and immune responses [4, 19–21]. Defects in the process of cell motility can induce serious consequences. The metastatic spread of cancer cells shows the great importance of understanding the mechanisms underlying cell motility.

In vivo, cells exhibit 1, 2, or 3-dimensional migration depending on their environment. For instance, cells can move along 1-dimensional paths on the fibers of the extracellular matrix [22]. 3-dimensional migration is seen when cells move in the extracellular matrix. However, the best studied case is the 2-dimensional migration of cells on surfaces. Despite the differences between different modes of motility, the insight that is gained from experiments on cells moving on substrates helps to understand the mechanisms of cell motility in general. To move on surfaces, cells usually employ flat or finger-like projections called lamellipodium and filopodium, respectively [23, 24]. Cell motility is usually classified into two types of motion (Fig. 1.1). First is the mesenchymal motility in which cells form strong adhesion with substrate and move utilizing actin-rich protrusions [25]. Contraction of the cell rear is also suggested to be critical in mesenchymal motility. The second type is amoeboid motility, with cells forming pseudopods and stable blebs due to hydrostatic pressure. The strength of adhesion to the substrate is weaker in this type of motility [25–27].

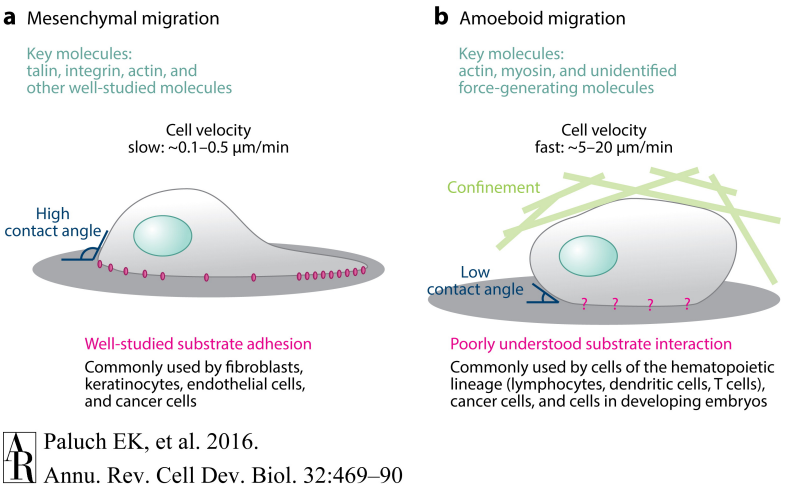

FIGURE 1.1: Two modes of motility. Main features of the Mesenchymal (a) and amoeboid (b) types of migration. Figure is taken from [1].

The context of this thesis is the mesenchymal motility of cells. We cover data analysis approaches and mathematical modeling of cell motion. In this chapter, we briefly describe the basic structures of the cell and provide biological background on the components involved in cell motility. Then, we review some fundamental constitutive relations related to cell motility. Finally, we review the related literature and describe our approach in this thesis.

1.1 Cell structures

1.1.1 Cell membrane

The plasma membrane of the cell is a thin (5 nm thick) lipid bilayer formed by phospholipid molecules that separates the interior and exterior of the cell. The cell membrane is essential in many biological functions of cells. All the interactions between the cell and the extracellular environment are through the plasma membrane. Many proteins exist in the membrane bilayer, which can act as receptors. In addition to signaling, the membrane also plays a mechanical role for the cell. The elastic properties of the membrane help cells to keep their integrity. Membrane Tension provides a means of force transmission between different parts of the cell [28]. It has been reported that there is a correlation between forces in the cell cytoskeleton and the membrane tension [29]. The membrane tension changes after polarization of the cell [30], and a back-to-front gradient

is observed in moving cells [30]. Experimental manipulation of membrane tension leads to a change in actin structure, density and cell velocity [31].

Right beneath the plasma membrane, a thin (a few hundred nanometers thick) F-actin network exists, which is called cortex. This cortex is linked with the membrane. The cortex increases the rigidity of the membrane and controls cell shape [32]. Cell membrane and cortex are directly involved in cell motility and lamellipodia dynamics [33–36].

1.1.2 Cytoskeleton

All the biological material enclosed by the cell membrane (except the cell nucleus) is called cytoplasm. The cytoplasm is comprised of cell organelles and cytosol, which is a viscous intracellular fluid. In the cytoplasm of animal cells, there is also a viscoelastic structure formed by various semiflexible biopolymers that functions as a support for the cell shape [37]. The mechanical properties of the cell and its ability to migrate mainly depend on this cytoskeleton. The main components of the cell cytoskeleton are microtubules, intermediate filaments, and actin filaments [38]. Actin filaments are the smallest filaments, with a diameter of 6nm, and have an essential role in cell motility [37].

1.1.3 F-actin and treadmilling

Actin is the most abundant protein in eukaryotic cells. It has a wide range of cellular functions, particularly in cell motility. There are two forms of actin in cells, monomeric (G-actin) and filamentous (F-actin). Features of the actin allow cells to turn F-actin to G-actin and vice versa rapidly. Consequently, cells are able to remodel their cytoskeleton on short time scales, which is a prerequisite for motility. These processes are regulated through various signaling pathways.

An actin filament is a two-stranded double helix with a diameter of $7-9$ nm [39]. The persistence length is a measure of the stiffness of a biopolymer. It is defined as a length above which the tangents at the two ends of the filament have no correlation. The persistence length of an actin filament is about 17 µm [40]. That is close to the typical size of cells. That explains the abundance of F-actin in the cytoskeleton providing structural support for the cell.

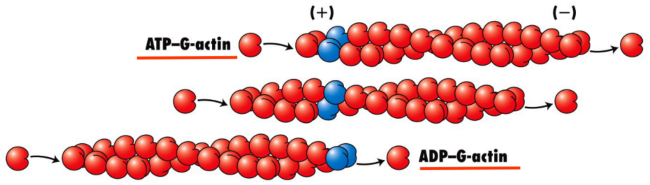

FIGURE 1.2: The process of actin treadmilling. ATP-actin monomers polymerize at the plus end and ADP-actin monomers depolymerize at the minus end. Figure is taken from [2].

At the plus end of filaments, ATP-actin monomers polymerize and elongate the filament. After the polymerization of a monomer, the associated ATP is hydrolyzed and releases the phosphate. That results in ADP trapped in the filament [41]. ADP actin monomers eventually leave the filament ends via depolymerization at the minus end [4, 42] (Fig. 1.2).

The two ends of the actin filament do not have similar properties, i.e., it is a polar structure [37]. At the barbed ATP-rich end (also called plus-end), the binding rate of monomers is fast, while at the pointed ADP-rich end (minus-end), the filament polymerizes slower. The polymerization rate is dependent on the concentration of G-actin in the solution. Actin monomers are also leaving the filament end. Unlike polymerization, depolymerization occurs at a constant rate and is independent of the cytosolic concentration of actin. At a critical concentration of G-actin in the solution, the rate of polymerization and depolymerization are equal for one of the filament ends. Since the polymerization rate is about ten times faster at the plus-end than at the minus-end, the critical concentrations of the two ends of the filament are not identical. In a range of cytosolic G-actin concentrations between the critical concentrations of the plus-end and the minus-end, the filament grows at one end and depolymerizes at the other. When the growth rate at the plus-end equals the dissociation rate at the minus-end of filaments, they reach a stable length. That is the mechanism of actin treadmilling, which is one of the main ways that cells convert chemical energy to mechanical work and produce force for motility [43–46]. Treadmilling is the main engine of cell motility machinery.

1.1.4 Actin Structures and regulatory proteins

Treadmilling of filaments provides the possibility to form stable actin structures that are actively extending in one direction. In mesenchymal motility, cells employ these active actin-based projections for motility. Lamellipodia are 2-dimensional flat structures with

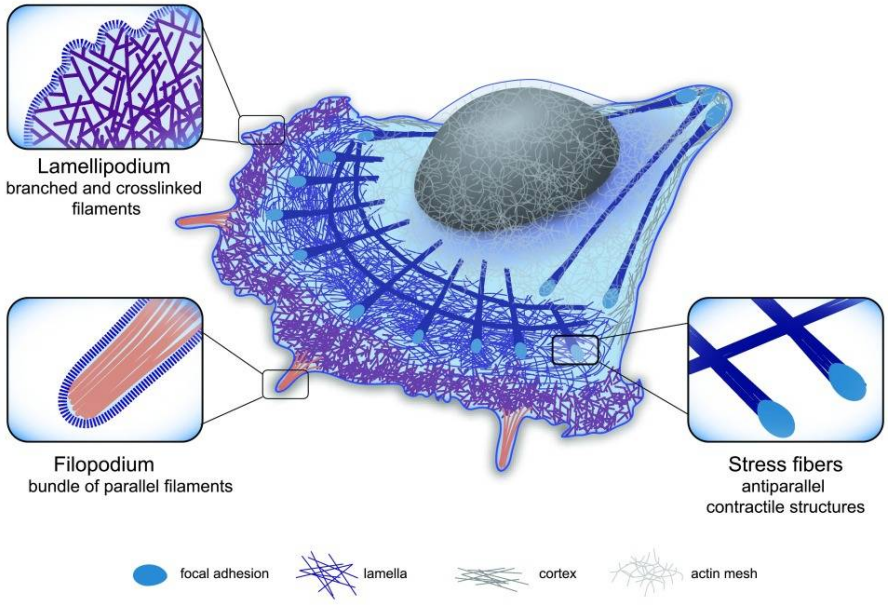

FIGURE 1.3: Different actin structures in the cell including lamellipodia, filopodia, lamella, actin cortex and stress fibers. Image is taken from [3].

a branched actin network that cells use for crawling on substrates [4, 42, 47]. Filopodia are 1-dimensional structures with parallel bundled actin filaments, which are also seen in crawling motion. These structures, as well as actin structures at the other parts of the cell, are illustrated schematically in Fig. 1.3. Long stress fibers are another type of actin structure that are present in many cell types [46]. Behind the lamellipodium there is a region called lamella. The actin filaments in the lamella are more bundled compared to those in the lamellipodium, in which the network is branched and cross-linked.

Several actin-binding molecules are responsible for forming the actin structures with different properties. The Arp2/3 complex has a major role in the formation of dendritic branched actin networks in the lamellipodia [48–50]. Arp2/3 binds to preexisting mother filaments and nucleates new daughter filaments [4]. The daughter filament is oriented at a 70 degrees angle from the mother filament. Hence, Arp2/3 can regulate the density and stability of the branched actin network. Several signaling pathways are known to activate Arp2/3 in lamellipodia, most importantly WASP-family proteins [51] (Fig 1.4).

Branching is a mechanism for the nucleation of new filaments in the network. Nevertheless, new filaments can also be generated by spontaneous stabilization of the actin dimers or trimer [52]. Formins are the second group of nucleators that can form unbranched new filaments (Fig 1.4).

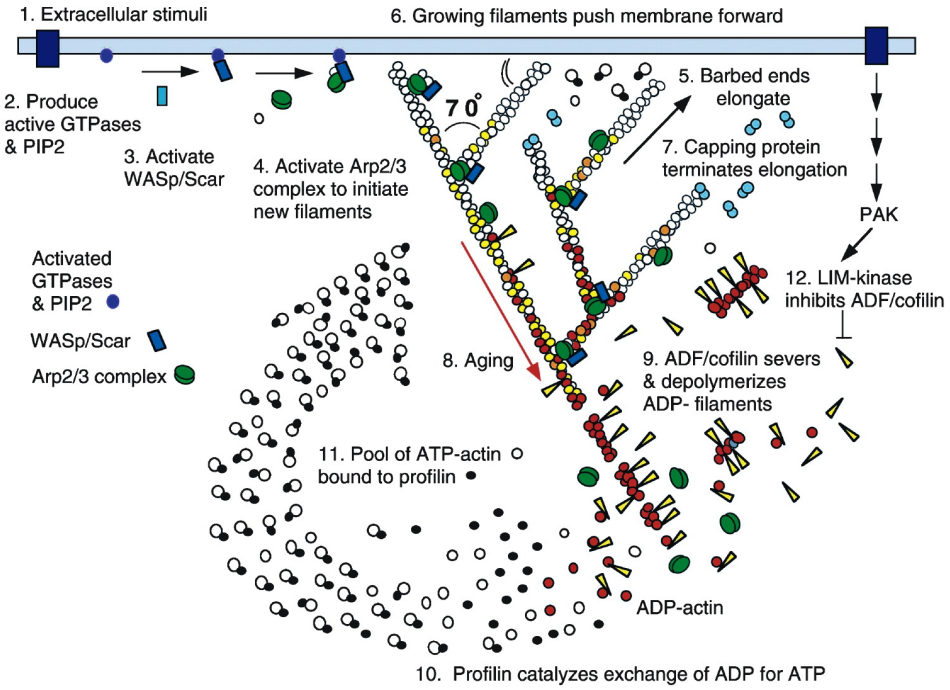

FIGURE 1.4: Important regulatory proteins of actin. The most important processes involved in dendritic nucleation and treadmilling of actin are shown with numbers. Figure is taken from [4].

Nucleation of new filaments is necessary for a stable network, but not sufficient. Fast elongation of the existing filaments is also crucial. Many proteins can promote the polymerization of actin monomers at the tip of filaments and enhance the elongation rate. For example, Formins and Ena-VASP proteins can control the rate of actin assembly and filament elongation [53, 54].

Capping protein (CP) binds to the barbed end of actin filaments and blocks polymerization. ADF/cofilin is a family of proteins that attach to actin filaments, severe the filaments and depolymerize microfilaments. Rapid depolymerization of F-actin mediated by cofilin replenishes the G-actin pool, which is required for treadmilling. The most important proteins involved in the dendritic nucleation and treadmilling of actin are shown in Fig. 1.4.

Filaments of a network should be linked together to form a stable structure. The linkage between filaments changes the mechanical properties of the network and makes it stiffer [55, 56]. That is a requirement for the F-actin structure in the lamellipodium since it should be capable of pushing the leading edge membrane [55, 57, 58]. The cross-linked F-actin network is formed by a group of cross-linker proteins: α-actinin, filamin family,

and Fascin are primary cross-linkers forming different actin structures in lamellipodia, lamella, and filopodia [59, 60].

Myosin is also a type of cross-linker that can additionally produce force. The contraction caused by Myosin is another primary process by which cells produce mechanical work from the ATP-ADP cycle (the other process is actin treadmilling) [61]. Myosin II has a substantial role in many biological processes. It is the main protein responsible for the contraction of muscle cells. In other cell types, myosin II is associated with actin structures and contracts the actin network. Thus, Myosin II, together with actin, are the most important molecules involved in cell motility.

1.1.5 Small GTPases family

Cell motility can occur due to an external signal. Neutrophils, Fibroblasts, and many other cell types can detect and follow chemical concentration gradients in a process called chemotaxis [62]. These external factors attach to the receptors on the cell surface and trigger internal signaling cascades, which in turn activate processes required for motility. However, cells can also move without external cues. For example, keratocyte cells can polarize and start moving without any chemoattractant [63]. In this case, cells do not move permanently in a given direction but rather keep their polarity for a limited time only. The polarization process and the mechanisms by which cells can keep their polarity are subject of current research. Different scenarios are suggested in different cell types. A lamellipodium that is formed at the cell front can suppress other lamellipodia through signaling or even mechanical tension [64]. The Rho family of GTPases is a group of proteins known for their crucial role in the signaling pathways related to cell motility. RhoA, Rac, and Cdc42 are three members of this family which have been studied extensively. These proteins can be found in either active or inactive states [65].

Activated Rho is mainly localized in the central and back regions of the cell [62]. Rho kinase (ROCK) is a downstream effector of Rho. Activation of ROCK promotes the myosin contraction and inhibits cofilin [66].

Growth factors attaching to the receptors on the cell membrane can activate PI3K, which activates Rac. Active Rac can activate the Arp2/3 complex through activation of the WAVE complex. It can also activate PAK, which in turn inhibits the myosin and cofilin

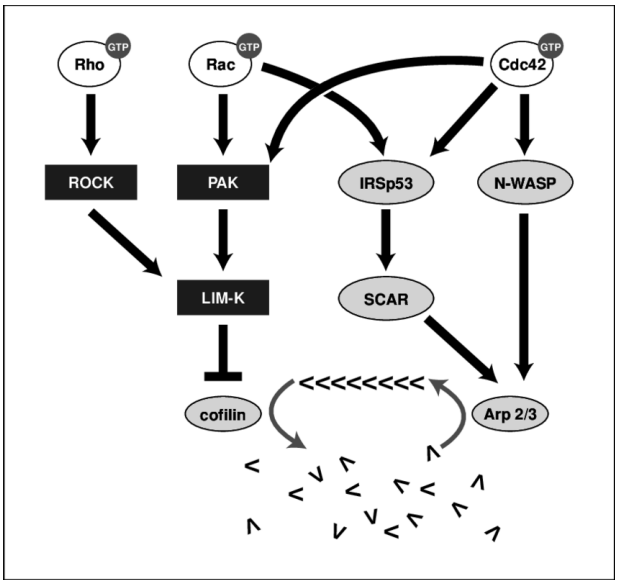

FIGURE 1.5: Small GTPases family. Small GTPases signaling proteins, including RhoA, Rac, and Cdc42, and their internal activation/inactivation pathways are shown with blocks and lines. Figure is taken from [5].

activity [67]. PAK also increases the crosslinking of the network via filamin. Promotion of actin branching and crosslinking caused by activation of Rac leads to lamellipodia formation. Active Rac can be mainly found in the lamellipodia [65].

The active Cdc42, which is known to be the main regulator of cell polarity, can be found at the cell front. It activates Arp2/3 complex through WASP family [68].

The activation of small GTPases does not occur necessarily through external cues. They can activate or inactivate other small GTPases. For example, Rho inactivates Rac. Rac activates or, in some conditions, inactivates Rho [67]. It is also reported that adhesion can activate small GTPases [69, 70]. Fig. 1.5 shows the most important GTPases signaling pathways.

1.1.6 Adhesion

Actin treadmilling is the core of the mesenchymal motility machinery in a cell which produces the propulsive force required for motion. But a cell is only able to move if it can transmit the force generated by actin polymerization to the substrate. Adhesion complexes between cell and substrate serve as traction points through which the cell can apply force and move forward [71–73]. Since the whole process of cell motility depends

on the force transmission between cell and environment, regulation of adhesion is of fundamental importance for controlling the motility behavior. Generally, the adhesion is regulated by the integrin-ligand interactions. Integrins are transmembrane cell receptors that connect cell and extracellular matrix mechanically. Integrins are also critical in mediating signaling between intracellular and extracellular environments. Ligands are the signaling molecules in the extracellular matrix that integrins can attach to. In addition to the integrin-ligand interaction, the force transmission between the treadmilling actin network and the substrate also depends on the linkage that connects the intracellular interface of integrins to actin filaments [74–76].

This linkage serves as a molecular clutch between the treadmilling actin network and the substrate [77] (Fig. 1.6). This molecular clutch system is built by several molecules such as focal adhesion kinase, α-actinin, paxillin, vinculin, and talin. The linkage strength of the molecular clutch is dependent on the composition of molecules. Some molecules like α-actinin tightly attach to the actin, while other molecules can detach and let the actin network slip over them. Thus, the molecular clutch system can be engaged or disengaged [69].

Adhesion structures are different in different parts of the cell. Integrins form small clusters in the regions close to the cell front, which are called nascent adhesions. The nascent adhesions usually disassemble in a few minutes after their formation. However, some of them can last longer and move to the proximal parts of the cell, lamella, and cell body. Those clusters grow into focal adhesions [70]. The focal adhesions are connected to the stress fibers. The effective adhesion strength is not uniform in all parts of the cell. It has been suggested that it is stronger at the regions close to the cell front and weaker at the back. This graded adhesion hypothesis implies that the pulling from the more adhesive front can detach back [39, 78, 79].

The strength of adhesion is regulated by many factors. A higher density of extracellular ligands increases the adhesion strength by providing more binding sites for integrins [70, 80]. It has been shown that there is an optimal density of ligands for faster cell migration [81].

Some studies suggested that mechanical force can increase the lifetime of the integrin-ligand bonds in a phenomenon called catch bond behavior [70]. Various intracellular

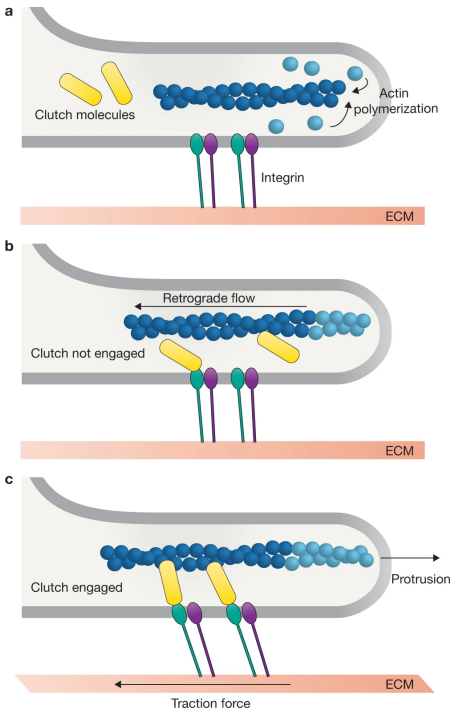

FIGURE 1.6: The clutch mechanism of cell adhesion. (a) Clutch molecules move to the interface between the flowing actin network and the intracellular side of the integrins. (b) They attach to either the actin network or the integrins. (c) They attach to the other side and engage the molecular clutch. Figure is taken from [6].

signaling pathways can regulate the molecular clutch system. In particular, there are some adhesion strengthening pathways mediated by myosin [13, 14, 82].

In summary, adhesion between cell and substrate is a key component of the mesenchymal cell motility, which can determine cell morphodynamics.

1.2 General constitutive relations in cell motility

Different cells exhibit various types of shapes and morphodynamics. Fish keratocytes are known for their fast and persistent migration. They form broad lamellipodia, and their shape does usually not vary during a migration. Dictyostelium discoideum is an amoeba that extends its pseudopodia in all directions. Those pseudopodia are very dynamic structures with protrusion and retraction cycles. Spread and moving cells can exhibit cycles of retraction and protrusion [83]. Lateral morphodynamic waves can travel around the edge in the spread and moving cells [84]. The morphodynamic pattern of the edge fluctuations can vary between different cell types or upon experimental manipulation of cells. Cell speed can vary at least one order of magnitude in different cell types. Despite

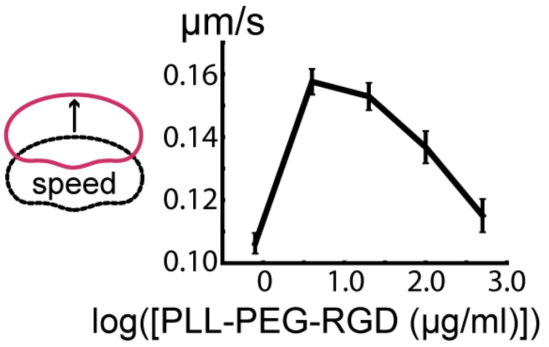

FIGURE 1.7: The biphasic dependency of cell velocity on adhesion. This relation is obtained from experiments on keratocyte cells plated on substrates coated with the indicated PLL-PEG-RGD concentrations. Figure is taken from [7].

the huge variability between different cell types and even between different cells of the same cell type, there are several universal observations in the mesenchymal motility of cells. Those observations are assumed to be universal since they have been reported in many cell types and various experimental conditions. In this section, we briefly describe some of these general observations. In the following chapters, we employ biophysical modeling and experiments on cells in different conditions to explain these fundamental relations of cell motility.

1.2.1 Biphasic adhesion-velocity relation

Adhesion sites are the means of force transmission between cell and the substrate [71–73]. The protrusive force that actin polymerization generates at the leading edge drives the retrograde flow of actin in the lamellipodia. The friction between this flow and the stationary structures in the cell produces a force that enables the cell to move forward. The density of such structures depends on the density of ligand proteins on the substrate [12–14, 85–87]. It has been shown that the cell velocity biphasically depends on the ligand density [12–14, 81, 85–87]. Upon increasing the ligand coating density on the substrate, the cell velocity increases initially and then, after a maximum value, decreases again (Fig. 1.7). That is a universal experimental observation that has been observed in many cell types. However, as yet, there is little mechanistic understanding of how adhesion controls the velocity. In chapter 3, we introduce a biophysical model which can explain the biphasic adhesion-velocity relation and the mechanisms shaping this relation.

1.2.2 Different dynamic states of cells

Cells can exhibit different states. In the absence of an external cue, a cell exists in the spread non-moving state or the moving state. A moving cell can naturally move in any direction. It has been shown that cells can spontaneously switch their state. Besides states of motility moving/spread, cells can also exhibit steady or oscillatory morphodynamic states. Cycles of protrusion and retraction can occur in cells in the spread or moving states. Observation of different states of cells and the apparently spontaneous transitions between them attracted attention towards multistability of cell motion in recent years [88–100]. In chapter 4, we analyze trajectories of MDA-MB-231 cells seeded on 1-dimensional patterns to characterize different states of cells. We employ a minimal biophysical model with the key components of the cell motility machinery to investigate how multistability arises from the competition of protrusions.

1.2.3 Universal coupling between cell speed and cell persistence (UCSP)

The movement of a cell can be described with different models of random motion. Due to this randomness, cells can not maintain their directions of motion permanently. The ability of cells to move without turning can be quantified by the persistence time. Persistence time is defined as the mean time during which cells keep their direction of motion. It has been shown that the persistence time of a cell is correlated with the cell velocity [101]. The faster cells move, the longer they keep their direction of motion. This correlation has been observed for many cell types and in different conditions (Fig. 1.8). Thus, it is believed that it is of similar universality as the adhesion-velocity relation.

A mechanism has been suggested by Maiuri et al. [8] to explain this robust universal relation based on the polarization caused by polarity factors advected with the F-actin retrograde flow in the cell. However, we find that this mechanism cannot explain the UCSP law in a condition with inhibited actin polymerization. In chapter 4, we investigate the UCSP law with our model based on the competition of protrusions. Our model provides mechanistic insight into the persistence time and its relation with velocity.

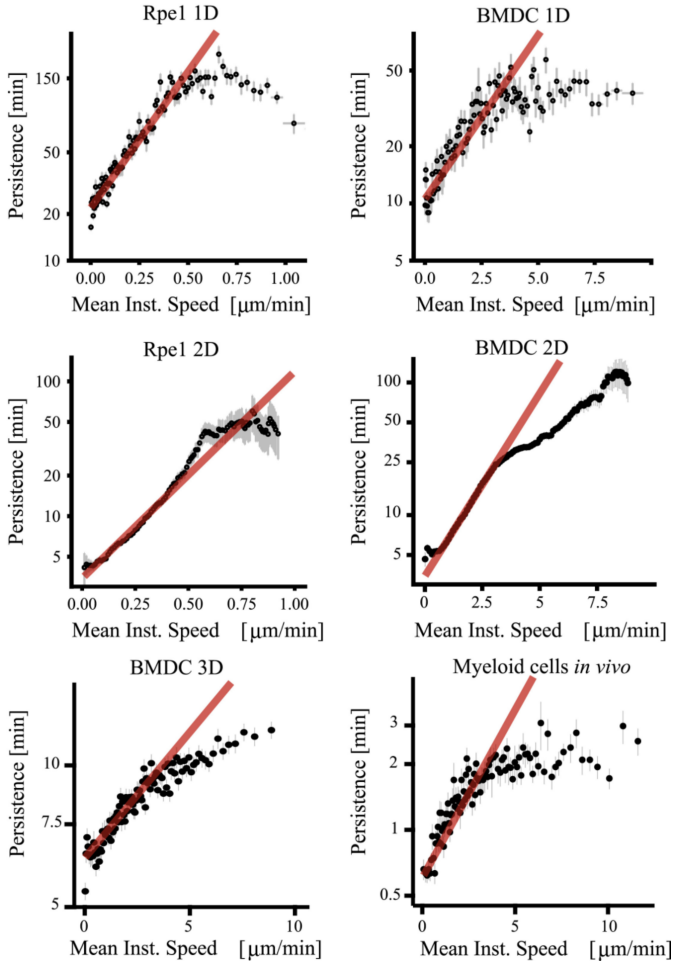

FIGURE 1.8: The universal coupling between persistence time and speed. UCSP is shown for 1-dimensional (top row), 2-dimensional (middle row), and 3-dimensional migration (bottom row). The red lines show exponential fits to the data. Figure is taken from [8].

1.3 Quantitative models of cell motility

Cell motility is a complex phenomenon with numerous molecular players and signaling pathways. Over the past decades, a vast amount of experimental data has been generated on motility components. In most cases, the system's complexity does not allow an intuitive explanation of the mechanisms in motility. That makes cell motility a very attractive field for mathematical modeling. Mathematical models can connect experiments to theories and provide mechanistic insight into different cell migration aspects. Modeling approaches in this field have been reviewed in detail in [102–105]. Here we mention some models on the major aspects of cell motility.

Actin polymerization is the basis of mesenchymal motility. Thus, many of the first modeling attempts in the field were filament models. "Brownian Ratchet Model" proposed a mechanism by which actin polymerization can produce force to push a membrane [106]. A gap between the filament tip and the membrane can show up from time to time because of the Brownian motion of the membrane. At those times, the actin monomers can enter the gap and attach to the tip of the filament. "Elastic Brownian Ratchet Model" takes the bending of filaments into account as well [107]. Some observations suggested attachment and detachment of filaments to the membrane, which led to the "Tethered Ratchet Model" [108]. The actin network's structure has also been modeled in several studies [109–114]. The arrangement and orientation of filaments in the network predicted by these models agree with the observations on dendritic networks in the cell lamellipodia. Network properties affect the relation between force and extension rate of the network at the leading edge [31, 115–117]. Some models could also reproduce the difference in the structure of actin networks in lamellipodia and lamella [118, 119].

Another category of models considers the actin network as a continuum gel [120–128]. These studies investigate the active behavior of actin networks, polymerization waves, and even vortices in active gels. The active polar gel theory by Kruse et al. [125] can predict actin flow network patterns, including the retrograde flow velocity at the leading edge and the traction force of the cell on a substrate.

Zimmermann et al. in [129] and [130] combined the gel description of the actin network with single filaments model close to the leading edge. With this approach, they could reproduce several dynamic aspects of the lamellipodia including membrane oscillations [129, 131, 132] and the dynamic force-velocity relation [15].

It is suggested by some studies that myosin contraction at the cell back plays a critical role in cell motility [4, 14, 133]. The contraction is usually modeled as an active stress in the gel [134]. The active stresses generated by actin polymerization or myosin contraction are transmitted to the substrate through adhesion.

The adhesion clusters form and mature in the cell. Their evolution and the effects of force and other factors on their strength are reviewed in [135, 136]. The first modeling study on the biphasic adhesion-velocity relation was by DiMilla, et al. [137]. This viscoelastic-solid model incorporates cell polarization, force generation, and dynamic adhesion in 1 dimension. The adhesion-velocity relation is also reproduced with a continuum model

for ameboid cell motility [138]. Both of these studies suggest that in a moving cell, the adhesion at the front should be stronger than at the back, i.e., the motion is the result of a tug of war between a highly adhesive front and a weakly adhesive back. Barnhart et al. reproduced the dependency of velocity on the adhesion strength in keratocyte cells, using a continuum model which includes adhesion, actin flow, and myosin contraction [7]. However, non of these studies could provide a comprehensive quantitative picture of the mechanisms shaping the biphasic adhesion-velocity relation. Also, the ability of cells to migrate from high to lower adhesion can not be explained by the existing models. Moreover, the nature of the front-back interaction required for the biphasic adhesion-velocity relation is not addressed yet.

Morphology and morphodynamics of the spread and motile cells has been another topic for the modelers to step in [97, 98, 132, 139–148]. Modeling studies on the morphodynamic patterns of motile cells are reviewed in detail in [83]. The dependency of the cell shape and area on the adhesion strength has been modeled for keratocytes [7]. Some studies investigated the role of the interaction between tension-sensitive molecules and membrane tension in cell morphodynamics [30, 149, 150]. The impact of membrane tension on the actin polymerization has also been suggested as a mechanism determining cell morphodynamics [104, 131, 141, 143]. Waves of actin polymerization can arise from the positive feedback in Arp2/3 branching [132, 145, 146]. GTPase signaling and its impact on the actomyosin network is another source of morphodynamic patterns in cells [96–98, 151].

Kuusela et al. have shown that myosin contraction is required for the formation of waves in the actin flow [152]. Another study could reproduce the morphodynamic pattern of the cell edge only with the actin boundary interaction and without myosin contraction [153].

Shao et al. proposed a model based on the phase field method, which can predict the experimentally observed relation between the cell velocity and the cell shape aspect ratio [121]. The model proposed by Barnhart et al. has shown that actin polymerization fluctuations are the source of protrusion waves, and promoting actin polymerization can switch wavy keratocytes to persistent cells [154]. This model suggests that negative mechanical feedback from the cell membrane is also critical for the protrusion waves.

Alonso et al. [155] proposed a mathematical model using phase field method and bistable kinetics of an effective polarity factor to describe the cell shape changes and locomotion

of D.discoideum cells. The model used a parameter to describe the balance between intracellular noise and polarity formation, and was able to reproduce the experimental cell shape and the overall intracellular patterns. This model could also reproduce the observed experimental coupling between cell speed and persistence time (see section 1.2.3). An extension of this model was used to study cell crawling modes, including amoeboid and fan-shaped forms[156, 157].

The turning of moving keratocytes has been investigated in some modeling studies [158, 159]. The model in [158] suggests that the cell changes its moving direction when myosin molecules accumulate in a spot at the cell rear and destabilize the axial symmetry of the cell. Allen et al. in [159] found that myosin contraction and adhesion at the cell back control the left-right asymmetries, which is the cause of turning. They suggest a form of "rear-wheel steering" independent of the actin polymerization at the cell front.

Cell polarization is a basic step of cell migration. Various mechanisms are suggested for cell polarization. Goehring and Grill reviewed mechanisms in which cell polarization arises from biochemical signaling pathways, mechanical signaling through forces, stresses, and transport, and mechanochemical interplay between mechanical and chemical signalling [160].

Cell polarization is suggested to be the result of spontaneous symmetry breaking [161], which is likely in low adhesion and high contractility condition. Several mechanisms are suggested for maintaining the cell polarity after it is established. Houk et al. [64] investigated different scenarios of long-range inhibition of actin assembly at sites other than the leading edge. They found that the increase of the membrane tension caused by leading edge protrusion is sufficient to inhibit the formation of secondary protruding segments on the cell's boundary. They suggest the membrane tension as the long-range inhibitor instead of diffusible molecules. That is in agreement with the results of another modeling study on the role of membrane tension in motility. Batchelder et al. [162] found that increasing membrane tension reduces lateral membrane protrusions and increases the cell velocity. Mueller et al. [163] increased and decreased the membrane tension by mechanical manipulation and found that actin network density and geometry adapt to the changes in membrane tension. This adaptation mechanism enables the cell to tune its protrusive force in response to external mechanical loads. Mechanisms controlling cell

dynamics based on the mechanical feedback rather than the chemical signaling circuitry are reviewed in [164].

Some other studies suggest mechanisms based on GTPase signaling responsible for maintaining the cell polarity. Bolado-Carrancio et al. introduced a model with RhoA–ROCK interactions at the rear and RhoA-DIA interactions at the front, which can reproduce oscillatory and steady motility of a cell [165]. This model suggests that distinct GTPase patterns at the cell back and front are coordinated through periodic GTPase waves. Another modeling study investigated the role of intracellular GTPase and extracellular matrix signalings and the interaction between them [166]. This study suggests that a model can explain the diverse migration patterns, including persistent polarity, oscillatory front and rear, and random dynamics if three elements are included in the model. Those critical elements are competition between lamellipodia for limited pools of GTPases, dependency of ECM signaling on the area of lamellipodia, and activation of Rho through ECM signaling. The modeling study in [167] also highlights the role of the activation of Rho signaling through the dynamic ECM-cell interaction on the states of the cell, namely random, oscillatory, and persistent.

Westendorf et al. [168] proposed a delayed feedback model in the regulatory network of the actin to explain the experimental evidences indicating that actin dynamics in chemotactic Dictyostelium cells work in a regime close to an oscillatory instability. Negrete et al. [169] have shown that adding noise to a generic nonlinear oscillator model can explain the large variability in the dynamics of actin polymerization of amoeboid cells.

Polarization of cytoskeleton components is usually considered as the first step of migration. A study by Hennig et al. [170] suggests that the stochastic detachment of one side of the cell caused by the stick-slip dynamics is sufficient for the initiation of motion without any polarized cytoskeleton.

The importance of stick-slip dynamics in cell motility is also highlighted by other studies. Ron et al. [99] proposed a 1-dimensional model showing smooth and stick-slip modes of motility. They suggested that large cell-to-cell variability in cell motility patterns can be explained by variability in the cell parameters like polymerization activity. The model introduced by Pierre Sens [100] showed that many dynamic patterns of cell motion could be reproduced by the interplay between the dynamics of cell-substrate adhesion

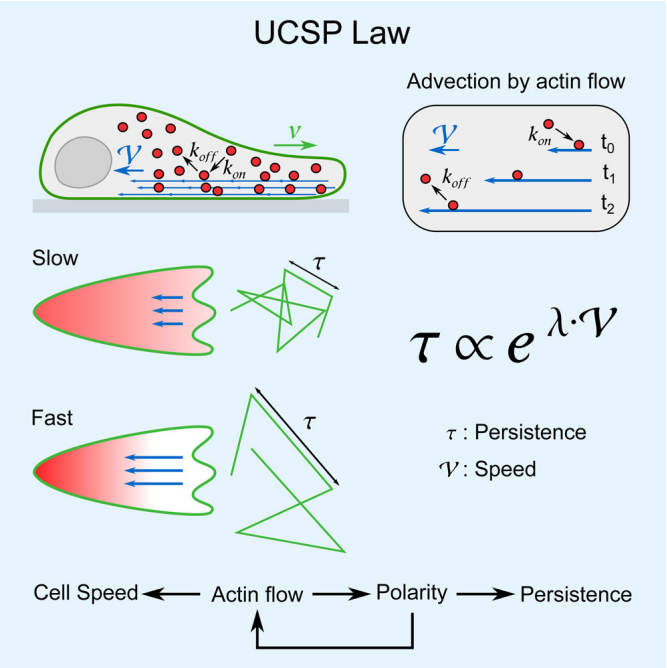

FIGURE 1.9: The UCSP mechanism based on the depletion of the polarity factor from the leading edge. Hypothetical polarity factors (red circles) attach to the drifting actin network (blue arrows) and drift backward. Actin extension rate is assumed to be faster in faster cells making the chemical polarity stronger. That, in turn, increases cell persistence. Figure is taken from [8].

and linear cellular mechanics. Although these models could reproduce spontaneous symmetry breaking, polarization of cells, and change of polarity direction, they do not explain how these processes are affected by intracellular and extracellular factors like substrate adhesion and cell velocity. They do not provide comparisons to well-established experimental relations in cell motility, like biphasic adhesion-velocity relation and UCSP law.

A notion that is closely related to cell polarity is cell persistence, which can be quantified by the persistence time. Investigation of motility behavior of various cell types in the first "world cell race" in [101] revealed a universal correlation between cell speed and persistence of motion. Maiuri et al. [8] studied the universal coupling of speed and persistence (USCP law) and proposed a mechanism based on the depletion of polarity factors attaching to the actin network from the leading edge due to retrograde flow (Fig. 1.9). Although this model was very successful in reproducing some experimental data, it can not justify the higher persistence time upon reduction of polymerization rate, as discussed in chapter 4 of this thesis. Furthermore, there is no experimental evidence of the F-actin binding polarity factors introduced in this mechanism.

The mechanism proposed by Maiuri et al., as well as many other mechanisms describing the persistence of cells, are memoryless, i.e., the motility behavior does not depend on the history of motion. D'Allesandro et al. [171] demonstrated that cells could remodel their environment and leave footprints, thus generating memory of their trajectories affecting their future exploration path.

Most of the models of cell motility can also predict the force-velocity relation. The first remarkable prediction of the force-velocity relation was made by the tethered ratchet model [108]. Mogilner and Oster predicted a convex relation between force and velocity, which was in agreement with the experimental results for single filaments. Then several studies proposed various models for the force-velocity relation of actin networks [114, 172, 173]. Unlike the dynamic force-velocity relation, the stationary relation has not been measured experimentally yet.

1.4 Our approach in this thesis

In this thesis, we study lamellipodial mesenchymal motility. We employ mathematics and physics to understand the complex phenomenon of cell motility better. Integrating and analyzing experimental data is the first step of a comprehensive study in such an interdisciplinary field. Numerous signaling pathways exist in the cell that are related to cell motility. These signaling pathways converge onto the structure of the cell cytoskeleton and the cell morphodynamics. The architecture of the filamentous structures in the cytoskeleton and whole cell morphodynamics are two sources of data that can be used to understand the internal mechanisms of cells. Some studies have analyzed these cell features for cell transformation characterization [174], cancer cell screens [175], and cell cycle [176, 177]. Cell cytoskeleton and morphodynamics are also associated with cell motility.

Experimental data can be generated on intracellular filamentous structures and cell morphodynamics using live cell imaging and cryo-electron tomography, respectively. These raw data sets need to be analyzed properly to exhibit meaningful biological information. In chapter 2, we will introduce two data analysis workflows to translate the raw cell data to relevant biological concepts. The actin filament network is one of the most important components of the molecular machinery of motility. The structural properties of this

network (as well as the other filamentous structures in the cell cytoskeleton) significantly influence the motility behavior of the cell. In the first part of chapter 2, we introduce a workflow that analyzes the structure of the filamentous networks, e.g., in lamellipodia or filopodia. This workflow generates biologically relevant metrics that can describe how efficient the structures of the networks are for their biological role.

In the second part of chapter 2, we introduce another workflow that analyzes the cell morphodynamics from the time-lapse movies of the cell. It generates multiple morphodynamic descriptors that quantify cell boundary patterns, such as lateral waves, coordinated protrusion-retraction cycles, and chaotic fluctuations. We test our analysis workflows by analyzing the cells treated with different drugs. That can provide insights into the underlying signaling pathways that regulate the structure of the filamentous networks and the whole cell morphodynamics.

Then in chapter 3, we investigate one of the constitutive relations in the field of cell motility, the biphasic adhesion-velocity relation. We combine experiments and theory to find the mechanisms shaping the adhesion-velocity relation. We analyzed MDA-MB-231 cells on 1-dimensional micro-lanes with fields of alternating ligand density. Our model with three basic relations for the force balance, force-dependent polymerization, and integrin signaling could explain the biphasic adhesion-velocity relations in all the studied cell types. We also perturbed the steady motion of cells by steps of ligand density to study the nature of front-back interaction in moving cells.

In chapter 4, we extend our model to study the dynamic features of 1-dimensional cell motion. We add the noisy clutch mechanism to our model. Based on our observation in experiments with MDA-MB-231 cells, we add a back protrusion that can compete with the front protrusion. Those changes enable us to investigate the constitutive relations related to cell dynamics. We first reproduce the biphasic adhesion-velocity relation and show that it is shaped by cooperative adhesion strengthening and force-dependent polymerization. Then we study the dynamic states of cells. We show that our model with mechanical competition between protrusions can reproduce all the dynamic states observed in the experiments. We also investigate the transitions between different states, including cell reversal. We show that the reversal mechanism that our model suggests matches our experimental observations very well. Finally, we provide a new explanation for the UCSP law, which unlike previous theories, can also explain the relation in

pharmacologically polymerization-inhibited cells. In the last chapter, we summarize our findings in this thesis.

Chapter 2

Quantitative characterization of cytoskeleton architecture and cell morphodynamics

A cell is a complex system with numerous signaling pathways regulating its functions, such as motility. Understanding this complex system is only possible through experimental observation and finding theories which explain those observations. A simple general experimental observation can be compared with the prediction of a theory qualitatively. In more complex cases, however, the experimental data should be quantified first.

Cytoskeleton architecture and cell morphodynamics are two sources of experimental data in the field of cell motility, which can provide insight into the internal signaling pathways of cells [178, 179]. However, they can not provide much information if used qualitatively. Quantification of these features of cells makes it possible to apply and test different theories. For example, applying a drug that blocks a signaling pathway in the cell may result in a subtle change in cell morphodynamics. By quantifying the morphodynamics with relevant descriptors, we can explain how much and in which aspects the drug and the blocked signaling pathway affect the morphodynamics. That allows hypothesizing about the involved biological mechanisms.

Actin cytoskeleton and its associated regulatory proteins are crucial in many cellular functions, including cell motility. The exact roles of many molecules in forming the

actin assemblies are yet to be understood. Recent developments in data acquisition and image processing tools need to be combined with quantitative analysis to allow characterizing the molecular machinery involved in cell migration. The first part of this chapter introduces the analysis techniques that can provide detailed quantitative descriptions of the mechanisms underlying actin network assembly and maintenance. We introduce a computational analysis toolbox that can be used for the quantitative characterization of actin filament networks from large Electron cryotomography (Cryo-ET) data sets. We test our toolbox for both branched and bundled actin networks. A detailed explanation of this toolbox has been published in [9]. I performed the conceptualization, methodology, mathematical analysis, and software development. The experimental data used in this section are produced at the Institute of Science and Technology Austria (ISTA) by Dr. Georgi Dimchev.

In the second part of the chapter, we introduce an analysis framework that characterizes the morphodynamics of motile cells. We compile the morphodynamics data of cells into the velocity and curvature maps, which makes morphodynamic patterns visually identifiable. We define several descriptors which parameterize the cell morphodynamics in smooth and erratic cells. Finally, we test the workflow for control and Lpd knockout cell populations and classify different groups based on their morphodynamic profiles. The description for our workflow of morphodynamic analysis has been published in [10]. I performed the conceptualization, methodology, mathematical analysis, and coding of the workflow. All the experimental morphodynamic data used to test the workflow are performed at Helmholtz Centre for Infection Research (HZI) by Dr. Georgi Dimchev.

2.1 A computational toolbox facilitating ultrastructural analysis of filament-rich structures

We developed a Matlab computational toolbox to facilitate a more streamlined approach of analyzing the filament populations and their characteristics in cryo-electron tomograms. In this section, the main features of this ultrastructural analysis toolbox are described.

The toolbox is compatible with any method for pre-processing of data. The toolbox performs the analysis on the coordinate data of filaments. However, it is blind towards

prior data preparation approaches. Thus, it does not limit the method of creating these coordinate files from the cryo-ET data. The workflow that is used in this thesis is an example of such methods for creating the filament coordinate file. In the first step, the tomograms are pre-processed in a deep learning-based tool such as Yapic. The goal of pre-processing is to segment filaments and increase the signal-to-noise ratio (SNR). The next step is to connect the segmented pieces appropriately. That can be done using the template matching approach [180] in a commercial software like Amira-Avizo (Thermo Fisher Scientific).

The graphical user interface (GUI) of our toolbox guides the user through multiple options for analysis, visualization, and extracting outputs from the input data sets. To characterize different filament architectures, such as branched networks (e.g., lamellipodia) or bundled filaments (e.g., filopodia/microspikes), a list of ultrastructural parameters is defined and calculated. A summary of the mathematical definition of all parameters is provided in section 2.1.1.

The process of creating the filament coordinates files usually produces some artifacts due to the high level of noise and missing wedge effect in cryo-ET data. That necessitates data cleaning and curation before ultrastructural analysis. Thus, we added multiple options for data cleaning in the toolbox. In Particular, it is possible to filter the data by custom ranges of angle, length, and bendiness. In order to compare filamentous assemblies with different fields of view or pixel sizes, there is an option in the toolbox to rescale the dimensions of coordinate files.

A visualization module is also included in the toolbox. It allows the user to review the analysis output for individual actin structures (Fig. 2.1 A). The GUI of the module offers many tools such as color-coding of filaments by various parameters (Fig. 2.1 B), 3D structure and arbitrary cross-section (Fig. 2.1 C). Another feature of the toolbox is the option to compare grouped data in desired aspects. Experimental groups can be compared with multiple parameters and graphs.

2.1.1 Ultrastructural parameters

In this section, we define some of the ultrastructural parameters by which filament structures can be characterized. Other parameters that are not described are self-explanatory.

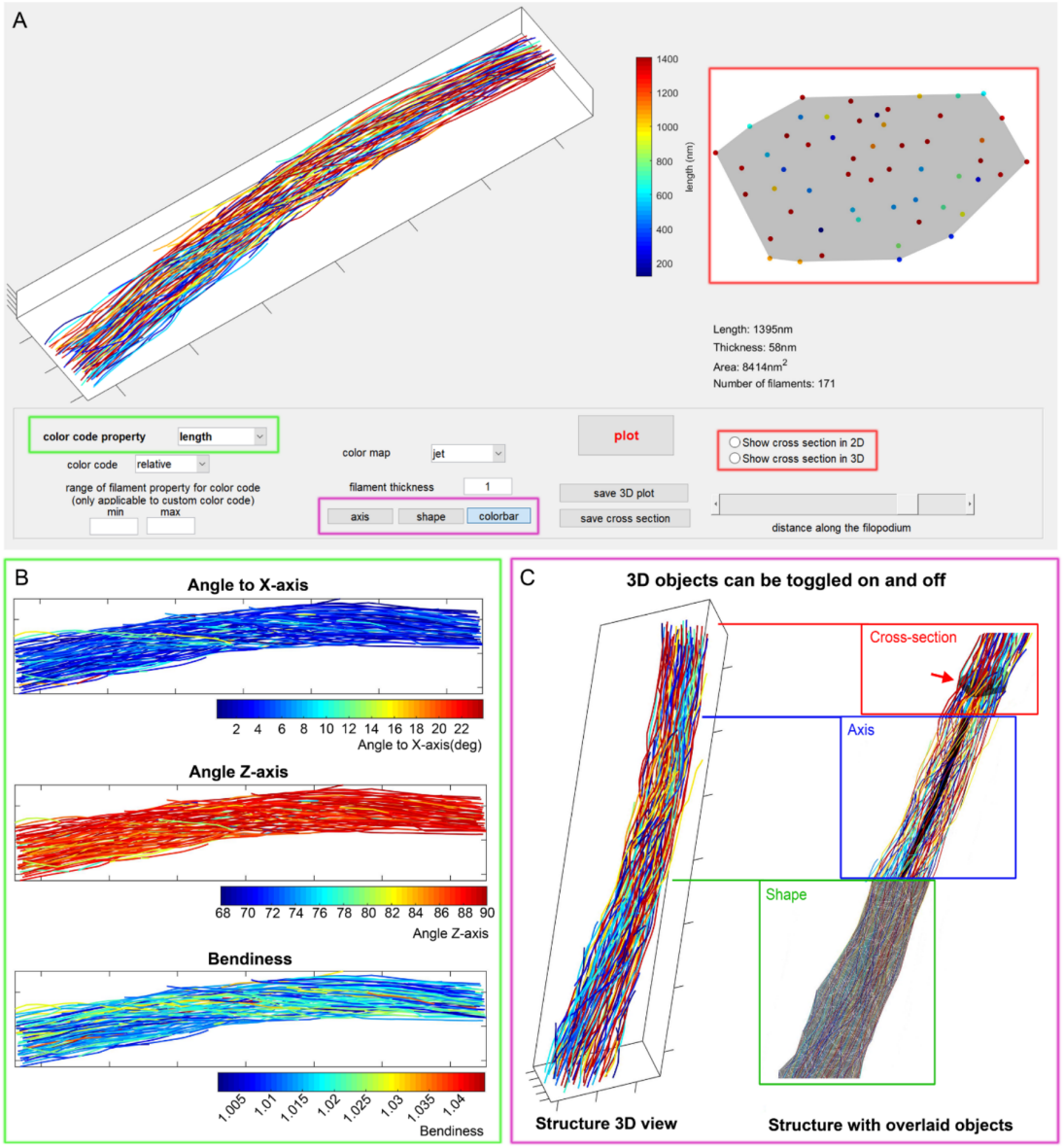

FIGURE 2.1: Visualization module. A-C) The GUI-based 3D visualization module integrated in the computational toolbox allows for customized structure visualization. Filament color coding can be based on custom ranges for length, bendiness, or angular orientation (the green rectangle shows the selected option in panel (A) and three alternative output examples shown in panel (B). Objects, such as axis, shape or color bar, can be displayed together with the structure (purple rectangles in (A) with respective examples in (C). The module allows visualizing the cross-sectional orientation of filaments (red rectangles in (A), with the position of the cross-section being adjustable along the axis of the structure (red arrow in (C). More information on the structure, such as length, thickness, area covered, and the number of filaments contained is also given below the cross-section visualization panel. This figure is originally published in [9].

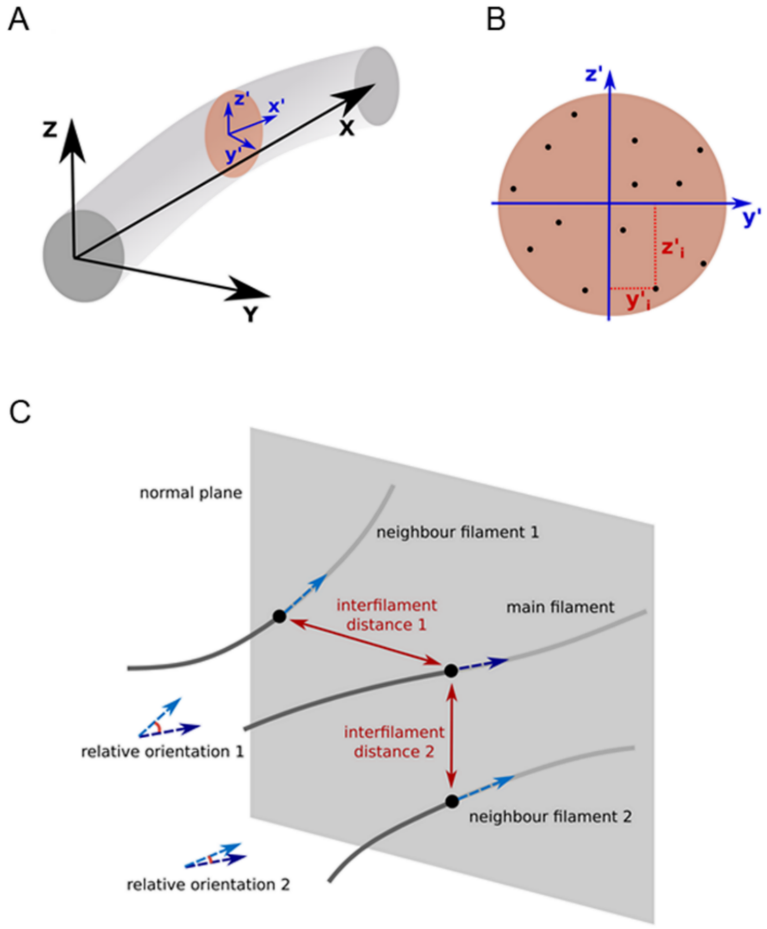

FIGURE 2.2: Definitions used for deriving ultrastructural parameters. A) The global frame of reference is shown with black letters and vectors. The local cross-sectional frame of reference is shown with blue letters and vectors for an arbitrary cross-section along the filopodium. B) The coordinates of a filament in the local cross-sectional frame of reference. Black dots indicate individual filaments intersecting with the cross section. C) Inter-filament distances and relative orientations at a certain point on a filament. A normal plane is defined as a plane perpendicular to the main filament at an arbitrary point. Black dots show the intersections of filaments with the depicted normal plane. Dashed vectors are the tangent vectors of the filaments at the intersection points. This figure is originally published in [9].

But first, we provide some basic definitions that are used to describe the parameters.

Reference direction: We require a reference direction to define the angle of filaments. In lamellipodia, the reference direction is the direction pointing toward the cell's leading edge membrane. In filopodia, it is the direction of a vector starting from the base and pointing to the tip of the filopodium (the "X" axis in Fig. 2.2 A).

Axis and cross sections: In addition to the reference direction, an axis is also required for some parameter definitions. We define the axis in lamellipodia as a straight line passing the center of the network and aligning in the direction of the leading edge

membrane. The axis in the filopodia, however, is a curved line from the base to the tip that follows the curve of the structure. We find this axis by fitting a second-order polynomial to the data points of the structure in the X-Y plane. We can now define the cross sections as the plane perpendicular to the axis of the structure at a certain point.

Frames of reference: We define two frames of reference. First, a global frame is defined with the three bases x, Y, Z (Fig. 2.2 A). X is aligned with the reference direction; Z shows the direction perpendicular to the cell plane (the plane that the structure is lying on). The axis Y can be found as the cross-product of Z and X. We also define a local frame of reference at points along the axis (Fig. 2.2 B). The basis x' is aligned with the local tangent of the axis of the structure. z' is defined similar to Z. y' is also found as the cross-product of z' and x'. We put the origin of the local frame of reference on the center of the mass of the cross-section.

Bending energy density of the structure: We define the bending energy density for the structure with its axis:

$$\frac{1}{L}\int_0^L \kappa^2 dl \tag{2.1}$$

With l being the distance along the contour, L the total length of the contour, and κ the local curvature.

Volume fraction of filaments: To calculate this parameter which is an indicator of the density in the structure, we assume filaments as cylinders with the diameter d (default value of d is 7 nm as in actin filaments).

Bending energy density of the filaments : We determine the bending energy density of individual filaments and then calculate the average in the whole structure.

Anisotropy of filaments : If the filaments form an isotropic structure, their angular distribution should be close to the uniform distribution. Thus, the mean squared deviation of the angular distribution from the uniform distribution is an indicator of the anisotropy of the structure:

$$\frac{1}{L}\int_0^{90} \left(P(\theta) - \frac{1}{90}\right)^2 d\theta \tag{2.2}$$

θ is the angle between a filament and the reference direction, and P is the probability distribution of angles.

Cross-sectional area fraction: We determine the average area fraction of a cross-section occupied by filaments in 50 equidistant cross sections along the axis. We assume the filaments' cross sections are circular with the diameter d (default value of d is 7 nm, as in actin).

Cross-sectional circularity of filopodia: Circularity of a cross-section is defined as the ratio of the area to the area of a circle with the same perimeter.

$$\frac{4\pi a}{p^2} \tag{2.3}$$

With a and p being the area and perimeter of the cross-section. Circularity is averaged over 50 equidistant cross-sections along the axis of the filopodia. If the cross-section of the structure is perfectly circular, its circularity is 1. For non-circular cross-sections, circularity is between 0 and 1.

Lateral bending stiffness of filopodia: To have a metric for the structure's resistance against lateral bending, we calculate the moment of inertia of the filaments in a cross-section about the z'-axis. We then average this moment of inertia over the 50 equidistant cross sections along the axis.

$$\sum_{i=1}^{n} y_i'^2 \tag{2.4}$$

With n being the number of filaments crossing the cross-section, and y_i' the distance of the i^{th} filament from the z'-axis (Fig. 2.2).

Vertical bending stiffness of filopodia: This property shows the resistance of the structure against vertical bending and is defined similar to the lateral bending stiffness.

$$\sum_{i=1}^{n} z_i'^2 \tag{2.5}$$

z_i' is the distance of the i^{th} filament from the y'-axis (Fig. 2.2).

Bendiness: We define bendiness as the ratio of the total length of a curve and its end-to-end distance. We calculate the bendiness for the whole structure (axis of the structure) and individual filaments (averaged over the whole structure). The value of bendiness is 1 for a straight line. Curved lines have bendiness larger than 1.

Parameters describing properties along the axis: The toolbox provides the option to illustrate the variation of the properties along the axis of the structure. We calculate the properties on cross-sections along the axis of the structure. To calculate the filament properties (bendiness, bending energy density, length, and angle) at a cross-section, we average that property over all the filaments intersecting the cross-section.

Parameters describing the spatial arrangement of filaments: We find the relative distance and angle of all pairs of filaments to describe the arrangement of the filaments in the structure. We select a filament as the reference filament and define a normal plane (perpendicular to the tangent) at a point on this filament (the grey plane in Fig. 2.2). Then we find the intersection of all other filaments with this plane. Distances of these intersection points from the reference filament are the interfilament distances. The angle between the tangent vector to a filament at its intersection point and the tangent vector to the reference filament is defined as the relative orientation (Fig. 2.2). We repeat this process for 200 points along each filament and reiterate it for all filaments of the structure.

2.1.2 Data analysis with the toolbox

In this section, we show the possibilities in the toolbox by analyzing two actin structures, lamellipodia and filopodia/microspikes. The data used here are obtained from frozen B16-F1 melanoma cells (Fig. 2.1C).

2.1.2.1 Branched actin networks

The actin structure in lamellipodia is a branched dendritic network. Arp2/3 complex is one of the major components of this structure that promotes filaments' branching. We used CK666, an inhibitor of the Arp2/3 complex, to investigate the effect of Arp2/3 inhibition on the architecture of the network. We used the toolbox to analyze CK666 treated and untreated (DMSO-control) cells. CK666 treatment led to a change in the network architecture. That is evident by comparing the angular distribution of filaments and their density with the untreated cells (Fig. 2.5B), which is in agreement with the literature [181].

Parameter set describing entire quasi-parallel filament structures(e.g. filopodia/ microspikes)		
Parameter name	Parameter short description and biological relevance	Unit [value ranges]
Length *(of structure)*	The axis length of the filopodium/ microspike.	nm
Bendiness *(of structure)*	Bendiness is defined as the ratio of the total axis length and its end-to-end distance. Bendiness of 1 defines a straight line. The more bent the structure, the higher the value.	a.u./ratio [≥1]
Bending energy density *(of structure)*	A metric of curvature and bending property of a contour, such as the axis of a filopodium/microspike. Bent structures have a higher value of bending energy. As compared to the bendiness parameter (described above), higher values of bending energy can also reflect various contour anomalies, such as edges or sharp change in directionality/curvature of a filament. *For a more detailed mathematical description, see methods section.*	nm^{-2}
Cross-sectional circularity *(of structure)*	Mean cross-sectional circularity of the structure averaged across a user-defined number of equidistant cross-sections along the axis. Circularity is defined as the ratio of the cross-sectional area to the area of a circle with the same perimeter. It characterizes how similar the average cross section of the structure is to a perfect circle. For a perfect circular cross-section circularity equals 1, while more flattened structures will have a lower value of this parameter. *For a more detailed mathematical description, see methods section.*	a.u./ratio [≤1]
Vertical bending stiffness *(of structure)*	The moment of inertia of filaments in a cross-section with respect to the y-axis. The parameter is associated with stiffness and describes the resistance of the structure against bending in z direction (e.g. filopodium tip rises from the substrate). Note that the parameter does not consider potential binding events between individual filaments or between filaments and other proteins, which might occur *in situ*. *For a more detailed mathematical description, see methods section.*	nm^2
Lateral bending stiffness *(of structure)*	The moment of inertia of the filaments in a cross-section with respect to z-axis. The parameter is associated with stiffness and describes the resistance against lateral bending, e.g. how resistant a filopodium/ microspike is to bending sideways along its axis. Note that the parameter does not consider potential binding events between individual filaments or between filaments and other proteins, which might occur *in situ*. *For a more detailed mathematical description, see methods section.*	nm^2
Parameter set describing entire network structures of randomly distributed filaments (e.g. lamellipodia)		
Parameter name	Parameter short description and biological relevance	Unit
Height *(of structure)*	Average height of the structure. It is averaged for a user-defined number of equidistant cross-sections, considering the lowest and highest Z-coordinate points in each cross-section.	nm

FIGURE 2.3: Description of parameters included in the computational toolbox, specific to either quasi-parallel filament arrays or dendritic networks. This table is originally published in [9].

Parameter set describing filaments in both quasi-parallel and randomly oriented networks (filopodia/microspikes/lamellipodia)		
Parameter name	Parameter short description and biological relevance	Unit
Length of filaments	Mean contour length of all filaments in the entire structure.	nm
Bendiness of filaments	Mean bendiness of the filaments averaged within the entire structure. The bendiness parameter for filaments is derived similarly to the one for the entire structure (see Table 1).	a.u./ratio [≥1]
Barbed/pointed ends	Density of filament start/end points along the axis of the structure, also known as pointed/barbed ends, respectively, for actin filaments. The pointed end of a filament is defined as the one closer to the base of the structure, while the barbed end as the one closest to the edge/tip.	um^{-3}
Anisotropy of filaments	Measures the preference of certain filament orientations towards the edge/tip. For a filament network of entirely random orientations, anisotropy is zero. For a structure with preferred angle of e.g. 70 degrees to the edge, anisotropy is higher. For bundled filament structures with parallel filament arrays, such as in filopodia, the value of the parameter is maximal. *For a more detailed mathematical description, see methods section.*	[0-~1]
Angle of filaments	Mean angle of the end-to-end vector of filaments to the reference direction, averaged across the whole actin structure.	Degrees [0–90]
Volume fraction of filaments	Ratio of the total volume of all filaments to the total volume of the structure. *For a more detailed mathematical description, see methods section.*	a.u./ratio [0–1]
Bending energy density of filaments	A metric of filament curvatures averaged within the entire structure. The bending energy density for filaments is derived similarly to bending energy density of structure (see Table 1). *For a more detailed mathematical description, see methods section.*	nm^{-2}
Number of filaments in the structure	Total number of individual filaments in the structure.	–
Cross-sectional area	Mean cross-sectional area of the structure averaged for a user-defined number of equidistant cross-sections along the axis.	nm^2
Cross-sectional density	Ratio of the number of filaments passing a cross-section to the area of the cross-section, averaged for a user-defined number of equidistant cross-sections along the axis.	nm^{-2}
Cross-sectional volume fraction	Ratio of the total cross-sectional area of filaments passing a cross-section to the area of the cross-section, averaged for multiple cross-sections along the axis. *For a more detailed mathematical description, see methods section.*	a.u./ratio [0–1]
Cross-sectional number of filaments	Number of filaments passing a cross-section, averaged for a user-defined number of equidistant cross-sections along the axis.	–
Additional parameters		
Base/tip ratio of Parameter X	The value of Parameter X in the first half of the structure (closer to the base) divided by the mean value of the Parameter in the second half of the structure (closer to the tip/edge).	a.u./ratio

FIGURE 2.4: Description of parameters included in the computational toolbox, valid for both quasi-parallel filament arrays and dendritic networks.This table is originally published in [9].

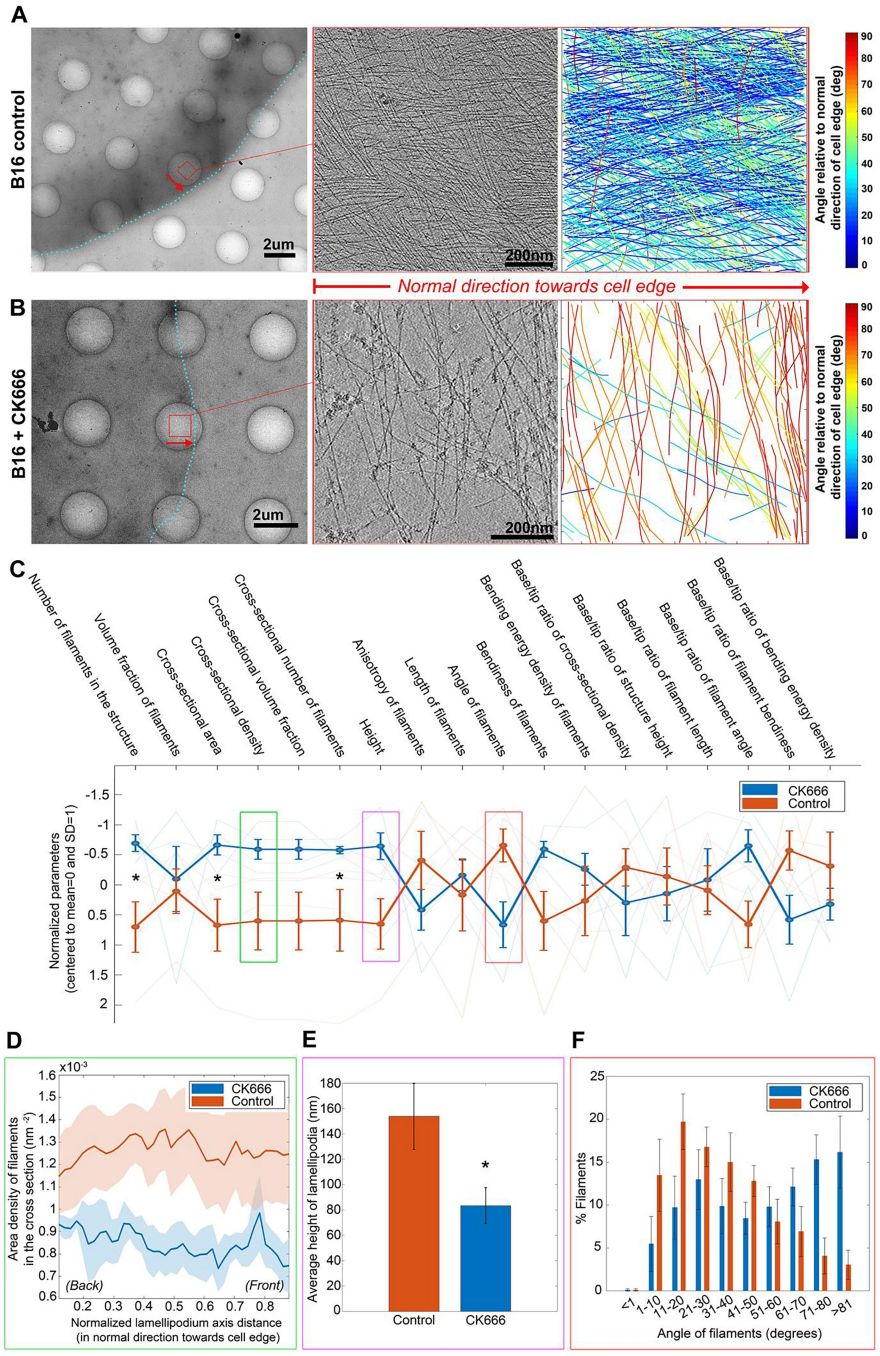

FIGURE 2.5: Analysis of branched networks. A-B) Analysis of filament networks in cryo-electron tomograms of lamellipodia of (A) B16-F1 mouse melanoma cells treated with DMSO control or (B) treated with 210 µmof the Arp2/3 inhibitor CK666. Left panels: Low-magnification images showing the cell peripheries. The cell edges are manually annotated by a cyan dotted line. Middle panels: 10 summed computational slices through bin8-tomograms of B16 lamellipodia. Right panels: Output generated by the computational toolbox, color coded for angular distribution relative to the normal direction. Red arrows indicate the orientation of the axis towards the edge. C) Normalized values of multiple ultrastructural parameters. Thick lines indicate the averaged values for all data files in a group, while thin lines show the values of individual data files. D-F) Parameters selected from the graph in panel (C) plotted individually. D) Cross-sectional filament density along the lamellipodial axis in normal direction to the cell edge. The transparent outlines indicate standard deviation. E) Average lamellipodium height. F) Angular orientation of filaments in lamellipodia. Statistical significance (paired t-test, p 0.05) between experimental groups is marked with *. N of tomograms is 4 for both control and CK666 groups. This figure is originally published in [9].

The toolbox provides a linear plot visualization including all the relevant parameters describing the filament networks. That illustrates an overall comparison of data sets (Fig. 2.5C). This general comparison can be followed by more detailed specialized visualization options. For example, Fig. 2.5C shows that the filament density is changed in CK666 treated cells. We can additionally show the density along the axis of the entire structure (Fig. 2.5D) to study the differences between the front and back regions. The toolbox provides histogram plots to compare the distribution of parameters like the orientation of filaments between experimental groups. Fig. 2.5F shows that in CK666 treated cells more filaments have angles of >60 degrees relative to the control cells. In addition, the toolbox offers the option to find correlations between all parameters in each experimental group or categorize data by e.g., principal component analysis. Another available analysis in the toolbox is the spatial distribution of filament's start and end points along the axis of the structure. That can show the differences in the density of pointed/barbed ends at different regions of lamellipodia for each experimental condition (Fig. 2.6). To remove the false positives on the edges of cropped area (Fig. 2.6A), the toolbox allows the user to set custom boundaries for detected pointed/barbed ends (Fig. 2.6B).

2.1.2.2 Bundled actin structures

We analyzed two bundled filament structures with our toolbox to find their characteristic differences. One of the structures is a protruding filopodium, and the other is the posterior regions of a non-protruding microspike (Fig. 2.7). The roots of microspikes are known to have a less uniform arrangement of filaments as compared to the protruding filopodia [182].

Similar to the branched networks, the toolbox allows displaying a linear plot with all related parameters of bundled filament structures (Fig. 2.8A). That rapidly highlights the main ultrastructural differences between filopodia and microspikes. Note that some of the associated parameters of the bundled structures differ from the parameters related to lamellipodia.

Different parameters can be studied in more detail with various graphs. As an example, Fig. 2.8B shows that the cross-section of the microspike is less circular in the back regions relative to the tip of the filopodia. That can be an indicator of less tight bundling or

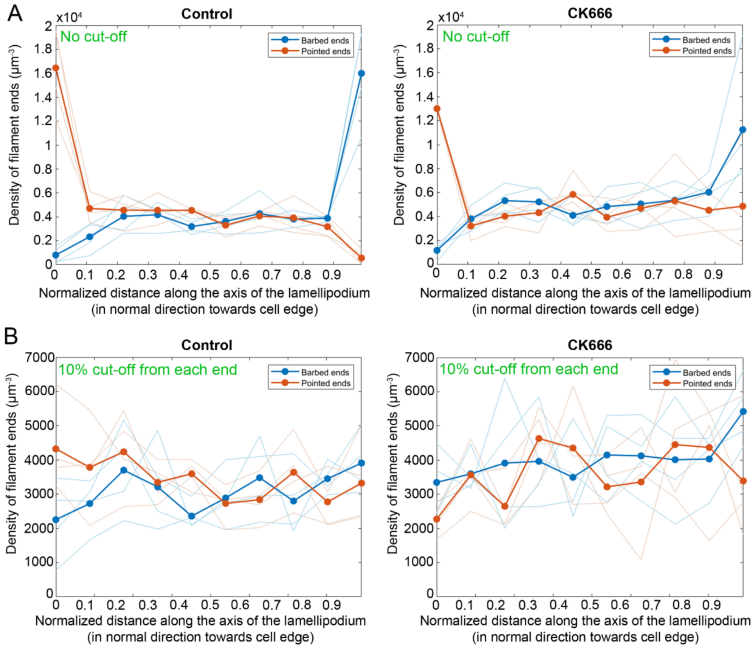

FIGURE 2.6: Distribution of filament barbed and pointed ends along the lamellipodial axis. A-B) The distribution of barbed and pointed ends of actin filaments is shown for B16-F1 cells treated with DMSO (as control, left panels) or with CK666 (right panels). A) No edge boundary cut-off was considered leading to an obvious accumulation of pointed and barbed ends at the back and front regions of the structure, respectively. B) Same representation of the distribution of filament barbed and pointed ends, excluding those positioned within the first and last 10% of the axis length. For all panels, thick lines indicate the values averaged for all data files in a group, while thin lines indicate the values for individual data files. This figure is originally published in [9].

irregularity of the arrangement of filaments at the base of the microspikes. That is also reflected in the lower values of the base/tip ratio of filament cross-sectional density and filament numbers in microspikes relative to that ratio for filopodia (Fig. 2.8A). Actin structures in filopodia and microspikes are also different with respect to angles relative to the axis (Fig. 2.8C), and filament bendiness (Fig. 2.8D).

Another approach for comparing the architecture of filaments is to show relative orientation and interfilament distance between filament pairs. That type of analysis has been used before in [183] to study the regularity of bundled structures.

This method identifies the regularly arranged filaments within the whole structure, which can be characteristic of tightly bundled structures like filopodia. We find an accumulation of parallel filaments with the interfilament distance of about 10 nm. (Fig. 2.8E, F) Such accumulation has not been found in the microspike (Fig. 2.8H). Finally, a visualization module allows the user to display the structure and its cross-sections at desired positions or characteristics (Fig. 2.1A).

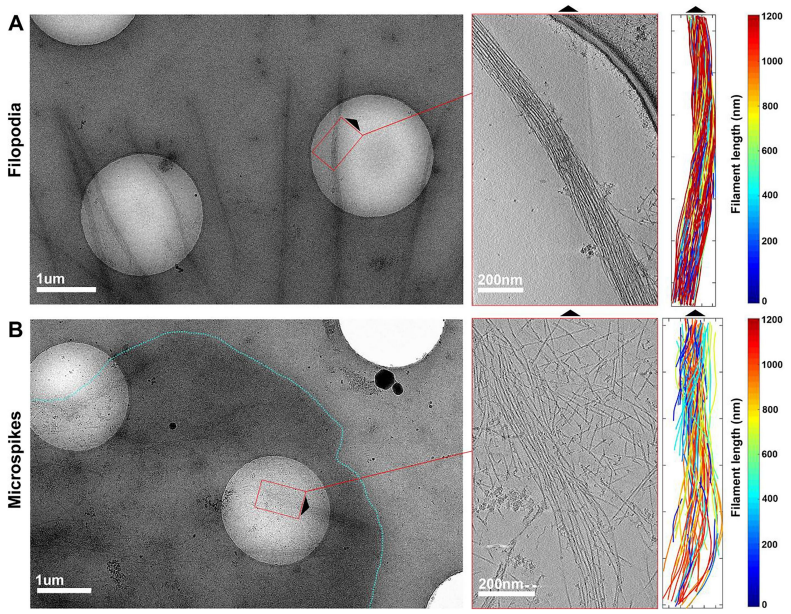

FIGURE 2.7: EM micrographs of filopodia and microspikes used for analysis. A) filopodia protruding beyond the cell edge B) posterior regions of microspikes embedded within lamellipodia. Filaments belonging to the lamellipodial networks were manually removed with IMOD. In (A) and (B), left panels show medium magnification maps of the cell periphery. The cell edge is manually annotated by a cyan dotted line. Middle panels show a tomogram slice of the analyzed region. Right panels show the output generated by the computational toolbox, color coded for filament length. Black arrowheads indicate the direction of the microspike/filopodial tip. This figure is originally published in [9].

2.2 A workflow for cell edge analysis

Many internal mechanical and biochemical regulatory networks are involved in the dynamics of the cell cytoskeleton. The cytoskeleton dynamics, in turn, affect the cell edge morphodynamics. Thus, in experimental investigations of the pathways that impact cell motility, cell-edge morphodynamics can be used as the readout of the state of the cytoskeleton. Cell morphodynamic data are mostly analyzed manually and qualitatively, despite their great importance in the study of molecular functions. Thus, a rigorous methodology for quantifying cell morphodynamics is still lacking. In this section, we introduce a framework for semi-automated analysis of cell morphodynamics. The input of the framework is time-lapse movies of cells on substrates. The first step for the analysis is to track the cell edge through all time frames and obtain the edge coordinates at each time point. In the next step, multiple mathematical metrics are defined that can characterize the morphodynamics of the edge.

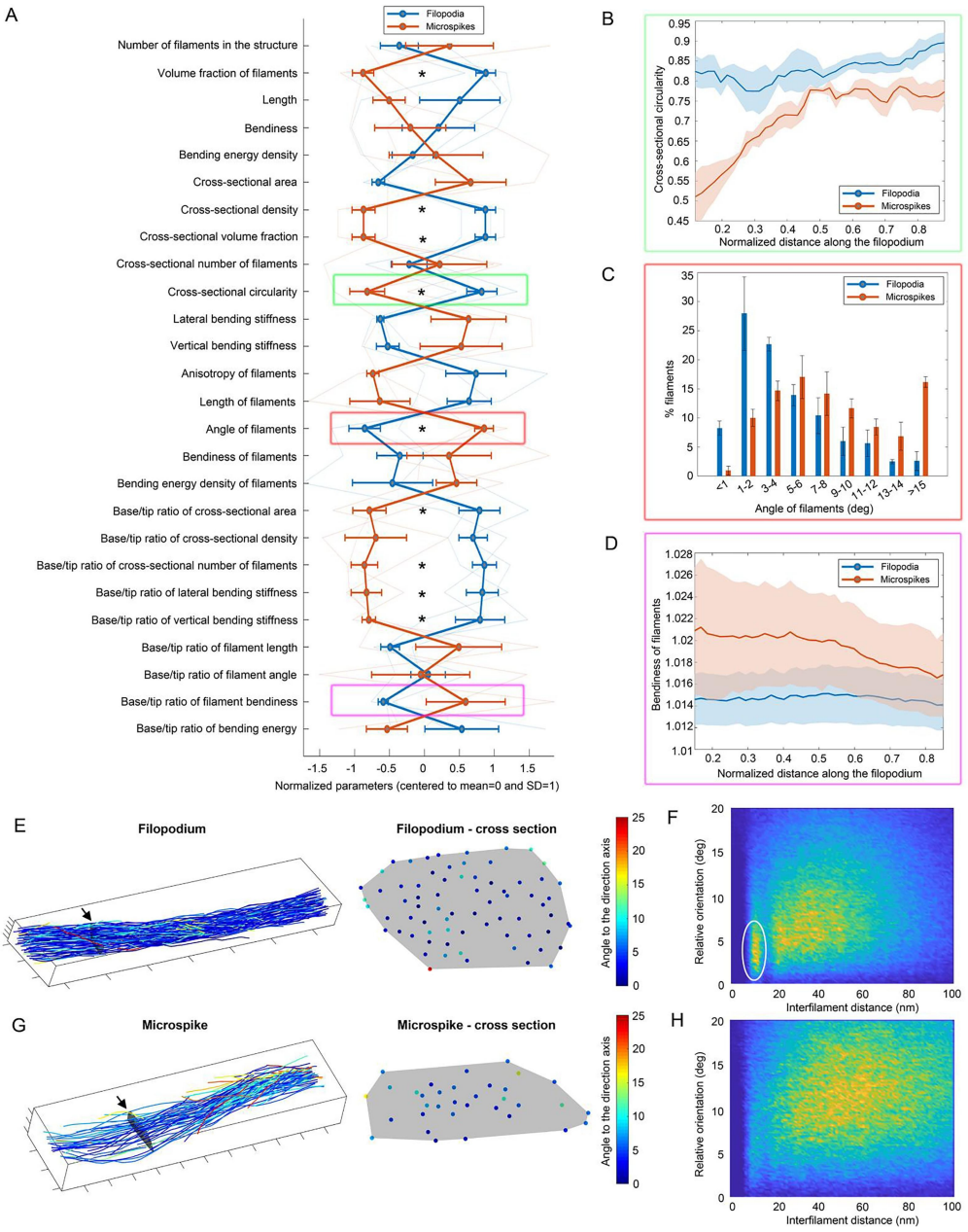

FIGURE 2.8: Analysis of bundled filament arrays. A) Normalized values of multiple ultrastructural parameters. B) Cross-sectional circularity of filopodia/microspikes (the transparent outlines indicate standard deviation), C) Angular orientation of filaments. D) Local bendiness of filaments along the axis of the structure. E, G) Spatial organization of filaments in protruding filopodium (E) and posterior microspike (G). Black arrows indicate the location of investigated cross-section along the axis. Filaments are Color-coded by their local angular orientation to the axis. F, H) Relating distances between filament pairs to their relative local orientations. White oval indicate a high number of tightly bundled and parallel oriented filaments in filopodia. Statistical significance (paired t-test, p 0.05) between experimental groups is marked with *. The number of tomograms is 3 for both filopodia and microspike groups. This figure is originally published in [9].

2.2.1 Cell-edge tracking

The time-lapse movies that are used for morphodynamic analysis should be acquired with high temporal resolution so that the edge fluctuations are not missed. Here we use time-lapse movies with a time interval of 1 s and length of 120 time frames (2 min of acquisition time). Pre-processing of the movies can also help the process of cell edge tracking. We processed the time-lapse movies in ImageJ with various filters, including Gaussian blur, smooth, enhance contrast, and find edges filters. Also, to have the optimal separation of the cell from the background, the contrast and brightness of the movies are adjusted. We used the JFilament 2D plugin [184] in ImageJ to find and track the cell edge in all frames of the time-lapse movies. The edge tracking method in JFilament is based on stretching open active contours, which can deform and align with the bright lines in an image, which are the cell edges in our case. The parameters of the algorithm can be adjusted depending on the movie. The output of the Jfilament plugin is a "snake" file that contains the coordinates of a number of representative points on the cell edge in all time frames. These snake files were fed into a Matlab workflow to calculate morphodynamic parameters.

2.2.2 Displacement field of the contour

We can calculate the displacement and velocity fields on the cell edge using the coordinates of the cell contour in all time frames that are obtained by edge tracking in Jfilmanet. A fixed number of representative nodes are considered on the cell edge at any given time frame. Then an algorithm is required to map the representative nodes on the curve in an arbitrary time step t (i.e., C_t) to the curve in the next time step $t+1$ (i.e., C_{t+1}). Here we introduce a mapping method using a set of springs. Two groups of springs are employed in our mapping algorithm, uniform and reference springs. Uniform springs connect neighboring representative nodes of a contour C_{t+1} (Fig. 2.9). Reference springs are the group of springs that connect these nodes on the curve C_{t+1} to the fixed reference points on that curve. We define the fixed reference points as the intersection of the lines perpendicular to the curve C_t at the representative nodes of C_t, with the curve C_{t+1}. In other words, if representative nodes of C_t radiate outward in the direction perpendicular to the curve C_t, they will reach the fixed reference points on curve C_{t+1}. In the parts of the cell edge where the curves C_t and C_{t+1} are almost

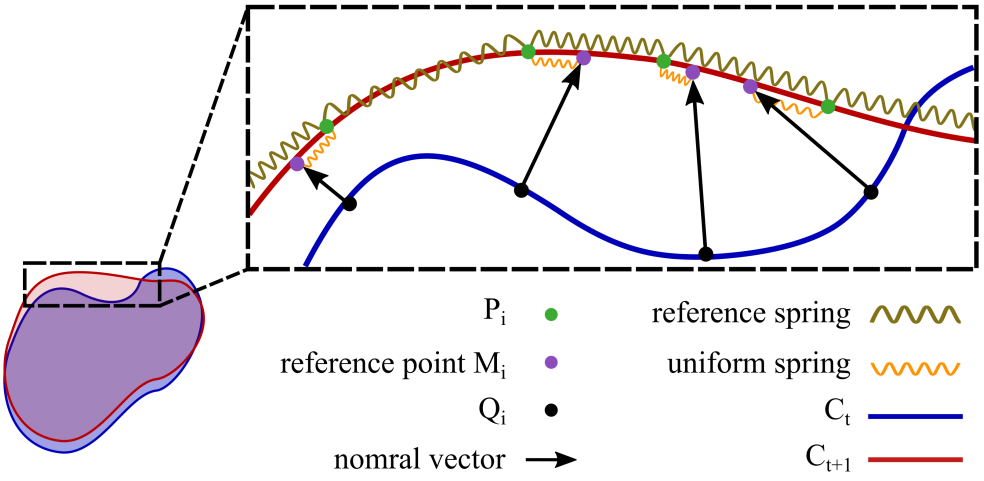

FIGURE 2.9: The mechanical system of springs and nodes for the mapping of boundary representative points between two consecutive time frames. The positions of the representative points P_i on the curve C_{t+1} are obtained by using the positions of representative points Q_i on C_t and solving the mechanical system of uniform springs and reference springs.

parallel, the assumption that the representative nodes move perpendicular to the curve is reasonable. Thus, the reference springs tend to keep the representative nodes on curve C_{t+1} close to the reference points.

On the other hand, in the parts of the cell edge with high deformations and enhanced convexity/concavity in the curves, keeping the representative nodes close to the reference points does not lead to a realistic distribution of representative nodes on curve C_{t+1} (the distances between neighboring nodes varies a lot, with some regions of very squeezed or stretched nodes). In those edge regions, uniform springs do not let the nodes be over-stretched or -squeezed. Thus, the uniform springs always tend to keep the distribution of nodes close to the equidistant distribution.

We combined the reference and uniform springs to have the advantages of both mappings in our mapping algorithm. To make the algorithm more adaptive to the deformation state of the curves, the two groups of springs have variable weights as a function of the curve's local deformation or parallelism degree. The mapping relies more on the reference mapping (with dominating effect of reference springs) in the regions with low deformation. In the high deformation regions, though, the uniform springs have larger weights and attenuate the inhomogeneity of the representative nodes distribution caused by reference springs.

To find the position of representative nodes on the curve C_{t+1}, we construct the mechanical system of spring as explained. A similar mechanical system is described previously in [185], with some differences. First, the springs responsible for reference mapping are linear in our method. Furthermore, all the springs in our method are attached to the curve. That simplified the nonlinear system of equations for finding the position of representative nodes on curve C_{t+1} to a linear one. Thus the computational cost of our method is much less without compromising precision for the mapping. Finally and most importantly, the adaptivity of our algorithm, caused by the dependency of spring constants on the local deformation degree, results in reasonable mapping regardless of the curve's deformation state.

The algorithm aims to find the position of N representative nodes P_i, i=1:N on C_{t+1} by using the position of N known representative nodes Q_i, i=1:N on C_t and solving a system of equations. The positions of Q_i nodes are known from the same procedure in the previous time frame. Uniform springs connect neighboring nodes on C_{t+1} (P_i and P_{i+1} for i=1:N). The rest length of these springs is defined as $l_{0,t+1}$=L_{t+1}/N, where L_{t+1} is the total length of the curve C_{t+1}. Reference springs connect each node P_i to its corresponding reference point M_i, i=1:N, which is defined as the intersection of the curve C_{t+1} and a vector perpendicular to C_t at the node Q_i. The rest length of these springs is zero. The strength of the attraction is dependent on the spring constant, which in turn defined to be a function of the local deformation degree.

We define the local degree of deformation at each node P_i as:

$$D_i = c_1.max\left(0, \frac{(l_i + l_{i+1})}{2} - l_{0,t}\right) + c_2.max\left(0, l_{i+1} + l_i\right) + c_3.max\left(0, -\left(l_{i+1} + l_i\right)\right) \tag{2.6}$$

c_1, c_2, c_3 are constants and l_i is the contour length between the nodes M_{i-1} and M_i on C_{t+1}. This length can be negative if M_i appears before M_{i-1}. The first term increases in the nodes where the curves C_t and C_{t+1} are not parallel (their direction is not similar). The second term increases in the nodes that the curvature on the curves C_t and C_{t+1} are not similar. The last term in the above equation is non-zero if there is a discrepancy between the order of Q nodes and P nodes. The function of this term is to increase the deformation degree at the regions with non-matching order of nodes in subsequent time

frames. Then we define the spring constants as functions of deformation degree.

$$K_{ref,i} = \frac{k_1}{k_1 + k_2 D_i} \tag{2.7}$$

$$K_{uni,i} = \frac{k_3 D_i}{k_1 + k_2 D_i} \tag{2.8}$$

$K_{ref,i}$ is the constant of the reference spring which connects node P_i to the reference point M_i. $K_{uni,i}$ is the uniform spring constant which connects the node P_i to the node P_{i-1}. k_1, k_2 and k_3 are constants. With these relations, the uniform springs are stiffer in the high deformation regions, and the reference springs are the dominant springs in the low deformation regions. The stiff uniform springs in high deformation regions try to keep the nodes P_i uniformly distributed on the curve C_{t+1}. If there is a topological violation in the order of reference points M_i, the deformation degree increases, and the uniform springs will be stiffer. That forces the P nodes to return to the same order as the previous time frame. At any time frame t, we find the position of the reference points on curve C_{t+1} using the nodes Q on curve C_t. Then, the deformation degree and the spring constant are calculated for i=1,2,..,N. Finally, we construct the governing system of equations using the force balance on all nodes P_i:

$$K_{uni,i+1}\left(S_{P,i+1} - S_{P,i} - l_{0,t+1}\right) - K_{uni,i}\left(S_{P,i} - S_{P,i-1} - l_{0,t+1}\right) - K_{ref,i}\left(S_{P,i} - S_{M,i}\right) = 0 \tag{2.9}$$

$S_{P,i}$ is the position of the point P_i in the coordinate system along the cell boundary C_{t+1}. Positions of points Q_i, P_{i-1}, and P_{i+1} are defined in the same coordinate system. We can find the position of nodes P_i on the curve C_{t+1} by solving this system of equations. Then, we can find the displacement and velocity fields on the curve, using the position of nodes Q_i on the curve C_t and the nodes P_i on the curve C_{t+1},

With this algorithm, the mapping and the resulted displacement and velocity fields at the regions close to the ends of the curves could be dependent on the position of end points. However, the position of end points, determined in the cell edge tracking process in JFilament (see the previous section) are not entirely reliable. Thus, we remove 5% of the contour lengths at both ends from the displacement and velocity maps.

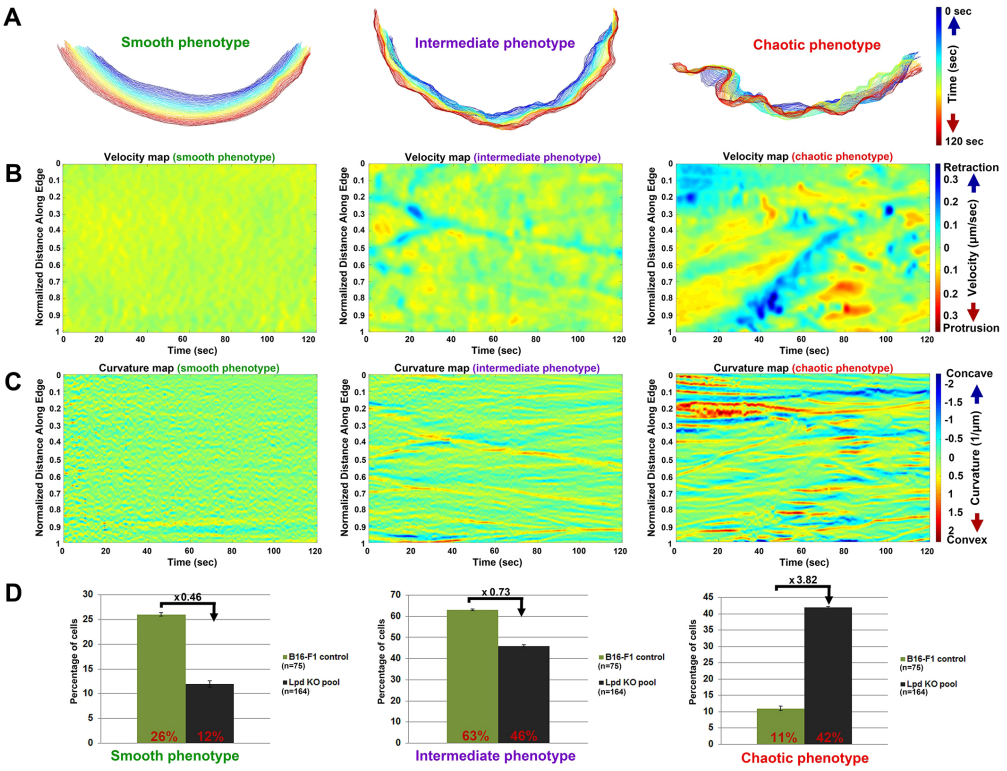

FIGURE 2.10: Deletion of Lpd in B16-F1 cells changes the balance between lamellipodial protrusion phenotypes. A) Spatiotemporal evolution of cell-edge in three distinct types of lamellipodial protrusion phenotypes in B16-F1 wild-type cells. B) Velocity maps, representing smooth, intermediate and erratic lamellipodial phenotypes. C) Example curvature maps for each protrusion phenotype. D) Quantification of the fraction of cells with the indicated genotypes displaying each lamellipodial phenotype (smooth, intermediate or erratic). This figure is originally published in [10].

2.2.3 Velocity and curvature maps and morphodynamic parameters

We find all positions of representative nodes on the curve in all time frames, with which the trajectory of all nodes during the whole measurement time can be found. Then the velocity and displacement fields along the curve in all time frames are calculated. The velocity map of the cell edge is plotted in a 2-dimensional coordinate system with x-axis showing the time and y-axis showing the distance along the edge (Fig 2.10). Since the tangential displacement of the nodes on the curve is not relevant to the morphodynamic behavior of the cell, we only consider the normal displacement and velocity. This normal velocity is illustrated with colors in the velocity map. In addition to the velocity map, we can also find the curvature map. With the position of all nodes on the curve in all time frames, we can calculate the local curvature of the curve. Similarly, the curvature map of the cell can be constructed to show the smooth and curved locations on the cell edge and their evolution in time (Fig. 2.10).

No.	Parameter name	Parameter description and biological relevance
1	Average Advancement Velocity	Parameter is equivalent to performing individual kymograph-based analyses of protrusion (as in Figure1C, D) on multiple points along the cell edge, thus subtracts retraction from protrusion rates at all points of the analyzed edge. If protrusion and retraction activities for each point were identical, the value of this parameter would be 0.
2	Effective Protrusion	Average protrusion velocity of all points considering the entire measurement period.
3	Protruding Edge Fraction	Average fraction of the edge protruding at any time during the period of measurement, expressed between 0 and 1, i.e. 1 representing the entire edge measured.
4	Length of Protruding Segments on Edge	Average length (in µm) of all protruding segments on measured edge. As opposed to parameter #3, where the average fraction of measured edge is calculated, this parameter defines average lengths of protruding segments over time.
5	Protrusion Episode Velocity	Average protrusion velocity of all points, considering only protrusive time periods.
6	Maximal Velocity during Protrusion	Corresponds to parameter # 5 in the highest quartile (top 25%).
7	Effective Retraction	Average retraction velocity of all points considering the entire measurement period.
8	Retracting Edge Fraction	Average fraction of the edge retracting at any time during the period of measurement, expressed between 0 and 1, i.e. 1 representing the entire edge measured.
9	Length of Retracting Segments on Edge	Average length (in µm) of all retracting segments on measured edge. As opposed to parameter #8, where the average fraction of measured edge is calculated, this parameter defines average lengths of retracting segments over time.
10	Retraction Episode Velocity	Average retraction velocity of all points, considering only retracting time periods.
11	Maximal Velocity during Retraction	Corresponds to parameter # 10 in the highest quartile (top 25%).
12	Retraction to Protrusion Ratio	This parameter is defined as the ratio of "Effective Retraction" (#7) over "Effective Protrusion" (#2). Values above 1 indicate retraction prevailing over protrusion.
13	Frequency of Oscillations	Frequency of oscillations/switches corresponds to the inverse of average time interval between consecutive velocity direction changes of each point along the measured edge (protrusion to retraction or *vice versa*).
14	Persistence of Edge Movement	Reflects the variance of velocity changes as determined for all points along measured edge in all time frames. If the measured cell edge protrudes/retracts with equal velocities in all time frames (i.e. acceleration is zero), the parameter will be 0.
15	Strength of Fluctuations	Average of peak to peak amplitude of velocity oscillations of all points on the cell edge. The value for each point is calculated by averaging the velocity amplitude of all oscillation events of the point. This parameter thus defines the strength of velocity fluctuations at the cell edge irrespective of their direction.
16	Predictability of Fluctuations	Obtained by calculating average values of absolute, normalized autocorrelation of velocity over time and along edge performed to explore repetitive patterns. Parameter allows distinguishing between regular, repetitive patterns and chaotic random behavior of cell edge dynamics.
17	Length of Concave Segments	The average length (in µm) of concave segments on measured edge.
18	Length of Convex Segments	The average length (in µm) of convex segments on measured edge.
19	Curvature Change over Time	Derived from the rate of change of curvature for all measured points along the edge over time, followed by calculating the variance of all of these rates.
20	Curvature Variability along Edge	Reflects the variance of curvature changes with respect to distance along the cell edge, so this parameter gives an estimate of the average rate of concave to convex (and *vice versa*) transitions along the cell boundary for each time frame. It thus constitutes a spatial value and not dynamic one.

FIGURE 2.11: Description of the morphodynamic parameters of the cell. This table is originally published in [10].

The majority of the morphodynamic data of the cell are stored in the curvature and velocity maps. This data, however, should be quantified to be useful for morphodynamic analysis. We defined 20 parameters that can characterize the cell morphodynamics. These parameters can be separated into 4 groups of protrusion-, retraction-, dynamics/velocity- or curvature/geometry-related parameters. These parameters are described in Fig. 2.11.

2.2.4 Morphodinamical analysis of Lpd knocked out cells

Cell morphodynamics is an informative indicator of the underlying molecular pathways that are involved in cell motility. In this section, we show the potential of morphodynamic analysis in studying the molecular mechanisms related to cell migration. In particular, we employ our morphodynamic analysis workflow to study the role of Lamellipodin (Lpd), which is a protein that is related to cell motility. Lpd regulates the cell motility and formation of lamellipodia by interacting with the WAVE complex to activate the Arp2/3 complex [186, 187]. Overexpression of Lpd increases the velocity of protrusion. It has been shown that conditional genetic knockout of Lpd impairs the lamellipodia formation [188]. However, the permanent loss of Lpd and its effects on motility has not been investigated yet. Therefore, B16-F1 mouse melanoma cell lines with genetically deleted Lpd are generated. We analyze the cell morphodynamics in the Lpd knockout cell lines and compare them with the control cells to study the effects of permanent Lpd loss on the cells.

We find that the variability in protrusion phenotypes is significant in the cells of the same population. This variability also exists in even a single cell at different times. We employed our workflow to quantify the cell edge morphodynamics, despite the phenotype variability. The spatiotemporal evolution of the cell contours over the period of 2 min is illustrated for 3 generic cases in Fig. 2.10A. All the different protrusion patterns in B16-F1 control and Lpd knockout populations can be classified into three classes of smooth, intermediate, and erratic. In the smooth class, the cell edge protrudes persistently and smoothly. In the intermediate case, the cell edge shows some fluctuations in protrusion. The erratic cells exhibit rapid fluctuations with significant retractions. The velocity maps of the cell contours are created for the same time periods. These velocity maps clearly show the differences in the morphodynamic patterns of different protrusion classes. The erratic case has intense protrusion/retraction regions with large velocities. A few of these intense protrusion/retraction spikes are also observed in the intermediate case (Fig. 2.10B). Curvature maps also show different curvature patterns between the three classes. For example, the cell edge in the erratic class includes many regions of high convex/concave curvature. The intermediate case also shows some highly curved areas (Fig. 2.10 C).

We analyzed several cells from the Lpd KO clones and investigated how the Lpd deletion alters the protrusion classes compared to controls. We find that the fraction of cells in the smooth and intermediate classes is decreased for the Lpd KO cells. The fraction of cells in the erratic class is increased by a factor of 3.82 in the Lpd KO cells compared to the control case. These results clearly show the role of Lpd in the stability of lamellipodial protrusion.

2.2.5 Lpd loss impacts morphodynamic regime of the lamellipodial protrusion

We compared Lpd KO and control cells additionally through 20 morphodynamic parameters. The values of these parameters are averaged and normalized for the sake of illustration. Fig. 2.12 shows the difference between the 2 cell groups. Many conclusions can be drawn from this figure. The 'Average Advancement Velocity' (parameter 1) is decreased significantly upon deletion on Lpd. Almost all of the protrusion-related parameters are reduced (parameters 2-6) in the Lpd KO cells.

The deletion of Lpd also increases the 'Retraction to Protrusion Ratio' (parameter 12). That is not only caused by the lower protrusion but also by higher retraction. The retraction-related parameters (7–11) are all increased in Lpd KO cells. Our analysis also shows that membrane fluctuations (parameter 13) are observed more frequently in Lpd KO cells. Furthermore, the fluctuations are more vigorous and less predictable (parameters 15 and 16, respectively). The geometry-related parameters show longer concave and convex segments in Lpd KO cells (parameters 17 and 18). That is consistent with the lower curvature variability over time and along the edge (parameters 19 and 20). This data suggests that Lpd also contributes to the local plasticity of the edge.

We further characterize the difference between the control and Lpd KO cell populations using the principal component analysis (PCA). We excluded the geometry/curvature-related parameters in this analysis. Our results show that 88% of the total variance of the whole data set of control and Lpd KO cells can be captured with two principal components, PC1 and PC2 (Fig. 2.13). We find 11 morphodynamic parameters to have the highest contribution to the first principal component PC1. Those are the parameters related to fluctuations or retractions. On the contrary, the parameters related to protrusion characteristics of the edge have the highest contribution to the second principal

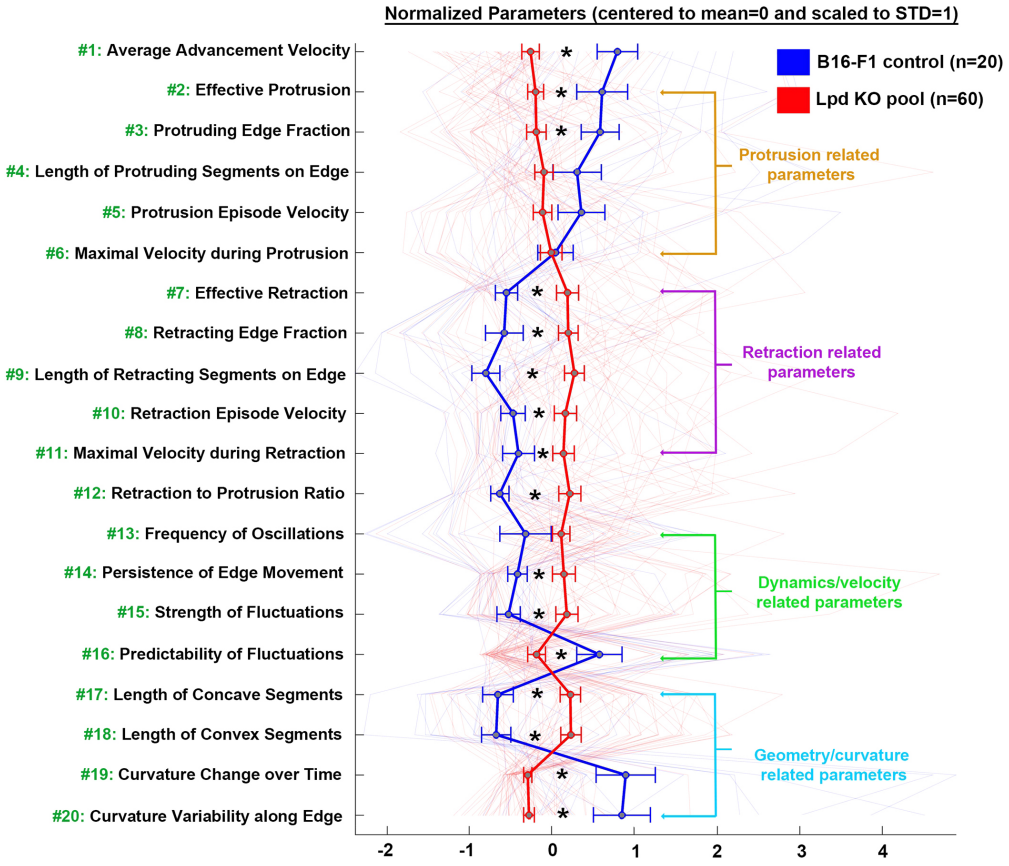

FIGURE 2.12: Morphodynamic analysis of B16-F1 control and Lpd KO cells. Parameters are classified into protrusion-, retraction-, dynamics/velocity- or geometry-related. Data are represented as arithmetic means±s.e.m. (*P<0.05). Selected morphodynamic parameters were each normalized by assigning their respective means to 0 and scaling their s.d. values to 1. For description of each parameter, see Fig. 2.11. This figure is originally published in [10].

component, PC2. Hence, PC1 and PC2 can be considered as the 'retraction activity' and 'protrusion activity' of the edge.

Cells with high PC1 are all from the Lpd KO population. All of the control cells show low values of PC1. That suggests increased retraction-fluctuation activity at least in a fraction of Lpd KO cells. The spread of cells along the PC2 axis seems to be similar. We can also distinguish 2 different regimes in the PC1-PC2 plane. In the first regime, which includes both control and Lpd KO cells, the correlation between PC1 and PC2 is negative. That means cells with higher protrusion activity have lower retraction-fluctuation activity. The second regime on the right side of the plane only includes cells from the Lpd KO group. We observe a positive correlation between protrusion and retraction-fluctuation activity in this regime. That exhibit a behavioral difference in the Lpd KO cells in this regime.

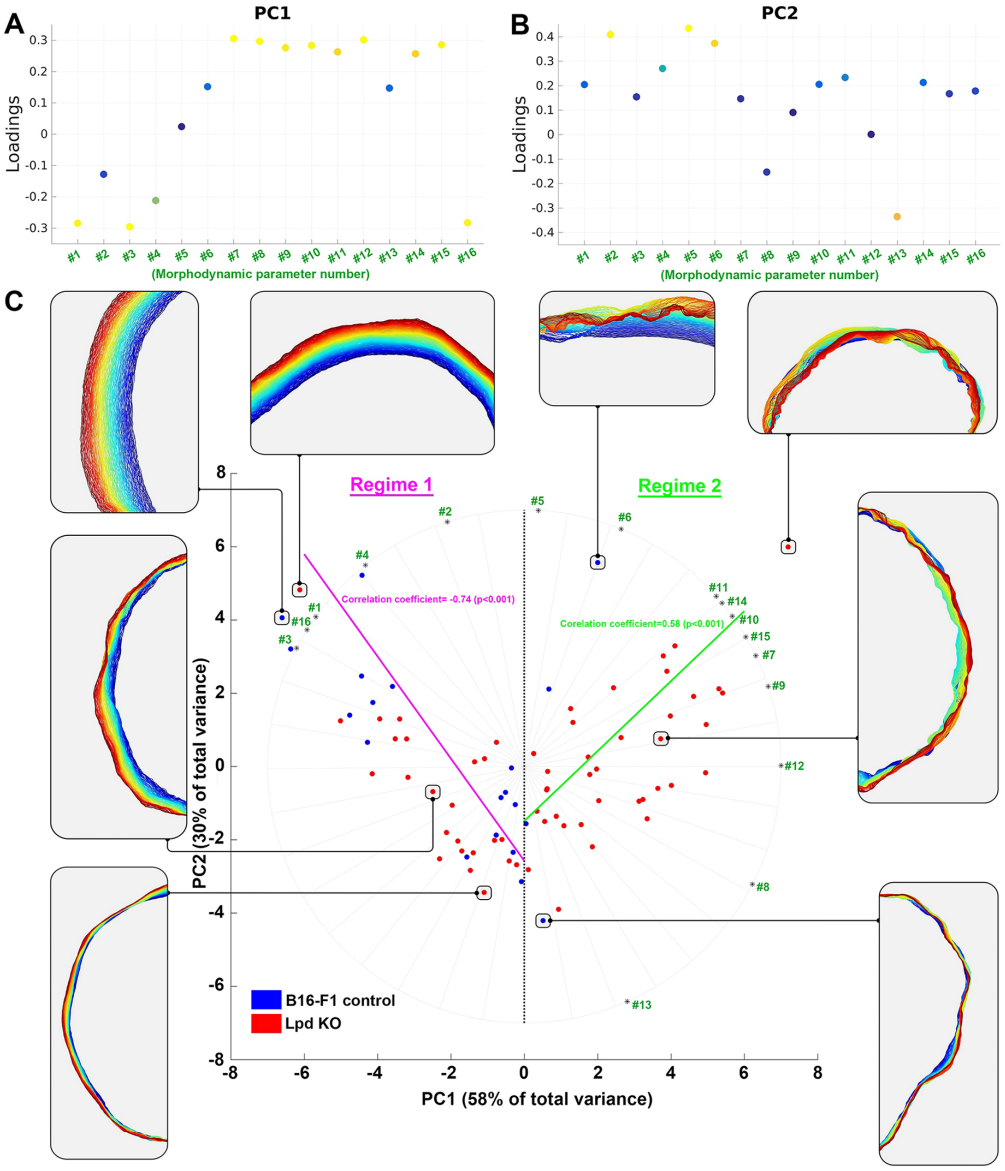

FIGURE 2.13: PCA reveals distinct lamellipodial protrusion regimes for B16-F1 control versus Lpd KO cells. A, B) Figures display the loadings of individual parameters to principal components 1 and 2 (A, PC1; B, PC2). The larger the absolute value of a given loading, the stronger a given parameter contributes to respective PC. Loadings of high contribution are marked in yellow. The parameter numbers correspond to those displayed in Fig. 2.12 and Fig. 2.11. PC1 mostly reflects retraction and PC2 reflects protrusion activity. C) B16-F1 control cells (blue) and Lpd KO cells (red) are plotted in PC1-PC2. Lamellipodial contours of eight selected cells (circles) are shown. Two regimes can be distinguished in our cells. Regime 1, containing most cells of the B16-F1 wild-type population and characterized by a negative correlation between PC1 and PC2 (indicated with the pink line and Spearman correlation coefficient of 0.74, $P<0.001$). Regime 2, comprised mostly of cells of the Lpd KO population and characterized by a positive correlation between PC1 and PC2 (indicated with the green line and Spearman correlation coefficient of 0.58, $P<0.001$). Projections of the direction of increasing individual parameters on the PC1-PC2 plane are shown with green numbers. This figure is originally published in [10].

2.3 Conclusion and summary

Cell morphodynamics and cytoskeleton architecture are used in the field of cell motility as indicators of internal signaling pathways. Although studies on cell functions, including motility, are highly dependent on quantitative analysis methods of data obtained from various imaging techniques, there are few publicly available general algorithms. Many researchers develop ad-hoc analysis algorithms for their studies [185, 189]. In this chapter, we implemented two general workflows for quantification and analysis of morphodynamics and structure of the filamentous networks in the cell cytoskeleton, which can contribute to the field of cell motility.

Recent improvements in cryo-ET sample preparation [190], automated data acquisition [191], image processing workflows [192], and data analysis allow the evaluation of large data sets of ultrastructural architecture of filamentous assemblies and comparison of various features between multiple experimental conditions. These improvements, although very suitable for being combined with the genetic manipulation of cell lines via CRISPR/Cas9 techniques, are yet to be routinely applied in workflows that facilitate the high-throughput analysis and comparison of ultrastructural characteristics between genetically modified cell lines.

In the first part of the chapter, we developed a computational toolbox for ultrastructural analysis of filamentous networks. Our toolbox require minimal MATLAB proficiency and no prior coding experience. Several graphical user interfaces (GUI) guide the user through extracting outputs from large data sets in a time efficient manner. We defined different ultrastructural parameters that could characterize the architecture of different filamentous structures. These descriptors define the structural profile of filament assemblies which can be compared between different filament structures. Our toolbox also provides additional detailed comparisons between different assemblies. The ultrastructural parameters can be calculated locally and compared between different regions of the filament structures. Histograms of many properties, such as the orientation of filaments, can be compared between cell groups. The toolbox can also find the correlations between all ultrastructural parameters in each experimental group.

We used cryo-ET data of B16-F1 melanoma cells to show the visualization and analysis possibilities in the toolbox. We analyzed several branched networks from lamellipodia

of different experimental cell groups, including the control group and cells treated with CK666. CK666 is an inhibitor of the Arp2/3 complex in the cell. CK666 application enabled us to study the role of Arp2/3 on the architecture of the network. Our analysis showed a change in the network architecture upon application of CK666. In particular, the angular distribution and density of filaments changed dramatically after inhibition of Arp2/3. This example showed the potential of the toolbox for discovering and characterizing the role of different regulatory molecules involved in cell motility. In summary, the GUI that we programmed for this toolbox facilitates data curation, noise reduction, data visualization, parameter extraction and characterization of filamentous assemblies.

Cell morphodynamics is the complex output of cytoskeletal dynamics and its regulatory pathways, which can be used as a readout of the intracellular events. Although some studies have used very simple descriptors for contour-based analysis of morphodynamics [193–196], a complete description of the protrusion and retraction phenotypes, which can differentiate between different modes of cells, requires a large number of elaborate metrics. Calculation of the morphodynamic descriptors requires the displacement field on the cell boundary. Some studies used Level Set Method (LSM) to describe the trajectory of points on the evolving cell boundary [197]. Machacek et al. proposed an alternative method for mapping cell boundaries in two subsequent time frames [185]. Although that method needs significant computations, it is computationally more efficient than the LSM approaches. However, the method in [185] shows topological violations in the mapping, particularly in the regions of cell boundaries with strong deformation. Another study by Schindler et al. [198] recently proposed a one-parameter family of regularized contour flows based on Gaussian process regression to describe the trajectory of points on the cell boundary.

In the second part of this chapter, we implemented a workflow to analyze cell morphodynamics. This workflow requires time-lapse movies of cells from the top view as input. We introduced an adaptive algorithm to map the points on the cell boundary curve in one time step to the curve in the next time step. Our mapping algorithm comprises a series of "uniform" and "reference" springs. We could find the corresponding position of each point on the curve in the next time step by solving a set of equations. We substantially improved the mapping algorithm proposed by Machacek et al. [185] by using a system of linear springs with adaptive stiffness as a function of local deformation degree.

Our method is computationally efficient and results in realistic trajectories of points on the boundary, even in high deformation regions.

Our algorithm can then find the displacement field on the cell boundary. The velocity and curvature maps of the cell can be obtained from that. Those maps contain all the morphodynamic information of a cell. We then defined about 20 elaborate descriptors for the cell morphodynamics from these maps. A detailed morphodynamic profile of the cell is defined with these descriptors, from which different morphodynamic modes can be detected.

We employed our morphodynamic analysis workflow to investigate the role of a motility-related protein, Lamellipodin (Lpd). Lamellipodin is believed to be a regulator of cell motility by interacting with WAVE complex, which activates Arp2/3. We find that deletion of Lpd decreases the number of cells with smooth morphodynamics. Furthermore, we found multiple differences between control and Lpd knockout populations concerning various aspects of protrusion, retraction, and geometry of cell edge. The impact of Lpd deletion is characterized additionally using the principal component analysis (PCA).

In summary, in this chapter, we developed two valuable tools for analyzing and quantifying edge morphodynamics and filamentous architecture in the cytoskeleton and showed their enormous potential for studying the regulatory proteins.

Chapter 3

adhesion-velocity relation and back-front interaction in 1-dimensional cell motility

3.1 Introduction

To understand the mechanisms that shape cell motility, one needs to analyze experimental data first and then provide biophysical models that illustrate how fundamental physical phenomena cause complex cell behaviors. In chapter 2, we introduced workflows for analyzing two types of experimental data that are very important in understanding cell motility.

In this chapter, we propose a biophysical model to study the effect of adhesion on cell velocity. Our goal in this chapter is to provide new insight into the biphasic adhesion-velocity relation as one of the constitutive relations in cell motility reported for many cell types. We simplify the analysis by restricting cells to 1-dimensional motility to focus on the basic rules that shape cell behavior. We analyze a large amount of data on the motion of MDA-MB-231 cells on microlanes with alternating Fibronectin densities. Individual cells are exposed to alternating adhesion strength in this setting. Our biophysical model can describe cell velocity in the steady motion on the Fibronectin fields. We find the basic elements required for the biphasic adhesion-velocity relation.

In the second part of this chapter, we focus on the cell behavior on Fibronectin steps. Steps of Fibronectin density on the microlanes provide the opportunity to observe cell behavior in situations where front and back of the cell sense different adhesion strength. We extend the model to capture the separate effects of adhesion at the front and back parts of the cell, and identify the nature of front-back interaction in moving cells.

The experiments used in this chapter are performed in the Department of Physics at Ludwig-Maximilians-University by Dr. Christoph Schreiber and Johannes C. J. Heyn in the laboratory of Prof. Joachim O. Rädler. All the results presented in this chapter have been published in [11].

3.2 Biphasic dependency of cell velocity on Fibronectin density in MDA-MB-231 cells

3.2.1 Experiments

A novel two-step microcontacting protocol is developed by Christoph Schreiber to create Fibronectin-coated microlanes with alternating densities. The width of the microlanes is 15 µm , which restricts cell migration to 1 dimension. MDA-MB-231 breast cancer cells are seeded on the microlanes (Fig. 3.3.2B, C). Nuclei are labeled fluorescently to identify the positions of the cells. We take images every 10 min for 48 h. We then use an adapted IDL particle tracking software to calculate the cell tracks. The time frames in which cells are closer than a minimal distance of 66 µm to other cells are excluded. Finally, we exclude the tracks shorter than a minimum duration of 5 h. That results in more than 15000 single-cell tracks.

Cells are restricted to one-dimensional motion on the Fibronectin microlanes and frequently traverse to fields with different densities (Fig. 3.3.2B, C). We analyzed the cell velocity in the population and found the biphasic behavior with maximal velocity for intermediate Fibronectin densities (Fig. 3.2B). This biphasic dependency was reported by several studies for different cell types [12–14, 85–87, 199]. However, the low statistics in the previously published data did not permit a clear distinction between a monotonous decrease of velocity and saturating velocity with increasing adhesion strength. The large

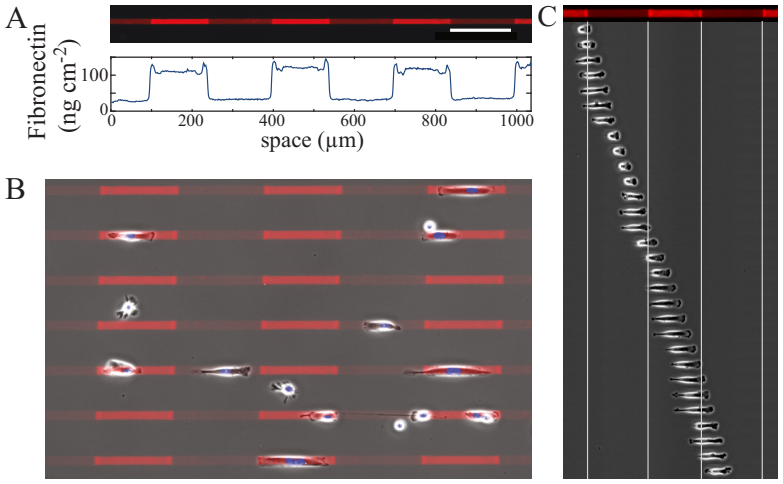

FIGURE 3.1: Fibronectin lanes and cell motion. A) Fluorescence image of a Fibronectin coated lane with fields of different Fibronectin density shown below. Scale bar is 150 µm. B) MDA-MB-231 cells seeded on Fibronectin lanes. Overlay of phase contrast and fluorescence images of patterns (red) and nuclei labelled with Hoechst (blue). Cells are restricted to one-dimensional motion on the microlanes and frequently traverse to fields with different Fibronectin densities. They sometimes also spontaneously reverse direction or stay at one position for some time. C) Time course of the position of a single cell migrating on the lane shown on top. Phase contrast images taken every 10 min. This figure is originally published in [11].

number of measurements allowed us to choose a small step size in coating densities. As a result, we find an apparent saturating effect of Fibronectin density on the cell velocity.

The stepped Fibronectin lanes also enabled us to analyze the velocity changes at transitions between different Fibronectin densities with regard to the biphasic relation. Fig. 3.2C presents increases (green) and decreases (red) of the median velocity during transitions from Fibronectin density, Fibronectin$_i$, to Fibronectin density Fibronectin$_j$.

Transitions from low to high density are shown above the diagonal (Fibronectin$_i$ = Fibronectin$_j$). Below the diagonal, transitions are from high to low density. The velocity does not change on the diagonal (full line in Fig. 3.2C). We find distinct pairs of Fibronectin concentrations around the maximal velocity with the same velocities. This means that the sharp step in Fibronectin concentration does not change the cell velocity. This is a consequence of the biphasic adhesion-velocity relation, and it is manifested as a second white diagonal line from top left to bottom right (dashed line in Fig. 3.2C). Two regimes are separated by this second diagonal line: The velocity increases with adhesion below the line. Thus it is in the rising phase of the adhesion-velocity relation. Above this line, we observe the falling phase of this relation, and velocity decreases with adhesion.

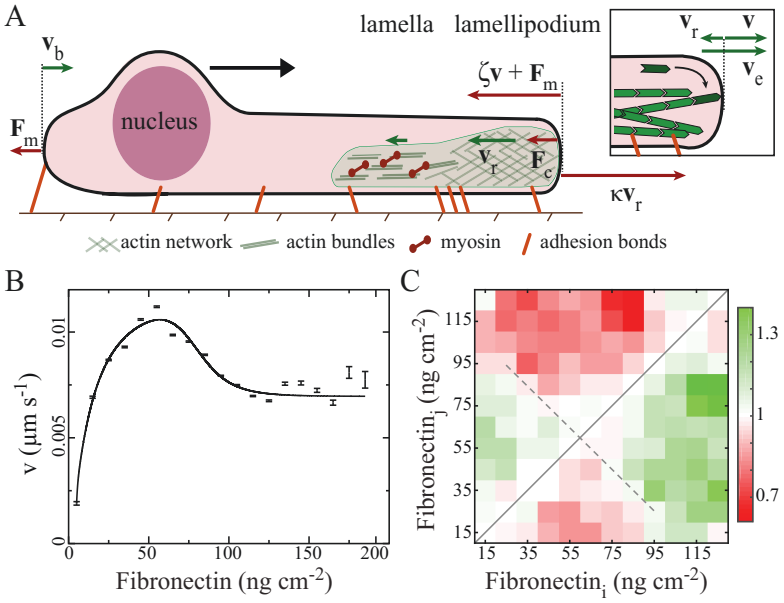

FIGURE 3.2: The adhesion-velocity relation. A) Sketch of a cell with velocities of the leading edge v, the retrograde flow v_r, the network extension rate v_e, the back velocity v_b and the related elements of the force balance of steady motion ζv and κv_r. B) Measured adhesion-velocity relation of MDA-MB-231 cells (symbols). The full line shows the fit to Eq. 3.9 with the parameters listed in Table 3.2. Each data point contains on average 1000 cell tracks, but with decreasing numbers for extreme Fibronectin densities. C) Relative velocities for all combinations of different Fibronectin densities. Distributions of velocities before and after a transitions from FN_i to FN_j have been measured for each pair of densities. The color coding compares the relation between the medians. This figure is originally published in [11].

3.2.2 Model

The cell velocity v, protrusion velocity, and velocity of the cell's rear are all equal during steady motion. We focus on this steady motion on areas with homogeneous Fibronectin density in this section. To describe the cell motion, we formulate a force balance at the leading edge of the cell, taking into account all the major forces acting there. Substrate exerts forces on the cell across their contact area. These forces act on different parts of the cell and are transmitted to the leading edge through different mediators. We also include these forces in the leading edge force balance.

The forces acting at the cell's leading edge are depicted in Fig. 3.2A. Individual growing filaments push the leading edge membrane with the force f. Adding a monomer to the tip of these filaments should work against f. The force f increases the activation energy for the polymerization reaction. Thus, f enters the Arrhenius factor $e^{-\frac{f d \cos\theta}{k_B T}}$ in the polymerization rate. d is the length increment by addition of a monomer, θ denotes the tilt angle of the filament, k_B the Boltzmann constant and T the temperature [116, 117,

200]. The average single filament force f is approximated by the total force per leading edge contour length F divided by the number of filaments per leading edge contour length N. With that, we can write the extension velocity of the network:

$$v_e = V_e^0 e^{-\frac{gd}{k_B T}\frac{F}{N}} - k^- \tag{3.1}$$

g is a geometric factor resulting from averaging over the tilt angle distribution of filaments. V_e^0 is the force-free extension rate, and k^- is the barbed end depolymerization rate. Now, We can evaluate intracellular forces based on the force-dependency of the polymerization rate. The newly polymerized actin network partly moves in the direction of cell protrusion and partly flows backward as the actin retrograde flow. The extension velocity v_e is the vectorial difference (sum of the absolute values in one spatial dimension) of the protrusion velocity v and retrograde flow velocity (Fig. 3.2A).

$$v_e = v + v_r. \tag{3.2}$$

Velocities are proportional to forces in the highly viscous environment of moving cells (low Reynolds number regime). The force that drives retrograde flow at the leading edge should overcome the resistance caused by the interaction between the actin flow and stationary structures in the cell. We model this force with viscous friction relation, i.e., κv_r.

In the following, we show how this coefficient κ is related to the local properties of the flow. κ integrates actin network and adhesion properties across the whole F-actin flow domain that is mechanically continuous to the lamellipodium [130]. Thus, we study a 1-dimensional viscoelastic flow with friction with the substrate. The advected Maxwell model and the force balance equation can describe this flow [18, 133]:

$$h\frac{\partial(\sigma)}{\partial x} = \xi(V - v) \tag{3.3}$$

$$4\eta\frac{\partial V}{\partial x} = (1 + \tau\frac{\partial}{\partial t} + \tau V\frac{\partial}{\partial x})(\sigma - \sigma_{myo}) \tag{3.4}$$

with V being the local velocity of the viscoelastic flow in the cell frame of reference, σ the tension in the network, σ_{myo} the contraction caused by myosin motors in the network, η viscosity, τ viscoelastic relaxation time, and h height of the actin network.

ξ is the viscous friction coefficient between the substrate and the flow. These equations are solved in the domain (0,l), with 0 being the cell leading edge and l the distance from the leading edge with stationary actin (zero retrograde flow velocity in the lab frame of reference). We can then find the cell velocity v and the actin network extension velocity v_e as functions of force and thus tension at the leading edge, $F = -h\sigma(0)$.

$$v_e = V_e^0 e^{\frac{ah\sigma(0)}{N}} - k^- \tag{3.5}$$

$$v = \frac{-h\sigma(0)}{\zeta} \tag{3.6}$$

We use these velocities to obtain boundary conditions for the viscoelastic flow equations (Eqs. 3.3, 3.4).

$$V(l) = -v, \qquad V(0) = v - v_e \tag{3.7}$$

With these boundary conditions, the steady-state flow profile across the domain (0,l) and thus the retrograde flow at the leading edge can be found. The ratio of force to the retrograde flow at the leading edge is then found to determine κ. We solve Eqs. 3.3, 3.4 for a range of values of ξ. The relation of κ and ξ can be well fitted with a power law (Fig. 3.3). The resulting fitting parameters show that κ is a linear function of the square root of ξl (table 3.1).

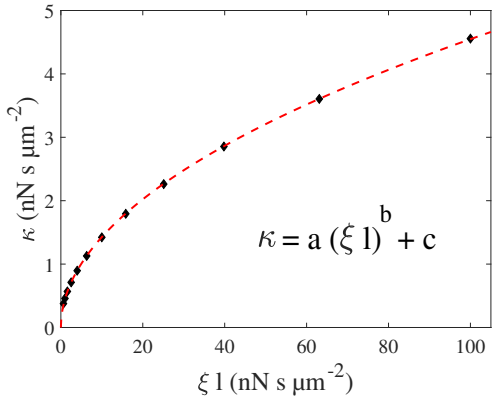

FIGURE 3.3: Dependency of κ on ξ in the reference simulations and the fitted equation (dashed lines). The model parameters used in the these simulations are: σ_{myo}= 0 kPa, v_0 = 0.05 µms^{-1}, k^- = 0.005 µms^{-1}, ζ = 5 nNs µm^{-2}, h = 0.2 µm, η = 5 kPas, l = 10 µm, a = 248 nN^{-1}, and N = 248 µm^{-1}. This figure is originally published in [11].

This analysis clearly shows that the resistance against the actin flow can be modeled with

	ref. simulations	$v_0 = 0.01$ µms^{-1}	$v_0 = 0.25$ µms^{-1}	$\eta = 1$ kPas	$\eta = 15$ kPas	σ_{myo}= 0.1 kPa	σ_{myo}= 0.5 kPa	$\zeta = 5$ nNs µm^{-2}
a	0.4261	0.4342	0.4438	0.1906	0.7942	1.25	0.8868	0.4274
b	0.5131	0.5059	0.511	0.5179	0.4898	0.5133	0.515	0.5121
c	0.03265	0.02315	0.0154	0.01096	0.03305	-0.3704	-1.402	0.03116

TABLE 3.1: The value of fitting parameters of the equation in Fig. 3.3 in a variety of simulations. In each set of simulations, one parameter has been changed with respect to the reference simulations (see caption of Fig. 3.3). The parameter b of the fitting is close to 0.5 in all of the cases and the parameter c is negligible when $\sigma_{myo} = 0$. This table is originally published in [11].

a viscous friction κv_r, with κ integrating the local properties of the flow and network. Thus, we simplify modeling the spatial interactions between the actin network and the stationary structures with the lumped parameter κ.

The force required to move the leading edge membrane is ζv, with the coefficient ζ comprising drag resistance of membrane motion on the substrate. The detachment of adhesion bonds at the rear of the cell is also included in the coefficient ζ. The force F pushes the leading edge membrane and drives retrograde flow at the same time in the opposite directions [15, 130]. We have

$$F = \kappa v_r - F_c = \zeta v + F_m. \tag{3.8}$$

F_m is a velocity-independent force acting on the leading edge membrane, e.g., from a force microscopy cantilever (positive when pushing against protrusion) or myosin activity pulling from the rear. F_c is a force acting on the network at the cell front, e.g., from contraction by myosin. With our choice of sign, contractile forces are positive. The cell velocity can be determined uniquely (Eq. 3.9) using the basic thermodynamic relation Eq. 3.1 and the low Reynolds number conditions of lamellipodial motility Eq. 3.8. The velocity solution uses the Lambert function W_0 [201]:

$$v = \frac{N}{a\zeta} W_0\left(\frac{aV_e^0\kappa\zeta}{N(\zeta+\kappa)} e^{\frac{a}{N(\zeta+\kappa)}(\zeta(F_c+\kappa k^-)-\kappa F_m)}\right) - \frac{F_c + F_m + \kappa k^-}{\zeta+\kappa}. \tag{3.9}$$

Eq. 3.9 relates the cell velocity to F-actin density via N, F-actin network structure via a, polymerization rate via V_e^0, the depolymerization rate k^-, cell geometry and adhesion via κ and ζ and the forces F_c and F_m. Many experimental parameters do not show up in Eq. 3.9 despite being known as affecting cell velocity. They do so via the parameters in Eq. 3.9. For instance, the concentration of polymerizable actin monomers G enters via

V_e^0 like $V_e^0 = k_e^0 G$, or the myosin activity via F_c and ζ. Parameters κ and ζ depend on the substrate adhesion. Adhesion determines the density of stationary structures inside the cell and thus the friction coefficient κ. Adhesion also determines the drag force and the required force to pull the cell rear off the adhesion bonds [12, 85–87, 202]. So the parameter ζ is also affected by the adhesion.

Adhesion bonds trigger myosin-dependent feedbacks on their own dynamics [13, 14]. This and other pathways [31, 71, 82, 203–205] shape the dependencies of κ and ζ on the coating density B. We will explore these dependencies $\kappa(B)$ and $\zeta(B)$ by fitting the equation for the velocity Eq. 3.9 to experimental results. If the affinities of all binding steps determining $\kappa(B)$ and $\zeta(B)$ are low, and surface binding is not saturated, a linear dependency on B is a reasonable starting point. However, since velocities saturate at large Fibronectin densities, $\kappa(B)$ and $\zeta(B)$ should also be saturating functions. thus, we choose

$$\kappa(B) = \frac{\kappa_{max} B^{n_\kappa}}{B^{n_\kappa} + K_\kappa^{n_\kappa}}, \qquad \zeta(B) = \frac{\zeta_{max} B^{n_\zeta}}{B^{n_\zeta} + K_\zeta^{n_\zeta}}. \tag{3.10}$$

Most of the parameters of Eq. 3.9 can be determined by fitting. But, the scaling properties of this equation do not allow for a complete parameter value set. The factor a/N, which is multiplied to both $\kappa(B)$ or $\zeta(B)$, can be scaled out of the equation. That means we can not determine a/N uniquely. We have chosen the (experimentally reasonable) value N=248 μm^{-1} [17, 47, 206], and that entails a/N=1 μm nN^{-1}.

3.2.3 Fitting experimental data to Equations

We fit the Eqs. 3.9, 3.10 to the measured experimental data of the MDA-MB-231 cells as well as the other cell types. The results of the fitting will be discussed in the following sections. In this section, we describe the methods used for the fitting.

We employed Levenberg-Marquardt-method [207] for fitting the experimental adhesion-velocity data. For the cell types that retrograde flow data were also available, we included that in our fitting by calculating the retrograde flow from Eqs. 3.8, 3.9. We tested the precision of the fitting by trying the Levenberg-Marquardt-method from different initial parameter values. We find that the parameter values can be reproduced with a few percent variability when starting with different initial conditions. Hence, we concluded that the fitting procedure is reliable.

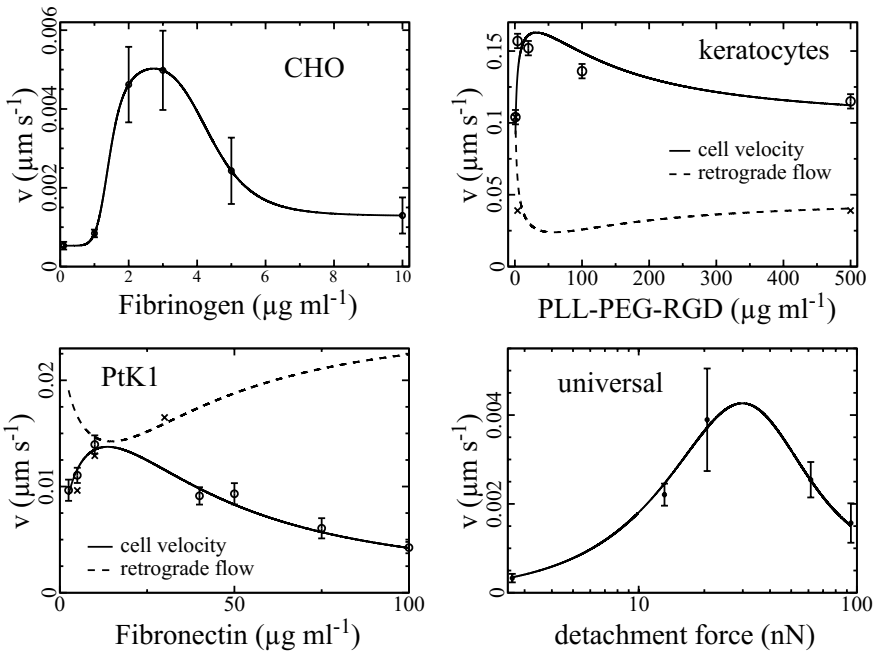

FIGURE 3.4: The dependency of the cell velocity on the substrate coating density in terms of the concentration of Fibronectin in the coating solution for CHO cells (data from [12]) and PtK1 cells (data from [13]), the concentration of Arg-Gly-Asp (RGD) functionalized poly-L-lysine-graft-(polyethylene glycol) copolymer (PLL-PEG-RGD) for keratocytes (data from [14]). The sets of experimental data (symbols) were fitted to Eq. 3.9. The parameter value results are listed in Table 3.2. There are also retrograde flow data (x) available for keratocytes and PtK1 cells, which we included in the fit. The fit for PtK1 cells deviates in the data point of retrograde flow at 5 µgml^{-1} from the experimental values. We discuss that deviation in the supplementary information. Palecek et al. could collapse several experimental sets to a single universal curve by relating the velocity to the detachment force, which is proportional to the adhesion bond density [12]. We fit this universal relation data to Eq. 3.9 in panel universal. However, the fit is not unique with 5 data points only and therefore we did not continue the analysis with this data set (see also Table 3.2). We found the introduction of (small) coating density independent terms $\kappa_0 8\ 10^{-5}$ nNsµm^{-2} and ζ_0=7 10^{-4} nNsµm^{-2} in Eq. 3.10 to be necessary to obtain the inflection point the velocity dependency of the CHO cells exhibits left of the maximum. They may indicate the relevance of physical interactions between cell and substrate or coating-independent surface bonds. This figrue is originally published in [11].

It is important to note that the precision of the fits is limited by our estimation of the filament density N and geometrical factor g. Our estimation of 0.375 for g is only valid for a uniform distribution of tilt angles between -70° and 70° [145]. However, different distributions of filament angles have been reported in the literature [145, 208–210]. The density of filaments is also reported within the range of 150-320 filaments per micron in the literature [17, 18, 47, 206]. These uncertainties on g and N lead to uncertainty in the estimated parameters of cells. The other factor that affects our fittings is cell variability. We can clearly see the cell variability by comparing the maximum velocity between the cells used in Fig. 3.2B and Fig. 3.14A. Thus, we expect that the uncertainty

on parameters is comparable to cell variability.

3.2.4 Analysis of the adhesion-velocity relation

The result of fitting Eq. 3.9 to the MDA-MB-231 data set shown in Fig. 3.2B reveals that the model can reproduce the velocity maximum and saturating behavior. We also analyzed a variety of experimental data for different cell types from literature including keratocytes [14], PtK1 cells [13], CHO cells [12], and a universal data set (Figs. 3.4, 3.8). Palecek et al. could collapse several experimental sets to a single universal curve by relating the velocity to the detachment force, which is proportional to the adhesion bond density [12]. However, since the the number of data points was not sufficient, we did not continue the analysis with this data set. (see Fig. 3.4 and Table 3.3).

The parameters resulting from the fits are listed in Table 3.2. The force F, retrograde flow velocity v_r and network extension rate v_e are calculated using the resulting parameters and Eqs. 3.2-3.10. We find that the forces in keratocytes are in the same range as the dynamic forces in [15, 211, 212]. They are also in agreement with experimental and theoretical analyses of membrane tension in moving keratocytes [213]. Interestingly, we find $\kappa >> \zeta$ in keratocytes (Fig. 3.8). This agrees with observations which show that adhesion density vanishes towards the rear of the cell in [214, 215]. Because of the good quantitative agreement with experimental results in Figs. 3.2, 3.4 and prior knowledge on keratocytes, we conclude that all major relevant processes in the formulation of the velocity equation are included (Eq. 3.9).

Our fitting results agree with all the experimental data points in all cell types except a point in PtK1 cells. The experimental data in PtK1 cells show low cell velocity and retrograde flow at small values of Fibronectin density (below 10 $\mu g ml^{-1}$). That entails a significant drop in actin extension rate at low adhesion. It is not clear what causes this drop. At low adhesion strength, the force is smaller, and the extension rate should be even larger. Our fitting exhibit an increase of retrograde flow in a way that the extension rate slightly increases (Fig. 3.8, PtK1 panel). We speculate that the experimental data for retrograde flow has been taken at a distant point from the leading edge, while the retrograde flow in our model is the flow rate at the edge. This can explain the discrepancy.

3.2.5 Forces

One of the most interesting findings is that the velocity-independent forces vanish, F_m=0 and F_c=0. That holds for all cell types except the universal set, in which F_c is very small (Tables 3.2 and 3.3). That is a significant finding because it shows that all the forces contributing directly to the leading edge force balance are velocity-dependent. Thus, contractile forces produced by myosin directly linking adhesion sites to the leading edge membrane or connecting adhesion sites by stress fibers do not noticeably enter the force relations. With F_m=0 and F_c=0, we can also find the ratio of cell drag and actin flow friction coefficients $\kappa/\zeta = v/v_r$. This relation provides a practical way to measure the ratio κ/ζ.

We find that increasing adhesion increases the force generated at the cell front. Since the extension rate of the actin network depends inversely on the force, v_e decreases with increasing adhesion. The reduction of v_e is usually less than 30%, starting close to the Fibronectin densities with the maximum velocity. Our fits show different relative values of κ and ζ in different cells. Since $\zeta \geq \kappa$ in PtK1 and CHO cells, a larger fraction of the actin network extension turns into retrograde flow. In MDA-MB-231 and keratocytes cells larger fraction of the actin network extension turns into the leading edge protrusion velocity. The two types of ζ and κ relation show that adhesion can have a more substantial effect on the cell front ($\kappa \geq \zeta$) or cell back ($\zeta \geq \kappa$). Cells are able to migrate in both situations.

3.2.6 Stationary force-velocity relation

Although the dynamic force-velocity relation has been studied experimentally and theoretically [15, 211, 212], this relation has not been investigated in the stationary state. From the experimental point of view, to obtain the stationary force-velocity relation, we should give cells enough time to adapt to an applied force and then measure the velocity. Our model provides a prediction for the stationary force-velocity relation. The external force enters the model as F_m in Eq. 3.9. We find an almost linear decrease of velocity with increasing force in keratocyte cells. This relation is different from the dynamic force-velocity relation with a concave down shape [130]. The dynamic force-velocity

relation has been measured with keratocytes pushing against an AFM cantilever until the stall force is reached.

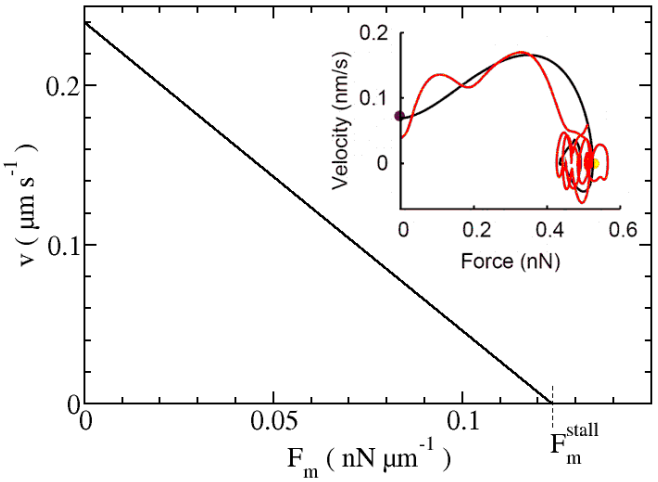

FIGURE 3.5: Stationary force-velocity relation of fish keratocytes as predicted by Eq. 3.9. The measured dynamic force-velocity relation reported in ref. [15] is shown in the inset. Note the different scales of the velocity axes. The inset shows the force on a leading edge stretch of 4.4 μm. We determined the parameters of Eq. 3.9 from the dynamic force-velocity relation with $v = 0.240$ μms^{-1} and $v_r = 0.068$ μms^{-1} of the force-free running cell and $F_m^{stall} = 0.1221$ nN μm^{-1} [15]: $\kappa = 0.435$ nNs μm^{-2}, $\zeta = 0.123$ nNs μm^{-2}, $V_e^0 = 0.316$ μms^{-1}, F_c=0.000353 nN μm^{-1}, k^-= 0.00378 μms^{-1} [16], $N = 300$ μm^{-1} [17], g = 0.375 [18] and $k_BT/d = 1.51\ 10^{-3}$ nN. This figure is originally published in [11].

The force required to stall the cell can be calculated from Eq. 3.9 with $v = 0$.

$$F_m^{stall} = \frac{N}{a} W_0\left(\frac{aV_e^0\kappa}{N} e^{\frac{a}{N}(F_c+k^-\kappa)}\right) - \kappa k^- - F_c. \tag{3.11}$$

The stall force is not dependent on the drag coefficient ζ. If there is no contraction, the stall force becomes zero when the friction coefficient κ vanishes. It can even get negative if the myosin contraction is strong enough.

We can also find the retrograde flow velocity in the stalled state.

$$v_r = \frac{N}{a\kappa} W_0\left(\frac{a\kappa {V_e}^0}{N} e^{\frac{a}{N}(F_c+k^-\kappa)}\right) - k^-. \tag{3.12}$$

The retrograde flow velocity in the stalled cell decreases with κ. It is maximal at κ=0 with the value of $V_e^0 e^{\frac{a}{N}F_c} - k^-$. At large values of κ it obeys the relation $(F_{max}^{pol} + F_c)/\kappa$.

The upper limit of the force that a cell can generate is the maximum stall force F_{max}^{pol}. That can be achieved with very large values of κ. This force stalls polymerization completely.

$$F_{max}^{pol} = \frac{N}{a} \ln \frac{V_e^0}{k^-}. \tag{3.13}$$

We determined the stall force for our four cell types (Fig.). Interestingly, we found that cells work in different force regimes. When $\kappa \ll \zeta$ the force is close to the stall force. That is the case for PtK1 and CHO cells. In particular, CHO cells have working forces almost equal to the stall force. Consequently, the velocity is very slow in this cell type. Forces are about one order of magnitude smaller than the maximal stall force F_{max}^{pol} in all the other cell types.

3.2.7 Dependency of κ and ζ on the ligand density

Our model entails that parameters κ and ζ increase with increasing ligand density B. We investigated that relation in cells by staining Paxillin and F-actin in Fig. 3.9. Paxillin is an adhesion site protein that can show the abundance of adhesion sites. Fig. 3.9A shows that MDA-MB-231 cells form higher adhesion site density on high Fibronectin concentration, than on low Fibronectin concentration (3.9B). Fig. 3.10A also shows a cell on a Fibronectin step. The adhesion site density increases a few µm behind the leading edge where the Fibronectin step is located. This experimental evidence confirms the direct relation between adhesion site density and ligand density.

The relation of κ and ζ with B resulting from our fits shows large values of n_κ and n_ζ in MDA-MB-231 and CHO cells (see Table 3.2). The biological interpretation of this result is that there is strong positive feedback from integrin to adhesion structures in these cell types. The velocity in these cell types increases very fast with increasing the coating density at low values of B (Figs. 3.2, 3.4). The increase of the force in dependence on B is also very steep (Fig. 3.8). Many factors contribute to the feedbacks from integrin to adhesion structures, including myosin activity [13, 14, 82, 216], F-actin flow [217], the force acting on adhesion structures and catch bonds [87, 218–224]. We will investigate the myosin contribution below.

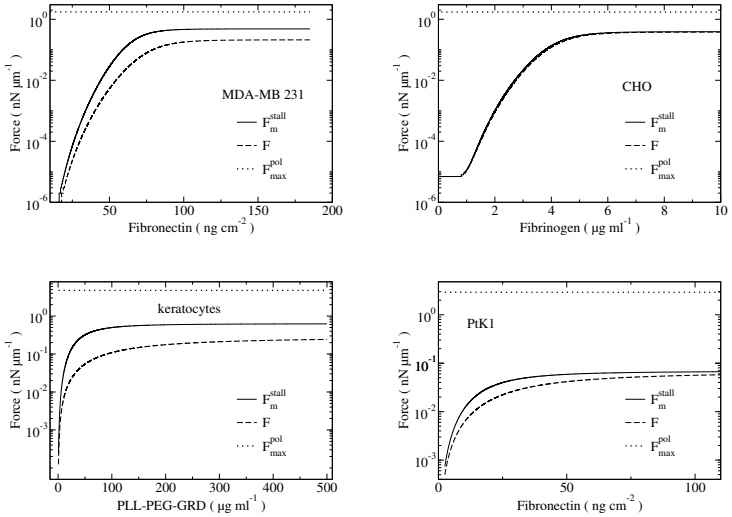

FIGURE 3.6: Predictions of Eqs. 3.8, 3.11, 3.13 with the parameters for the different cell types listed in Table 3.2 resulting from the fits of experimental data to Eqs. 3.9, 3.10 shown in Figs. 3.2B, 3.4. The stall force F_m^{stall} (Eq. 3.11) and the force F (Eq. 3.8) in the moving cell are set by adhesion and polymerization parameters, the maximal force F_{max}^{pol} (Eq. 3.13) is set by polymerization parameters only.

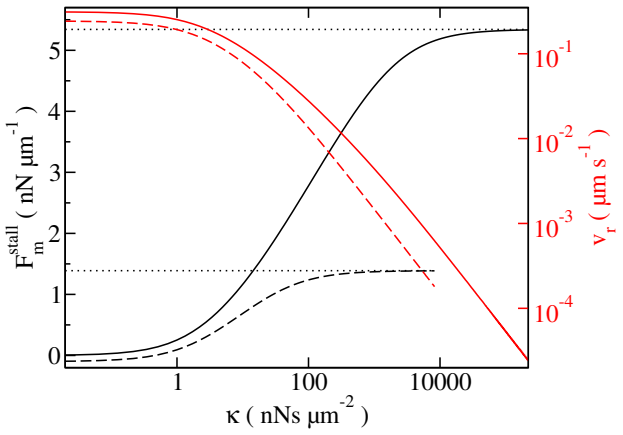

FIGURE 3.7: The stall force F_m^{stall} (Eq. 3.11) and the retrograde flow velocity v_r (Eq. 3.12) in the stalled state in dependency on the retrograde flow velocity coefficient κ. The parameters are the same as in Fig. 3.5 for the full lines. The dashed lines show results with F_c=0.1 nN µm^{-1}, k^-= 0.1 µms^{-1}. The dotted lines show the maximal force F_{max}^{pol} (Eq. 3.13) for each parameter value set. This figure is originally published in [11].

The other two cell types, PtK1 cells and keratocytes show rather small values of n_κ and n_ζ. Velocity and force rise slower with increasing B in these cell types (Figs. 3.4, 3.8). In keratocytes, the lateral extensions and wings are the regions with the main response to ligand density increase [14]. The stress in the direction of motion is five times smaller than the stress orthogonal to that direction [225, 226]. Thus, only a small part of the

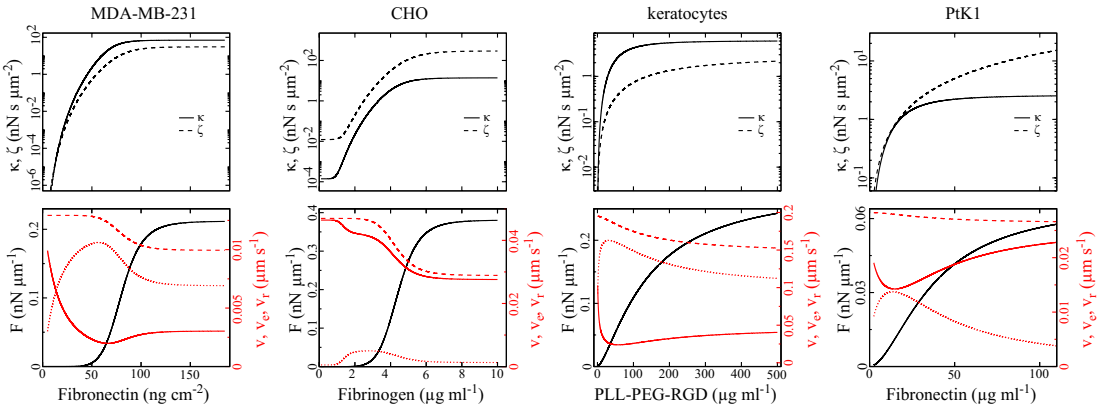

FIGURE 3.8: Upper row: Analysis of the experimental data with respect to retrograde flow velocity friction coefficient κ and membrane drag coefficient ζ (Eqs. 3.10) as resulting from the fits to Eqs. 3.9, 3.10 shown in Figs. 3.2B, 3.4 and Table 3.2. Lower row: Analysis of the experimental data with respect to extension velocity v_e (dashed line, Eq. 3.2), retrograde flow velocity v_r (full line, Eq. 3.8), cell velocity v (dotted line, Eq. 3.9) and the force F (Eq. 3.8) acting on the leading edge membrane as resulting from the fits to Eqs. 3.9, 3.10 shown in Figs. 3.2B, 3.4. This figure is originally published in [11].

response may contribute to the propulsion. That can explain the small value of n_κ and n_ζ for keratocytes.

We applied Blebbistatin, Calyculin A, and Latrunculin A to MDA-MB-231 cells to further study the positive feedback from integrin to adhesion structures. Blebbistatin is an inhibitor of myosin II activity. We find that Blebbistatin-treated cells (10 µM) are slower by about 40% (Fig. 3.10C). In this case, the adhesion velocity relation is closer to a monotonic curve than a biphasic one. We also find that n_κ and n_ζ are substantially decreased compared to the control case (Table 3.2.9). We can quantify the action of drugs on positive feedback with the ratio of κ (protrusive forces) to ζ (resisting forces). This ratio increases with increasing B in all conditions. However, Blebbistatin treatment decreases the κ to ζ ratio compared to the control case. That shows that myosin contributes significantly to the positive feedback from Fibronectin to adhesion structures.

Contrary to Blebbistatin, Calyculin A is an amplifier of myosin II activity. The application of Calyculin A (0.25 nM) results in a broader maximum in the adhesion-velocity relation (Fig. 3.10C). We also find that Calyculin A increases the ratio κ/ζ compared to the control case. Thus, it strongly increases the density of adhesion structures in the front regions of the cell where the protrusive force is generated.

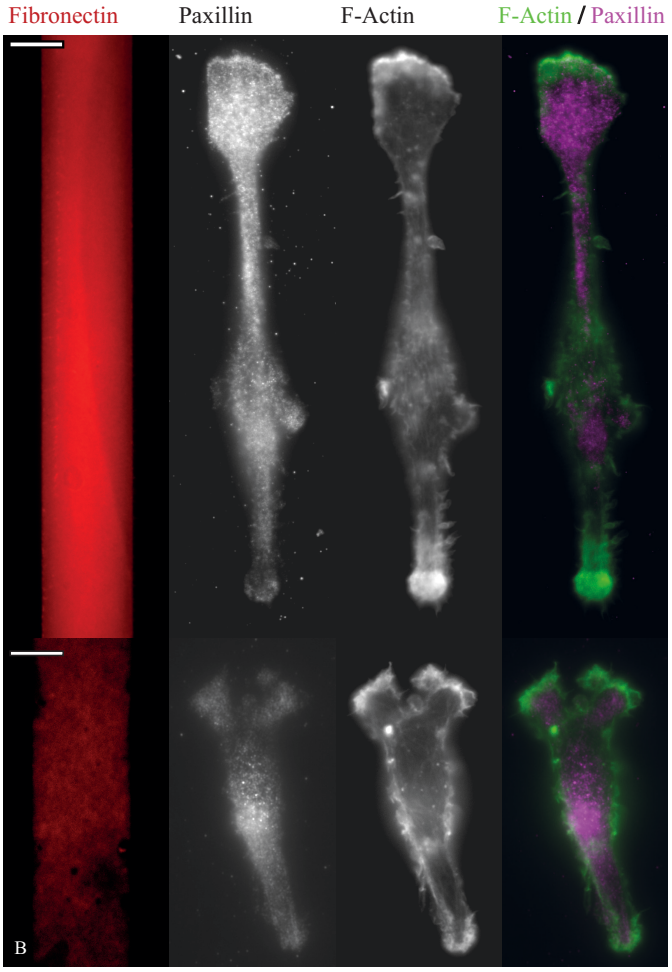

FIGURE 3.9: **Immunofluorescence of F-actin and paxillin.** Row (A) shows a cell on a high (40 ngcm^{-2}), row (B) on a low Fibronectin density field (8 ngcm^{-2}), both migrating upwards. Cells are typically more elongated on high Fibronectin fields than on low Fibronectin fields. Scale bars equal 10 µm. This figure is originally published in [11].

Latrunculin A is an inhibitor of actin polymerization. We observed a much smaller velocity after the application of Latrunculin A (0.1 µM). The adhesion-velocity relation is monotonic in this case. Our fit shows a substantial reduction in the force-free polymerization value V_e^0 (Table 3.2.9). That is consistent with the drug's effect as an inhibitor of polymerization.

3.2.8 Parameters and their values

We find the parameters of the cells for each experimental data set by fitting the model to the data. The parameter values for fitting the adhesion-velocity relation in MDA-MB-231, CHO cells, keratocytes, and PtK1 cells are shown in Table 3.2. The parameters

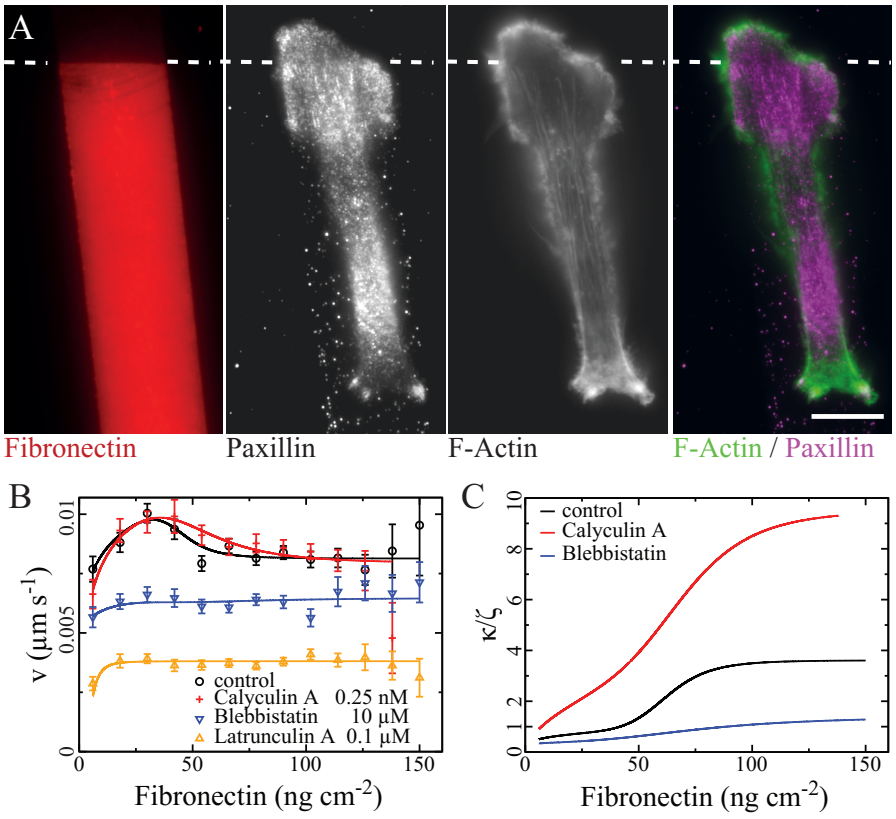

FIGURE 3.10: F-actin, adhesion sites and effects of inhibitors in MDA-MB-231 cells A) fixed cell on a Fibronectin step (moving up, 8 ngcm^{-2} - 40 ngcm^{-2}). Images of labelled Fibronectin and Phalloidin stained F-actin are acquired with epi fluorescence, and antibody stained Paxillin with TIRF microscopy. Scale bars equal 10 µm. B) Velocity adhesion relation of MDA-MB-231 H2B mCherry control cells and cells treated with 10 µM (+-)-Blebbistatin, 0.1 µM Latrunculin A, or 0.25 nM Calyculin A. C) Ratios of friction coefficients κ and ζ resulting from the fits in (B). This figure is originally published in [11].

related to the universal data set are listed in Table 3.3 (see Fig. 3.4). Table 3.2.9 show the values for the parameters from the fits of the drug application data sets (see Fig. 3.10). Finally, the estimations of parameter values found in literature are presented in Table 3.5.

3.2.9 Comparison of parameters to values from literature

The agreement between the measured cell velocities and our fit results support the parameter values that we found. The stall force that we found for keratocytes also supports the cell parameters that we found (Fig. 3.5). To validate our results, we additionally conclude some of the cell parameters indirectly from available experimental

	MDA-MB-231	CHO	keratocytes	PtK1	Units	Eq.
V_e^0	0.0156	0.0571	0.197	0.030	μms^{-1}	3.1
k^-	0.0027	0.010	0.0017	0.0016	μms^{-1}	3.1
n_κ	8.77	7.712	1.94	2.11		3.10
K_κ	73.6	4.63	66.1	22.3	μgml^{-1}, $ngcm^{-2}$	3.10
n_ζ	7.59	7.528	1.36	1.53		3.10
K_ζ	85.7	5.33	218.6	382	μgml^{-1}, $ngcm^{-2}$	3.10
κ_{max}	70.1	13.8	6.12	2.60	$nNs\mu m^{-2}$	3.10
ζ_{max}	30.8	296.0	2.86	117	$nNs\mu m^{-2}$	3.10
F_c	0	0	0	0	$nN\mu m^{-1}$	3.8
F_m	0	0	0	0	$nN\mu m^{-1}$	3.8
$\frac{F_{max}^{pol}}{N}$	0.007	0.007	0.019	0.012	nN	3.13

TABLE 3.2: Parameter values resulting from the fit of Eqs. 3.9, 3.10 to the data sets shown in Fig. 3.4 . The values g = 0.375 [18], gd/k_BT=248 nN^{-1}, N=248 μm^{-1} were used for all fits. This table is originally published in [11].

Parameter	universal	Units
F-actin network extension Eq. 3.1:		
force-free network extension rate V_e^0	0.0374	μms^{-1}
network depolymerization rate k^-	0.0038	μms^{-1}
retrograde flow friction coeff. $\kappa(B)$ Eq. 3.10:		
Hill coefficient n_κ	3.50	
half-max. value K_κ	4.0	nN
max. value κ_{max}	1.0	$nNs\mu m^{-2}$
membrane drag coefficient $\zeta(B)$ Eq. 3.10:		
Hill coefficient n_ζ	2.22	
half-max. value K_ζ	11.0	nN
max. value ζ_{max}	27.77	$nNs\mu m^{-2}$
forces Eq. 3.8:		
F_c	$3\ 10^{-4}$	$nN\mu m^{-1}$
F_m	0	$nN\mu m^{-1}$

TABLE 3.3: Parameter values resulting from the fit of Eqs. 3.9, 3.10 to the universal data set. The values g = 0.375 [18], gd/k_BT=248 nN^{-1}, N=248 μm^{-1} were used for all fits. The five data points of the set universal were not sufficient to really constrain the parameters of Eq. 3.9. We could determine the ratio ζ_{max}/κ_{max} (κ_{max}=1.0), but not the individual values. This table is originally published in [11].

data in the literature for different cell types. The results of the literature search for cell parameters are listed in Table 3.5.

The parameter V_e^0 in our model is proportional to the polymerization rate at the tip of a single filament. This rate is proportional to the G-actin concentration [G] and $k_{on} \approx 10\ \mu M^{-1}\ s^{-1}$ according to [16, 234]. Some mechanisms like funneling can increase

Parameter	control	Calyculin A	Blebbistatin	Latrunculin A	Units
F-actin network extension Eq. 3.1:					
force-free network extension rate V_e^0	0.0227	0.0143	0.0226	0.0038	μms^{-1}
network depolymerization rate k^-	0.0006	0.0004	0.0008	0.0001	μms^{-1}
retrograde flow friction coeff. $\kappa(B)$ Eq. 3.10:					
Hill coefficient n_κ	6.72	4.68	2.87	7.89	
half-max. value K_κ	63.5	75.1	80.3	217.4	$ngcm^{-2}$
max. value κ_{max}	344.9	587.0	155.9	164.1	$nNs\mu m^{-2}$
membrane drag coefficient $\zeta(B)$ Eq. 3.10:					
Hill coefficient n_ζ	6.45	4.10	2.77	4.68	
half-max. value K_ζ	51.6	60.5	53.0	1860	$ngcm^{-2}$
max. value ζ_{max}	95.6	61.6	109.5	23.3	$nNs\mu m^{-2}$
forces Eq. 3.8:					
F_c	0	0	0	0	$nN\mu m^{-1}$
F_m	0	0	0	0	$nN\mu m^{-1}$

TABLE 3.4: Results of the fits of the experimental data in Fig. 3.10B to Eqs. 3.9, 3.10. The data show consequences of applying Calyculin A, Blebbistatin and Latrunculin A to MDA-MB-231 cells. The values g = 0.375 [18], gd/k_BT=248 nN^{-1}, N=248 μm^{-1} were used for all fits. This table is originally published in [11].

	MDA-MB-231	keratocytes	PtK1	Units
polymerization rate		$\approx$ 0.27 [227]		μms^{-1}
force free network extension rate V_e^0		$\approx$ 0.17 [228]		μms^{-1}
retrograde flow velocity v_r	order of 0.01 [229]	Fig. 3.4, 0.04 [14, 128], 0.07 [230]	Fig. 3.4, 0.015 [13, 73, 231]	μms^{-1}
retrograde flow friction coefficient κ	$\approx$ 100 [232]	$\approx$ 4 [227], 10[225]	$\approx$ 6 [73], 4 [231]	$nNs\mu m^{-2}$
force on leading edge F		few hundreds [15, 211, 230, 233]		$pN\mu m^{-1}$

TABLE 3.5: Experimental results on cell parameters in different cell types. We did not find any values for CHO cells. Retrograde flow velocities usually depend on the distance from leading edge. In the cases of radial retrograde flow profile, the average value over the lamellipodium width is reported in the table. This table is originally published in [11].

the G-actin concentration available for polymerization at the cell front [235]. In keratocyte, [G]$\approx$10 µM , while the force-free network extension rate V_e^0 is $\approx$ 0.17 μms^{-1} [228]. This polymerization rate is very close to our fitting results (Table). The high values of force-free polymerization rate in these cells can be explained by the funneling mechanism [227]. Other factors like modulators of polymerization/depolymerization can also limit the polymerization rate [236].

We see a large variability in the network extension rate v_e of different cell types (from high value of about 0.17 μms^{-1} for keratocytes [228] to low value of about 0.007 μms^{-1} for fibroblasts [237])). The reduction of extension rate by force can not explain this large range. Thus, we expect that V_e^0 also varies significantly, which can be explained by the cell-type variability of the concentration of polymerization modulators and G-actin. The variation in k^- can also be explained by the variation in the modulators of

depolymerization [236].

The parameter κ is an effective friction coefficient, that is defined as the ratio of protrusive force, F, to the retrograde flow velocity, v_r. F can be estimated experimentally from the membrane tension at the leading edge membrane[233]. Measurement of the stall force is another way to estimate the force. In keratocytes, the value of a few hundreds of pNμm^{-1} is reported for both methods [15, 211, 230]. In other cell types, the force has not been measured directly yet. However, we can still estimate the force by integrating the traction stress over the regions close to the edge.

$$\widehat{T} = \int_0^l T(x)dx \tag{3.14}$$

$T(x)$ is the local traction stress and l the width of a region close to the leading edge, in which retrograde flow generates traction stress. The integral of traction $\widehat{T}$ can provide an estimation for the force at the leading edge F. We can then find the parameter κ by dividing the estimated force by the retrograde flow velocity. We find a good agreement between the κ from our fittings and the indirect estimation of κ from literature (Table 3.5).

3.3 Interaction of front and rear

So far in this chapter, we have considered the 1-dimensional steady motion of cells on Fibronectin lanes to get an idea of intracellular forces based on the force dependency of polymerization. The whole cell moves like a rigid body in steady motion, and we can not investigate the interaction between the front and rear of the cell. Thus, a perturbation of motion is required to study the mechanical properties of the front-rear interaction. Fibronectin density step is a perturbation that disturbs the steady state force balance. The dynamic response of the cell front and rear to the perturbation provides insights into the front-rear interaction (Fig. 3.11). During transitions between areas with differential Fibronectin density, the front and rear of the cell sense different coating densities (Fig. 3.11A). The cell velocity adapts to the Fibronectin density between transitions.

Fig. 3.11B shows the velocity of the cell during several transitions. The cell velocity increases when the front enters a region with high Fibronectin density. After a while, when

the cell rear reaches the high adhesion region, the velocity slightly decreases (Fig. 3.11). On a low-adhesion to high-adhesion transition, the cell shows the opposite behavior. When the cell front enters the low Fibronectin region, the velocity decreases, and when its rear reaches that low-adhesion region, velocity increases again (Fig. 3.11). This observation confirms the idea that adhesion at the rear resists motion while adhesion at the front supports motion.

In order to study the dynamics of the front and rear during the transition, the time resolution of 10 min we used in our first experiments is not sufficient, as during this time the cells usually move about 10 µm. Thus, we did a second set of experiments with 20 s time resolution to capture the dynamics. Due to the 1-dimensional nature of the cell movement, it is possible to make kymographs from the phase-contrast movies (using the middle line of the lanes) that nicely illustrate the dynamics of the cell motion over time and allow to detect front and rear positions (Fig. 3.11A). These kymographs reveal that the front motion is smooth with gradual velocity change over the Fibronectin steps (Fig. 3.11B). On the contrary, the rear moves less smoothly with large fluctuations. We find that even a transient protrusion can form and extend backwards at the cell rear. To study the behavior of the front and rear on the steps separately, we introduce the velocity of the back v_b. The front velocity is the same as the cell velocity v. The velocity of the cell rear fluctuates a lot, but on average, it is also equal to the cell velocity v during the steady state motion.

The force resisting motion should be studied in more detail to understand the difference between v and v_b. Analyzing the cell length L on the Fibronectin steps reveals that it is mainly determined by the adhesion density at the cell rear. Based on that observation, we split the resisting force into two parts. The first contribution is from the drag force required to pull the cell body and the front part of the cell $\zeta_c v$. The second part is the force required to pull the cell off the adhesion bonds at the rear $\zeta_b v_b$ (Fig. 3.12A). In this case, the length dynamics $\dot{L}$ also enters the force balance equation. Thus, the stationary force balance Eq. 3.8 turns into (taking $F_c = F_m = 0$ into account):

$$\zeta v - \zeta_b \dot{L} \;=\; \zeta_c v + \zeta_b v_b \;=\; \kappa v_r \tag{3.15}$$

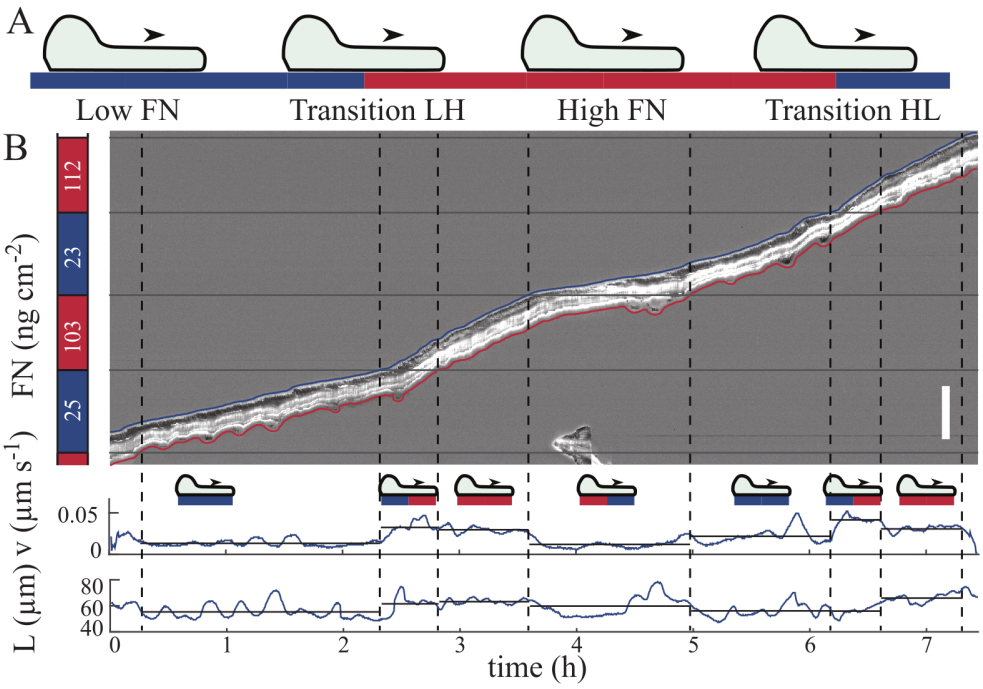

FIGURE 3.11: Perturbation of steady motion at steps of different Fibronectin densities. A) We distinguish phases where cells are completely on one density segment, and transition phases where cell front and back are on different densities. B) Kymograph of a cell running through areas of different Fibronectin densities (given on the left). We trace front (blue) and back (red) and provide the time course of front velocity and cell length. Mean velocities and mean length are indicated by horizontal lines for each phase. Scale bar is 100 µm . This figure is originally published in [11].

Travelling across a Fibronectin step takes about 50 min. That is sufficient to reach a stationary state. In these stationary states, front and back move on different Fibronectin densities but with the same velocities, $v = v_b$. The cell length also does not change, $\dot{L}$=0. Thus, we have:

$$\kappa v_r = (\zeta_c + \zeta_b)v \tag{3.16}$$

with $\zeta = \zeta_c + \zeta_b$. We start our experimental investigations with the question for an intrinsic Fibronection-related cell length. We analyzed the cell length on different Fibronectin densities to discover whether it is dependent on the history of the cell. If the cell length is independent of the cell history, the cell length should mainly be set by the current Fibronectin density B under the cell. We consider the length of a cell on one density and the length after transitions to the other density and back. The distribution of the ratio of the new length and the old length peaks around 1 (Fig. 3.12B, C). Thus, we conclude that cells have an intrinsic adhesion-dependent length $L_0(B)$.

This observation motivates us to phenomenologically choose an elastic force as the the force resisting cell stretching $F_S = E(L - L_0)$. Thus, the force pulling on the rear elastically stretch the cell $\zeta_b v_b = E(L - L_0)$ (Fig. 3.12A). Our data do not allow to find the mechanisms by which cells realise this spring-like behavior. Two possible mechanisms are a fast interaction of front and rear reported by Maiuri et al. [8] or a 1d-analogon to a preferred shape in 2d [14, 238, 239].

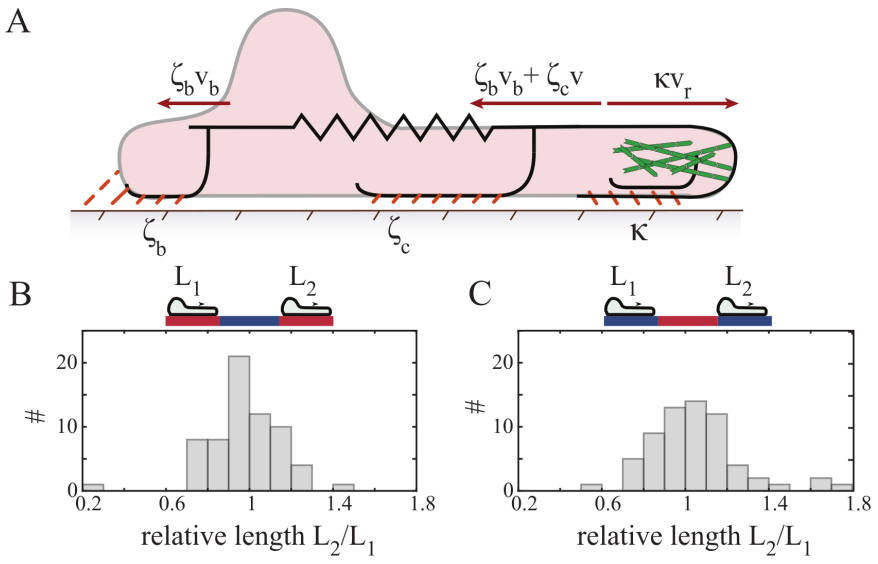

FIGURE 3.12: Extended model with separate contributions of front and back regions to the drag force. A) Sketch of the cell model with spring like front-rear interaction force. B, C) The ratio of the mean lengths of individual cells after to before crossing a density region. This figure is originally published in [11].

On the Fibronectin steps, the velocities of the cell ends depend on the local Fibronectin density and also the density at the other end. The information from the other side of the cells is transmitted by the elastic force F_S. We define four different density combinations by averaging across all measured data points in the different regimes. 99 single-cell tracks with a time resolution of 30 s were analyzed. We find 562 individual Fibronectin situations at the front and back of the cell. These cases are then classified into 4 groups, low Fibronectin at the back and front (LL), low Fibronectin at the back and high Fibronectin at the front (LH), high Fibronectin at the back and low Fibronectin at the front (HL), and finally high Fibronectin at the back and front (HH). We define high and low as above or below 50 ngcm^{-2}. Fig. 3.13 shows all the data points in the four density combinations at front and back.

We measured the velocities of the front and back edges separately. This data and the

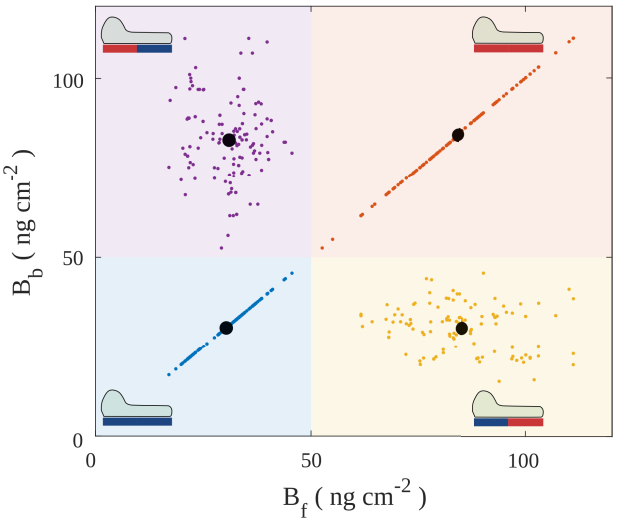

FIGURE 3.13: Measured Fibronectin density combinations. 562 different combinations of front and and back Fibronectin density were found (Colored points) from 99 single-cell tracks. 4 generic phases (LL bottom left, LH bottom right, HL up left and HH up right.) are defined according to the Fibronectin density at front and back of the cell. Average density of Fibronectin in high and low fields are 80 and 30 ngcm^{-2}, respectively (Black points). Low and high are defined as Fibronectin densities lower and higher than 50 ngcm^{-2}. This figure is originally published in [11].

cell length in different combinations of Fibronectin at the front and back provide a basis for our analysis of front and back forces. The friction coefficient κ is between the retrograde flow and stationary structures in the front part of the cell. Thus, it only depends on the Fibronectin density at the front. The drag coefficient ζ depends on the Fibronectin density both at the front and back. We found that a Hill function can reasonably represent the dependency of κ and ζ to the Fibronectin density B. We define the dependency of $\zeta(B_b, B_f)$ on the B_f and B_b similarly with a Hill function.

$$\kappa(B_f) = \frac{\kappa_{max} B_f^{n_\kappa}}{B_f^{n_\kappa} + K_\kappa^{n_\kappa}}, \qquad \zeta(B_b, B_f) = \frac{\zeta_{max}\big(wB_b + (1-w)B_f\big)^{n_\zeta}}{\big(wB_b + (1-w)B_f\big)^{n_\zeta} + K_\zeta^{n_\zeta}}. \tag{3.17}$$

w describes the contribution of B_b to ζ. w is not known a priori and will be estimated from the dynamic behavior of cells on Fibronectin steps . With Eq. 3.17, $\zeta(B_b, B_f)$ reduces to Eq. 3.10 when the cell is on a homogeneous part of the Fibronectin lane (w=1 or w=0). We can then describe the contributions of front and back to the resisting force separately:

$$F = \kappa v_r = \zeta_b v_b + \zeta_c v, \tag{3.18}$$

F_c= 0 and F_m= 0 are taken into account in Eq. 3.18. When the front and back velocities are equal (steady motion), $\zeta = \zeta_c + \zeta_b$, and Eq. 3.18 turns into Eq. 3.8. ζ_c is dependent

on both front and back Fibronectin densities. But ζ_b depends on the Fibronectin density at the back of the cell only

$$\zeta_b = \frac{\zeta_{b,max} B_b^{n_\zeta}}{B_b^{n_\zeta} + K_\zeta^{n_\zeta}}, \tag{3.19}$$

With that, we find ζ_c as $\zeta_c(B_b, B_f) = \zeta(B_b, B_f) - \zeta_b(B_b)$. For simplicity, we choose that only the saturation value in Eq. 3.19 is different from Eq. 3.10 and not the parameters K_ζ and n_ζ. In the steady motion, the cell length that mediates front and back is affected by ζ_b

$$\zeta_b v_b = E(L - L_0). \tag{3.20}$$

We can then find the cell velocity in each of the 4 different combinations of front and back Fibronectin density according to Eq. 3.9:

$$v_{LL} = \frac{N}{a\zeta_{LL}} W_0\left(\frac{aV_e^0\kappa_L\zeta_{LL}}{N(\zeta_{LL}+\kappa_L)} e^{\frac{a}{N(\zeta_{LL}+\kappa_L)}(\zeta_{LL}\kappa_L k^-)}\right) - \frac{\kappa_L k^-}{\zeta_{LL}+\kappa_L} \tag{3.21}$$

$$v_{HH} = \frac{N}{a\zeta_{HH}} W_0\left(\frac{aV_e^0\kappa_H\zeta_{HH}}{N(\zeta_{HH}+\kappa_H)} e^{\frac{a}{N(\zeta_{HH}+\kappa_H)}(\zeta_{HH}\kappa_H k^-)}\right) - \frac{\kappa_H k^-}{\zeta_{HH}+\kappa_H} \tag{3.22}$$

$$v_{LH} = \frac{N}{a\zeta_{LH}} W_0\left(\frac{aV_e^0\kappa_H\zeta_{LH}}{N(\zeta_{LH}+\kappa_H)} e^{\frac{a}{N(\zeta_{LH}+\kappa_H)}(\zeta_{LH}\kappa_H k^-)}\right) - \frac{\kappa_H k^-}{\zeta_{LH}+\kappa_H} \tag{3.23}$$

$$v_{HL} = \frac{N}{a\zeta_{HL}} W_0\left(\frac{aV_e^0\kappa_L\zeta_{HL}}{N(\zeta_{HL}+\kappa_L)} e^{\frac{a}{N(\zeta_{HL}+\kappa_L)}(\zeta_{HL}\kappa_L k^-)}\right) - \frac{\kappa_L k^-}{\zeta_{HL}+\kappa_L} \tag{3.24}$$

We estimate ζ and κ at different Fibronectin combinations using the average low and high Fibronectin densities B_L and B_H, respectively (3.13). κ only depends on the front Fibronectin density, while ζ depends on both front and back Fibronectin. We can find these parameters from Eq. 3.17:

$$\kappa_L = \kappa(B_L), \qquad \kappa_H = \kappa(B_H) \tag{3.25}$$

$$\zeta_{HH} = \zeta(B_H, B_H), \quad \zeta_{HL} = \zeta(B_H, B_L), \quad \zeta_{LL} = \zeta(B_L, B_L), \quad \zeta_{LH} = \zeta(B_L, B_H) \tag{3.26}$$

We used the velocity and length experimental data in each of the 4 Fibronectin situations to find the parameters of the Eqs. 3.17-3.24. The results of the fits are presented in Figs. 3.14, 3.15, 3.16, and Table 3.6.

The model can reproduce the velocity not only for the homogeneous Fibronectin case but also for the situations with different adhesion at the front and back. We find that ζ is mainly determined by the Fibronectin density at the front (Figs. 3.15, 3.16, Table 3.6).

Thus, a substantial part of the resistance against the motion comes from the resistance of the front part (including the cell body) $\zeta_c v$. The contribution of different cell parts to the resistance against motion is also reflected in the behavior of length L on the steps. L is mainly determined by the Fibronectin at the back edge. The force stretching the spring is $\zeta_b v_b$. When the cell back is on low Fibronectin, the length is minimal due to lower stretching force, and it is maximal when the back is on high Fibronectin (Fig. 3.14B). This agrees with the results of Hennig et al. [88]. Our simulations show the same behavior and exhibit the most extended cells when both front and rear are on high coating density (Fig. 3.14B) and forces are the strongest (Fig. 3.8).

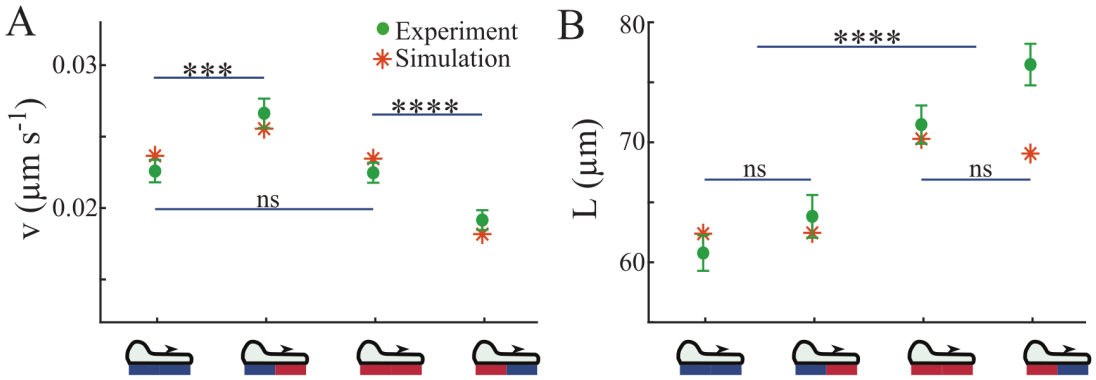

FIGURE 3.14: Average velocity and length of cells in 4 combinations of Fibronectin density at the front and back. A) Front velocity averaged over individual phases measured from 99 kymographs set in relation to simulation results. Error bars show the standard error of the mean. B) Length averaged for individual phases and compared to simulation results. Results of two-sided t-test: *** p<0.001, **** p<0.0001, ns not significant. This figure is originally published in [11].

We could classify the cells into 2 groups with respect to their velocity behavior. Some cells moving across the density regions in a given experiment are in the rising phase of the adhesion–velocity relation and exhibit a smaller velocity v on low Fibronectin than on high Fibronectin ($v_{LL} < v_{HH}$), and some are in the falling phase and show ($v_{LL} > v_{HH}$). Cells in the group ($v_{LL} < v_{HH}$) of the adhesion–velocity relation show the higher velocities when the cell front is on high density, since increasing Fibronectin density also increases and, therefore, the force generated by the front region (Fig. 3.15). With cells in the group ($v_{LL} > v_{HH}$), κ is close to saturation on both high and low Fibronectin density (Fig. 3.16). Increasing adhesion at the front increases force generation not via κ in this phase, but by increasing retrograde flow on the expense of the cell velocity v. Therefore, velocities are the highest when resistance to motion is the lowest, i.e., when

the cell rear is on low density. These observations nicely illustrate that the biphasic character of the adhesion–velocity relation results from competing forces.

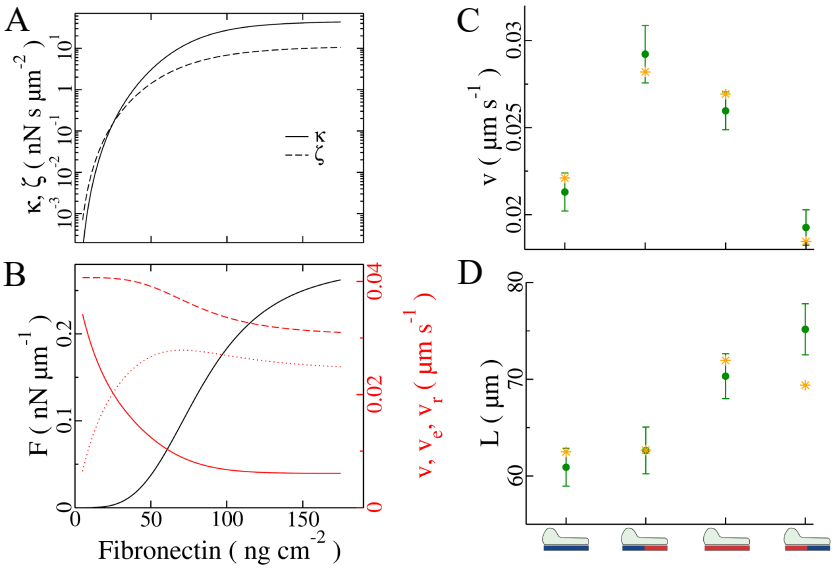

FIGURE 3.15: A) Analysis of the experimental data in the group $v_{LL} < v_{HH}$ with respect to retrograde flow velocity, friction coefficient κ, and membrane drag coefficient ζ as resulting from the fits to Eqs. 3.17 and 3.24. B): Analysis of the experimental data in the group $v_{LL} < v_{HH}$ with respect to extension velocity v_e (dashed line), retrograde flow velocity v_r (full line), cell velocity v (dotted line), and the force F-acting on the leading edge membrane as resulting from the fits to Eqs. 3.17 and 3.24.C) Front velocity averaged over individual phases measured from 44 kymographs set in relation to simulation results. Error bars show the standard error of the mean. D) Length averaged for individual phases from the same kymographs as in C) and compared to simulation results. This figure is originally published in [11].

	cells with $v_{LL} < v_{HH}$	all cells	cells with $v_{LL} > v_{HH}$	Units	Eq.
V_e^0	0.0420	0.0374	0.0364	$\mu m s^{-1}$	3.24
k^-	0.0013	0.0005	0.0012	$\mu m s^{-1}$	3.24
n_κ	4.3883	4.1921	4.8513		3.17
K_κ	91.5122	85.8609	53.1185	$ng cm^{-2}$	3.17
n_ζ	3.3569	3.5093	3.0509		3.17
K_ζ	90.5096	99.3621	99.9418	$ng cm^{-2}$	3.17
κ_{max}	45.6928	35.1310	25.8810	$nNs\mu m^{-2}$	3.17
ζ_{max}	11.6791	15.6424	21.9652	$nNs\mu m^{-2}$	3.17
$\zeta_{b,max}$	0.9628	1.2736	2.0525	$nNs\mu m^{-2}$	3.19
w	0.0679	0.1142	0.1828		3.17
E	0.0010	0.0011	0.0015	$nN\mu m^{-2}$	3.20

TABLE 3.6: The parameter values corresponding to the plots in Fig. 3.15 ($v_{LL} < v_{HH}$), the simulations in Figs. 3.14, , 3.18 (all cells), and the plots in Fig. 3.16 ($v_{LL} > v_{HH}$). The values g = 0.375 [18], gd/k_BT=248 nN^{-1}, N=248 μm^{-1},F_c=0 $nN\mu m^{-1}$, F_m=0 $nN\mu m^{-1}$, and L_0=62 µm , were used for all fits. This table is originally published in [11].

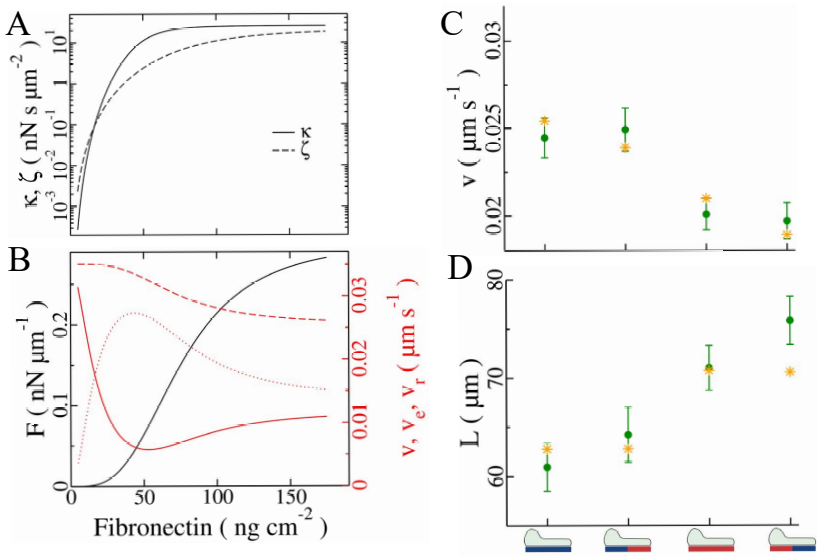

FIGURE 3.16: A) Analysis of the experimental data in the group $v_{LL} > v_{HH}$ with respect to retrograde flow velocity, friction coefficient κ, and membrane drag coefficient ζ as resulting from the fits to Eqs. 3.17 and 3.24. B): Analysis of the experimental data in the group $v_{LL} > v_{HH}$ with respect to extension velocity v_e (dashed line), retrograde flow velocity v_r (full line), cell velocity v (dotted line), and the force F-acting on the leading edge membrane as resulting from the fits to Eqs. 3.17 and 3.24.C) Front velocity averaged over individual phases measured from 42 kymographs set in relation to simulation results. Error bars show the standard error of the mean. D) Length averaged for individual phases from the same kymographs as in (C) and compared to simulation results. This figure is originally published in [11].

3.3.1 Elastic modulus

We find the elastic modulus value $E \approx 0.001$ nNµm^{-2} from the fittings to length and velocity data of different Fibronectin combinations 3.14. We analyzed the dynamics of the back edge in single-cell tracks to check the validity of our estimation of E. Unlike the front edge, which moves smoothly, the back edge exhibits much more dynamics. The back velocity varies due to the formation and collapse of the back lamellipodia. We investigate this topic in the next chapter in more detail. Here, we only use the variations of back velocity to find another estimation for the parameter E.

Eq. 3.20 provides a relation between length, back velocity, back drag coefficient and elastic modulus, i.e. $\frac{\Delta v_b}{\Delta L} = \frac{E}{\zeta_b}$. We analyzed the back velocity in single-cell tracks and found the variation of length and back velocity during the slippage of the back edge. We calculated Δv_b and ΔL between the moment that back velocity peaks and the next time frame. We only considered significant peaks of back velocity for this analysis to minimize the error. Fig. 3.17 shows the histogram of the $\frac{\Delta v_b}{\Delta L}$ for all the analyzed

cells. We find the mean value of about 0.01 s^{-1}. The Fibronectin density values of the analyzed cells are in the range of 20-110 $ngcm^{-2}$. For this range of Fibronectin density, we find $\widehat{\zeta_b}$ ≈0.2 $nNs\mu m^{-2}$, using Eq.3.19 and parameter values in Table 3.6. E can now be estimated as $E = \widehat{\frac{\Delta v_b}{\Delta L}}\widehat{\zeta_b}$ ≈0.002 $nN\mu m^{-2}$. This is reasonably close to our initial estimation from the step data fits. We also find the amplitude of typical length oscillation to be about 20 μm, with some rare large length oscillations with amplitudes up to 70 μm. With these numbers, we can estimate the variation of the elastic force $E(L - L_0)$ in typical oscillations to be about 0.04 $nN\mu m^{-1}$, and in large oscillations up to 0.14 $nN\mu m^{-1}$.

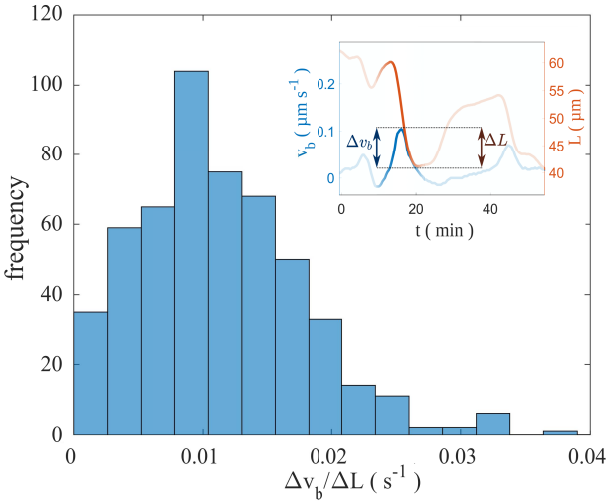

FIGURE 3.17: Histogram of $\frac{\Delta v_b}{\Delta L}$ in rapid retractions of the cell rear. Inset: Δv_b and ΔL in retraction phase of a significant back oscillation event. This figure is originally published in [11].

We can also compare our estimation of elastic modulus with the literature. The parameter E in our model is related to the Young modulus γ of the cell.

$$E = \gamma h / L_0, \tag{3.27}$$

h is the height of the cell. We assume an average value of 0.5 μm for the height. That gives us the γ for the MDA-MB-231 cells in the order of 0.1 kPa. The experimental value of γ for MDA-MB-231 cells reported in [240] is in the same range, ≈0.2-0.3 kPa. Using oscillatory magnetic twisting cytometry, Wang et al. found the stiffness of adherent HASM cells to be ≈ 0.25 kPa [241], and the shear modulus of smooth muscle cells to be on the order of 0.1 kPa [242]. Other studies reported the Young modulus of adherent alveolar epithelial cells in the range of 0.029–0.258 [243] kPa, NIH/3T3 cell

lines ≈ 0.1 kPa [244], adherent HASM cells ≈ 0.25 kPa [241], and smooth muscle cells about 0.1 kPa [242]. This shows that our estimation of elasticity is consistent with the experimental data.

3.3.2 The dynamic cell behavior on Fibronectin steps

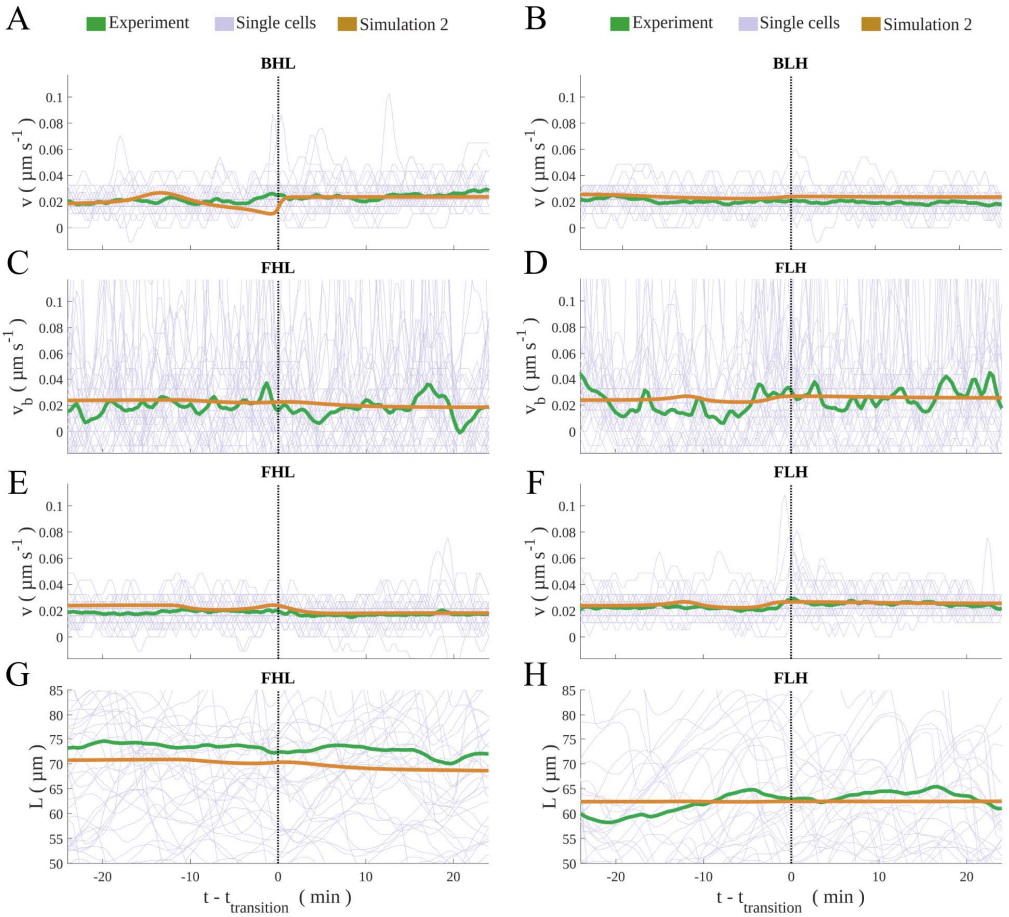

FIGURE 3.18: Simulation of the transient behavior of cells upon Fibronectin coating density change. Thin lines are individual measured trajectories, the green line shows the average value. Simulation results with the detailed Fibronectin profile with additional bumps as in Fig. 3.3.2 are shown by the yellow line. A, B) Front velocity during a transition of the back from high to low Fibronectin (BHL) and low to high (BLH). C, D) Back velocity during a transition of the front from high to low Fibronectin (FHL) and low to high (FLH). E, F) Front velocity during FHL and FLH transitions. G, H) Length dynamics during FHL and FLH transitions. The values of parameters used in these simulations are shown in Table 3.6. This figure is originally published in [11].

We can now simulate the dynamics of a cell moving on a Fibronectin step using the equations describing back and front velocity separately. The dynamics of the length can

then be calculated as the difference between edge velocities. We have

$$\begin{aligned} v &= \frac{N}{a\zeta_c} W_0\left(\frac{aV_e^0\kappa\zeta_c}{N(\zeta_c+\kappa)} e^{\left(\frac{a\kappa}{N(\zeta_c+\kappa)}(\zeta_c k^- - E(L-L_0))\right)}\right) - \frac{E(L-L_0)+\kappa k^{-1}}{(\kappa+\zeta_c)} \\ v_b &= \frac{E(L-L_0)}{\zeta_b} \\ \frac{dL}{dt} &= v - v_b. \end{aligned} \tag{3.28}$$

Motion of cells on Fibronectin steps is simulated using Eqs. 3.17-3.19 and 3.28. At the same time, we tracked the edges in our 99 cell tracks to find the dynamics of cells on steps. Analysis of the front and back velocities during the transitions between Fibronectin densities reveals different characteristics of the front and back. We study different types of transitions; front edge moves from low to high Fibronectin density (FLH), front edge moves from high to low Fibronectin density (FHL), back edge moves from low to high Fibronectin density (BLH), and back edge moves from high to low Fibronectin density (BHL). We find that the front edge velocity v adapts rapidly and smoothly to the new conditions upon transition to a different Fibronectin segment (FHL and FLH transitions in Fig. 3.18). Our simulations with the parameters estimated in the previous sections agree very well with the experimental data of the front transition dynamics.

However, we observe a different behavior during the back transitions BHL and BLH than the front transitions. We find a peak of v_b in the BHL transition (Fig. 3.19A). Our simulations show the same peak during the BHL transition (Fig. 3.19A).

Interestingly, the back velocity also peaks during a BLH transition (although with a smaller peak than BHL transitions). However, the simulation of the BLH transition with a simple step of Fibronectin density does not show such behavior (Fig. 3.19B). We investigated the density profile of Fibronectin on the lanes in more detail, and it turned out that there is a small density maximum and smaller density minima on the border of the low and high Fibronectin segments (A). The peak of the back velocity during the BLH transition can be reproduced when we take into account these details of the Fibronectin profile in our simulations (Fig. 3.19A, B). We also find that the front velocity does not show such peaks during the BHL and BLH transitions (Fig. 3.18A, B).

The length of the cell drops abruptly during the BHL transition because of the peak of the back velocity (Fig. 3.14C). There is also an increase of the length prior to this

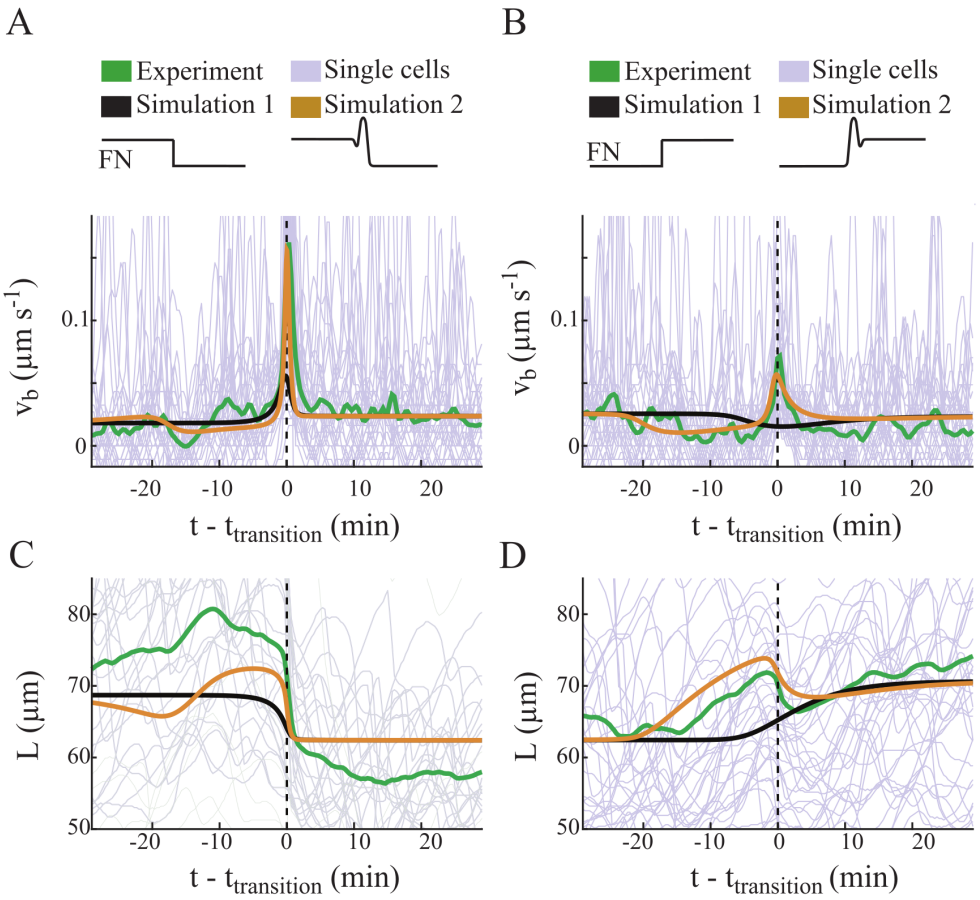

FIGURE 3.19: Back velocity and cell length on the Fibronectin steps. A) Back velocity during a transition of the back from high to low Fibronectin (BHL) and B) from low to high Fibronectin (BLH). A-D) Thin lines are individual measured trajectories, the green line shows their average values. The black line show the simulated time courses for a simple step profile of the Fibronectin density. Simulation results with the detailed Fibronectin profile with additional bumps as in Fig. 3.3.2 are shown by the yellow lines. C, D) Cell length for BHL and BLH transitions. This figure is originally published in [11].

drop. Both observations are reproduced in simulations with detailed Fibronectin density profiles. During the BLH transitions, the cell length increases first and then drops. The simulations also reproduce that. The remarkable conclusion of our simulations on the dynamic cell behavior during the transitions is that even small Fibronectin density variations on the substrate can affect cell migration.

The other conclusion is that with our choice of the elastic force mediating the interaction of front and back, we were able to reproduce the cell behavior in the transitions. The time scale of the action of this elastic force is a few minutes. That is longer than the viscoelastic relaxation time of cells [245]. This supports our choice of elastic force.

3.4 Conclusion and summary

In this chapter, we studied the effect of adhesion on the balance of propulsive and resisting forces and cell velocity. We investigated the nature of the forces that couple the front and back of the cell and the adaptation of cell migration behavior to varying adhesiveness of substrate.

We restricted cell motility to one-dimensional motion, which substantially simplified the analysis by avoiding shape changes occurring on two-dimensional substrates. In addition, since heterogeneities within cell populations easily obscure weak effects of adhesion, we subjected individual cells to steps of adhesion strength and measured relative velocity changes of single cells. For that, our experimental partners employed a novel two-step microcontact printing technique to fabricate patterned Fibronectin lanes with steps of coating density.

We investigated the mechanism of the biphasic adhesion–velocity relation and the character of the front–rear interaction by studying motion of cells on Fibronectin lanes fabricated with two-step microcontact printing. We started with recapitulating the biphasic adhesion–velocity relation for MDA-MB-231 cells. For that, we analyzed data of more than 15000 single-cell tracks. The force balance at the leading edge and force dependency of polymerization allowed derivation of a mathematical model and, thus, for quantitatively analyzing our results and also published data for keratocytes, PtK1 cells, and CHO cells. This quantitative analysis provided mechanistic insight into the biphasic relation. The stationary case with cell front and back moving on homogeneous Fibronectin density with the same velocity was not sufficient to investigate the coupling between front and rear. Therefore, we perturbed motion by alternating Fibronectin density steps and analyzed the dynamics of cells during transition across the density interfaces. This provided insight into the adhesion–length relation and the character of the force mediating front–rear interaction.

In the first part of the chapter, we focused on the biphasic adhesion-velocity relation to study the underlying mechanisms and, in particular forces in cells. We found how the adhesion promotes both propulsive forces and resisting forces, which has been established in many studies [12, 13, 31, 72, 85–87, 199, 202]. The traction forces beneath the cell are directly related to the adhesion. Traction forms a dipole of opposing forces on the

substrate [246, 247]. Cells exert tension on the substrate in the kPa-range [72, 246, 248, 249]. That is equivalent to forces in the range of 100 nN [250]. Our results show that motion-related forces acting on the leading edge membrane are in the range of 0.1 nNµm^{-1}. That is in line with the experimental measurements of the forces [15, 211, 212] and membrane tension [213, 251]. We conclude that traction forces do not directly control cell motion. Otherwise, the difference between two huge opposing forces of 100 nN should be stabilized in a range of 0.1 nN.

Our mechanism suggests that the adhesion-controlled friction forces at the leading edge control the cell velocity, not the traction forces. Leading edge adhesion-controlled forces are 3 orders of magnitude smaller than the traction forces. Polymerization generates a propulsive force that pushes the membrane forward and drives the retrograde flow. This force is transmitted to the substrate through friction, in agreement with the molecular clutch theory suggested in [252]. On the rising branch of the adhesion-velocity relation (low adhesion values), when the adhesion increases, the friction and κ increase, which in turn increase the pushing force at the leading edge and the cell velocity. On the falling branch of the adhesion-velocity relation (high adhesion values), increasing the adhesion leads to a rise of the resisting forces. That decreases the force-dependent polymerization rate. The retrograde flow also increases, and a larger fraction of the actin extension rate transforms to retrograde flow. As a result, the cell velocity decreases again. It is important to note that all the forces involved in this mechanism are velocity-dependent. The immediate feedback that is caused by velocity-dependency provides a fundamental mechanism that can coordinate velocities of the front and back of the cell.

The force at the leading edge is proportional to retrograde flow and the friction coefficient κ. Thus, cells have two ways to increase the propulsive force to overcome the stronger adhesion at the back. They can either increase κ by more adhesion at the cell front or increase the retrograde flow by less protrusion. We found that both approaches are employed by cells. They adapt their adhesion for more powerful force generation [13, 14, 252]. When the κ is saturated and can not be increased more by adhesion, they may increase the retrograde flow velocity (Fig. 3.8, MDA-MB-231 cells, PtK1 cells, keratocytes). Our mechanism implicates a roughly conserved network extension rate which is in line with earlier studies [18, 228, 253].

The dependencies of κ, ζ on the ligand density B are mediated by intracellular signaling

pathways that are triggered by adhesion bonds (Eq. 3.10). Our results show strong cooperativity in MDA-MB-231 and CHO cells (large values of n_κ and n_ζ). At low coating density, velocity rises very fast by about a factor 6 (Fig. 3.2, 3.4) in these cell types. The rise of the force also occurs very fast (Fig. 3.8). This can be an indicator of the feedback on adhesion strengthening by myosin [13, 14, 82, 216]. On the other side, keratocytes and PtK1 cells exhibit smaller values of n_κ and n_ζ. The rise of the force and initial rise of velocity is slower in these cell types (Fig. 3.4, 3.8).

The fits of the adhesion-velocity relation Eq. 3.9 to the experimental data suggest velocity-independent forces to be negligible, i.e. F_c =0 and F_m =0. That result raises a question about the role of myosin in controlling cell velocity. Myosin contraction generates a velocity-independent force. There are diverse experimental results on the myosin role. Some studies show a weak effect of myosin inhibition [252, 254–256], while others suggest strong impact of myosin on the cell velocity [257–260]. Myosin density is highest in lateral and central regions of cells [14]. Contraction and the resulting flow occur mainly in those regions [260]. Our results do not rule out the contribution of myosin to motion. It only suggests that velocity-independent forces are not needed for steady motion. Myosin may contribute to the actin flow and detachment of adhesion sites at the cell back. However, according to our results, its contribution is not significant enough to render forces velocity-independent.

It has been suggested in some studies that a gradient of adhesion is always required for cell motion, such that the adhesion strength is stronger at the front than at the back [78, 79]. In that picture, motion is the result of a tug of war between strong adhesion sites at the front and weak ones at the back. Our experimental results show that cells can move from high Fibronectin to low Fibronectin. On such Fibronectin steps, the adhesion strength at the cell back can be stronger than at the front. With the tug of war mechanism, we would expect to find a maximum Fibronectin step size at which the transition motion stops. Our results within the step heights up to 90 ngcm^{-2} (which is the dynamic range for the adhesion-velocity relation in MDA-MB-231 cells) show that there is no such maximum Fibronectin step size (Fig. 3.8). Furthermore, we find that the resisting forces of the cell motion are mainly generated in the same regions as the protrusive force. Thus, there is no spatial separation for the tug of war mechanism.

In this chapter, we used a mechanical model to study the adhesion-velocity relation.

Our conclusions supplement the earlier studies on the pathways controlling cell motility, e.g., through myosin activation, F-actin density, and other feedbacks. Restricting cells to one-dimensional motion allowed the mechanistic study of basic mechanisms involved in motility without complications of a general two-dimensional case. The Fibronectin steps enabled us to investigate cell adaptation to varying adhesion. We showed that the mechanism with only velocity-dependent forces allows cells to move from high to low adhesion and thus heterogenous substrates, as they encounter within organisms or 'outside the lab'. Studying the transitions also provided insight into the front-rear interaction. The quantitative mathematical framework that is proposed in this chapter can explain the adhesion-velocity relation in all investigated cell types.

Chapter 4

multistability and velocity-persistence relation in 1-dimensional cell motility

In chapter 3, we modeled the basic mechanisms involved in cell motility to investigate the biphasic adhesion–velocity relation and the character of the front-rear interaction. In that context, we looked at the motion of cells in the stationary state with front and back edges moving on homogeneous Fibronectin density with the same velocity. We also studied cell dynamics in situations where alternating Fibronectin steps perturb the motion. Analysis of cells in these situations could provide insight into the character of the front-rear force. The model we introduced in chapter 3 explains the general steady motion of cells on long time scales and the average character of front-rear interaction in the non-stationary case.

When we look on cell kymographs, we can see protrusion activities at the back of the cell, which hints towards a back lamellipodium. We found oscillatory and non-oscillatory states and rich dynamical behavior with MDA-MB-231 cells on time scales of about 10-30 min. Also, cell trajectories exhibit frequent turns due to state and shape dynamics processes. In 1-dimensional motion, change of direction represents transitions between discrete states 'up going' and 'down going'. The existence of the back protrusion and this rich dynamic behavior cannot be captured with the model introduced in chapter 3.

In this chapter, we again restrict cell motion to one spatial dimension to study different states of cells and transitions between these states. We extend our model using non-linear friction as motivated by the clutch mechanism. We also add a competitor lamellipodium at the cell rear and modify the mechanical coupling of the front and rear accordingly. We find that the new extended model can capture the dynamic states of the MDA-MB-231 cells. Using our extended mathematical model and our experiments on the motion of cells in a range of Fibronectin concentrations, we search for a mechanism reproducing universal characteristics of mesenchymal cell motility. The biphasic relation between adhesion and velocity that is shaped by integrin signaling is one of these universal characteristics, which we studied in chapter 3. The other well-established universal characteristic of mesenchymal cell motility is the relation between persistence time and cell velocity (UCSP) [261]. We find that the competition of lamellipodia can explain the cell turns and provide a new mechanism for the UCSP. Our model shows that the biphasic relation between retrograde flow velocity and friction force is a key element of the oscillation mechanism, state transitions, and coupling between persistence time and speed.

The experiments used in this chapter are performed in the Department of Physics at Ludwig-Maximilians-University by Johannes C. J. Heyn and Dr. Christoph Schreiber in the laboratory of Prof. Joachim O. Rädler. All the results presented in this chapter have been published in [262].

4.1 Dynamic cell states

Tracking MDA-MB-231 cells over many hours reveals different dynamic states of these cells. Those states can be captured in kymographs of cell motion. The kymographs are produced using images of cells with time intervals of 20 s. We first identified these dynamic states in our data from chapter 3, i.e., on the stepped Fibronectin lanes (Fig. 4.1).

To test whether different states of cells and transitions between them are associated with the Fibronectin density steps, we seeded MDA-MB-231 cells on Fibronectin lanes with homogeneous density. Interestingly, we find the same dynamic features in the kymographs of cells on homogeneous Fibronectin lanes (Fig. 4.2). Thus, the dynamic states and transitions are intrinsic features of cells.

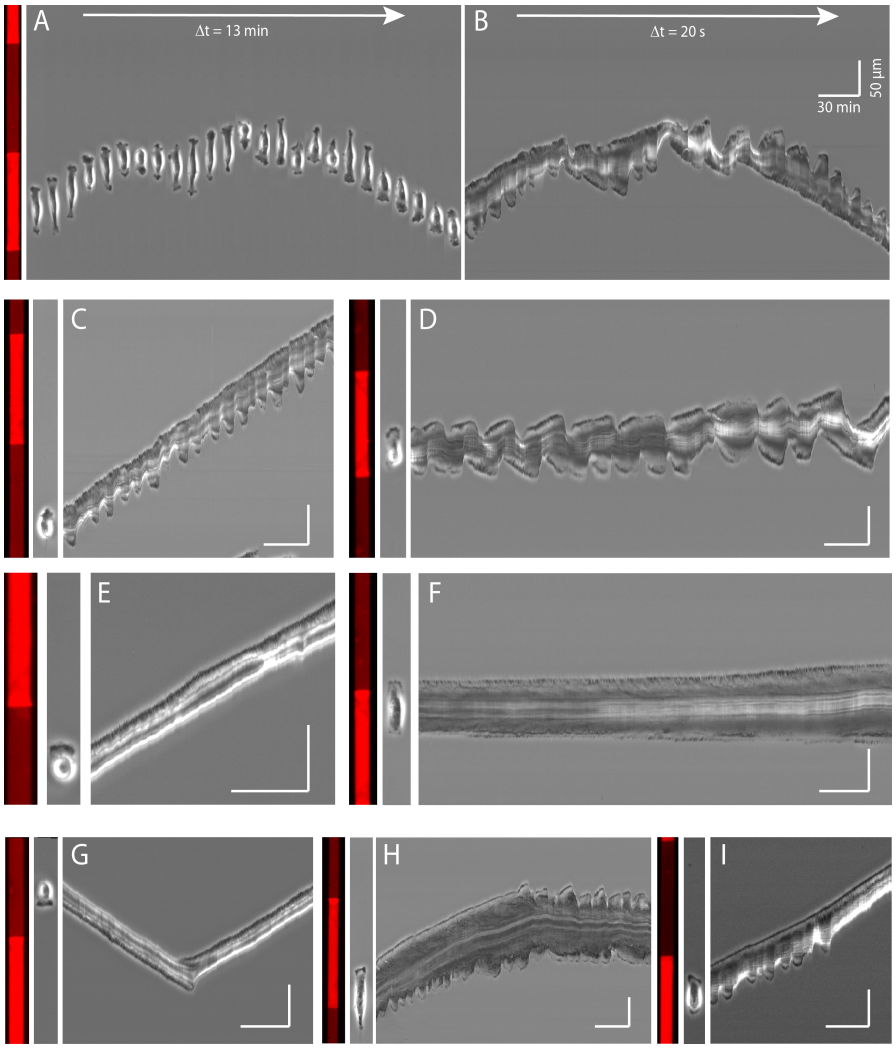

FIGURE 4.1: Different dynamic states of MDA-MB-231 cells on stepped Fibronectin lanes. A) Compilation of cell images in time intervals of 13 min. B) Kymograph resulting from the cell trajectory in A. C-F) Different states of moving and spread cells. G-I) Transitions between dynamic states.

We find cells in 4 different dynamic states. The first state is the spread (non-moving) cell with a steady length (4.2B-E). In addition to the spread steady (SS) state, the spread cells are also found in the oscillatory (SO) state. In the SO state, the cells' length exhibit protrusion and retraction cycles. Cells can move in two different ways: moving steady (MS) and oscillatory (MO) states. In the MO state, the back protrusion exhibit cycles of growth and retraction. The rear edge of the cell oscillates, exhibiting edge velocities opposite to the cell velocity in certain phases of the oscillation. The outward motion of the back edge can not arise from sticking of the edge to the substrate arresting it in the lab frame of reference. But rather, it requires active pushing in the direction opposite to cell motion. Cells can move in both up and down directions. Thus, we observe 6 different dynamic states in total. We have the unpolarized spread states SS and SO,

and the polarized states MS and MO moving either up or down.

Cells can also switch to a different state spontaneously (4.2F-K). These state transitions are taking place on homogeneous Fibronectin lanes without any external stimulation. The cell states and transitions between them will be discussed in detail below.

There is of course a protrusion at the front edge of a moving cell. The occurrence of many phases of negative (backward) back edge velocity indicates the existence of an additional back protrusion. In our experiments, state transitions happen when both front and back protrusions exist. The existence of the back protrusion is not obvious in the MS state (4.2D). However, it is clear from the position of the nucleus that if there exists a back protrusion, it is shorter than the front protrusion. It can also be observed in the state transitions out of MS that the back protrusion emerges or extends prior to the transitions. This observation suggests that the competition between front and back protrusions leads to state transitions.

4.2 Mathematical Model

The observation of the existence of back protrusion and different cell states and transitions in Fig. 4.2 motivated us to extend our model of cell motility presented in chapter 3 to a model with two protrusions at the front and back. Similar to chapter 3, we study the 1-dimensional motility of cells on Fibronection microlanes. We keep our modeling approach as in chapter 3 to model basic phenomena as simple as possible so that the theory can represent the general behavior in many cell types.

In the model we introduce in this chapter, the cell body mediates the interaction of the front and back protrusions (Fig. 4.3). We write the force balance equations of the equivalent mechanical system of the cell (Fig. 4.3), including the front protrusion (Eq. 4.1), cell body (Eq. 4.2), and back protrusion (Eq. 4.3).

$$F_f - E(L_f - L_0) - \zeta_f v_f = 0 \tag{4.1}$$

$$E(L_f - L_0) - E(L_b - L_0) - \zeta_c v_c = 0 \tag{4.2}$$

$$-F_b + E(L_b - L_0) - \zeta_b v_b = 0 \tag{4.3}$$

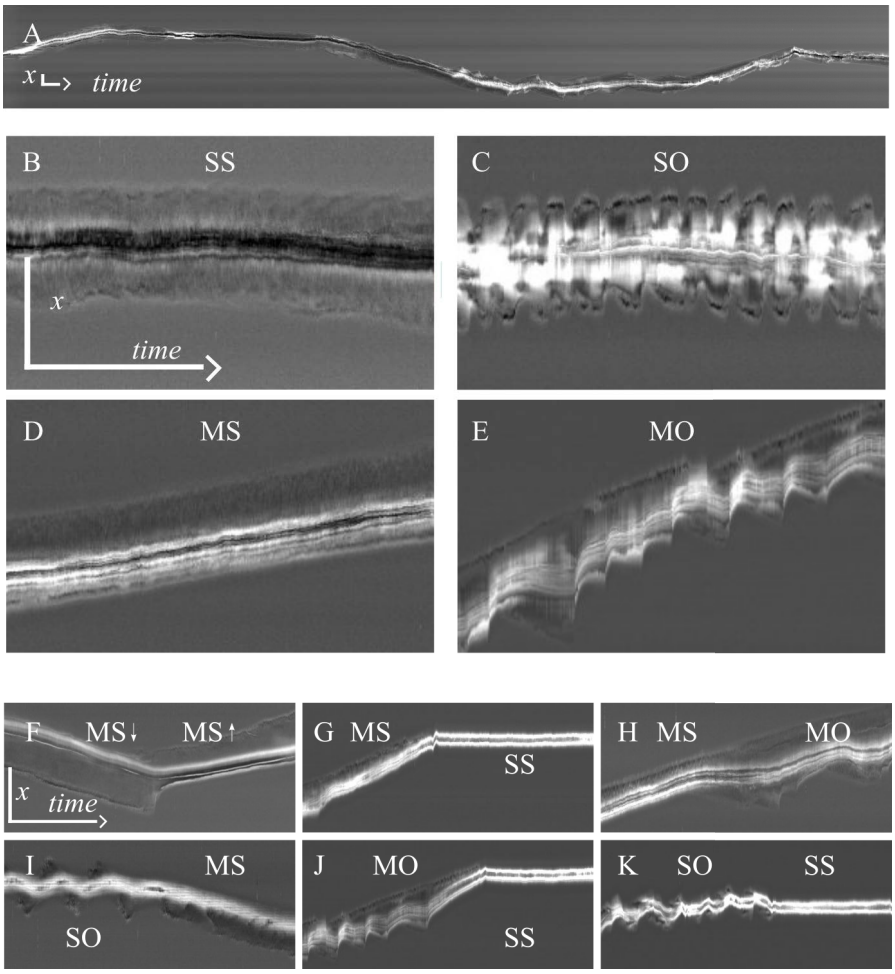

FIGURE 4.2: Different dynamic states of MDA-MB-231 cells on homogeneous Fibronectin lanes. A) A typical trajectory of a MDA-MB-231 cell. B) Spread steady state (SS) C) Spread oscillatory state (SO). D) Moving steady state (MS). E) Moving oscillatory state (MO). F-K) Spontaneous transitions between different dynamic states. Kymographs are created using cell images with the time interval of 30 s. The horizontal scale bar represents 60 min and the vertical scale bar 100 μm.

The relation between the force that couples the front and back of the cell and the length is described well with an elastic spring based on chapter 3. We use the same elastic force for front-nucleus and back-nucleus coupling. This elastic forces can be produced by membrane tension [213, 222, 263–265] or any cytoskeletal element that is length-dependent. The elastic forces are the 1-dimensional equivalent of the volume homeostasis of the cell. There is a drag force between the moving cell and the surrounding environment (substrate and surrounding fluid). We split the total cell drag into the contributions from different parts of the cell. Drag coefficients ζ_f, ζ_b, and ζ_c describe the drags of the front and back protrusions and the cell body. Finally, the forces produced by polymerizing actin pushing the front and back edge membrane are denoted by F_f and F_b, respectively. The positive sign of F_f and F_b indicates pushing the membrane outward. F_f and F_b

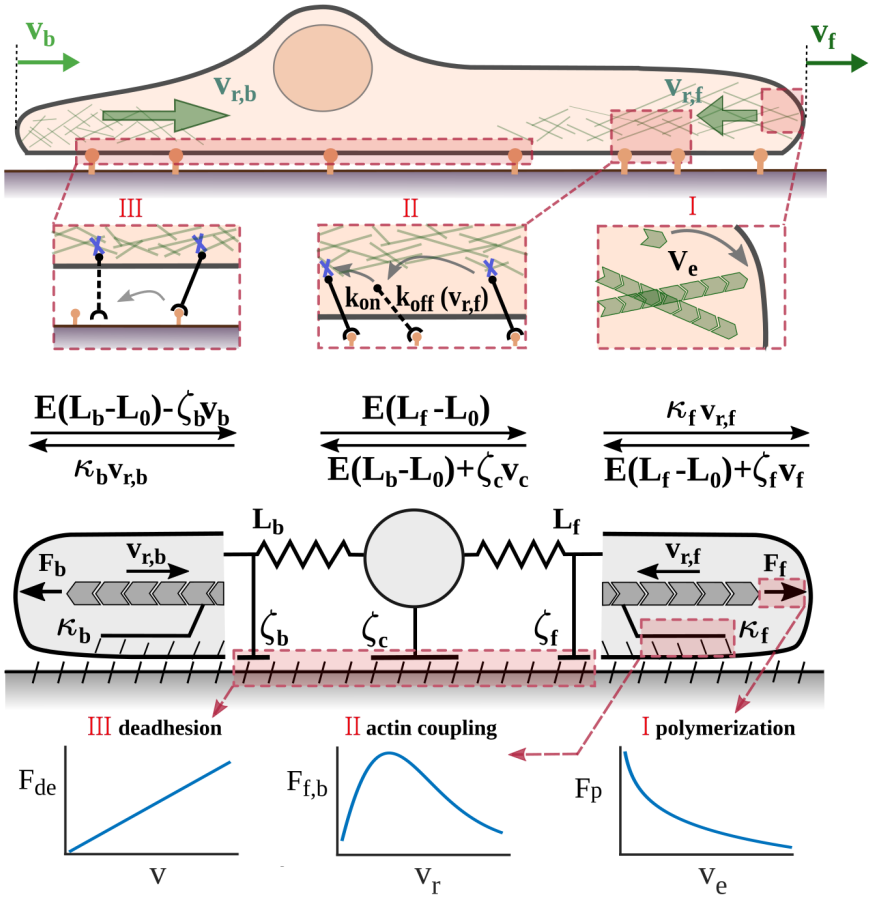

FIGURE 4.3: Schematic illustration of moving cell (top) and the mechanical model cell (bottom). The actin polymerization produces forces F_b, and F_f at the front and back edges. Front and back protrusion edges move with velocities v_f and v_b, respectively. The retrograde flow rates in the front and back protrusions are $v_{r,f}$ and $v_{r,b}$. The friction forces $\kappa_b v_{r,b}$ and $\kappa_f v_{r,f}$ resist the flow of actin. The front and back protrusions and cell body experience drag with the coefficients ζ_f and ζ_b, resp. Elastic forces $E(L_f - L_0)$ and $E(L_b - L_0)$ connects front and back parts of the cell to the cell body. The panels at the bottom show the essential forces considered in the model and their dependencies on velocities. The force required to detach the back of the cell from substrate F_{de} is linearly related to cell velocity. The friction force of the actin retrograde flow exhibits a biphasic dependency on the retrograde flow. The protrusion force F_p is logarithmically related to the extension rate of the actin network v_e.

balance in the spread state. When these forces are asymmetric, they cause motion. The vectorial difference between edge velocity and retrograde flow velocity at the cell edges equals the network extension rate. The extension rate of the actin network depends on the pushing force (see chapter 3). That results in two equations for the front and back edges:

$$v_{r,f} + v_f = V_e^0 e^{-\frac{aF_f}{N}} - k^- \tag{4.4}$$

$$v_{r,b} - v_b = V_e^0 e^{-\frac{-aF_b}{N}} - k^-. \tag{4.5}$$

The factor a is defined similarly to chapter 3 and accounts for filament orientation. V_e^0 is the force-free elongation rate of the network, k^- is the depolymerization rate, and N is the number of filaments per unit length of the edge contour. The lengths of the back and front protrusions $L_{b,f}$ dynamic variables, now. They change when the velocities of the cell's front, back, and nucleus are not equal.

$$\frac{dL_f}{dt} = v_f - v_c \tag{4.6}$$

$$\frac{dL_b}{dt} = v_c - v_b. \tag{4.7}$$

The forces generated by actin network extension at the cell edges also drive the retrograde flow.

$$F_f = \kappa_f v_{r,f} \tag{4.8}$$

$$F_b = \kappa_b v_{r,b} \tag{4.9}$$

The friction between the flow and stationary structures in the cell quantified by the coefficients $\kappa_{f,b}$ resists retrograde flow. Adhesion site density sets the value of the friction coefficients according to the equation in Fig. 3.3.

The edge velocities and the retrograde velocities at the front and back protrusions can be found in dependence on the dynamic variables $L_{f,b}$ and $\kappa_{f,b}$ from the equations above.

$$v_f = \frac{1}{\zeta_f} W_0\left(\frac{V_e^0 \kappa_f \zeta_f}{\zeta_f + \kappa_f} exp\left(\frac{\kappa_f(k^-\zeta_f - E(L_f - L_0))}{\zeta_f + \kappa_f}\right)\right) - \frac{E(L_f - L_0) + k^-\kappa_f}{\zeta_f + \kappa_f}, \tag{4.10}$$

$$v_b = -\frac{1}{\zeta_b} W_0\left(\frac{V_e^0 \kappa_b \zeta_b}{\zeta_b + \kappa_b} exp\left(\frac{\kappa_b(k^-\zeta_b - E(L_b - L_0))}{\zeta_b + \kappa_b}\right)\right) + \frac{E(L_b - L_0) + k^-\kappa_b}{\zeta_b + \kappa_b} \tag{4.11}$$

Analogously, the retrograde flow velocities can also be found in dependence on L and κ

$$v_{r,f}(\kappa_f, L_f) = \frac{1}{\kappa_f} W_0\left(\frac{V_e^0 \kappa_f \zeta_f}{\zeta_f + \kappa_f} exp\left(\frac{\kappa_f(k^-\zeta_f - E(L_f - L_0))}{\zeta_f + \kappa_f}\right)\right) - \frac{-E(L_f - L_0) + k^-\zeta_f}{\zeta_f + \kappa_f} \tag{4.12}$$

$$v_{r,b}(\kappa_b, L_b) = \frac{1}{\kappa_b} W_0\left(\frac{V_e^0 \kappa_b \zeta_b}{\zeta_b + \kappa_b} exp\left(\frac{\kappa_b(k^-\zeta_b - E(L_b - L_0))}{\zeta_b + \kappa_b}\right)\right) - \frac{-E(L_b - L_0) + k^-\zeta_b}{\zeta_b + \kappa_b} \tag{4.13}$$

We can also write the forces at the front and back edges as a function of L and κ

$$F_f = W_0\left(\frac{V_e^0 \kappa_f \zeta_f}{\zeta_f + \kappa_f} \exp\left(\frac{\kappa_f(k^-\zeta_f - E(L_f - L_0))}{\zeta_f + \kappa_f}\right)\right) + \frac{\kappa_f(E(L_f - L_0) - k^-\zeta_f)}{\zeta_f + \kappa_f} \tag{4.14}$$

$$F_b = W_0\left(\frac{V_e^0 \kappa_b \zeta_b}{\zeta_b + \kappa_b} \exp\left(\frac{\kappa_b(k^-\zeta_b - E(L_b - L_0))}{\zeta_b + \kappa_b}\right)\right) + \frac{\kappa_b(E(L_b - L_0) - k^-\zeta_b)}{\zeta_b + \kappa_b} \tag{4.15}$$

In the equations above, we have assumed the reasonable values $N_f = N_b$ =248 μm^{-1} for simplicity. With those values we have $\frac{a}{N_f} = \frac{a}{N_b} = 1$ μm /nN (as in chapter 3). The velocity of the cell nucleus can be obtained from the force balance:

$$v_c = \frac{E(L_f - L_b)}{\zeta_c} \tag{4.16}$$

The flow of actin is opposed by the friction between actin and stationary structures in the cell. Particularly, stress fibers and the intracellular interface of adhesion sites generate frictional resistance against the retrograde flow of actin [217, 252, 266]. This friction is the primary way of force transmission to the substrate [15, 71–73, 217, 225, 252, 266].

Unlike in chapter 3 where we focused on the stationary properties, here we study the dynamic behavior. We use the noisy clutch dynamics to model the interaction of the treadmilling actin network and the stationary structures in the cell,. This means that the friction coefficient κ is a dynamic variable. The clutch mechanism is suggested and supported by many theoretical and experimental studies [71–73, 217, 225, 252, 266]. It has been shown that actin flow friction force has a biphasic relation with retrograde flow

rate [73, 252, 267–269]. At small retrograde flow rates, the force increases with velocity, and after a critical flow speed, the force decreases (Fig. 4.3). This biphasic relation entails a stick-slip dynamics. If the retrograde flow increases in a working regime close to the critical flow velocity, the friction force decreases while the protrusive force is maintained. That accelerates the retrograde flow, and the protrusion slips. Stick-slip dynamic is a common observation in nature and it is also suggested to be relevant in cell motility [99, 100, 269].

The strength of the friction coefficient depends on the number of transient bonds between the actin network and the intracellular interface of adhesion sites. The detachment of these bonds is dependent on the retrograde flow in a nonlinear way. At slow retrograde flow, the binding rate increases more than the unbinding rate with increasing retrograde flow. Thus, the number of bonds increases with the retrograde flow in this regime. On the contrary, at high retrograde flow speed, the unbinding rate exceeds the binding rate when the retrograde flow increases. Consequently, the number of bonds decreases with the retrograde flow rate. This motivates the choice of an unbinding rate term exponentially dependent on the retrograde flow velocity like, which originates from lowering the activation energy for the dissociation reaction by strain on the bond maintained by the relative motion [269, 270]. So, for the κ dynamics, we have:

$$\frac{d\kappa_f}{dt} = c_1(\kappa_f^{lim} - (\kappa_f - \kappa_0)) - c_2 e^{\frac{|v_{r,f}|}{c_3}}(\kappa_f - \kappa_0) + \eta_f(t) \tag{4.17}$$

$$\frac{d\kappa_b}{dt} = c_1(\kappa_b^{lim} - (\kappa_b - \kappa_0)) - c_2 e^{\frac{|v_{r,b}|}{c_3}}(\kappa_b - \kappa_0) + \eta_b(t), \tag{4.18}$$

κ_0 and κ^{lim} are the minimum and maximum values of the retrograde flow friction coefficient. The stochastic nature of the association and dissociation of bonds can cause some noise on top of the deterministic dynamics in systems as small as protrusions [271]. Several studies have shown the relevance of the noise for cell adhesion and actin flow dynamics [269, 272–275]. We added the noise terms $\eta_{f,b}(t)$ to take this stochasticity into account at the front and back protrusions.

$$\langle \eta_{b,f}(t) \rangle = 0 \tag{4.19}$$

$$\langle \eta_{b,f}(t)\eta_{b,f}(t') \rangle = \frac{c_1(\kappa_{b,f}^{lim} - \kappa_{b,f}) + c_2 e^{\frac{|v_{r,b,f}|}{c_3}} \kappa_{b,f}}{\alpha \kappa_{b,f}^{lim}} \delta(t - t') \tag{4.20}$$

The biphasic relation between the force and retrograde flow described above can be obtained as the stationary state of Eqs. 4.17, 4.18.

$$F_{f,b} = v_{r,f,b} \left(\kappa_0 + \frac{\kappa^{lim}}{1 + (c_2/c_1) e^{\frac{v_{r,f,b}}{c_3}}} \right), \tag{4.21}$$

The maximum force is obtained at the critical flow rate $v_{r,cr}$

$$v_{r,cr} = c_3 W_0 \left(1 + \frac{c_1}{c_2} e^{-1} \right). \tag{4.22}$$

W_0 denotes the Lambert-W$_0$ function. The biphasic relation between force and retrograde flow is shown in Fig. 4.3.

Adhesion and integrin signaling affect the retrograde flow friction via $\kappa_{f,b}^{lim}$. The maximum friction coefficients $\kappa_{f,b}^{lim}$ as well as the drag coefficients $\zeta_{f,b}$ are Hill-type functions of the Fibronectin density under the respective part of the cell $B_{f,b,c}$ (see chapter 3).

$$\kappa_f^{lim} = \kappa_0 + \frac{\kappa^{max} B_f^{n_\kappa}}{K_\kappa^{n_\kappa} + B_f^{n_\kappa}}, \qquad \kappa_b^{lim} = \kappa_0 + \frac{\kappa^{max} B_b^{n_\kappa}}{K_\kappa^{n_\kappa} + B_b^{n_\kappa}}. \tag{4.23}$$

The drag coefficients ζ at different regions of the cell are:

$$\zeta_f = \zeta_0 + \frac{\zeta^{max} B_f^{n_\zeta}}{K_\zeta^{n_\zeta} + B_f^{n_\zeta}}, \qquad \zeta_b = \zeta_0 + \frac{\zeta^{max} B_b^{n_\zeta}}{K_\zeta^{n_\zeta} + B_b^{n_\zeta}}, \qquad \zeta_c = b \left(\zeta_0 + \frac{\zeta^{max} B_c^{n_\zeta}}{K_\zeta^{n_\zeta} + B_c^{n_\zeta}} \right) \tag{4.24}$$

ζ_0 is the minimum level of drag coefficient when there is no Fibronectin coating on the substrate. The relative contribution of the cell body to the cell drag is described with the parameter b.

The state of a cell can be described with 4 variables L_f, L_b, κ_f, and κ_b. The dynamics of the cell is explained by a 4th order dynamical system of Eqs. 4.6-4.7, 4.17, and 4.18. In

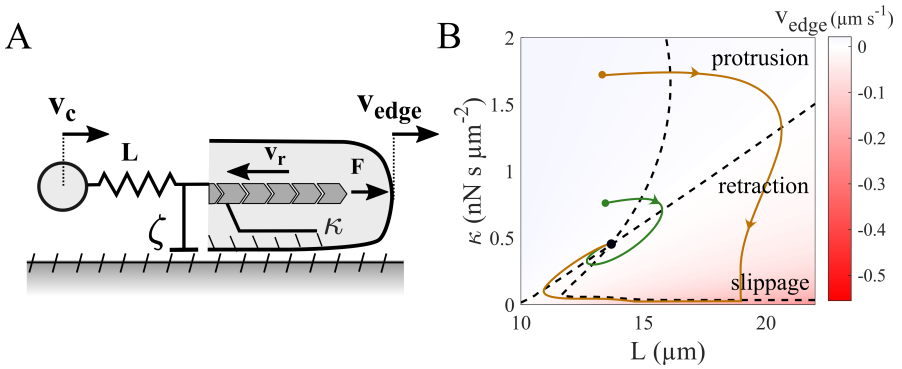

FIGURE 4.4: A) Schematic illustration of the simplified model for one protrusion. B) The phase plane of a protrusion in the spread state ($v_c = 0$). Nullclines of the system are shown with black dashed lines. Two example trajectories with different behaviours are illustrated in the phase plane. The green and orange lines show the variation of the state after a small and large perturbations. The cell edge velocity is shown as the background color.

the following sections, we simulate cells on 1-dimensional Fibronectin lanes in different conditions using these equations.

4.2.1 Decoupled protrusions model

Studying cell behavior in phase space provides crucial insight. The phase space of our system is a 4-dimensional space of the dynamic variables L_f, L_b, κ_f, and κ_b. Illustration and investigation of the system behavior in this 4-dimensional space are not intuitive. In this section, we introduce a simplified version of our model to help understand the mechanisms producing dynamic behaviors. The cell body couples front and back in our model. We can decouple the front and back dynamics by assuming a fixed v_c. That splits up the fourth order system into two second order systems describing front and back protrusions. The effect of the other protrusion then appears in the parameter v_c (Fig. 4.4A). With that assumption, we have:

$$\frac{d\kappa}{dt} = c_1(\kappa^{lim} - (\kappa - \kappa_0)) - c_2 e^{\frac{|v_r|}{c_3}}(\kappa - \kappa_0) \tag{4.25}$$

$$\frac{dL}{dt} = v - v_c = \frac{1}{\zeta} W_0\left(\frac{V_e^0 \kappa\zeta}{(\zeta+\kappa)} e^{\frac{\kappa(k^-\zeta - E(L-L_0))}{(\zeta+\kappa)}}\right) - \frac{E(L-L_0) + k^-\kappa}{\zeta+\kappa} - v_c \tag{4.26}$$

$$v_r(\kappa, L) = \frac{1}{\kappa} W_0\left(\frac{V_e^0 \kappa \zeta}{(\zeta+\kappa)} e^{\frac{\kappa(k^- \zeta - E(L-L_0))}{(\zeta+\kappa)}}\right) - \frac{-E(L-L_0)+k^-\zeta}{\zeta+\kappa} \tag{4.27}$$

The dynamic variables of a protrusion are L and κ. We can now illustrate the phase plane of a protrusion. Fig. 4.4B shows the phase plane in a spread cell (v_c=0). Dashed lines show the nullclines of the system on which $d\kappa/dt = 0$ or $dL/dt = 0$. The intersection of the nullclines shows the equilibrium state of the system. If the state of the system is perturbed to any point in the phase plane, it will go back to the equilibrium state. Two trajectories of such perturbed states are shown in Fig. 4.4. There is a qualitative difference between these two trajectories. The green line shows the return trajectory for a small perturbation, i.e., the initial point of the trajectory is rather close to the equilibrium point. This trajectory exhibits a quick and smooth return to equilibrium. The brown line shows the return trajectory for a large perturbation. In this case, the length L grows first at almost constant κ. Then κ falls rapidly to very tiny values. Finally, the protrusion collapses (decreasing L) since the clutch disengages (small κ). This is a slippage event through which the state of the system returns to equilibrium. The lower right corner of the phase plane corresponds to the slippage phenomenon with large negative edge velocities. In summary, we find that the trajectories experience qualitatively different returns to the equilibrium depending on the initial perturbation. Based on these notions, we introduced a basin of attraction in the phase planes in the next sections (see Fig. 4.19).

4.3 Simulations and experiments

4.3.1 Simulations and data sets

We analyze the experimental cell tracks on 1-dimensional Fibronectin microlanes and our simulated cell tracks with the same analysis methods. We draw biophysical conclusions from our model based on the agreement between experiments and simulations. In difference to the experiments in chapter 3, we created Fibronectin lanes with homogeneous Fibronectin density. All the experiments and simulations in this chapter are done on homogeneous Fibronectin lanes, except the experiments and simulations related to perturbing motion by Fibronectin steps in section 4.6.4. Fibronectin densities of the

Name of data set	**Temporal resolution**	**Treatment**	**Number of cell tracks**	**Total trajectory time**
1_ctrl_30s	30 s	control	221	2878 h
2_lat_30s	30 s	Latrunculin A	127	2343 h
3_blebb_30s	30 s	Blebbistatin	65	1165 h
4_ctrl_10min	10 min	control	9497	96577 h
5_lat_10min	10 min	Latrunculin A	3368	54809 h
6_blebb_10min	10 min	Blebbistatin	3728	47638 h
7_untreated_10min	10 min	untreated	6261	65378 h
stepped lanes	10 min	untreated	6158	76759 h

TABLE 4.1: List of experimental data sets.

lanes are determined via fluorescence intensity as in chapter 3. Time-lapse imaging is also performed as in the previous chapter. We took the phase contrast images of cells as well as the epi-fluorescence images of cell nuclei. Time-lapse imaging of cell and nuclei are performed at 10 min or 30 s intervals for low temporal resolution and high temporal resolution analyses. Images are analyzed using a combination of MATLAB R2020a (MathWorks) scripts and FIJI23 (ImageJ) macros. We obtain the trajectory of the position of nuclei from the low temporal resolution data with time intervals of 10 min. For the high temporal resolution data with time intervals of 30 s, we find the data of the front and back edges of the cell and front and back edges of the nuclei through manual segmentation of cell and nuclei kymographs. With that, we can study the dynamics of the cell edges. Due to time-consuming procedure of manual segmentation, the number of cell tracks with the high temporal resolution is limited. Our high temporal resolution data set includes about 400 single-cell tracks (about 6400 h imaging of single-cells) on homogeneous Fibronectin microlanes with densities ranging from 0 to 40 ngcm^{-2}.

The automatic procedure of cell nuclei tracking in low temporal resolution data allows analysis of much more cell tracks. We can study the characteristics like adhesion-velocity relation and persistence-velocity relation with these large data sets. Our low temporal resolution data sets (including control and drug-treated conditions) contain about 22900 single-cell tracks in total. Cells are seeded on homogeneous Fibronectin lanes with densities ranging from 0 to 120 ng cm^{-2}. In addition, we also have one data set of untreated cells and one data set on stepped Fibronectin lanes (from chapter 3). Table 4.1 lists all experimental data sets used in this chapter.

We simulate the cells on 1-dimensional Fibronectin lanes using the dynamical system

described in section 4.2. We performed groups of simulations with a single set of parameters (Table 4.2) for each experimental data set (Table 4.1). The parameters of each simulation group were obtained from fitting to the experimental results. We have two experimental control data sets, "1_ctrl_30s" and "stepped lanes". Thus, we also have 2 control simulation groups, one on the homogeneous lanes (set 1) and one on the stepped lanes (set 4). The parameters in these two simulation groups vary slightly. That could be the result of the seasonal variability of cell behavior, since the experiments were carried out with a time difference of several months (Table 4.2). Each simulation group includes a few thousand simulated single cell tracks, each on a Fibronectin lane chosen according to the Fibronectin densities in the corresponding experimental data set. We simulated each cell for 15 h, starting from a random initial state (moving up, down, or spread). In addition to the control data sets, we also have Latrunculin-treated cells and Blebbistatin-treated data sets. The fitting of simulation results to the experimental results allows finding the parameter sets related to these conditions (sets 2 and 3 in Table 4.2). We find that fitting the application of Latrunculin requires only to reduce the force-free actin polymerization rate V_e^0. This agrees with the known biochemical action of Latrunculin [276]. Blebbistatin treatment inhibits myosin, which in turn affects integrin signaling pathways. That varies the parameters κ and ζ in the model (see chapter 3). We find that a change of the parameters κ^{max} and ζ^{max} is sufficient to observe similar results in simulations and experiments (set 3 in Table 4.2). Thus, our results in this chapter confirm the results in chapter 3 about the action of Blebbistatin on integrin signaling pathways.

Cells in a single experiment do not behave all the same. To include the cell-to-cell variability in our simulations, we imposed random parameter value fluctuations of $\pm 5\%$ from the reference parameter values listed in Table 4.2.

4.3.2 Identifying cell states

We start our analysis of the dynamic states of cells by introducing a method to identify different states of cells from their kymographs. We first need an algorithm to find the time points at which the cell state changes significantly. We employ an iterative change point analysis like in [277] based on the cumulative sum. We can find the transition points between two states of a cell. An episode with a single state is then defined as

Parameter	**Set 1: control**	**Set 2: Latrunculin**	**Set 3: Blebbistatin**	**Set 4: stepped lanes**	**Units**
Figures	Figs. 4.4 4.6 4.7, 4.8, 4.9, 4.10, 4.11, 4.12, 4.14, 4.15, 4.16, 4.17, 4.19, 4.20, 4.21, 4.25	Figs. 4.13, 4.17, 4.21	Figs. 4.13, 4.18	Figs. 4.23, 4.24	
E	3e−3	3e−3	3e−3	3e−3	$\mathrm{nN\mu m^{-1}}$
L_0	10	10	10	10	µm
V_e^0	3e−2	2.2e−2	3e−2	3e−2	$\mathrm{\mu ms^{-1}}$
k^-	5e−3	5e−3	5e−3	3e−3	$\mathrm{\mu ms^{-1}}$
c_1	1.5e−4	1.5e−4	1.5e−4	2e−4	$\mathrm{s^{-1}}$
c_2	7.5e−5	7.5e−5	7.5e−5	1e−4	$\mathrm{s^{-1}}$
c_3	7.8e−3	7.8e−3	7.8e−3	8e−3	$\mathrm{\mu ms^{-1}}$
κ^{max}	35	35	20	30	$\mathrm{nNs\mu m^{-2}}$
K_κ	35	35	35	20	$\mathrm{ngcm^{-2}}$
n_κ	3	3	3	3	
κ_0	1e−2	1e−2	1e−2	1e−1	$\mathrm{nNs\mu m^{-2}}$
ζ^{max}	1.4	1.4	1.2	2.4	$\mathrm{nNs\mu m^{-2}}$
K_ζ	50	50	50	50	$\mathrm{ngcm^{-2}}$
n_ζ	4	4	4	4	
b	3	3	3	2	
ζ_0	1e−1	1e−1	1e−1	2e−1	$\mathrm{nNs\mu m^{-2}}$
α	2e−1	2e−1	2e−1	2e−1	

TABLE 4.2: Parameters used for simulations. Simulations with parameter sets 1, 2, and 3 are related to the experimental data on homogeneous Fibronectin lanes. Parameter set 1 is the control condition, set 2 is the Latrunculin-treated condition, and set 3 is the Blebbistatin-treated condition. Parameter set 4 is used for the simulations on stepped Fibronectin lanes in section 4.6.4.

the time between two consecutive change points. Since the time scale of oscillations in cells is shorter than 1 h, we require a cell to be in a given state in order to appoint that state to the cell. Thus, we exclude very short periods and append them to the preceding episodes. Fig. 4.5B shows the detected change points for a cell kymograph.

The next step is to identify the state in each episode. In order to do that, we defined two criteria to distinguish oscillatory/steady and spread/moving states. We calculate the average velocity of cells during an episode. If the average velocity is smaller than a critical speed of $0.002\mathrm{\mu ms^{-1}}$, we consider the episode a spread state. Otherwise, the cell is considered to be moving.

Investigation of the kymographs of the cells reveals that cells exhibit different modes of oscillation. In-phase oscillations of the cell edges lead to a stationary cell body and oscillatory cell length. On the other hand, anti-phase oscillations of the cell edges make the cell body move in an oscillatory trajectory while having a fixed cell length. Thus, to capture all the oscillation modes, an oscillation index is defined based on the dynamics of cell length and the trajectory of the cell body. The kymographs of cells contain small

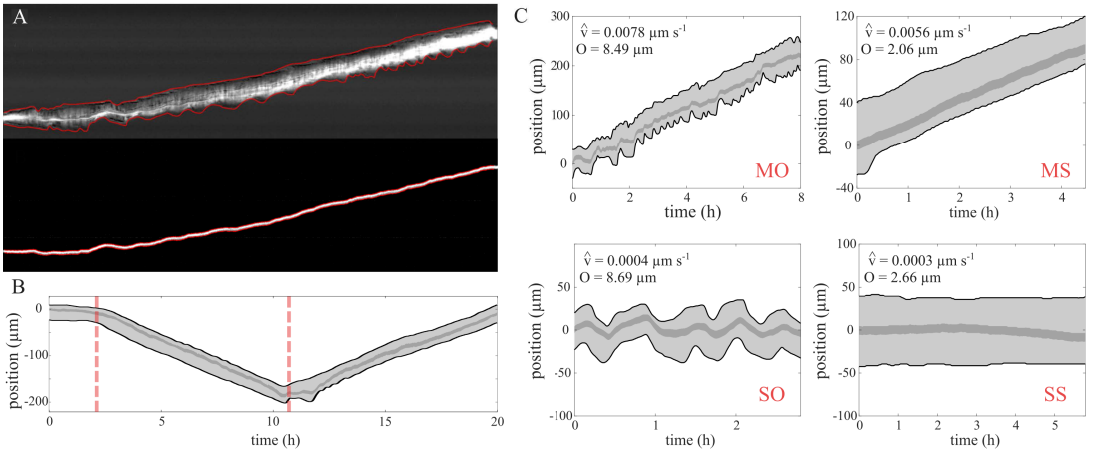

FIGURE 4.5: Steps of identifying cell states. A) Manual segmentation (red lines) of the cell (upper panel) and nucleus kymographs (lower panel). B) State change points with significant dynamic behavior change in a single-cell track. C) 4 examples of identified states with respective values of the average velocity and oscillation metric.

fluctuations, which are not related to the mechanisms we are discussing here. Therefore, we filter the data to remove tiny fluctuations in the length and nuclear position before calculating the oscillation index. Furthermore, the very slow variations of length can not be considered as oscillation. They might be caused by slow mechanisms that change membrane tension and cell elasticity. Long-term variations of nuclear position are also related to the general movement of the cell, not oscillations. Thus, we apply a band-pass filter with cutoff frequencies of 1 and 6 h^{-1} (the equivalent of 10 min and 1 h.) to the nuclear position and length data to exclude the very fast and very slow trends in the data. The level of oscillations can now be found from the filtered data. The length and nuclear position vary more from their mean values in oscillatory cells. Thus, we can define the oscillation index as the summation of the average absolute deviation of data from the mean.

$$O = \frac{1}{n}\sum_{i=1}^{n}\left(|L_{f,i}| + |X_{f,i}|\right)] \tag{4.28}$$

O is the oscillation index, $X_{f,i}$ and $L_{f,i}$ are the filtered nuclear position and length of the cell at time frame i, respectively, and n is the number of time frames of the episode. This oscillation index is then compared with the critical value of (5 μm) to assess whether the cell is oscillatory or steady in the episode. The critical values of velocity and oscillation index are obtained by manual inspection of cell kymographs for the best classification of states. The calculated oscillation index and average velocity are shown for four different cell episodes in Fig. 4.5C.

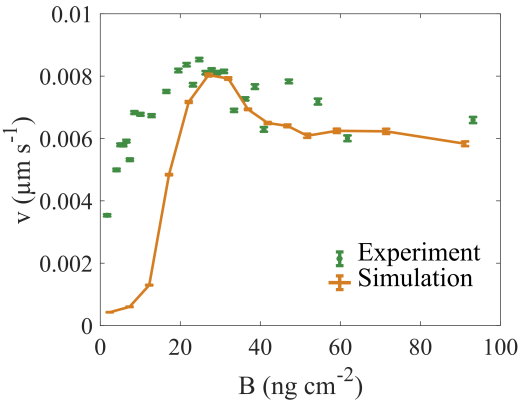

FIGURE 4.6: The biphasic adhesion-velocity relation in the experiments (green) on untreated MDA-MB-231 cells (Table 4.1), and simulations (orange) with parameters of set 1 (Table 4.2).

4.4 Adhesion-velocity relation

The first biophysical relationship we investigated is the relation between Fibronectin density and cell velocity in our untreated data set (data set 7_untreated_10min). The model extensions compared to chapter 3 require to redo this analysis. At any given Fibronectin density, we averaged the velocity over all of the cell tracks on the lanes with that Fibronectin density. We find the biphasic adhesion-velocity relation in our experimental data as in chapter 3. At low Fibronectin densities, the cell velocity increases with increasing Fibronectin density. After the maximum velocity at $B \approx 25$ ng cm^{-2}, the velocity decreases with increasing Fibronectin density. We also find the saturation of velocity at large Fibronectin densities (Fig. 4.6). We calculated the adhesion-velocity relation from our simulation group 1 (Table 4.2). We find the same biphasic relation, including the saturation of velocity at large Fibronectin densities (Fig. 4.6). Thus, the extended model with 2 protrusions is also able to show the biphasic adhesion-velocity relation. This shows that the Fibronectin signaling on drag and friction, which we included in the extended model similar to the model in chapter 3, is a key element of the model for the biphasic adhesion-velocity relation.

Fig. 4.6 illustrates a choice we have made for our study. Rather than fitting each experimental observation perfectly, we decided to fit all experimental observations from a single data set also with a single parameter set as good as possible.

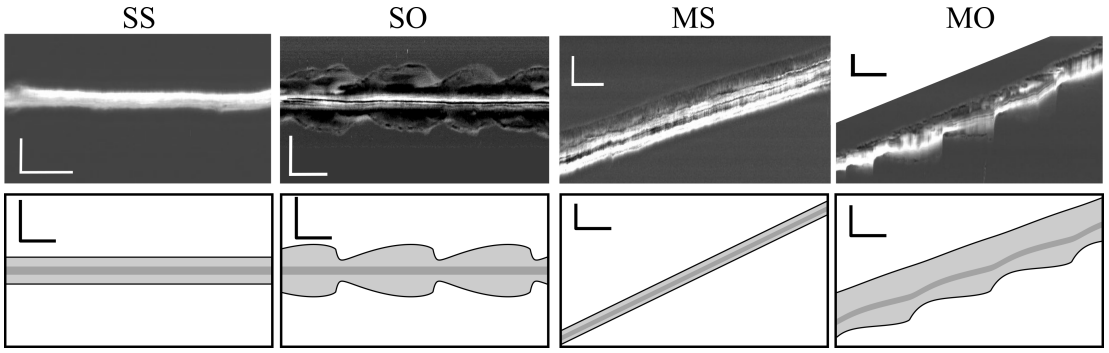

FIGURE 4.7: Dynamic cell states in experiments (upper sub-panels) and model (lower sub-panels).

4.5 Dynamic cell states

4.5.1 Cell states

Firstly, we investigated whether the model is able to reproduce all the dynamic states that we observed in the experimental data sets. For that reason, we simulated cells without noise in the model. We found all 4 states of MDA-MB-231 cells in the simulations (Fig. 4.7). The simulation results agree with experimental results regarding characteristics like oscillation amplitude, frequency, and velocity. We also find that only the back protrusion exhibits oscillations in the moving state, not the front protrusion. That also agrees with the experimental kymographs (Fig. 4.7). We find that in the steady and oscillatory moving states (MS and MO), the front protrusion dominates the back protrusion. They work in an asymmetric manner while having symmetric parameters. This 'mechanical polarization' does not need any signaling. The front and back protrusions work in different regimes. The front protrusion has retrograde flow slower than the critical retrograde flow $v_{r,cr}$ with strong friction between the actin flow and stationary structures in the cell. The front protrusion can generate a strong force in this working regime. On the other side, the back protrusion works in a completely different regime. The retrograde flow is faster than $v_{r,cr}$, since the actin network extension rate is added to the cell velocity. The actin flow friction coefficient κ_b is small, and therefore the force that the back protrusion can produce is also small (Fig. 4.8A). The cell is symmetric in spread states (SS and SO), and both protrusions work in the same regime.

4.5.2 Oscillation mechanism

We describe an oscillation cycle in the state MO to understand the mechanism that causes oscillations (Fig. 4.8A, B). We start from the moment that the friction coefficient κ_b starts to decrease. The force pulling the edge $F_b = E(L - L_0) + \zeta_b v_b$ drives the retrograde flow. With decreasing friction coefficient the retrograde flow $v_{r,b}$ speeds up. The faster retrograde flow leads to further decrease of the friction coefficient κ, because of the exponential dissociation rate (Eqs. 4.17, 4.18). With the accelerated retrograde flow, the back edge velocity increases, since the polymerized actin network mainly flows inward rather than pushing the membrane outward. The decrease of edge velocity decreases the drag force $\zeta_b v_b$. The length of the back protrusion starts to decrease gradually, which in turn decreases the elastic force. This process continues until κ_b is too small to to balance F_b by friction forces. At that moment, the actin network slips with a large peak of $v_{r,b}$. At the same time, κ_b decreases further to its minimum value. The leading edge membrane also retracts. The length and force of the back protrusion collapse, and the protrusion can not transmit any force to the substrate. With the drop in force, the retrograde flow also decreases. At this time, the bonds between the actin network and stationary structures in the cell start to form again, which increases κ_b. The increase of friction slows down the retrograde flow further. With the slower retrograde flow, the polymerized actin network drive edge progression more effectively. Thus, v_b increases, which in turn increases the length and elastic force. This growing phase continues until the time that the stretched protrusion collapses again. The front does not exhibit active oscillations in the state MO. However, the oscillations at the back protrusion cause some low amplitude passive oscillations at the front.

4.5.3 Excitation

Small perturbations can lead to large responses in an excitable system. We find that the spread states SS and MS are excitable. The membrane velocities $v_{f,b}$ are zero in the SS state, and the retrograde flow velocity v_r equals the network extension rate. The cell is in a tense state with two opposing forces from the two protrusions. Supercritical perturbations of κ can disrupt this tense stats and trigger a cycle of protrusion-retraction (Fig. 4.8C). This perturbation of κ may arise from the concurrent binding of some bonds between the actin network and stationary structures in the cell. Random attachment

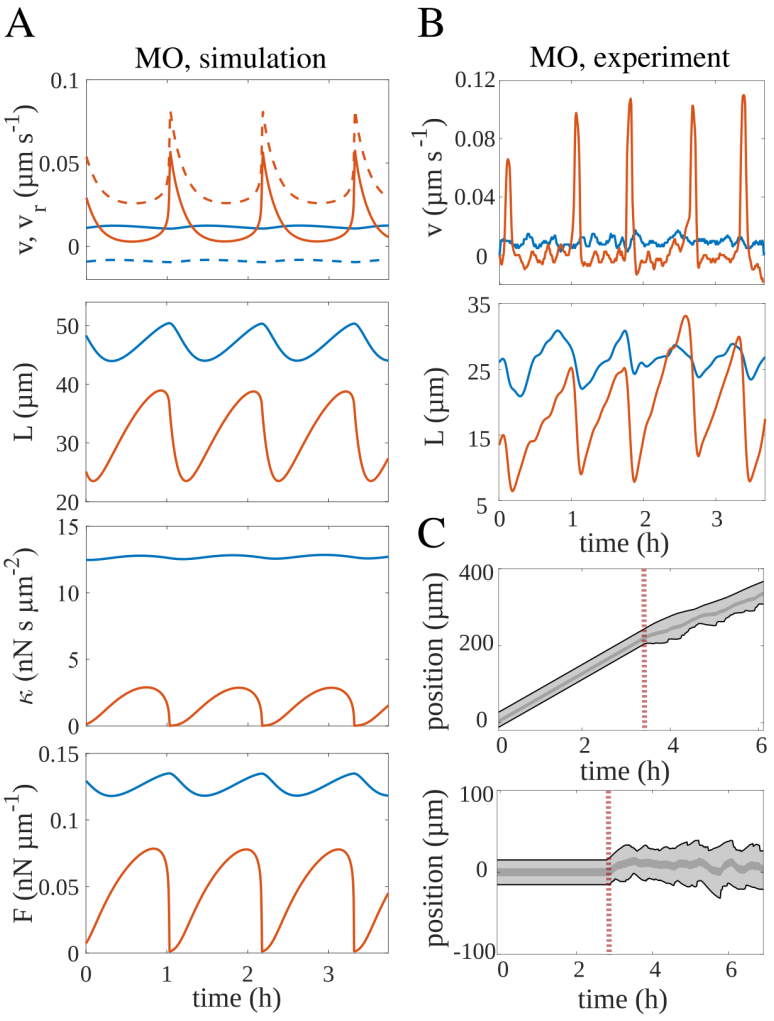

FIGURE 4.8: Oscillatory and excitable states. A) Simulated time course of the edge velocity v, retrograde flow v_r, cell length L, friction coefficient κ and force F in simulated state MO shown in Fig. 4.7 (blue front, red back). B) Measured time course of edge velocity and cell length in the experimental state MO shown in Fig. 4.7 (blue front, red back). C) Transition of the steady states MS (upper panel) and SS (lower panel) to excitable with noise. Noise is switched on at the time marked by the red line.

and detachment of bonds create the chemical noise in the dynamics of κ, which is taken into account in the model by the Gaussian white noise in Eqs. 4.17 and 4.18.

The protrusion-retraction cycle in the excitable states is very similar to the dynamics of an oscillation cycle described in the previous section. Thus, the noisy dynamics of attachment and detachment of bonds between actin network and stationary structures causes oscillation-like behavior. The amplitude of the noise, as well as all other cell parameters, determine whether the noise is supercritical - i.e. causing a large response - or not. Thus, steady states with a low amplitude of noise exhibiting deterministic behavior coexist with the oscillatory-like states with a high amplitude of noise. Fig. 4.7

shows examples of experimental observations close to deterministic behavior, Fig. 4.2 shows also the noisy states, which are observed more frequently than the deterministic ones.

4.5.4 Multistability

The bifurcation diagram in Fig. 4.9 shows that different cell states can coexist for a range of Fibronectin densities. That illustrates the multistability in the system. At very low values of Fibronectin density B, the system can only exist in the SS state. Beyond the Fibronectin density, which is shown as the branch point, a protrusion can work in 3 regimes, high κ (front), intermediate κ, and low κ (back). If a protrusion is in the high κ regime, the opposing protrusion works in the low κ regime and vice versa. The working regime of protrusions determines the dominating protrusion and the front and back of the cell in the moving state. The cell velocities are shown for the three branches in Fig. 4.9B. The other possibility is that both protrusions work in the intermediate κ regime, which implicates the spread state. The green diamond markers show the Hopf bifurcation points on the three branches. At the Fibronectin densities larger than the Hopf bifurcation points, the state of the cells changes to oscillatory. The Hopf bifurcation of the middle branch (the spread state) occurs at lower Fibronectin densities than the other two branches. In this case, we observe the coexistence of SO and MS states in a range of Fibronectin densities.

We find that the relative position of Hopf bifurcation points on the three branches of the system can change at other parameter values. Three other possibilities for the relative position of the Hopf bifurcation points on the system branches are shown in Fig. 4.10. Those different situations are generated by only a slight change in parameter values. Possible transitions between cell states corresponding to each case are shown in the lower panels of Fig. 4.10. Thus, considering the cell-to-cell variability within cells both in experiments and simulations, the states SS and MO can also coexist. In summary, both moving states can coexist with both spread states.

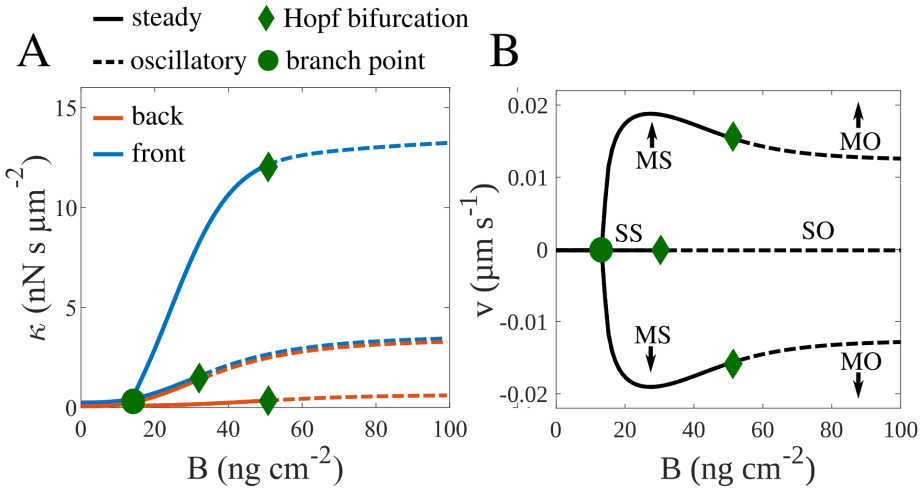

FIGURE 4.9: Bifurcation diagrams showing multistability in cells. Cell states (noise-free model) presented by their value of the friction coefficient κ for a range of B (A) and the cell velocity (B). At low B, only the state SS exists. At concentrations larger than the branch point, moving states (top and bottom branches) and a spread state (middle branch) coexist. At concentrations larger than the Hopf bifurcations points, the steady states become oscillatory.

4.5.5 Probability of dynamic cell states and transitions between them

We analyzed the kymographs created from our high temporal resolution experimental data sets to determine the states of cells. The kymographs of simulated cells are also analyzed with a same method. Then the fractions of time that cells spend in each dynamic state are calculated for the whole experimental and simulation data sets (Fig. 4.11). We find a very good agreement between simulations and experiments in the control sets.

All observed transitions are depicted in Fig. 4.12A. Fig. 4.12B shows the fraction of transitions from a given state in the experimental data. The agreement between the experimental and simulation results shown in Fig. 4.12C is very good. The dark blue lines in Fig. 4.12A are the transitions that can be explained with the multistability arising from our model. Both spread states can coexist with both moving states. Also, a moving state in the downward direction can coexist with its upward moving analog. The noise terms in the variable κ of the model can drive the transitions between coexisting states. We assume that the state transitions in the real cells are also caused by the noise in adhesion dynamics. Thermal noise affects cells as a microscopic system in many aspects [278–281]. The effect of thermal noise on the adhesion sites is even more significant because the length scale of an adhesion site is at least two orders of magnitude smaller than the cell size. Furthermore, we observed that cells change their state spontaneously

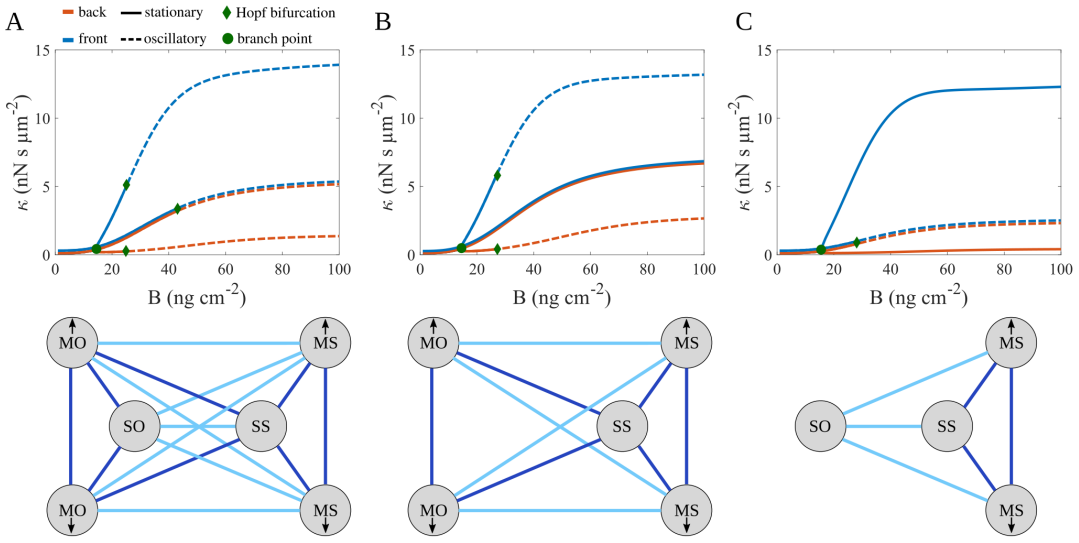

FIGURE 4.10: Multistability in cells with 3 different parameter values. The upper row shows the cell states presented by their value of the friction coefficient κ for a range of B. Dashed lines show the oscillatory regime. The lower row shows the possible transitions between cell states related to the bifurcation diagrams in the upper row. Transitions between states coexisting in the model are shown by the dark blue lines. The parameter values of set 1 are used (Table 4.2), with (A) $c_3 = 0.009$ µms^{-1} , (B) $c_3 = 0.01$ µms^{-1} , and (C) $c_3 = 0.007$ µms^{-1} .

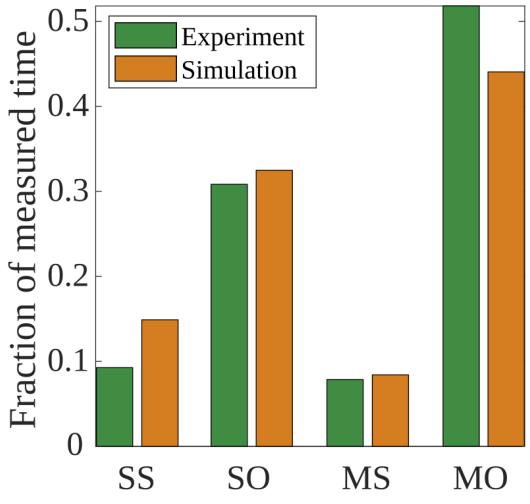

FIGURE 4.11: Probability of occurrence of the 4 cell states. The probabilities obtained for experiments and simulations on the same range of Fibronectin concentrations (see 4.3.1).

without any apparent external stimulation. That is also in line with the noise-induced transition hypothesis. Another important experimental observation that supports the noise in the κ dynamics is the transitions caused by tiny bumps of Fibronectin density (Fig. 4.24). This shows that even a tiny change in the value of κ, caused by noise instead of bumps in Fibronectin density, can trigger a transition to a different state. We

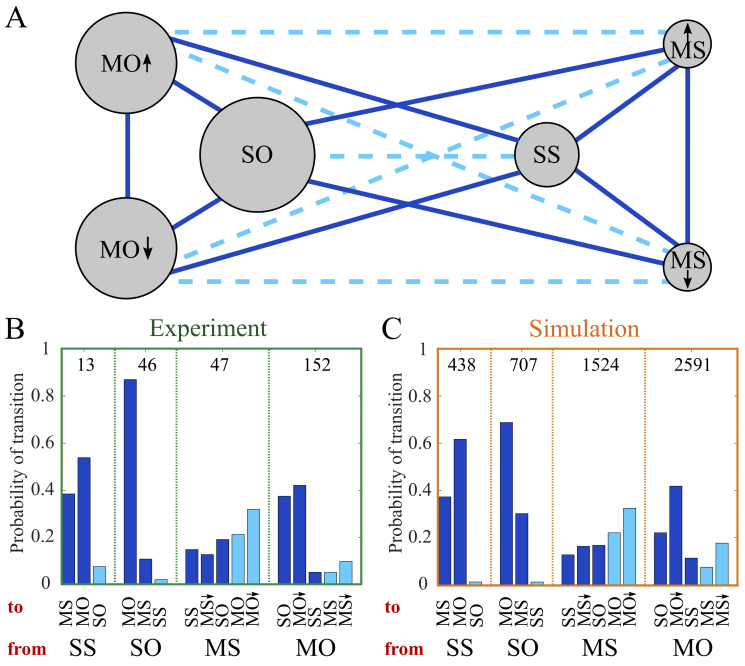

FIGURE 4.12: The transitions between the cell states in control conditions. A) All the 6 dynamic states, including upward and downward motion in moving states (shown with arrows). Transitions between coexisting states in the model are illustrated with dark blue lines. B, C) Probability of transitions between different states in experiments (B) and simulations (C). The bars are color-coded as in panel A.

discuss the effect of tiny bumps of Fibronectin density in section 4.6.4. In summary, the mentioned arguments and the good agreement between the simulations and experiments results make us conclude that the noise in adhesion dynamics is the cause of transitions between cell states.

We also observed some transitions that can not be explained with the multistability of the system. That includes the transitions between SO and SS and between MO and MS. These transitions are shown with light blue color in Fig. 4.12. We believe that these transitions might arise from the state classification algorithm we used. Our state classification method can not distinguish an oscillatory state from a noisy excitable state. The shortest dwell time of a cell in a state is 1 h in our state classification method. Having such a minimum duration criterion is necessary for state classification. It is possible that noisy excitable cells both in experiments and simulations do not show significant oscillation-like dynamics in a period of time longer than 1 h and then start to show such behavior. Our state classification algorithm detects two different states in this situation, and thus a transition from steady to oscillatory. The transitions from oscillatory to steady states can be detected similarly. We applied the same state classification method to the experiments and simulations and obtained similar statistics

for transitions. Since the parameters are kept constant in time for a simulated cell, we can attribute the transitions oscillatory$\longleftrightarrow$steady to the occurrence of steady periods during a noisy excitable state. Interestingly, while this statistics might report in part duration statistics of silence (activity) in the excitable state, experiments and simulations do pretty well agree with regard to it.

4.5.6 States and transitions in drug-treated cells

In addition to the control cells, we also analyzed Latrunculin- and Blebbistatin-treated cells to find the fraction of states and transitions. Fig. 4.13A shows a lower fraction of moving states upon application of Latrunculin. The probability of oscillatory states is also decreased in Latrunculin-treated cells. We find a good agreement between the fraction of states in simulations and experiments. The probabilities of transitions resulting from the simulations also agree very well with the experimental results. It is important to note that we only reduced the value of network extension rate V_e^0 in Latrunculin simulations compared to the control simulations. We have changed this parameter directly according to the biological role of Latrunculin as an inhibitor of actin polymerization. That is also in line with our results in chapter 3. Surprisingly, only this change in the parameters can reproduce the results of the Latrunculin-treated cells. Thus, we can conclude that a lower extension rate is directly associated with reducing the probability of oscillatory and moving states.

Analyzing Blebbistatin-treated cells reveals that the probabilities of states are almost similar to the control condition (Fig. 4.13B). We again find a very good agreement between simulations and experiments both for states and transition probabilities. For simulating the effect of Blebbistatin, we only changed two parameters κ^{max} and ζ^{max} such that the ratio κ/ζ decreases. That is according to our results on the effect of Blebbistatin application in chapter 3.

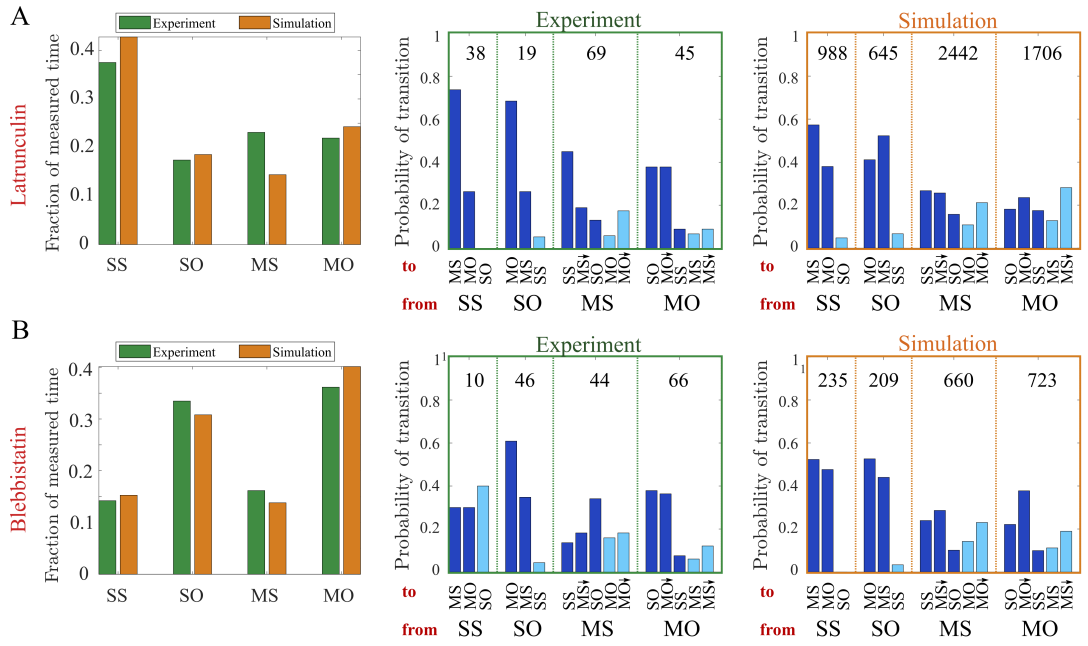

FIGURE 4.13: Dynamic cell states and transitions in Latrunculin (A) and Blebbistatin (B) treated cells. Left column: Fraction of cells in the dynamic cell states in experiments and simulations in a (same) range of B. Middle column: Probabilities of state transitions in the experiments. Right column: Probabilities of state transitions in the simulations. Latrunculin A and Blebbistatin simulations are conducted with the parameter values listed in Table 4.2.

4.6 Cell persistence and UCSP

4.6.1 Reversal of direction

In principle, we can imagine a reversal of direction to occur by the disappearance of the front protrusion, termination of cell motion, subsequent formation of a new protrusion at the other side of the cell, and motion in the new direction. However, that is not what we observed. We observed that reversal only occurs when a back protrusion exists and competes with the front protrusion before the reversal. Front and back protrusion swap roles during the transition.

We need to have a closer look at the front and back edge velocities during the reversal of direction (in both MS and MO states) to study the reversal mechanism. Edge velocities are shown in Fig. 4.14A, B. Thin lines are velocities of single cells, and the thick lines show the average of all cells. t_{rev} is the moment that the cell nucleus changes direction of motion. We find that about 10 min before t_{rev}, the back edge velocity starts to slow down. A few minutes before t_{rev}, the back edge velocity gets negative, i.e., starts to

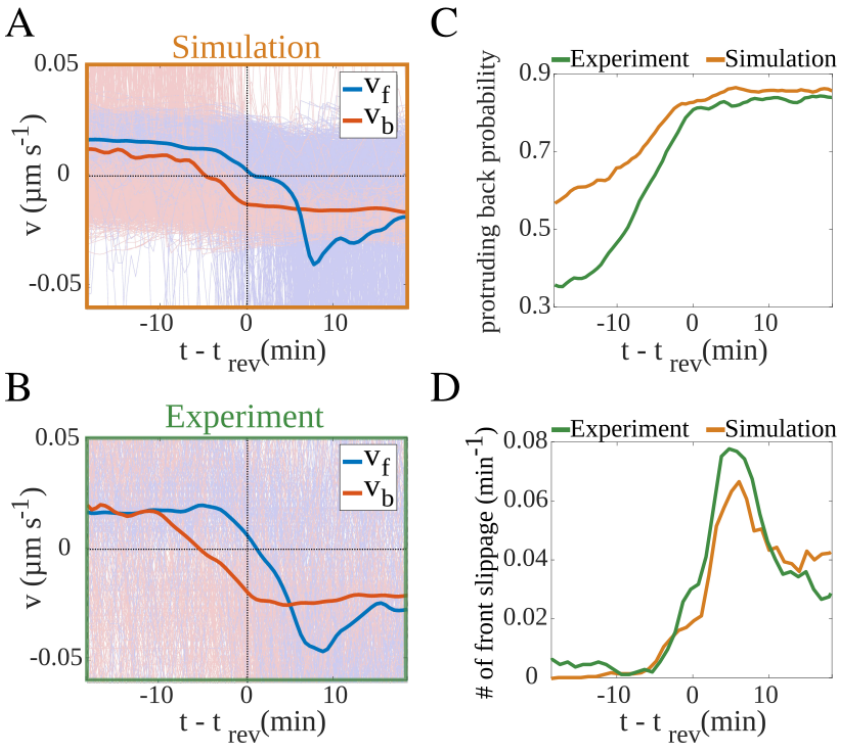

FIGURE 4.14: Edge dynamics during the reversal of direction. A, B) Front (v_f) and back (v_b) velocities during a reversal in experiments (A) and simulations (B). Thin lines show individual cells and thick lines are average over all cell tracks. t_{rev} is the time when the cell nucleus changes direction. C) The probability of back protruding (negative velocity) around the reversal time t_{rev}. D) The probability of front slippage (negative peak of front velocity larger than 0.1 μms^{-1}) around the reversal time t_{rev}.

protrude in the opposite direction. The front velocity slows down with some delay after the back. The front edge keeps moving in the same direction a few minutes longer than the back edge. A few minutes later, the front can not resist the pulling of the back anymore and retracts fast. That is a slippage event that shows up as a negative peak in Fig. 4.14A, B. The probability of back protruding (negative velocity) around the reversal time is shown in Fig. 4.14C. This probability starts to increase from its background level (related to the back oscillations) a few minutes before the reversal time t_{rev}. It is close to the new background value of 0.8 at the reversal time. Fig. 4.14D shows the probability of front slippage, which is defined as the peak of front velocity larger than 0.1 μms^{-1} toward the cell body. Front slippage probability increases after the reversal time. These results strongly support a mechanism in which active protrusion of the rear stops front motion, reverses the direction of cell motion, and entails the collapse of the former front protrusion in a slippage event. We find that the simulation results agree very well with the experiments.

4.6.2 Force-retrograde flow regimes of back and front protrusions

The force-retrograde flow relation is biphasic (see Eq. 4.21) in the stationary state. This creates two different regimes a protrusion can work in. The first regime is the rising branch of the biphasic relation, i.e., $v_r < v_{r,cr}$ in which the force increases with the increasing retrograde flow velocity. The second regime is the falling branch, $v_r > v_{r,cr}$ in which the force decreases with the increasing retrograde flow velocity. Since the retrograde flow equals the vectorial sum of edge velocity and network extension rate, it is not symmetric for front and back protrusions. At the front, extension rate and edge velocity are in the opposite directions, while at the back protrusion, the extension rate and edge velocity are in the same direction. That entails lower retrograde flow velocity v_r at the front protrusion (see Fig. 4.22). We find that the front protrusion in a moving cell always works on the rising branch, while the back works on the falling branch of the force-retrograde flow velocity relation. The separation of back and front retrograde flow velocities depends on the cell velocity. In fast cells, the asymmetry in the values of retrograde flow velocities of back and front is larger than in slow cells (Fig. 4.15). The roles of front and back swap in a reversal of direction. Thus, the reversal should be harder in faster cells whose protrusions have very asymmetric retrograde flow velocities. In other words, there must be a relation between cell velocity and reversal probability. We looked at the front and back retrograde flow velocities in the simulations during the reversal of motion direction. The right panel in Fig. 4.15 shows that initially, the retrograde flow at the front is lower than at the back. After the reversal the retrograde flow velocity values also swap.

There is a characteristic difference between the two regimes of force-retrograde flow velocity. If the back pulls and slows down the front edge motion, retrograde flow increases. This increase of retrograde flow entails higher force generation, which opposes the pulling of the back and tends to weaken the decrease of front edge velocity due to pulling. If the front pulls stronger and speeds up the back edge motion, the retrograde flow velocity also increases. However, in this case, the increase of retrograde flow velocity entails lower force resisting motion, since the back retrograde flow operates on the falling branch of the friction force - velocity relation.. Thus, the back protrusion even amplifies the effect of pulling from the front.

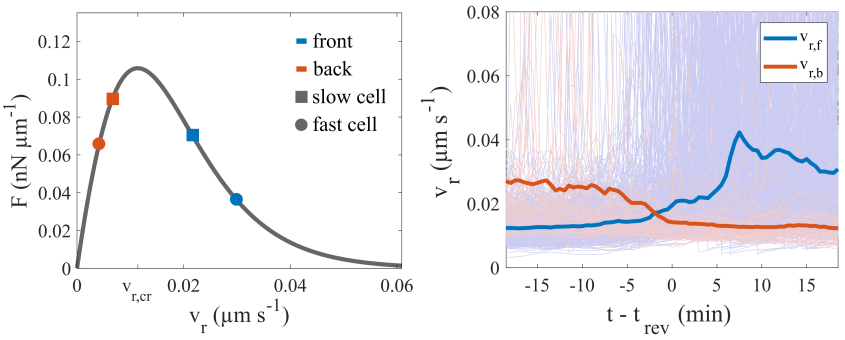

FIGURE 4.15: Left: The biphasic force-retrograde flow relation in the stationary state. $v_{r,cr}$ is the critical flow rate with maximal force. The stationary states of back and front protrusions in a fast and a slow cell are shown with symbols. Right: Retrograde flow in both protrusions of moving cells during a direction reversal. Thin lines show individual cells, and thick lines are average over all the cell tracks. t_{rev} is the time when the cell nucleus changes direction. The results are obtained from the simulations shown in 4.14B.

We investigated the change of force-retrograde flow regimes in front and back protrusions during a reversal of direction. Here, the noise is not present, and the reversal is triggered by instantaneous perturbation of κ at the back. If this perturbation is not strong enough, the reversal is not successful, and protrusions return to their initial working regime after a while (Fig. 4.16A). The trajectory of front and back protrusions in the force-retrograde flow plane is shown in the bottom panel. A sufficiently large perturbation can trigger a successful reversal (Fig. 4.16B). In this case, the front and back swap their steady states on the rising and falling phases of the force-retrograde flow velocity curve (Fig. 4.16B, bottom panels) . We used the single protrusion model to obtain the flux lines of the system in the force-retrograde flow velocity plane (instead of the κ-L plane). Fig. 4.16C shows these flux lines for a front protrusion with positive v_c (upper panel), a back protrusion with negative v_c (bottom panel), and a protrusion in the spread state with zero v_c (middle panel). It is important to note that these plots are obtained by assuming fixed cell body velocity. Nevertheless, they can still approximate the flux lines of the full model with coupled front and back and variable v_c. It can be seen that the flux lines converge to a steady state point which is located on the rising branch for the front protrusion, the falling branch for the back protrusion, and again the falling branch for the spread protrusion. Transition of the stationary state from the rising to the falling branch of the clutch upon $v_c \rightarrow -v_c$ is another illustration of the role swap of protrusions during direction reversal.

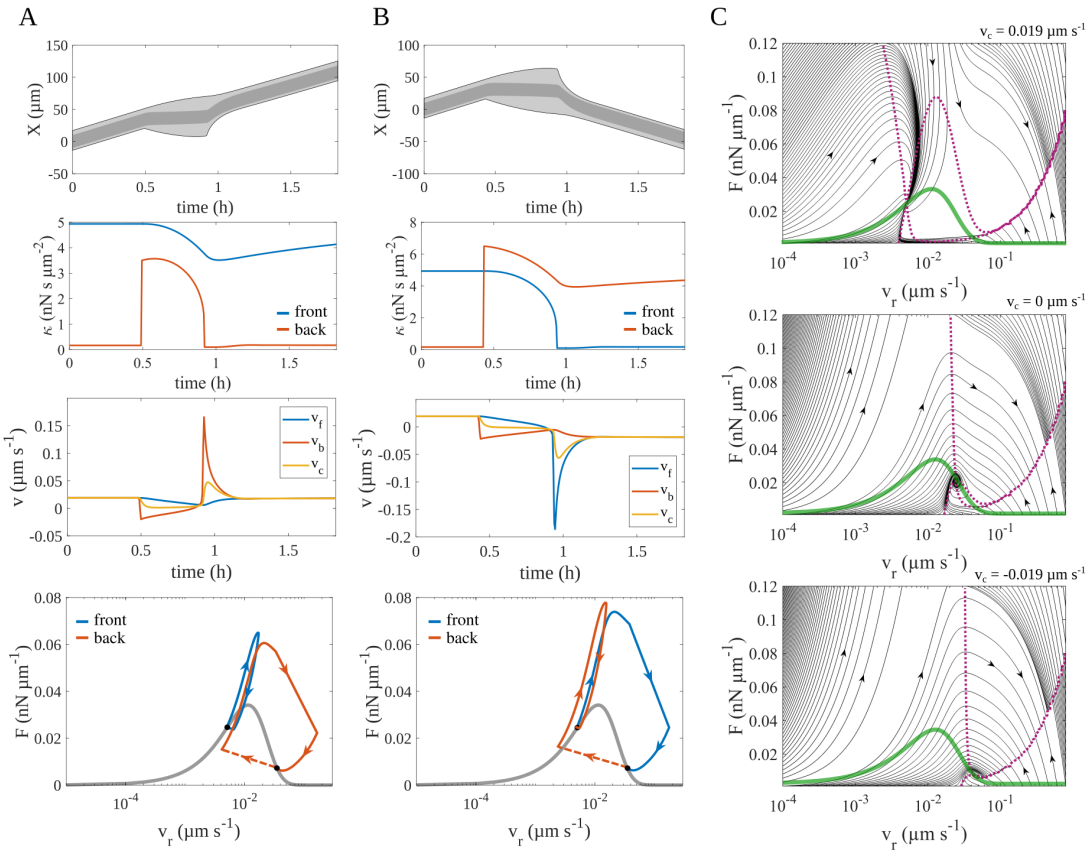

FIGURE 4.16: Force and retrograde flow at both protrusions of a moving cell during a direction reversal. A, B) An unsuccessful (A) and successful (B) back excitation. The successful back excitation leads to cell reversal. Kymograph, friction coefficient κ, and velocity are shown during a back excitation. Blue and red indicate the front and back protrusions. An instantaneous increase of κ triggers the back excitation. The trajectories of the state of back and front protrusions in the force-retrograde flow plane are shown in the lower panels. The initial perturbations of κ_b are indicated by the dashed part of the red line. The steady-state biphasic force-retrograde flow is illustrated with the gray line. (C) Flux lines in the force-retrograde flow plane obtained using the model for a single protrusion (4.2.1). The cell velocity is assumed to be positive (up), zero (middle), and negative (bottom). The green line shows the stationary biphasic force-retrograde flow relation. Nullclines of the system are shown with purple dotted lines. The simulations in this figure are performed using the parameter values of set 1 with $B = 20$ ng cm^{-2}.

4.6.3 The UCSP

In the previous sections, we investigated the mechanism of the reversal of direction. The probability and frequency of reversal events can be quantified with the persistence time. The persistence time is defined as the average period of time that cells keep their direction of motion (between two consecutive reversals). We determined the average velocity of cells during a unidirectional motion episode from the distance between

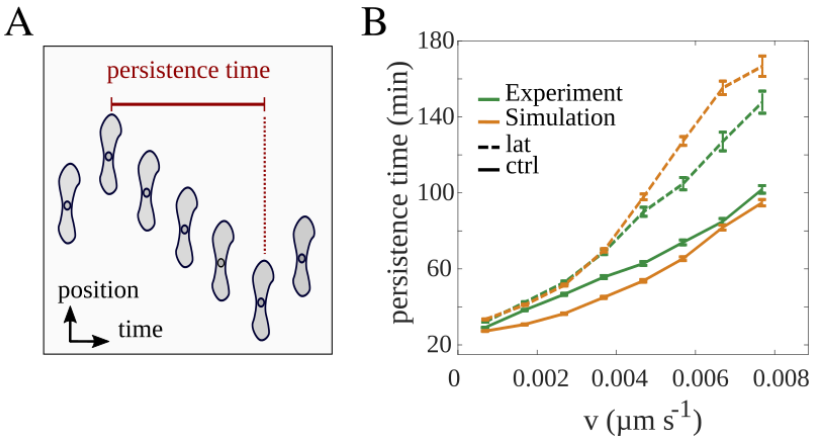

FIGURE 4.17: Persistence-velocity relation. A) Definition of the persistence time. B) The relation between persistence time and cell velocity in control and Latrunculin-treated cell populations.

nuclear positions in consecutive reversals divided by the time period between those reversals. Fig. 4.17 shows the relation between the cell velocity and cell persistence. We find an increasing relation between cell velocity and persistence, as reported in earlier studies [8]. This universal coupling between cell speed and persistence time (UCSP) is another general experimental observation reported for many cell types and in 1, 2, and 3-dimensional migration. Some theories have been proposed to explain this relation, including a mechanism based on the attachment of polarity factors to the actin network and a depletion zone at the leading edge that appeared as a result of the actin flow [8]. On the basis of this mechanism, Mauiri et al. predict that cell persistence depends exponentially on the network extension rate (and consequently, cell velocity).

We found also increasing persistence with increasing cell velocity in our experiments similar to Mauiri et al. (Fig. 4.17). The results of our simulations also match the experiments very well, not only in the control condition but also in Latrunculin A-treated cells (and Blebbistatin-treated cells in Fig. 4.18). We find that the application of Latrunculin A, which decreases the F-actin polymerization rate, increases the persistence time of the cell. We simulated the Latrunculin A effect by decreasing the parameter V_e^0 (Table 4.2). Interestingly, we find that our experimental results on the effect of Latrunculin A on cell persistence time are in contradiction to the prediction of [8]. With the mechanism of [8], Latrunculin A-treated cells with lower network extension rates should have lower persistence times.

We have taken the agreement between simulations and experiments as an encouragement

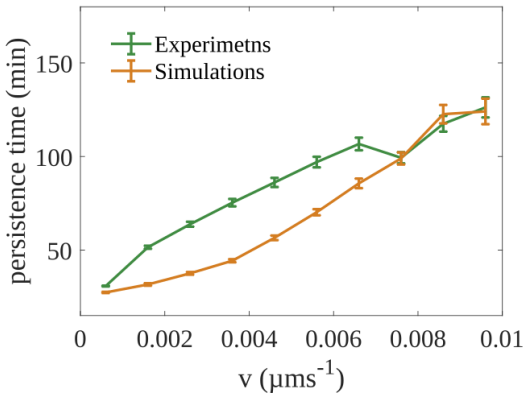

FIGURE 4.18: The relation between persistence time and cell velocity in Blebbistatin-treated cell population.

to investigate the reversal mechanism with the model in more detail. We conclude from the existence of front and back protrusions at the reversal time and the growth of back protrusion before the reversal time that the cell reversal occurs as a result of competition between the back and front protrusions. We investigate the stability of back and front protrusions to understand the competition mechanism and how it is affected by velocity. The single protrusion model (section 4.2.1) is used to obtain the phase planes of front and back protrusions in the MS state (Fig. 4.19). We defined a basin of attraction in the phase plane of each protrusion based on the characteristic difference between the trajectories (see section 4.2.1). When a protrusion is perturbed from the steady state, it can either go directly back to the steady state or experience a collapse. If the perturbation moves the state of the system to a point inside the basin of attraction (the gray area in Fig. 4.19), it returns to the steady state without collapsing. Comparing the basins of attraction in fast and slow cells reveals that the front protrusion of a fast cell has a larger basin of attraction than the front protrusion of a slow cell. This means that the front protrusion is more stable in fast cells. However, for the back protrusion, the situation is the other way around. The basin of attraction of fast cells is smaller than that of slow cells. Thus, the back protrusion in fast cells is less stable than the one of slow cells. In summary, increasing velocity makes the front protrusion more stable and the back protrusion less stable. We also find that a sufficiently large increase of length (moving from the equilibrium point to the right) is a perturbation that can draw the state of a front protrusion out of its basin of attraction and make it collapse (Fig. 4.19). Hence, an strong pulling of the back protrusion, which increases the length, can force the front protrusion to collapse.

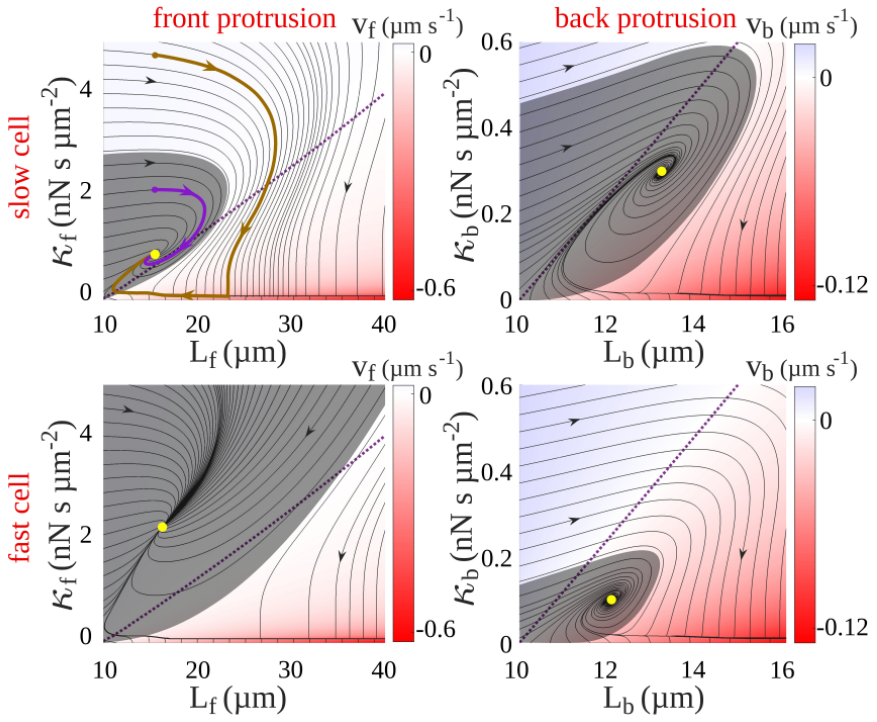

FIGURE 4.19: Basin of attraction in the phase plane of protrusions. The grey area illustrates the basin of attraction, and black lines show flux lines. Trajectories starting outside of the basin of attraction experience a collapse before reaching steady state (red dot). Trajectories starting within the basin of attraction lead to the steady state without collapse.

In the MS state, when the back protrusion goes through an excitation, it pulls the front via the cell body (Fig. 4.20). The stronger and longer the back pulls, the larger is the collapse probability. This probability also depends on the resistance of the front protrusion against the pulling from the back. To understand how back excitation duration depends on the cell parameters, we simulated hundreds of cells with parameters chosen randomly in a wide range (from 0.2 to 2 times the parameter values of the control condition in Table 4.2). In these simulations, we applied the noise only at the back of the cells to minimize the impact of the front protrusion on the back excitation. Interestingly, we find that the retrograde flow velocity at the back protrusion correlates very well with the duration of the back excitation, regardless of the cell parameters. We conclude that retrograde flow velocity is the main determinant of the back excitation duration. In other words, the variation of cell parameters can only affect the back excitation duration through variation of retrograde flow.

Similarly, we performed a set of simulations with cells of random parameters to investigate the front resistance. In those simulations, the motion of the nuclei of steadily

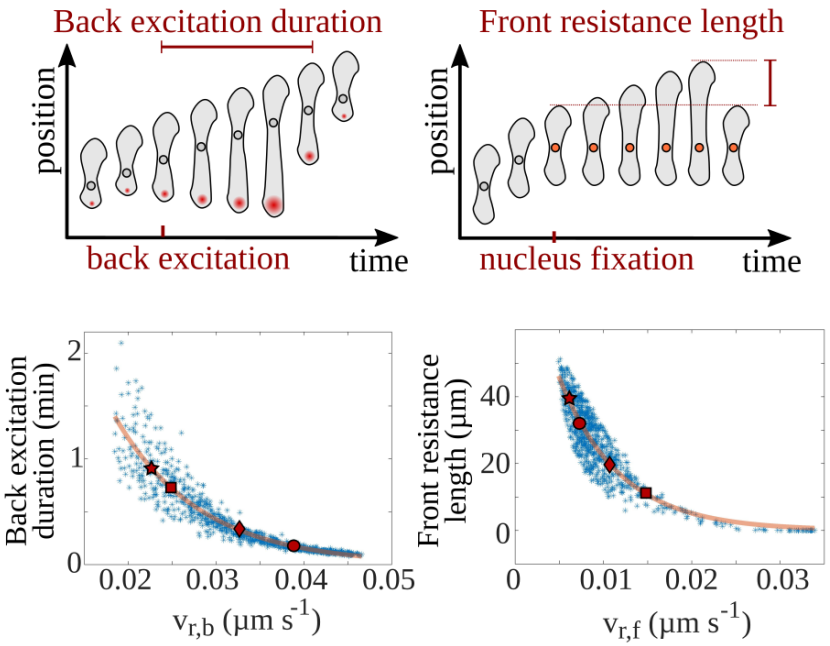

FIGURE 4.20: Duration of back excitation, front resistance time, and resistance length. The cartoon illustrations in the upper row define these characteristics. The lower panels show the duration of back excitation and resistance length in dependence on the retrograde flow rate at the back and front protrusions. Each dot is the result of a simulated cell with parameter values randomly chosen from large parameter ranges. The red markers indicate the cells in Fig. 4.22

moving cells has been stopped instantaneously. The front edge continues to protrude after the nucleus arrest until the length of the front protrusion becomes so long that it cannot resist the pulling by the elastic force anymore and collapses. We looked at the dependency of the front resistance length on cell parameters. Fig. 4.20 shows that higher retrograde flow decreases the stability of a protrusion. Again, we find that the retrograde flow velocity at the front protrusion can describe the front resistance length regardless of the cell parameters. Thus, the relations between stability characteristics of front and back protrusions and retrograde flow are fundamental and robust features.

A cell should have a stable front and an unstable back for persistent motion. Generally, higher cell velocity decreases the retrograde flow velocity at the front and increases that at the back. That is shown schematically in Fig. 4.22A. The network extension rate equals the vectorial difference of membrane velocity and retrograde flow velocity. Since the dependency of the extension rate on the force is not strong, for simplicity, we assume equal extension rates at front and back. Thus, the back retrograde flow speed equals the extension rate plus the cell velocity, and the front retrograde flow equals the extension rate minus the cell velocity (see Fig. 4.22A). Fast cells have slow retrograde flow at the

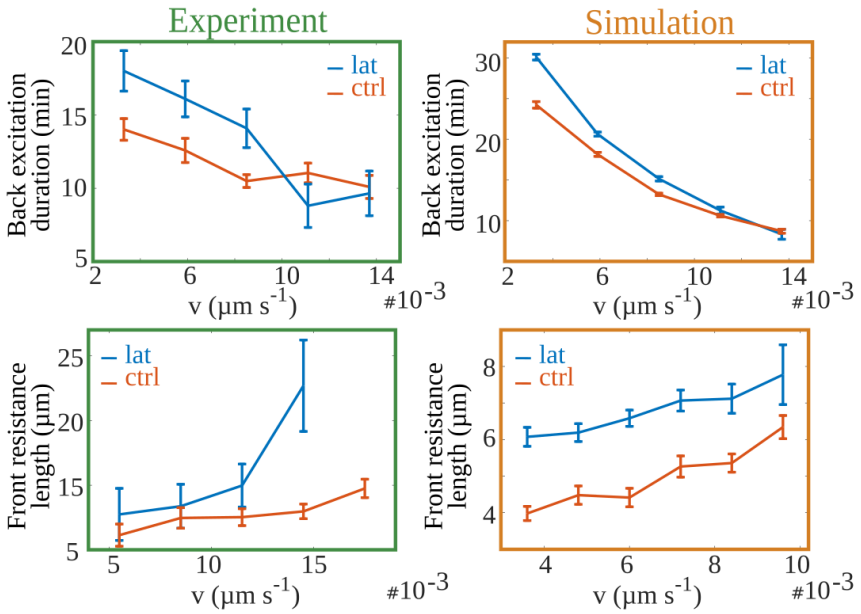

FIGURE 4.21: Duration of back excitation and front resistance length in dependence on the cell velocity in the MDA-MB-231 experimental data and simulations.

front and fast retrograde flow at the back, which results in a stable front, an unstable back, and thus a persistent motion.

We investigated the relationship between the duration of back excitation and front resistance length in dependence on the cell velocity also experimentally. We find the duration of back excitation episodes and their average over a moving state of a cell. We then determine the average velocity of the cell body over the same moving episode and relate it to the duration of back excitation in Fig. 4.21.

We calculate the resistance length of the front protrusion by finding the collapse events. A collapse is defined as a retraction (negative velocity) of the front with at least 2 μms^{-1} shrinkage. The resistance length of the front is defined as the shrinkage length in the collapse. We then relate the resistance length to the average velocity of the cell body during the protruding episode before the collapse in Fig. 4.21. We find a good agreement between the experiments and simulations on the relations of front resistance length and back excitation duration with the cell velocity. We find that increasing cell velocity increases front resistance length and decreases the duration of back excitation. These relations hold not only in the control condition but also in Latrunculin A-treated cells.

Application of Latrunculin A inhibits actin polymerization and thus decreases the extension rate. Therefore, the retrograde flow velocity decreases both at the front and the

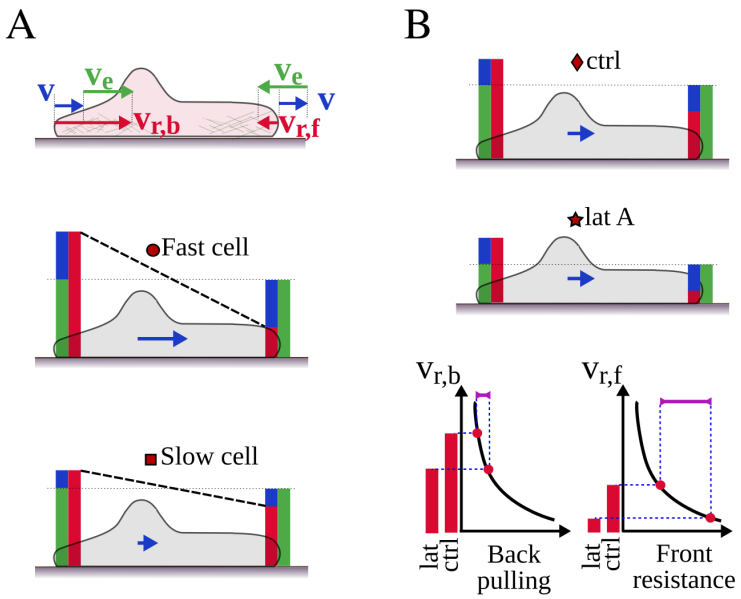

FIGURE 4.22: Relations between retrograde flow rates at the front and back protrusions in different conditions. A) Cartoon of the velocities in fast and slow cells. In the front protrusion, retrograde flow is the difference between extension rate and cell velocity. At the back, retrograde flow is the sum of extension rate and cell velocity. The difference between back and front retrograde flow velocities is larger in the fast cells. B) The effect of Latrunculin on retrograde flow and cell persistence. Extension rate is slower in Latrunculin-treated cells. Thus, retrograde flow is slower at both front and back protrusions. Slower retrograde flow increases back pulling slightly and front resistance substantially, which increases cell persistence.

back (Fig. 4.22B). The slower retrograde flow at the back increases the duration of back excitation. At the same time, the slower retrograde flow velocity at the front increases the front resistance length. We find that due to the convexity of the relations of back excitation duration and front resistance length with the retrograde flow, the application of Latrunculin A affects the front protrusion more than the back protrusion. The back excitation lasts longer, but the front resists even more. That makes a cell more persistent.

In summary, we find that the mechanical competition between front and back protrusions can explain the UCSP and the effect of Latrunculin A on the persistence time. The key elements of this mechanism are the elastic interaction of front and back protrusions and the noisy clutch mechanism (nonlinear friction of retrograde flow and stationary structures in the cell).

4.6.4 Perturbing motion by Fibronectin steps

Studying cells on homogeneous Fibronectin lanes enabled us to investigate the mechanisms that shape the general relations in cell motility. However, in vivo cells usually need to migrate in diverse conditions with heterogeneous adhesion. In this section, we study the effect of heterogeneous adhesion on cell behavior. We used our control experiments in chapter 3 with the cells moving on the Fibronectin density steps (data set 'stepped lanes' in Tables 4.1 and 4.2), to investigate how asymmetric adhesion affects the front and back protrusions.

Front and back of the cell sense different adhesion on a Fibronectin density step. The possible deterministic scenarios of a cell located on a Fibronectin step are illustrated in the two-parameter bifurcation diagram in Fig. 4.23A. Parameters B_1 and B_2 are the Fibronectin densities before and after a step, with before and after are defined according to the positive direction of the distance axis along the Fibronectin lane (positive and negative velocities are also defined accordingly). For simplicity, we assume the Fibronectin density at the cell body B_c to be the average of the Fibronectin densities at the cell protrusions, B_1 and B_2. We find that the system is bistable on the Fibronectin steps (the green area in Fig. 4.23A). The two stable states have opposite velocity directions - either into the high or into the low adhesion area. Consequently, cells do not move towards the high adhesion necessarily for a wide range of Fibronectin density combinations, since they might be in the state with velocity toward the low adhesion area. Indeed, we observe motion in both directions in experiments (see Fig. 4.24C). Thus, the multistability of the model can also explain the cell behavior on Fibronectin steps. Only in the extreme cases of very large steps (purple regions) the deterministic model entails that cells are moving towards the high adhesion field.

Although the cells are able to move in both directions in the noise-free model in a wide range of step heights, their absolute velocities are not identical in the two directions (Fig. 4.23B).

When the leading edge of the moving cell crosses the Fibronectin step, the adhesion strength changes at the front protrusion. Therefore, we investigated the effect of Fibronectin density on the stability of the front protrusion in such a situation. Fig. 4.23C and D show the basin of attraction that we defined in the previous sections for a front protrusion moving to a high Fibronectin density field and a low Fibronectin density

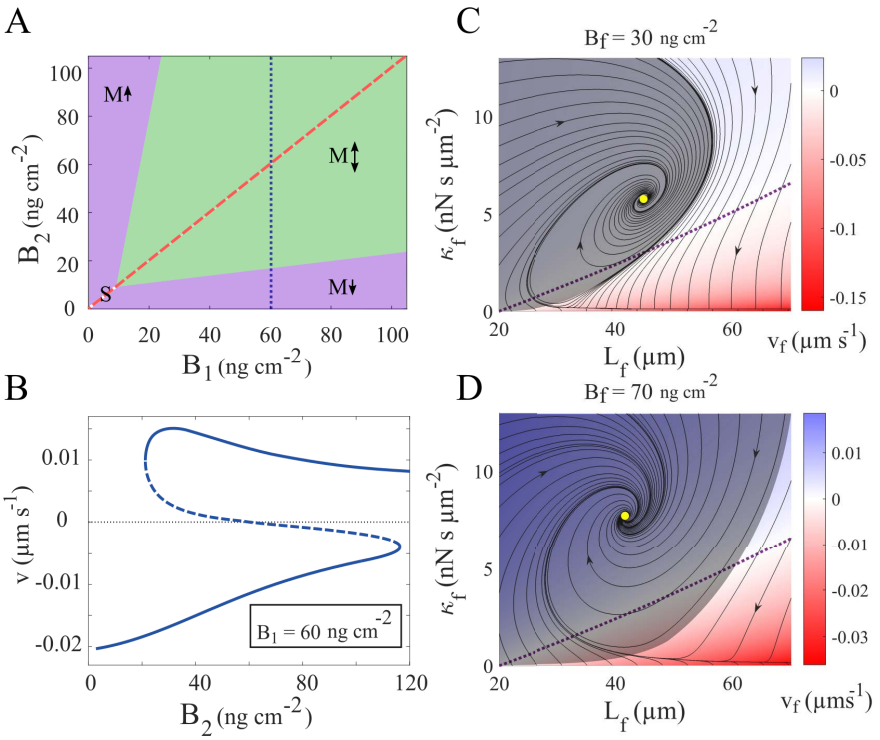

FIGURE 4.23: Cell states on Fibronectin steps. A) 2D bifurcation diagram with respect to Fibronectin densities forming the step B_1 and B_2. The purple regions correspond to very large step heights in which Cells can move only in one direction. In the green regions, cells are bistable with both upward and downward moving states. B) Cell velocity for a range of Fibronectin densities at the front B_2 and fixed Fibronectin density at the back B_1=60 ng cm^{-2} (along the dotted line in panel A). C, D) The basin of attraction (gray area) and state trajectories (black lines) in the phase plane for different values of Fibronectin density at the front.

field, resp. We find that higher adhesion increases the size of the basin of attraction at the front protrusion and makes it more stable. Thus, we can conclude that when the front protrusion moves to a higher Fibronectin density field, the probability of reversal decreases and the probability of passage increases.

We quantified the probability of cells moving in either direction with the passing and turning around probabilities (Fig. 4.24A). The other possible scenario is when cells get stuck on the step. We find a good agreement between simulations and experiments. The bottom right and top left corners in Fig. 4.24C and D indicate moving to lower and higher adhesion strengths, respectively. Fig. 4.24B shows the probability of passage over the step in dependence on the step height (B). We find a larger probability of passage toward higher Fibronectin density. That is consistent with our conclusion from the basins of attractions in Fig. 4.23C and D.

We saw small local maxima of Fibronectin densities on the border of neighboring fields,

in chapter 3. Here we use these artifacts to check the effect of small Fibronectin perturbation on cell motility behavior. We found all the steps to have heights smaller than 10 ng cm^{-2}. The Fibronectin densities on the two sides of the step are almost similar with those small and short steps, and only the local peak of Fibronectin density might affect the cells' behavior. We find that these Fibronectin 'bumps' change the probabilities of passage, getting stuck, and reversal compared to the cell motion on a homogeneous segment with the same density.

Our simulations also show that even in very large Fibronectin step heights (purple regions in Fig. 4.23 A), the transient, moving state caused by noise can last enough that enables cells to cross a step toward lower adhesion strength (Fig. 4.24). Thus unlike the noise-free model, we find some cells moving towards the lower adhesion fields even with very large step heights.

We conclude that the mechanisms introduced in our model can also explain the cell behavior in heterogeneous Fibronectin conditions.

4.7 Stationary force-velocity relation and stall force

In the last part of this chapter, we investigate the stationary force-velocity relation for a moving cell and find the stall force. For that, we study a cell with an external force applied to its leading edge membrane. Thus, we added the external force F_m to our force balance equation and derived the velocity.

$$F_f - E(L_f - L_0) - \zeta_f v_f - F_m = 0 \tag{4.29}$$

With the new force balance at the front, Eq. 4.10 changes to:

$$v_f = \frac{N_f}{a\zeta_f} W_0\left(\frac{V_e^0 a\kappa_f\zeta_f}{N_f(\zeta_f+\kappa_f)} exp\left(\frac{a\kappa_f(k^-\zeta_f - E(L_f-L_0) - F_m)}{N_f(\zeta_f+\kappa_f)}\right)\right) - \frac{E(L_f-L_0)+F_m+k^-\kappa_f}{\zeta_f+\kappa_f}, \tag{4.30}$$

Eq. 4.30 is used together with the other equations to find the velocity in the stationary state. We only discuss the results of the deterministic model here. In Fig. 4.25, forces, the cell and retrograde flow velocities are shown in dependence on F_m. We find that increasing F_m decreases the cell velocity. At low values of F_m, increasing the external

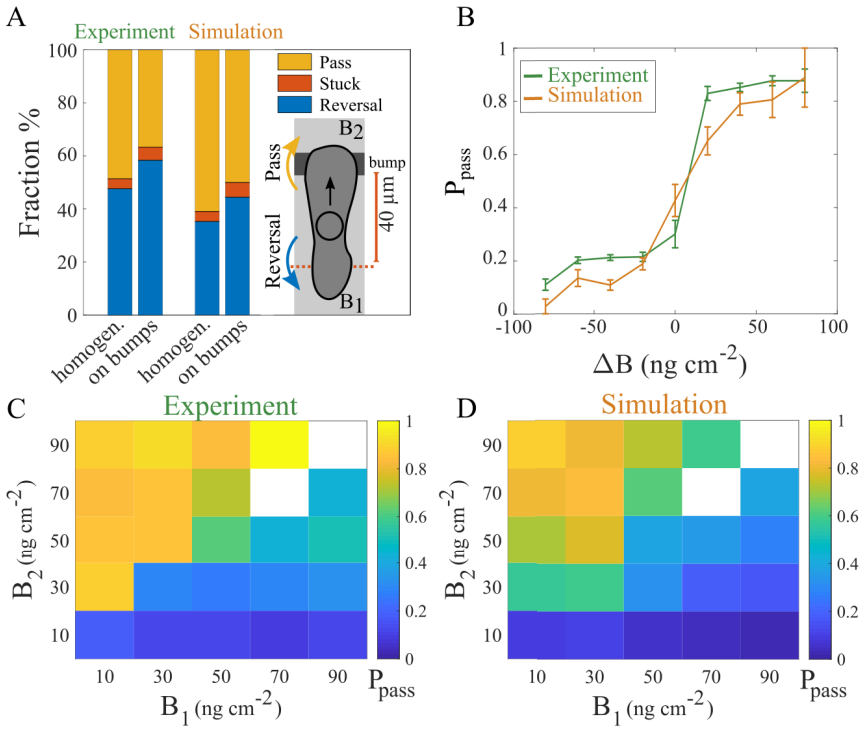

FIGURE 4.24: Cell behavior at Fibronectin steps. A) Probabilities of passing, reversing direction, and getting stuck on the midlane homogeneous area and at Fibronectin steps with a height up to 10 ng cm^{-2} (bumps). The cell nucleus is observed in the range between the step and 40 µm before the step. A direction reversal is defined when the cell exits the range from the entry point (40 µm before the step). A pass is counted when cell crosses the step. If the cell nucleus remains in the range longer than a dwell time of 5.5 h (defined according to our definition of a spread cell), it got stuck. B) The probability of passing P_{pass} in dependence on the step height averaged over all the steps. C, D) P_{pass} in dependence on the B_1 (before the step) and B_2 (after the step). White color indicates data not measured.

force decreases the membrane velocity, which in turn increases the retrograde flow velocity. Here the front protrusion is working on the rising branch of the force-retrograde flow curve. Thus, the force at the front F_f also increases with F_m. By further increasing F_m, the retrograde flow velocity at the cell front $v_{r,f}$ reaches the critical retrograde flow $v_{r,cr}$ (Fig. 4.25, middle). This situation corresponds to the maximum force in Fig. 4.15. Beyond this point, F_f is saturated and can not be increased by further increasing F_m (Fig. 4.25, right). That is a new regime of stationary force velocity with an almost linear relation.

$$v_f = \frac{1}{\zeta_f}\left(\kappa_f v_{r,cr} - (E(L_f - L_0) + F_m)\right) \tag{4.31}$$

The stall force can be found as the force by which the motion stalls, i.e., $\kappa_f v_{r,cr} = E(L_f - L_0) + F_m$.

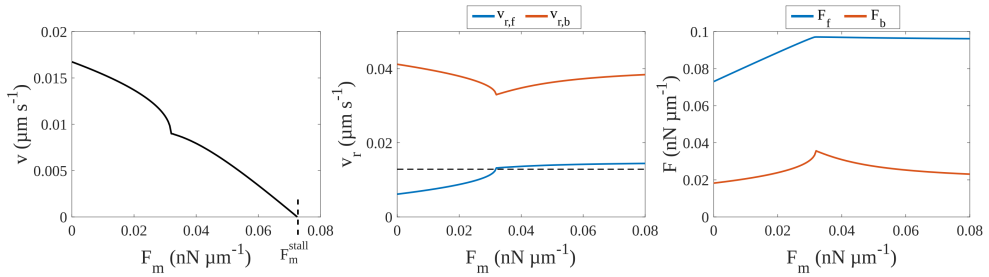

FIGURE 4.25: Stationary force-velocity relation. Left: The dependency of the cell velocity v to the external force F_m.F_m^{stall} is the force that stalls the cell motion. Middle: Retrograde flow in both protrusions of a moving cell in dependence on the external force F_m. The critical velocity $v_{r,cr}$ is shown with the dashed line (see section 4.2.) Right: Forces at both protrusions of a moving cell in dependence on the external force F_m. The parameter values of set 1 (Table 4.2) with Fibronectin density B=45 ng cm^{-2} are used in this analysis.

Similar to our prediction in chapter 3, here we also find a monotonously decreasing dependency of velocity to the external force in the stationary state. However, unlike chapter 3 and other models that use linear friction and find linear force-velocity relation [130], here we predict a nonlinear relation with two different regimes.

4.8 Conclusion and summary

Following our biophysical model in chapter 3, which could provide mechanistic inside into the biphasic adhesion-velocity relation, in this chapter, we focused on other constitutive relations in cell motility. In addition to biphasic adhesion-velocity relation, state dynamics, and the UCSP appear to describe the motile behavior of many different cell types. Their generality and concurrency strongly suggest that a single mechanism should explain all three of them. In this chapter, we extended our model to search for such a mechanism. Our experimental collaborators carried out a series of experiments with MDA-MB-231 cells on 1-dimensional lanes in a range of Fibronectin concentrations. We analyzed more than 23000 single-cell tracks. We extended our model based on the basic experimental observations. We then used our experimental data on MDA-MB-231 cells to validate our theory.

The hypothesis guiding our study in this chapter was that the intracellular dynamics generating multistability also determines the physical characteristics of cell motion. Accordingly, we first established the multistable dynamics and verified it with the state dynamics of MDA-MB-231 cells. We expected that the same parameterized dynamics

exhibits physical motion characteristics of MDA-MB-231 cells like the cellular response to adhesion strength (adhesion-velocity relation), to external force (force-velocity relation) and the characteristics of random motion (UCSP).

In the first part of this chapter, we focused on the internal cell mechanisms that produce different dynamic states, and analyzed the motion of MDA-MB-231 cells on 1-dimensional Fibronectin lanes with homogeneous density instead of stepped density profiles to exclude the effect of external perturbation. We also analyzed the dynamic reaction of cells to the Fibronectin steps in the last part of the chapter. Restricting cells to 1-dimensional motion turned direction changes into a transition between two discrete and easily distinguishable states up and down.

We could distinguish 4 dynamic states of cells on the 1-dimensional lanes. Cells can be spread or moving and exhibit either steady or oscillatory morphodynamics. We find the coexistence of oscillatory and steady morphodynamics in cells. That is the experimental manifestation of multistability.

Based on our experimental observations on the activities at the back of the cell, we added a protrusion at the back and the cell body. The main constituents of the final model are the force balance, the integrin signaling, and additionally the noisy clutch mechanism of friction between the actin network and stationary structures in the cell, to capture the dynamic states of cells. We found that our model reproduces all the dynamic states of MDA-MB-231 cells observed in the experiments. The front edge moves with almost constant velocity in all moving states. The biphasic dependency of this velocity on the adhesion can also be reproduced with the extended two-protrusion model despite the back protrusion activity.

The new model also reproduces the transitions and their statistics between the dynamic states. These noise-induced transitions show the multistability of the system, similar to our experimental observations. A critical component of the model required for the multistability of the system is the clutch mechanism of retrograde flow. This nonlinear element of the model leads to oscillatory dynamics in certain situations. Also, it results in different working regimes of protrusions, including the symmetric protrusions that emerge in spread cells and dominant-submissive protrusions that occur in moving cells. A 'mechanical polarization' appears in the moving cells with the slower retrograde flow in the dominant protrusion at the front and faster flow at the submissive back

protrusion. Noise in the dynamics of the clutch mechanism can change the working regime of protrusions leading to the transition between dynamic states of cells, including start or stop of motion and reversal of the motion direction.

We studied the UCSP and provided an explanation for the positive correlation of cell velocity and persistence time based on the mechanical stability of competing protrusions. We found that the inhibition of actin polymerization by application of Latrunculin A leads to longer persistence times for moving cells. This finding can not be explained by the current theory for the UCSP proposed by Maiuri et al. [8]. The mechanism in [8] predicts a shortening of the persistence time upon decreasing the network extension rate. However, our mechanism, based on the competition of front and back protrusions and retrograde flow as the most important indicator of the stability of protrusions, predicts a longer persistence time upon Latrunculin application in agreement with our experimental results.

We also analyzed the perturbation of cell motion by Fibronectin density steps. We measured and simulated the passing probability of MDA-MB-231 cells across steps and find very good agreement between our theory and experiemts. We found that cells are not necessarily moving to the higher Fibronectin density fields, as explained by the bistability of the model in the heterogeneous Fibronectin density case. The probability of cells passing a step towards higher Fibronectin density is larger, due to the more stable front protrusion.

Our model also provides a prediction for the stationary force-velocity relation. This relation has not been measured experimentally yet. However, our prediction (also our prediction in chapter 3) is very similar to earlier studies, e.g., in [130]. Interestingly, the stationary force velocity relation exhibits specific features set by the friction law of retrograde flow. Models with linear friction provide an (almost) linear stationary force-velocity relation. Our model using the clutch friction law, provides a relation with two regimes separated by a kink in the relation. Hence, experiments of the stationary force-velocity relation applying an external force could reveal the intracellular retrograde flow friction law.

Finally, we showed that the mechanical system comprising actin network and membrane tension is sufficient to explain many general properties of cells, including adhesion-velocity relation, oscillatory dynamics, multistability, and UCSP. Signaling pathways

affect this system by setting its parameters, but do not cause multistability and the state dynamics. Our drug treatment experiments provided additional perturbations for verification of our theory. Latrunculin A perturbed the network extension rate, and Blebbistatin the adhesion structure density. Parameter changes reflecting only these biochemical actions of these drugs were sufficient to reproduce the experimental results. That provides strong confirmation for our theory - strong confirmation for the right choice of processes and interactions defining it. The Latrunculin application allowed us to test and compare the predictions of our model with the previous theories. The main conclusion of this chapter is that a model comprising well-established basic constituents can reproduce constitutive relations in cell motility, which explains the universality of these relations.

Chapter 5

Summary and conclusion

Eukaryotic cells have various fundamental features that are conserved across different organisms over hundreds of millions of years of evolution. One of these basic features is motility. This ancient behavior of cells still plays a crucial role in the development and maintenance of different species, including humans. One of the leading causes of death is also closely related to cell motility. Cancer is responsible for about one in six deaths worldwide. The most significant clinical challenge in controlling this disease is the metastatic spread of cancer cells. This highlights the great importance of understanding the mechanisms controlling cell motility.

Although modes of motility vary largely between different cells, some features and relations are observed universally in all cell types. Those universal constitutive relations hint toward fundamental mechanisms that all cells share. Understanding those basic mechanisms could be a critical step toward gaining the capability to manipulate and control cell migration clinically.

In this thesis, we employed biophysical analysis and modeling to study cell motility. All the attempts to understand the complex system of a cell start with some experimental observations. Cell morphodynamics and the architecture of the cytoskeleton are two important sources of experimental data used to understand the cell's internal signaling pathways. New cell imaging techniques provide large data sets of the time evolution of cell boundary and complete contour data of filaments in the cell volume. Those are both complex observations, which in the raw form may not provide much insight into the internal cell mechanisms. However, quantifying these experimental observations can help

to understand underlying mechanisms that shape cell morphodynamics and cytoskeletal structure.

In chapter 2, we presented two workflows for the ultrastructural analysis of filamentous networks in the cytoskeleton and the morphodynamic analysis of cell boundary. In the first part of chapter 2, we developed a computational toolbox for the semi-automatic quantification of filamentous networks from pre-processed cryo-electron tomograms, facilitating the analysis and cross-comparison of multiple experimental conditions. GUI-based components of the toolbox simplify the processing of data and allow users to obtain a large number of ultrastructural parameters describing filamentous assemblies. We demonstrated the feasibility of this workflow by analyzing cryo-ET data of untreated and chemically perturbed branched actin filament networks and that of parallel actin filament arrays. We compared the data of B16-F1 melanoma cells from the control population and the cell population treated with CK666. We showed the change in the architecture of the branched actin networks upon inhibition of the Arp2/3 complex by CK666. We further analyzed bundled filament assemblies and showed the structural difference between a filopodium and a microspike. We showed that our ultrastructural analysis toolbox can ease the identification of key differences between experimental groups and facilitate the in-depth analysis of ultrastructural data in a time-efficient manner.

In the second part of chapter 2, we introduced an analysis workflow that characterizes the morphodynamics of the cell edge in moving or spread states. The first step was calculation of the displacement field on the cell boundary. For that, we proposed a mapping algorithm based on a mechanical system of springs to determine the trajectory of points on the cell boundary over subsequent time frames. We substantially improved the mapping algorithm proposed by Machacek et al. [185] by using linear springs with adaptive stiffness as a function of local deformation degree. Our method is computationally efficient and results in realistic trajectories of points on the boundary, even in high deformation regions. The velocity and curvature maps of the cell edge are then analyzed using our mapping algorithm. We then defined morphodynamic profiles for cells using 20 mathematical descriptors, which can be separated into four groups of protrusion-, retraction-, dynamics- or geometry-related parameters.

We used our morphodynamic analysis workflow to demonstrate the role of a motility-related protein, Lamellipodin (Lpd), in the persistent motion of cells. The difference

between morphodynamic profiles of B16-F1 melanoma cells from the control population and the Lpd knockout population revealed morphodynamic effect of Arp2/3 deactivation through Lpd deletion. We also discovered two different morphodynamic regimes in control and Lpd knockout cells using principal component analysis (PCA). One regime found only with Lpd knockout cells is associated with a positive correlation between retraction/fluctuation activity and protrusion activity. The other one, comprising a mixture of Lpd knockout and control cells, is associated with a negative correlation between retraction/fluctuation activity and protrusion activity. This example demonstrates the potentials of our morphodynamics analysis workflow for studying the regulatory proteins of motility.

After familiarizing ourselves with morphodynamics and motility by intense data analysis, we introduced our biophysical model to study the constitutive relations in cell motility. We started with the biphasic adhesion-velocity relation. Cell motion was restricted to 1 dimension by 1-dimensional Fibronectin lanes with alternating density. That simplification enabled us to study the basic mechanisms shaping the biphasic adhesion-velocity relation without dealing with the complications arising in 2-dimensional motility. We analyzed data from more than 15.000 single-cell tracks. We constructed our model using three well-established components, the force balance, the basic thermodynamic relation for actin polymerization, and the integrin signaling. We derived an analytical expression for the adhesion-velocity relation comprising the dependency of cell velocity on forces, drag and friction coefficients, and a simple response function for the effect of integrin signalling on these coefficients.

Our model suggests that the adhesion-controlled friction and drag forces at the leading edge regulate cell velocity, not the traction force from stress fibers connecting adhesion sites, despite them being three orders of magnitude larger. Actin polymerization extends the network and pushes the membrane forward. The reaction force from the leading edge membrane drives the retrograde flow of actin. The propulsive force is transmitted to the substrate through friction dependent on the substrate's adhesiveness. The drag forces resisting cell motion also depend on the substrate's adhesiveness. Our mechanism suggests that in the rising phase of the adhesion-velocity relation, increasing adhesion mainly increases the propulsive forces at the cell front. At the falling phase of the adhesion-velocity relation, however, increasing adhesion increases the resisting forces at the cell rear and body. That increases the membrane tension at the leading edge,

which in turn decreases the force-dependent actin polymerization rate. Furthermore, the fraction of actin extension rate, which turns into the retrograde flow, increases as well. Hence, the cell velocity decreases with increasing adhesion in this phase.

We found the motility parameters by fitting the model to the data of 4 different cell types. The propulsive force at the leading edge depends on retrograde flow velocity and the friction coefficient between actin network and stationary structures in the cell. We found that different cells employ different strategies to increase their propulsive forces. They can either increase the friction coefficient of the actin flow κ by more adhesion at the cell front, or increase the retrograde flow, especially after saturation of κ. One of the most important findings from our analysis was that we found negligible velocity-independent forces in all cell types. This finding suggests that myosin contraction, which is velocity-independent, is not required for cell motion. Myosin may contribute to actin flow and detachment of cell trailing edge, but its contribution is not significant in the studied cell types. Alternatively, our mechanism suggests a critical role for myosin in the amplification of integrin signaling. Our experimental data on the cells treated with blebbistatin (a myosin inhibitor) confirm this role of myosin in the signaling pathways from integrins.

The alternating Fibronectin densities on the micro-lanes used in our experimental setting allowed investigation of the back-front relation in moving cells. We extended the model to incorporate the separate effects of adhesion at the cell back and front. We analyzed the data of the back and front edges of the cells passing over Fibronectin steps. A comparison of the cell length before and after crossing a Fibronectin segment revealed that cells have an intrinsic length that is dependent on the adhesion. Thus, we modeled the front-back interaction with an elastic force and showed that this force could reproduce the behavior of the back edge of cells moving on a Fibroncetin step. We also found an estimate for the elastic modulus of MDA-MB-231 cells, which is in agreement with the literature.

Another critical experimental observation in MDA-MB-231 cells was that cells could move from high to low Fibronectin density. It has been suggested before that motion arises from a tug of war between the back and front of the cell [78, 79]. In that picture, the adhesion strength in moving cells should be stronger at the front. We could not find any maximum Fibronectin density step height for cell motion in our data. Our mechanism suggests that cells are able to move even from very high Fibronectin density

to low densities and do not get stuck at local maxima of adhesion on substrate. That is due to the fact that all the forces involved in cell motility are velocity-dependent forces. Thus, the stronger adhesion at the cell back only decreases the cell velocity and can not stall motion.

Another picture of cell motility is compatible with our data, which accounts for the ambivalent role of myosin. It is obvious, that contraction can pull a load only up to the point of attachment of the contracting fiber to the substrate. Something has to go ahead and create the new attachment points. This going ahead would be one function of the protrusion mechanisms we describe. At the same time, the small forces we describe cannot move large loads. This might be the function of myosin contraction. That leads to a picture with myosin running a heavy duty machinery dragging the heavy load like nucleus and cell body, and actin polymerization forces move only a tent covering the heavy duty machinery. Both motions are synchronised by the generation of adhesion sites for stress fibers in substrate regions newly conquered by polymerization driven protrusion.

We could provide a mechanistic picture of the forces shaping biphasic adhesion-velocity relation and the front-back interaction in moving cells. We then focused on the more dynamic aspects of cell motility. By analyzing the front and back edge dynamics of MDA-MB-231 cells on micro-lanes with homogeneous Fibronectin coating, we found four dynamic states, moving with steady length, moving with oscillatory length, spread with steady length, and spread with oscillatory length. We also found transitions between these states in single cells. The cell's back edge can protrude in oscillatory and excitable states. Moving cells could also change their direction of motion. We found that the back edge always protrudes before the reversal of the direction of motion. Based on these evidences, we added an active protrusion at the back of the cell in our model. Moreover, we modified the friction coefficient between the actin network and stationary structures in the cell, κ, to a dynamic variable. We defined the dynamics of κ based on the well-established clutch mechanism, including attachment of bonds and velocity-dependent detachment of bonds. That implies the accelerated rupture of bonds with a faster retrograde flow of the actin network.

The modified model reproduces all the dynamic states of the MDA-MB-231 cells. We find that the cell's front edge moves with almost constant velocity in all dynamic moving

states, as captured with our initial model. The oscillatory back dynamics could also be reproduced with our extended model. The adhesion-velocity relation in the extended model was also biphasic, and the activities caused by back protrusion did not affect this relation qualitatively. Thus, we concluded that the main factors controlling adhesion-velocity relation are protrusive and resisting forces and integrin signaling.

Our extended model showed that cells are multistable systems with different coexisting stable states. We found that the noise included in our 'noisy clutch mechanism' can explain and reproduce all the state transitions and their statistics we observed in our experimental data. That noise is caused by the stochastic formation and breakage of bonds. The probabilities of states and transitions in our simulations perfectly matched the experimental results. Analysis of the back and front edges of the cells during the reversal of motion direction showed that the reversal process is started and caused by the back edge protruding and pulling the front. In other words, the reversal results from a mechanical competition between the back and front protrusions. Our model showed the exact same mechanism of cell reversal. We then studied another universal experimental observation, the UCSP law. Our model could reproduce the positive correlation between cell speed and persistence time. We additionally investigated the UCSP law in cells treated with Latrunculin A, an inhibitor of actin polymerization. We find the same positive correlation between cell velocity and persistence in our experiments and simulations. Strikingly, we found that Latrunculin A treatment increases cell persistence. That result contradicts the current theory for UCSP by Maiuri et al. [8].

Maiuri et al. explain the UCSP by a mechanism centered around the network extension rate: the fast network extension in fast cells advects an F-actin-binding inhibitor of network growth away from the protrusion tip and thus renders random protrusion collapse unlikely. Maiuri et al. conclude that the faster the network extension rate the more persistent the cell moves [8].

The reasoning of Maiuri et al. leading to the inhibitor advection mechanism requires the data in their Fig. 2A as essential component [8]. They show increasing persistence time with increasing network extension rate for mature bone marrow dendritic cells migrating in a confined environment. Maiuri et al. report that no correlation between persistence time and cell velocity across different adhesion conditions was observed in these data [8], i.e., the UCSP is violated under their experimental conditions. That makes it difficult to

discuss that data in the context of a UCSP mechanism. In line with the UCSP-violation, the data are not compatible with our UCSP mechanism, and neither with the inhibitor advection mechanism of Maiuri et al., since cell velocity and network extension rate are not proportional within this data set. Another shortcoming of the inhibitor advection mechanism is that an endogenous F-actin binding inhibitor of network extension has not been identified yet.

The mechanism proposed in [8] predicts shorter cell persistence upon Latrunculin A application. Alternatively, our model suggests that faster cell motion is associated with slower and faster retrograde flow at the front and back protrusions, respectively. We find that the stability of a protrusion is inversely correlated with its retrograde flow. Hence, faster cells are more persistent due to their more stable front protrusion and less stable back protrusion. Application of Latrunculin A reduces actin extension rate and retrograde flow at both front and back protrusions. Nevertheless, the drop of retrograde flow has a stronger impact on increasing the stability of front protrusion than the back. That is due to the convex relation between stability measures and retrograde flow and slower flow rate at the front protrusion than at the back.

With our approach and our data, the noisy clutch is sufficient to explain the UCSP by spontaneous direction reversals based on protrusion competition.

We again studied the motion of cells on stepped Fibronectin lanes, this time with our extended model. We find that cells on the steps are bistable and can move in both directions. Our model suggests that the higher probability of moving towards higher adhesion is due to the higher stability of the front protrusion in that case. The model also provides a prediction for the stationary force-velocity relation. However, this relation has not been measured experimentally yet, and further experimental studies are required.

In conclusion, we presented tools to analyze experimental data and a biophysical model to understand the mechanisms of cell motility. We started our study with the aim of understanding the universal constitutive relation in cell motility. A theory describing a universal phenomenon should be as simple as possible, such that the large variety of systems exhibiting the phenomenon can meet the theory's requirements. Thus, we constructed our model with only well-established basic physical and biological constituents. This approach led to a quantitative theory comprising several general observations of mesenchymal motility: biphasic adhesion-velocity relation, universal coupling between

cell speed and persistence (UCSP), multistability with different dynamic states, and stationary force-velocity relation.

Bibliography

[1] Ewa Kamila Paluch, Irene M Aspalter, and Michael Sixt. Focal adhesion-independent cell migration. 2016.

[2] Harvey F Lodish, Arnold Berk, S Lawrence Zipursky, Paul Matsudaira, David Baltimore, and James Darnell. *Molecular cell biology*, volume 4. Citeseer, 2006.

[3] Gaëlle Letort, Hajer Ennomani, Laurène Gressin, Manuel Théry, and Laurent Blanchoin. Dynamic reorganization of the actin cytoskeleton. *F1000Research*, 4, 2015.

[4] Thomas D Pollard and Gary G Borisy. Cellular motility driven by assembly and disassembly of actin filaments. *Cell*, 112(4):453–465, 2003.

[5] Liqun Luo. Actin cytoskeleton regulation in neuronal morphogenesis and structural plasticity. *Annual review of cell and developmental biology*, 18(1):601–635, 2002.

[6] Tatyana M. Svitkina and Gary G. Borisy. Arp2/3 complex and actin depolymerizing factor/cofilin in dendritic organization and treadmilling of actin filament array in lamellipodia. *J Cell Biol*, 145(5):1009–1026, 1999. doi: 10.1083/jcb.145.5.1009.

[7] Erin L Barnhart, Kun-Chun Lee, Kinneret Keren, Alex Mogilner, and Julie A Theriot. An adhesion-dependent switch between mechanisms that determine motile cell shape. *PLoS biology*, 9(5):e1001059, 2011.

[8] Paolo Maiuri, Jean-Franccois Rupprecht, Stefan Wieser, Verena Ruprecht, Olivier Bénichou, Nicolas Carpi, Mathieu Coppey, Simon De Beco, Nir Gov, Carl-Philipp Heisenberg, Carolina Lage Crespo, Franziska Lautenschlaeger, Mael Le Berre, Ana-Maria Lennon-Dumenil, Matthew Raab, Hawa-Racine Thiam, Matthieu Piel, Michael Sixt, and Raphael Voituriez. Actin flows mediate a universal

coupling between cell speed and cell persistence. *Cell*, 161(2):374–386, 2015. ISSN 0092-8674. doi: https://doi.org/10.1016/j.cell.2015.01.056. URL http://www.sciencedirect.com/science/article/pii/S0092867415001804.

[9] Georgi Dimchev, Behnam Amiri, Florian Fäßler, Martin Falcke, and Florian KM Schur. Computational toolbox for ultrastructural quantitative analysis of filament networks in cryo-et data. *Journal of Structural Biology*, 213(4):107808, 2021.

[10] Georgi Dimchev, Behnam Amiri, Ashley C Humphries, Matthias Schaks, Vanessa Dimchev, Theresia EB Stradal, Jan Faix, Matthias Krause, Michael Way, Martin Falcke, et al. Lamellipodin tunes cell migration by stabilizing protrusions and promoting adhesion formation. *Journal of cell science*, 133(7):jcs239020, 2020.

[11] Christoph Schreiber, Behnam Amiri, Johannes C. J. Heyn, Joachim O. Rädler, and Martin Falcke. On the adhesion–velocity relation and length adaptation of motile cells on stepped fibronectin lanes. *Proceedings of the National Academy of Sciences*, 118(4), 2021. ISSN 0027-8424. doi: 10.1073/pnas.2009959118. URL https://www.pnas.org/content/118/4/e2009959118.

[12] Sean S. Palecek, Joseph C. Loftus, Mark H. Ginsberg, Douglas A. Lauffenburger, and Alan F. Horwitz. Integrin-ligand binding properties govern cell migration speed through cell-substratum adhesiveness. *Nature*, 385(6616):537–540, 1997.

[13] Stephanie L. Gupton and Clare M. Waterman-Storer. Spatiotemporal feedback between actomyosin and focal-adhesion systems optimizes rapid cell migration. *Cell*, 125(7):1361 – 1374, 2006. ISSN 0092-8674. doi: DOI:10.1016/j.cell.2006.05.029.

[14] Erin L. Barnhart, Kun-Chun Lee, Kinneret Keren, Alex Mogilner, and Julie A. Theriot. An Adhesion-Dependent Switch between Mechanisms That Determine Motile Cell Shape. *PLoS Biol*, 9(5):e1001059, 05 2011. doi: 10.1371/journal.pbio.1001059.

[15] Juliane Zimmermann, Claudia Brunner, Mihaela Enculescu, Michael Goegler, Allen Ehrlicher, Josef Käs, and Martin Falcke. Actin filament elasticity and retrograde flow shape the force-velocity relation of motile cells. *Biophys J*, 102(2):287 – 295, 2012.

[16] TD Pollard. Rate constants for the reactions of ATP- and ADP-actin with the ends of actin filaments. *J Cell Biol*, 103(6):2747–2754, 1986. doi: 10.1083/jcb.103.6.2747.

[17] Vivek C. Abraham, Vijaykumar Krishnamurthi, D. Lansing Taylor, and Frederick Lanni. The actin-based nanomachine at the leading edge of migrating cells. *Biophys J*, 77(3):1721 – 1732, 1999. ISSN 0006-3495. doi: DOI:10.1016/S0006-3495(99)77018-9.

[18] Setareh Dolati, Frieda Kage, Jan Mueller, Mathias Müsken, Marieluise Kirchner, Gunnar Dittmar, Michael Sixt, Klemens Rottner, and Martin Falcke. On the relation between filament density, force generation, and protrusion rate in mesenchymal cell motility. *Molecular Biology of the Cell*, 29(22):2674–2686, 2018.

[19] Klemens Rottner, Jan Faix, Sven Bogdan, Stefan Linder, and Eugen Kerkhoff. Actin assembly mechanisms at a glance. *J. Cell Science*, 130(20):3427–3435, 2017. ISSN 0021-9533. doi: 10.1242/jcs.206433.

[20] Omotola F. Omotade, Stephanie L. Pollitt, and James Q. Zheng. Actin-based growth cone motility and guidance. *Molecular and Cellular Neuroscience*, 84:4 – 10, 2017.

[21] Alexia I Bachir, Alan Rick Horwitz, W James Nelson, and Julie M Bianchini. Actin-Based Adhesion Modules Mediate Cell Interactions with the Extracellular Matrix and Neighboring Cells. *Cold Spring Harb Perspect Biol*, 9(7):a023234, 2017.

[22] Andrew D Doyle, Francis W Wang, Kazue Matsumoto, and Kenneth M Yamada. One-dimensional topography underlies three-dimensional fibrillar cell migration. *Journal of cell biology*, 184(4):481–490, 2009.

[23] K. Anderson, Y. L. Wang, and J. V. Small. Coordination of protrusion and translocation of the keratocyte involves rolling of the cell body. *J. Cell Biology*, 134:1209–18, 1996.

[24] A. B. Verkhovsky, T. M. Svitkina, and G. G. Borisy. Self-polarization and directional motility of cytoplasm. *Curr. Biology*, 14:11–20, 1999.

[25] J. P. Thiery and J. P. Sleeman. Complex networks orchestrate epithelial-mesenchymal transitions. *Nature Reviews; Molecular Cell Biology*, 7:131–42, 2006.

[26] J. Guck, F. Lautenschlager, S. Paschkeband, and M. Beil. Critical review: cellular mechanobiology and amoeboid migration. *Integrative Biology*, 2:575–83, 2010.

[27] K. Pankova, D. Rosel, M. Novotny, and J. Brabek. The molecular mechanisms of transition between mesenchymal and amoeboid invasiveness in tumor cells. *Cell Mol. Life Sci*, 67:63–71, 2010.

[28] Pierre Sens and Julie Plastino. Membrane tension and cytoskeleton organization in cell motility. *Journal of Physics: Condensed Matter*, 27(27):273103, 2015.

[29] A. D. Lieber, S. Yehudai-Resheff, E. L. Barnhart, J. A. Theriot, and K. Keren. Membrane tension in rapidly moving cells is determined by cytoskeletal forces. *Current Biology*, 108(23):1409–1417, 2011.

[30] Andrew R. Houk, Alexandra Jilkine, Cecile O. Mejean, Rostislav Boltyanskiy, Eric R. Dufresne, Sigurd B. Angenent, Steven J. Altschuler, Lani F. Wu, and Orion D. Weiner. Membrane tension maintains cell polarity by confining signals to the leading edge during neutrophil migration. *Cell*, 148(1–2):175–188, 2012. ISSN 0092-8674. doi: 10.1016/j.cell.2011.10.050.

[31] Jan Mueller, Gregory Szep, Maria Nemethova, Ingrid de Vries, Arnon D. Lieber, Christoph Winkler, Karsten Kruse, J. Victor Small, Christian Schmeiser, Kinneret Keren, Robert Hauschild, and Michael Sixt. Load adaptation of lamellipodial actin networks. *Cell*, 171(1):188 – 200.e16, 2017.

[32] Guillaume Salbreux, Guillaume Charras, and Ewa Paluch. Actin cortex mechanics and cellular morphogenesis. *Trends in cell biology*, 22(10):536–545, 2012.

[33] N. C. Gauthier, T. A. Masters, and M. P. Sheetz. Mmechanical feedback between membrane tension and dynamics. *Trends in Cell Biology*, 22(10), 2012.

[34] Kinneret Keren. Membrane tension leads the way. *Proc Nat Acad Sci USA*, 108 (35):14379–14380, 2011. doi: 10.1073/pnas.1111671108.

[35] D. Raucher and M. P. Sheetz. Cell spreading and lamellipodial extension rate is regulated by membrane tension. *J. Cell Biology*, 148:127–136, 2000.

[36] Ellen L. Batchelder, Gunther Hollopeter, Clément Campillo, Xavier Mezanges, Erik M. Jorgensen, Pierre Nassoy, Pierre Sens, and Julie Plastino. Membrane tension regulates motility by controlling lamellipodium organization. *Proceedings of the National Academy of Sciences*, 108(28):11429–11434, 2011. ISSN 0027-8424. doi: 10.1073/pnas.1010481108. URL https://www.pnas.org/content/108/28/11429.

[37] Bruce Alberts, Alexander Johnson, Julian Lewis, Martin Raff, Keith Roberts, and Peter Walter. The cytoskeleton and cell behavior. In *Molecular Biology of the Cell. 4th edition*. Garland Science, 2002.

[38] Robert S Fischer and Velia M Fowler. Thematic minireview series: the state of the cytoskeleton in 2015. *Journal of Biological Chemistry*, 290(28):17133–17136, 2015.

[39] Alex Mogilner. Mathematics of cell motility: have we got its number? *Journal of mathematical biology*, 58(1):105–134, 2009.

[40] Oliver I Wagner, Sebastian Rammensee, Neha Korde, Qi Wen, Jean-Francois Leterrier, and Paul A Janmey. Softness, strength and self-repair in intermediate filament networks. *Experimental cell research*, 313(10):2228–2235, 2007.

[41] MF Carlier and Do Pantaloni. Direct evidence for adp-inorganic phosphate-f-actin as the major intermediate in atp-actin polymerization. rate of dissociation of inorganic phosphate from actin filaments. *Biochemistry*, 25(24):7789–7792, 1986.

[42] J. Victor Small, Theresia Stradal, Emmanuel Vignal, and Klemens Rottner. The lamellipodium: where motility begins. *Trends Cell Biol*, 12(3):112 – 120, 2002. ISSN 0962-8924. doi: DOI:10.1016/S0962-8924(01)02237-1.

[43] Thomas D. Pollard and John A. Cooper. Actin, a Central Player in Cell Shape and Movement. *Science*, 326(5957):1208–1212, 2009. doi: 10.1126/science.1175862.

[44] B Bugyi, D Didry, and MF Carlier. How tropomyosin regulates lamellipodial actin-based motility: a combined biochemical and reconstituted motility approach. *EMBO J.*, 29:14–26, 2010.

[45] Christophe Le Clainche and Marie-France Carlier. Regulation of actin assembly associated with protrusion and adhesion in cell migration. *Physiological Reviews*, 88(2):489–513, 2008. doi: 10.1152/physrev.00021.2007.

[46] G. Letort, H. Ennomani, L. Gressin, M. Thery, and L. Blanchoin. Dynamic reorganization of the actin cytoskeleton. *F1000Research*, 4, 2015. doi: https://doi.org/10.12688/f1000research.6374.1.

[47] Frieda Kage, Moritz Winterhoff, Vanessa Dimchev, Jan Mueller, Tobias Thalheim, Anika Freise, Stefan Brühmann, Jana Kollasser, Jennifer Block, Georgi Dimchev, Matthias Geyer, Hans-Joachim Schnittler, Cord Brakebusch, Theresia E. B. Stradal, Marie-France Carlier, Michael Sixt, Josef Käs, Jan Faix, and Klemens Rottner. FMNL formins boost lamellipodial force generation. *Nature Communications*, 8:14832, 2017.

[48] I. Rouiller, X. Xu, K. J. Amann, C. Egile, S. Nickell, D. Nicastro, R. Li, T. D. Pollard, N. Volkmann, and D. Hanein. The structural basis of actin filament branching by the arp2/3 complex. *J Cell Biol*, 180:887–95, 2008.

[49] Boris Praveen Suraneni, Jay R. Rubinstein, Michael Unruh, Dorit Durnin, and R. Licorresponding Hanein. The arp2/3 complex is required for lamellipodia extension and directional fibroblast cell migration. *J. Cell Biol.*, 197(2):239–251, 2012.

[50] Congying Wu, Sreeja B. Asokan, Matthew E. Berginski, Elizabeth M. Haynes, Norman E. Sharpless, Jack D. Griffith, Shawn M. Gomez, and James E. Bear. Arp2/3 is critical for lamellipodia and response to extracellular matrix cues but is dispensable for chemotaxis. *Cell*, 148(5):973 – 987, 2012. ISSN 0092-8674. doi: 10.1016/j.cell.2011.12.034.

[51] Max Rodnick-Smith, Qing Luan, Su-Ling Liu, and Brad J Nolen. Role and structural mechanism of wasp-triggered conformational changes in branched actin filament nucleation by arp2/3 complex. *Proceedings of the National Academy of Sciences*, 113(27):E3834–E3843, 2016.

[52] Melissa A Chesarone and Bruce L Goode. Actin nucleation and elongation factors: mechanisms and interplay. *Current opinion in cell biology*, 21(1):28–37, 2009.

[53] J. E. Bear, J. J. Loureiro, I. Libova, R. Fässler, J. Wehland, and F. B. Gertler. Negative regulation of fibroblast motility by ena/vasp proteins. *Cell*, 101(7):717–728, 2000.

[54] J.E. Bear and Gertler F. B. Ena/vasp: towards resolving a pointed controversy at the barbed end. *J. Cell Sci*, 122(7):1947–53, 2009.

[55] A. Mogilner and G. Oster. Cell motility driven by actin polymerization. *Biophys.J.*, 71:3030–3045, 1996.

[56] T. R. Coleman and M. S. Mooseker. Effects of actin filament cross-linking and filament length on actin-myosin interaction. *J. Cell Biol.*, 101:1850–7, 1985.

[57] Martin Falcke. Concentration profiles of actin-binding molecules in lamellipodia. *Physica D: Nonlinear Phenomena*, 318/319:50 – 57, 2016. ISSN 0167-2789.

[58] M. L. Gardel, J. H. Shin, F. C. MacKintosh, L. Mahadevan, P. Matsudaira, and D. A. Weitz. Elastic behavior of cross-linked and bundled actin networks. *Science*, 304(5675):1301–1305, 2004. ISSN 00368075.

[59] CC Cunningham, JB Gorlin, DJ Kwiatkowski, JH Hartwig, PA Janmey, HR Byers, and TP Stossel. Actin-binding protein requirement for cortical stability and efficient locomotion. *Science*, 255(5042):325–327, 1992. doi: 10.1126/science.1549777.

[60] Yiider Tseng, Benjamin W. Schafer, Steven C. Almo, and Denis Wirtz. Functional synergy of actin filament cross-linking proteins. *Journal of Biological Chemistry*, 277(28):25609–25616, 2002. doi: 10.1074/jbc.M202609200. URL http://www.jbc.org/content/277/28/25609.abstract.

[61] W. Hwang and M. J. Lang. Mechanical design of translocating motor proteins. *Cell Biochem. Biophys.*, 54(1):11–12, 2009.

[62] Harvey Lodish, Arnold Berk, Chris A Kaiser, Chris Kaiser, Monty Krieger, Matthew P Scott, Anthony Bretscher, Hidde Ploegh, Paul Matsudaira, et al. *Molecular cell biology*. Macmillan, 2008.

[63] Alexander B Verkhovsky, Tatyana M Svitkina, and Gary G Borisy. Self-polarization and directional motility of cytoplasm. *Current Biology*, 9(1):11–S1, 1999.

[64] Andrew R Houk, Alexandra Jilkine, Cecile O Mejean, Rostislav Boltyanskiy, Eric R Dufresne, Sigurd B Angenent, Steven J Altschuler, Lani F Wu, and Orion D Weiner. Membrane tension maintains cell polarity by confining signals to the leading edge during neutrophil migration. *Cell*, 148(1-2):175–188, 2012.

[65] Catherine D Nobes and Alan Hall. Rho, rac, and cdc42 gtpases regulate the assembly of multimolecular focal complexes associated with actin stress fibers, lamellipodia, and filopodia. *Cell*, 81(1):53–62, 1995.

[66] Matthias Machacek, Louis Hodgson, Christopher Welch, Hunter Elliott, Olivier Pertz, Perihan Nalbant, Amy Abell, Gary L Johnson, Klaus M Hahn, and Gaudenz Danuser. Coordination of rho gtpase activities during cell protrusion. *Nature*, 461 (7260):99–103, 2009.

[67] Keith Burridge and Krister Wennerberg. Rho and rac take center stage. *Cell*, 116 (2):167–179, 2004.

[68] Anne J Ridley, Martin A Schwartz, Keith Burridge, Richard A Firtel, Mark H Ginsberg, Gary Borisy, J Thomas Parsons, and Alan Rick Horwitz. Cell migration: integrating signals from front to back. *Science*, 302(5651):1704–1709, 2003.

[69] Miguel Vicente-Manzanares, Colin Kiwon Choi, and Alan Rick Horwitz. Integrins in cell migration–the actin connection. *Journal of cell science*, 122(2):199–206, 2009.

[70] Margaret L Gardel, Ian C Schneider, Yvonne Aratyn-Schaus, and Clare M Waterman. Mechanical integration of actin and adhesion dynamics in cell migration. *Annual review of cell and developmental biology*, 26:315, 2010.

[71] Daniel Choquet, Dan P Felsenfeld, and Michael P Sheetz. Extracellular matrix rigidity causes strengthening of integrin–cytoskeleton linkages. *Cell*, 88(1):39 – 48, 1997. ISSN 0092-8674.

[72] S. Munevar, Y. Wang, and M. Dembo. Traction force microscopy of migrating normal and h-ras transformed 3t3 fibroblasts. *Biophysical Journal*, 80(4):1744–1757, 2001.

[73] Margaret L. Gardel, Benedikt Sabass, Lin Ji, Gaudenz Danuser, Ulrich S. Schwarz, and Clare M. Waterman. Traction stress in focal adhesions correlates biphasically

with actin retrograde flow speed. *J Cell Biol*, 183(6):999–1005, 2008. doi: 10.1083/jcb.200810060.

[74] J. G. Lock, B. Wehrle-Haller, and Strömblad S. Cell-matrix adhesion complexes: master control machinery of cell migration. *Cancer Biol.*, 18:65–76, 2007.

[75] Claire M Brown, Benedict Hebert, David L Kolin, Jessica Zareno, Leanna Whitmore, Alan Rick Horwitz, and Paul W Wiseman. Probing the integrin-actin linkage using high-resolution protein velocity mapping. *Journal of cell science*, 119(24): 5204–5214, 2006.

[76] Stephanie L Gupton and Clare M Waterman-Storer. Spatiotemporal feedback between actomyosin and focal-adhesion systems optimizes rapid cell migration. *Cell*, 125(7):1361–1374, 2006.

[77] Lindsay B Case and Clare M Waterman. Integration of actin dynamics and cell adhesion by a three-dimensional, mechanosensitive molecular clutch. *Nature cell biology*, 17(8):955–963, 2015.

[78] P. A. DiMilla, K. Barbee, and D. A. Lauffenburger. Mathematical model for the effects of adhesion and mechanics on cell migration speed. *Biophys J*, 60(1):15–37, 1991.

[79] Maria A Gracheva and Hans G. Othmer. A continuum model of motility in ameboid cells. *Bulletin of Mathematical Biology*, 66:167–193, 2004.

[80] Elisabetta Ada Cavalcanti-Adam, Tova Volberg, Alexandre Micoulet, Horst Kessler, Benjamin Geiger, and Joachim Pius Spatz. Cell spreading and focal adhesion dynamics are regulated by spacing of integrin ligands. *Biophysical journal*, 92(8):2964–2974, 2007.

[81] Sean P Palecek, Joseph C Loftus, Mark H Ginsberg, Douglas A Lauffenburger, and Alan F Horwitz. Integrin-ligand binding properties govern cell migration speed through cell-substratum adhesiveness. *Nature*, 385(6616):537–540, 1997.

[82] Grégory Giannone, Benjamin J. Dubin-Thaler, Olivier Rossier, Yunfei Cai, Oleg Chaga, Guoying Jiang, William Beaver, Hans-Günther Döbereiner, Yoav Freund, Gary Borisy, and Michael P. Sheetz. Lamellipodial actin mechanically links myosin

activity with adhesion-site formation. *Cell*, 128(3):561 – 575, 2007. ISSN 0092-8674. doi: DOI:10.1016/j.cell.2006.12.039.

[83] Gillian L Ryan, Naoki Watanabe, and Dimitrios Vavylonis. A review of models of fluctuating protrusion and retraction patterns at the leading edge of motile cells. *Cytoskeleton*, 69(4):195–206, 2012.

[84] Hans-Günther Döbereiner, Benjamin J Dubin-Thaler, Jake M Hofman, Harry S Xenias, Tasha N Sims, Grégory Giannone, Michael L Dustin, Chris H Wiggins, and Michael P Sheetz. Lateral membrane waves constitute a universal dynamic pattern of motile cells. *Physical review letters*, 97(3):038102, 2006.

[85] A Huttenlocher, M H Ginsberg, and A F Horwitz. Modulation of cell migration by integrin-mediated cytoskeletal linkages and ligand-binding affinity. *Journal of Cell Biology*, 134(6):1551–1562, 09 1996. ISSN 0021-9525. doi: 10.1083/jcb.134.6.1551. URL https://doi.org/10.1083/jcb.134.6.1551.

[86] Miguel Vicente-Manzanares, Colin Kiwon Choi, and Alan Rick Horwitz. Integrins in cell migration - the actin connection. *Journal of Cell Science*, 122(2):199–206, 2009.

[87] J. Thomas Parsons, Alan Rick Horwitz, and Martin A. Schwartz. Cell adhesion: integrating cytoskeletal dynamics and cellular tension. *Nat Rev Mol Cell Biol*, 11 (9):633–643, 2010.

[88] K. Hennig, I. Wang, P. Moreau, L. Valon, S. DeBeco, M. Coppey, Y. A. Miroshnikova, C. Albiges-Rizo, C. Favard, R. Voituriez, and M. Balland. Stick-slip dynamics of cell adhesion triggers spontaneous symmetry breaking and directional migration of mesenchymal cells on one-dimensional lines. *Science Advances*, 6(1): eaau5670, 2020. doi: 10.1126/sciadv.aau5670. URL https://advances.sciencemag.org/content/advances/6/1/eaau5670.full.pdfhttps://www.ncbi.nlm.nih.gov/pmc/articles/PMC6941913/pdf/aau5670.pdf.

[89] A.B. Verkhovsky, T.M. Svitkina, and G.G. Borisy. Self-polarization and directional motility of cytoplasm. *Current Biology*, 9(1):11–20, 1999.

[90] R. J. Hawkins, R. Poincloux, O. Benichou, M. Piel, P. Chavrier, and R. Voituriez. Spontaneous contractility-mediated cortical flow generates cell migration in three-dimensional environments. *Biophysical Journal*, 101(5):1041–1045,

2011. ISSN 0006-3495. doi: 10.1016/j.bpj.2011.07.038. URL <GotoISI>://WOS:000294653800004.

[91] F. Ziebert, S. Swaminathan, and I. S. Aranson. Model for self-polarization and motility of keratocyte fragments. *Journal of the Royal Society Interface*, 9(70):1084–1092, 2012. ISSN 1742-5689. doi: 10.1098/rsif.2011.0433. URL <GotoISI>://WOS:000302134300026https://www.ncbi.nlm.nih.gov/pmc/articles/PMC3306635/pdf/rsif20110433.pdf.

[92] Elsen Tjhung, Davide Marenduzzo, and Michael E. Cates. Spontaneous symmetry breaking in active droplets provides a generic route to motility. *Proc Nat Acad Sci USA*, 109(31):12381–12386, 2012. ISSN 0027-8424. doi: 10.1073/pnas.1200843109. URL https://www.pnas.org/content/109/31/12381.

[93] V. Ruprecht, S. Wieser, A. Callan-Jones, M. Smutny, H. Morita, K. Sako, V. Barone, M. Ritsch-Marte, M. Sixt, R. Voituriez, and C. P. Heisenberg. Cortical contractility triggers a stochastic switch to fast amoeboid cell motility. *Cell*, 160(4):673–685, 2015. ISSN 0092-8674. doi: 10.1016/j.cell.2015.01.008. URL <GotoISI>://WOS:000349208800011.

[94] Michael M. Kozlov and Alex Mogilner. Model of polarization and bistability of cell fragments. *Biophys J*, 93(11):3811 – 3819, 2007. ISSN 0006-3495. doi: DOI: 10.1529/biophysj.107.110411.

[95] A. J. Lomakin, K. C. Lee, S. J. Han, D. A. Bui, M. Davidson, A. Mogilner, and G. Danuser. Competition for actin between two distinct f-actin networks defines a bistable switch for cell polarization. *Nature Cell Biology*, 17(11):1435–1445, 2015. ISSN 1465-7392. doi: 10.1038/ncb3246. URL <GotoISI>://WOS:000364270500009.

[96] William R. Holmes, JinSeok Park, Andre Levchenko, and Leah Edelstein-Keshet. A mathematical model coupling polarity signaling to cell adhesion explains diverse cell migration patterns. *PLOS Computational Biology*, 13(5):1–22, 05 2017. doi: 10.1371/journal.pcbi.1005524. URL https://doi.org/10.1371/journal.pcbi.1005524.

[97] JinSeok Park, William R. Holmes, Sung Hoon Lee, Hong-Nam Kim, Deok-Ho Kim, Moon Kyu Kwak, Chiaochun Joanne Wang, Leah Edelstein-Keshet, and

Andre Levchenko. Mechanochemical feedback underlies coexistence of qualitatively distinct cell polarity patterns within diverse cell populations. *Proceedings of the National Academy of Sciences*, 114(28):E5750–E5759, 2017. ISSN 0027-8424. doi: 10.1073/pnas.1700054114. URL https://www.pnas.org/content/114/28/E5750.

[98] Alfonso Bolado-Carrancio, Oleksii S Rukhlenko, Elena Nikonova, Mikhail A Tsyganov, Anne Wheeler, Amaya Garcia-Munoz, Walter Kolch, Alex von Kriegsheim, and Boris N Kholodenko. Periodic propagating waves coordinate rhogtpase network dynamics at the leading and trailing edges during cell migration. *eLife*, 9:e58165, jul 2020. ISSN 2050-084X. doi: 10.7554/eLife.58165. URL https://doi.org/10.7554/eLife.58165.

[99] Jonathan E. Ron, Pascale Monzo, Nils C. Gauthier, Raphael Voituriez, and Nir S. Gov. One-dimensional cell motility patterns. *Phys. Rev. Research*, 2:033237, Aug 2020. doi: 10.1103/PhysRevResearch.2.033237. URL https://link.aps.org/doi/10.1103/PhysRevResearch.2.033237.

[100] Pierre Sens. Stick–slip model for actin-driven cell protrusions, cell polarization, and crawling. *Proceedings of the National Academy of Sciences*, 117(40):24670–24678, 2020. ISSN 0027-8424. doi: 10.1073/pnas.2011785117. URL https://www.pnas.org/content/117/40/24670.

[101] Paolo Maiuri, Emmanuel Terriac, Perrine Paul-Gilloteaux, Timothée Vignaud, Krista McNally, James Onuffer, Kurt Thorn, Phuong A. Nguyen, Nefeli Georgoulia, Daniel Soong, Asier Jayo, Nina Beil, Jürgen Beneke, Joleen Chooi Hong Lim, Chloe Pei-Ying Sim, Yeh-Shiu Chu, Andrea Jiménez-Dalmaroni, Jean-Franccois Joanny, Jean-Paul Thiery, Holger Erfle, Maddy Parsons, Timothy J. Mitchison, Wendell A. Lim, Ana-Maria Lennon-Duménil, Matthieu Piel, and Manuel Théry. The first world cell race. *Current Biology*, 22(17):R673–R675, 2012. doi: 10.1016/j.cub.2012.07.052. URL http://www.sciencedirect.com/science/article/pii/S0960982212008779.

[102] G. Danuser, J. Allard, and A. Mogilner. Mathematical modeling of eukaryotic cell migration: Insights beyond experiments. *Annu Rev Cell Dev Biol.*, 29:501–528, 2013.

[103] Alex Mogilner. Mathematics of cell motility: have we got its number? *J. Math. Biol.*, 58:105–134, 2009.

[104] Mihaela Enculescu and Martin Falcke. *Modeling Morphodynamic Phenotypes and Dynamic Regimes of Cell Motion*, volume 736 of *Advances in Experimental Medicine and Biology*, chapter 20, pages 337–358. Springer, 2012.

[105] Anders E. Carlsson and David Sept. Mathematical modeling of cell migration. In Dr. John J. Correia and III Dr. H. William Detrich, editors, *Biophysical Tools for Biologists, Volume One: In Vitro Techniques*, volume 84 of *Methods in Cell Biology*, pages 911 – 937. Academic Press, 2008. doi: DOI:10.1016/S0091-679X(07)84029-5.

[106] Charles S Peskin, Garrett M Odell, and George F Oster. Cellular motions and thermal fluctuations: the brownian ratchet. *Biophysical journal*, 65(1):316–324, 1993.

[107] Alexander Mogilner and George Oster. Cell motility driven by actin polymerization. *Biophysical journal*, 71(6):3030–3045, 1996.

[108] Alex Mogilner and George Oster. Force generation by actin polymerization ii: the elastic ratchet and tethered filaments. *Biophysical journal*, 84(3):1591–1605, 2003.

[109] Thomas E Schaus, Edwin W Taylor, and Gary G Borisy. Self-organization of actin filament orientation in the dendritic-nucleation/array-treadmilling model. *Proceedings of the National Academy of Sciences*, 104(17):7086–7091, 2007.

[110] AE Carlsson. Structure of autocatalytically branched actin solutions. *Physical review letters*, 92(23):238102, 2004.

[111] Julian Weichsel and Ulrich S Schwarz. Two competing orientation patterns explain experimentally observed anomalies in growing actin networks. *Proceedings of the National Academy of Sciences*, 107(14):6304–6309, 2010.

[112] Anders E Carlsson. Growth of branched actin networks against obstacles. *Biophysical journal*, 81(4):1907–1923, 2001.

[113] Erdincc Atilgan, Denis Wirtz, and Sean X Sun. Morphology of the lamellipodium and organization of actin filaments at the leading edge of crawling cells. *Biophysical journal*, 89(5):3589–3602, 2005.

[114] Juliane Zimmermann, Claudia Brunner, Mihaela Enculescu, Michael Goegler, Allen Ehrlicher, Josef Käs, and Martin Falcke. Actin filament elasticity and retrograde flow shape the force-velocity relation of motile cells. *Biophysical journal*, 102(2):287–295, 2012.

[115] F. Motahari and A. E. Carlsson. Thermodynamically consistent treatment of the growth of a biopolymer in the presence of a smooth obstacle interaction potential. *Phys. Rev. E*, 100:042409, Oct 2019.

[116] Azam Gholami, Jan Wilhelm, and Erwin Frey. Entropic forces generated by grafted semiflexible polymers. *Phys Rev E*, 74(4):041803, Oct 2006. doi: 10.1103/PhysRevE.74.041803.

[117] Alex Mogilner and George Oster. Force Generation by Actin Polymerization II: The Elastic Ratchet and Tethered Filaments. *Biophys J*, 84(3):1591–1605, 2003.

[118] Florian Huber, Josef Käs, and Björn Stuhrmann. Growing actin networks form lamellipodium and lamellum by self-assembly. *Biophysical journal*, 95(12):5508–5523, 2008.

[119] Tom Shemesh, Alexander B Verkhovsky, Tatyana M Svitkina, Alexander D Bershadsky, and Michael M Kozlov. Role of focal adhesions and mechanical stresses in the formation and progression of the lamellum interface. *Biophysical journal*, 97(5):1254–1264, 2009.

[120] Wolfgang Alt, Martin Bock, Christoph Mo, et al. Coupling of cytoplasm and adhesion dynamics determines cell polarization and locomotion. In *Cell Mechanics*, pages 107–150. Chapman and Hall/CRC, 2010.

[121] Danying Shao, Wouter-Jan Rappel, and Herbert Levine. Computational model for cell morphodynamics. *Phys Rev Lett*, 105(10):108104, Sep 2010. doi: 10.1103/PhysRevLett.105.108104.

[122] Fabien Gerbal, Paul Chaikin, Yitzhak Rabin, and Jacques Prost. An Elastic Analysis of Listeria monocytogenes Propulsion. *Biophys J*, 79(5):2259–2275, 2000.

[123] Karin John, Philippe Peyla, Klaus Kassner, Jacques Prost, and Chaouqi Misbah. Nonlinear study of symmetry breaking in actin gels: implications for cellular motility. *Physical review letters*, 100(6):068101, 2008.

[124] Yann Marcy, Jacques Prost, Marie-France Carlier, and Cécile Sykes. Forces generated during actin-based propulsion: A direct measurement by micromanipulation. *Proc Nat Acad Sci USA*, 101(16):5992–5997, 2004. doi: 10.1073/pnas.0307704101.

[125] Alexander Zumdieck, Marco Cosentino Lagomarsino, Catalin Tanase, Karsten Kruse, Bela Mulder, Marileen Dogterom, and Frank Jülicher. Continuum description of the cytoskeleton: Ring formation in the cell cortex. *Phys Rev Lett*, 95 (25):258103, Dec 2005. doi: 10.1103/PhysRevLett.95.258103.

[126] F. Jülicher, K. Kruse, J. Prost, and J.-F. Joanny. Active behavior of the Cytoskeleton. *Physics Reports*, 449(1-3):3 – 28, 2007. ISSN 0370-1573. doi: DOI:10.1016/j.physrep.2007.02.018. Nonequilibrium physics: From complex fluids to biological systems III. Living systems.

[127] K. Doubrovinski and K. Kruse. Cell motility resulting from spontaneous polymerization waves. *Phys Rev Lett*, 107:258103, Dec 2011. doi: 10.1103/PhysRevLett.107.258103.

[128] Boris Rubinstein, Maxime F. Fournier, Ken Jacobson, Alexander B. Verkhovsky, and Alex Mogilner. Actin-myosin viscoelastic flow in the keratocyte lamellipod. *Biophys J*, 97(7):1853 – 1863, 2009. ISSN 0006-3495.

[129] Juliane Zimmermann and Martin Falcke. Formation of transient lamellipodia. *PLoS ONE*, 9(2):e87638, 02 2014. doi: 10.1371/journal.pone.0087638. URL http://dx.doi.org/10.13712Fjournal.pone.0087638.

[130] Juliane Zimmermann, Mihaela Enculescu, and Martin Falcke. Leading edge - gel coupling in lamellipodium motion. *Phys Rev E*, 82(5):051925, Nov 2010. doi: 10.1103/PhysRevE.82.051925.

[131] Azam Gholami, Mihaela Enculescu, and Martin Falcke. Membrane waves driven by forces from actin filaments. *New Journal of Physics*, 14(11):115002, 2012.

[132] Dylan T. Burnette, Suliana Manley, Prabuddha Sengupta, Rachid Sougrat, Michael W. Davidson, Bechara Kachar, and Jennifer Lippincott-Schwartz. A role for actin arcs in the leading-edge advance of migrating cells. *Nat Cell Biol*, 13(4): 371–382, 2011.

[133] F Jülicher K Kruse, J F Joanny and J Prost. Contractility and retrograde flow in lamellipodium motion. *Physical Biology*, 3(2):130–137, 2006.

[134] Danying Shao, Herbert Levine, and Wouter-Jan Rappel. Coupling actin flow, adhesion, and morphology in a computational cell motility model. *Proceedings of the National Academy of Sciences*, 109(18):6851–6856, 2012.

[135] Amelia Ahmad Khalili and Mohd Ridzuan Ahmad. A review of cell adhesion studies for biomedical and biological applications. *International journal of molecular sciences*, 16(8):18149–18184, 2015.

[136] Alexander Bershadsky, Michael Kozlov, and Benjamin Geiger. Adhesion-mediated mechanosensitivity: a time to experiment, and a time to theorize. *Current opinion in cell biology*, 18(5):472–481, 2006.

[137] Paul A DiMilla, Kenneth Barbee, and Douglas A Lauffenburger. Mathematical model for the effects of adhesion and mechanics on cell migration speed. *Biophysical journal*, 60(1):15–37, 1991.

[138] Maria E Gracheva and Hans G Othmer. A continuum model of motility in ameboid cells. *Bulletin of mathematical biology*, 66(1):167–193, 2004.

[139] Grégory Giannone, Benjamin J Dubin-Thaler, Hans-Günther Döbereiner, Nelly Kieffer, Anne R Bresnick, and Michael P Sheetz. Periodic lamellipodial contractions correlate with rearward actin waves. *Cell*, 116(3):431 – 443, 2004. ISSN 0092-8674. doi: DOI:10.1016/S0092-8674(04)00058-3.

[140] Hans-Günther Döbereiner, Benjamin J. Dubin-Thaler, Jake M. Hofman, Harry S. Xenias, Tasha N. Sims, Gregory Giannone, Michael L. Dustin, Chris H. Wiggins, and Michael P. Sheetz. Lateral membrane waves constitute a universal dynamic pattern of motile cells. *Phys Rev Lett*, 97(3):038102, 2006.

[141] A. Gholami, M. Falcke, and E. Frey. Velocity oscillations in actin-based motility. *New Journal of Physics*, 10:033022, 2008.

[142] Mihaela Enculescu, Azam Gholami, and Martin Falcke. Dynamic regimes and bifurcations in a model of actin-based motility. *Physical Review E*, 78(3):031915, 2008. doi: 10.1103/PhysRevE.78.031915.

[143] Mihaela Enculescu, Mohsen Sabouri-Ghomi, Gaudenz Danuser, and Martin Falcke. Modeling of protrusion phenotypes driven by the actin-membrane interaction. *Biophys J*, 98(8):1571 – 1581, 2010.

[144] Jun Allard and Alex Mogilner. Traveling waves in actin dynamics and cell motility. *Current Opinion in Cell Biology*, 25(1):107 – 115, 2013. ISSN 0955-0674. doi: 10.1016/j.ceb.2012.08.012. ¡ce:title¿Cell architecture¡/ce:title¿.

[145] Stefan A. Koestler, Sonja Auinger, Marlene Vinzenz, Klemens Rottner, and J. Victor Small. Differentially oriented populations of actin filaments generated in lamellipodia collaborate in pushing and pausing at the cell front. *Nat Cell Biol*, 10(3): 306–313, 2008.

[146] Juliane Zimmermann and Martin Falcke. Formation of transient lamellipodia. *PLoS ONE*, 9(2):e87638, 02 2014. doi: 10.1371/journal.pone.0087638. URL http://dx.doi.org/10.1371%2Fjournal.pone.0087638.

[147] F. Ziebert and I. S. Aranson. Effects of adhesion dynamics and substrate compliance on the shape and motility of crawling cells. *Plos One*, 8(5), 2013. ISSN 1932-6203. doi: ARTNe6451110.1371/journal.pone.0064511. URL <GotoISI>://WOS:000319799900047.

[148] Erin L. Barnhart, Jun Allard, Sunny S. Lou, Julie A. Theriot, and Alex Mogilner. Adhesion-dependent wave generation in crawling cells. *Current Biology*, 27(1):27 – 38, 2017. ISSN 0960-9822. doi: https://doi.org/10.1016/j.cub.2016.11.011. URL http://www.sciencedirect.com/science/article/pii/S0960982216313367.

[149] Alba Diz-Muñoz, Daniel A. Fletcher, and Orion D. Weiner. Use the force: membrane tension as an organizer of cell shape and motility. *Trends in Cell Biology*, 23(2):47–53, 2013. ISSN 0962-8924. doi: https://doi.org/10.1016/j.tcb.2012.09.006. URL https://www.sciencedirect.com/science/article/pii/S0962892412001778.

[150] Alba Diz-Muñoz, Kevin Thurley, Sana Chintamen, Steven J. Altschuler, Lani F. Wu, Daniel A. Fletcher, and Orion D. Weiner. Membrane tension acts through pld2 and mtorc2 to limit actin network assembly during neutrophil migration. *PLOS Biology*, 14(6):1–30, 06 2016. doi: 10.1371/journal.pbio.1002474. URL https://doi.org/10.1371/journal.pbio.1002474.

[151] Eugene Tkachenko, Mohsen Sabouri-Ghomi, Olivier Pertz, Chungho Kim, Edgar Gutierrez, Matthias Machacek, Alex Groisman, Gaudenz Danuser, and Mark H. Ginsberg. Protein kinase A governs a RhoA-RhoGDI protrusion-retraction pacemaker in migrating cells. *Nat Cell Biol*, 13(6):660–667, 2011.

[152] Esa Kuusela and Wolfgang Alt. Continuum model of cell adhesion and migration. *Journal of mathematical biology*, 58(1):135–161, 2009.

[153] Mihaela Enculescu, Mohsen Sabouri-Ghomi, Gaudenz Danuser, and Martin Falcke. Modeling of protrusion phenotypes driven by the actin-membrane interaction. *Biophysical journal*, 98(8):1571–1581, 2010.

[154] E. L. Barnhart, J. Allard, S Lou, J. A. Theriot, and A Mogilner. Adhesion-dependent wave generation in crawling cells. *Curr. Biol.*, 27:27–38, 2017.

[155] Sergio Alonso, Maike Stange, and Carsten Beta. Modeling random crawling, membrane deformation and intracellular polarity of motile amoeboid cells. *PloS one*, 13(8):e0201977, 2018.

[156] Eduardo Moreno, Sven Flemming, Francesc Font, Matthias Holschneider, Carsten Beta, and Sergio Alonso. Modeling cell crawling strategies with a bistable model: From amoeboid to fan-shaped cell motion. *Physica D: Nonlinear Phenomena*, 412: 132591, 2020.

[157] Ted Moldenhawer, Eduardo Moreno, Daniel Schindler, Sven Flemming, Matthias Holschneider, Wilhelm Huisinga, Sergio Alonso, and Carsten Beta. Spontaneous transitions between amoeboid and keratocyte-like modes of migration. *arXiv preprint arXiv:2207.06919*, 2022.

[158] Masoud Nickaeen, Igor L Novak, Stephanie Pulford, Aaron Rumack, Jamie Brandon, Boris M Slepchenko, and Alex Mogilner. A free-boundary model of a motile cell explains turning behavior. *PLoS computational biology*, 13(11):e1005862, 2017.

[159] Greg M Allen, Kun Chun Lee, Erin L Barnhart, Mark A Tsuchida, Cyrus A Wilson, Edgar Gutierrez, Alexander Groisman, Julie A Theriot, and Alex Mogilner. Cell mechanics at the rear act to steer the direction of cell migration. *Cell systems*, 11(3):286–299, 2020.

[160] Nathan W Goehring and Stephan W Grill. Cell polarity: mechanochemical patterning. *Trends in cell biology*, 23(2):72–80, 2013.

[161] M. Nickaeen, I. Novak, S. Pulford, A. Rumack, J. Brandon, B. M. Slepchenko, and A. Mogilner. A free-boundary model of a motile cell explains turning behavior. *PLoS Comput. Biol.*, 13:e1005862, 2017.

[162] Ellen L Batchelder, Gunther Hollopeter, Clément Campillo, Xavier Mezanges, Erik M Jorgensen, Pierre Nassoy, Pierre Sens, and Julie Plastino. Membrane tension regulates motility by controlling lamellipodium organization. *Proceedings of the National Academy of Sciences*, 108(28):11429–11434, 2011.

[163] Jan Mueller, Gregory Szep, Maria Nemethova, Ingrid De Vries, Arnon D Lieber, Christoph Winkler, Karsten Kruse, J Victor Small, Christian Schmeiser, Kinneret Keren, et al. Load adaptation of lamellipodial actin networks. *Cell*, 171(1):188–200, 2017.

[164] Alexander B Verkhovsky. The mechanisms of spatial and temporal patterning of cell-edge dynamics. *Current Opinion in Cell Biology*, 36:113–121, 2015.

[165] Alfonso Bolado-Carrancio, Oleksii S Rukhlenko, Elena Nikonova, Mikhail A Tsyganov, Anne Wheeler, Amaya Garcia-Munoz, Walter Kolch, Alex von Kriegsheim, and Boris N Kholodenko. Periodic propagating waves coordinate rhogtpase network dynamics at the leading and trailing edges during cell migration. *Elife*, 9:e58165, 2020.

[166] William R Holmes, JinSeok Park, Andre Levchenko, and Leah Edelstein-Keshet. A mathematical model coupling polarity signaling to cell adhesion explains diverse cell migration patterns. *PLoS computational biology*, 13(5):e1005524, 2017.

[167] JinSeok Park, William R Holmes, Sung Hoon Lee, Hong-Nam Kim, Deok-Ho Kim, Moon Kyu Kwak, Chiaochun Joanne Wang, Leah Edelstein-Keshet, and Andre Levchenko. Mechanochemical feedback underlies coexistence of qualitatively distinct cell polarity patterns within diverse cell populations. *Proceedings of the National Academy of Sciences*, 114(28):E5750–E5759, 2017.

[168] Christian Westendorf, Jose Negrete Jr, Albert J Bae, Rabea Sandmann, Eberhard Bodenschatz, and Carsten Beta. Actin cytoskeleton of chemotactic amoebae operates close to the onset of oscillations. *Proceedings of the National Academy of Sciences*, 110(10):3853–3858, 2013.

[169] Jose Negrete Jr, Alain Pumir, Hsin-Fang Hsu, Christian Westendorf, Marco Tarantola, Carsten Beta, and Eberhard Bodenschatz. Noisy oscillations in the actin cytoskeleton of chemotactic amoeba. *Physical review letters*, 117(14):148102, 2016.

[170] K Hennig, I Wang, P Moreau, L Valon, S DeBeco, M Coppey, YA Miroshnikova, C Albiges-Rizo, Cyril Favard, R Voituriez, et al. Stick-slip dynamics of cell adhesion triggers spontaneous symmetry breaking and directional migration of mesenchymal cells on one-dimensional lines. *Science advances*, 6(1):eaau5670, 2020.

[171] Joseph D'alessandro, Victor Cellerin, Olivier Benichou, René Marc Mège, Raphaël Voituriez, Benoît Ladoux, et al. Cell migration guided by long-lived spatial memory. *Nature Communications*, 12(1):1–10, 2021.

[172] Kun-Chun Lee and Andrea J Liu. Force-velocity relation for actin-polymerization-driven motility from brownian dynamics simulations. *Biophysical journal*, 97(5): 1295–1304, 2009.

[173] AE Carlsson. Growth velocities of branched actin networks. *Biophysical journal*, 84(5):2907–2918, 2003.

[174] Susan E Leggett, Jea Yun Sim, Jonathan E Rubins, Zachary J Neronha, Evelyn Kendall Williams, and Ian Y Wong. Morphological single cell profiling of the epithelial–mesenchymal transition. *Integrative Biology*, 8(11):1133–1144, 2016.

[175] Thomas M Hermans, Didzis Pilans, Sabil Huda, Patrick Fuller, Kristiana Kandere-Grzybowska, and Bartosz A Grzybowski. Motility efficiency and spatiotemporal synchronization in non-metastatic vs. metastatic breast cancer cells. *Integrative Biology*, 5(12):1464–1473, 2013.

[176] Joao M Monteiro, Pedro B Fernandes, Filipa Vaz, Ana R Pereira, Andreia C Tavares, Maria T Ferreira, Pedro M Pereira, Helena Veiga, Erkin Kuru, Michael S VanNieuwenhze, et al. Cell shape dynamics during the staphylococcal cell cycle. *Nature communications*, 6(1):1–12, 2015.

[177] Galina Reshes, Sharon Vanounou, Itzhak Fishov, and Mario Feingold. Cell shape dynamics in escherichia coli. *Biophysical journal*, 94(1):251–264, 2008.

[178] Chris Bakal, John Aach, George Church, and Norbert Perrimon. Quantitative morphological signatures define local signaling networks regulating cell morphology. *science*, 316(5832):1753–1756, 2007.

[179] Zheng Yin, Amine Sadok, Heba Sailem, Afshan McCarthy, Xiaofeng Xia, Fuhai Li, Mar Arias Garcia, Louise Evans, Alexis R Barr, Norbert Perrimon, et al. A screen for morphological complexity identifies regulators of switch-like transitions between discrete cell shapes. *Nature cell biology*, 15(7):860–871, 2013.

[180] Alexander Rigort, David Günther, Reiner Hegerl, Daniel Baum, Britta Weber, Steffen Prohaska, Ohad Medalia, Wolfgang Baumeister, and Hans-Christian Hege. Automated segmentation of electron tomograms for a quantitative description of actin filament networks. *Journal of structural biology*, 177(1):135–144, 2012.

[181] John H Henson, Mesrob Yeterian, Richard M Weeks, Angela E Medrano, Briana L Brown, Heather L Geist, Mollyann D Pais, Rudolf Oldenbourg, and Charles B Shuster. Arp2/3 complex inhibition radically alters lamellipodial actin architecture, suspended cell shape, and the cell spreading process. *Molecular biology of the cell*, 26(5):887–900, 2015.

[182] Tatyana M Svitkina, Elena A Bulanova, Oleg Y Chaga, Danijela M Vignjevic, Shin-ichiro Kojima, Jury M Vasiliev, and Gary G Borisy. Mechanism of filopodia initiation by reorganization of a dendritic network. *The Journal of cell biology*, 160(3):409–421, 2003.

[183] Marion Jasnin, Shoh Asano, Edith Gouin, Reiner Hegerl, Jürgen M Plitzko, Elizabeth Villa, Pascale Cossart, and Wolfgang Baumeister. Three-dimensional architecture of actin filaments in listeria monocytogenes comet tails. *Proceedings of the National Academy of Sciences*, 110(51):20521–20526, 2013.

[184] Matthew B Smith, Hongsheng Li, Tian Shen, Xiaolei Huang, Eddy Yusuf, and Dimitrios Vavylonis. Segmentation and tracking of cytoskeletal filaments using open active contours. *Cytoskeleton*, 67(11):693–705, 2010.

[185] Matthias Machacek and Gaudenz Danuser. Morphodynamic profiling of protrusion phenotypes. *Biophysical journal*, 90(4):1439–1452, 2006.

[186] Klemens Rottner and Matthias Schaks. Assembling actin filaments for protrusion. *Current opinion in cell biology*, 56:53–63, 2019.

[187] Ah-Lai Law, Anne Vehlow, Maria Kotini, Lauren Dodgson, Daniel Soong, Eric Theveneau, Cristian Bodo, Eleanor Taylor, Christel Navarro, Upamali Perera, et al. Lamellipodin and the scar/wave complex cooperate to promote cell migration in vivo. *Journal of Cell Biology*, 203(4):673–689, 2013.

[188] Guillaume Carmona, Upamali Perera, Cheryl Gillett, Alexandra Naba, Ah-Lai Law, Ved P Sharma, Jian Wang, Jeffrey Wyckoff, Michele Balsamo, Fuad Mosis, et al. Lamellipodin promotes invasive 3d cancer cell migration via regulated interactions with ena/vasp and scar/wave. *Oncogene*, 35(39):5155–5169, 2016.

[189] Alexander Anielski, Eva KB Pfannes, and Carsten Beta. Cell shape recognition and segmentation in fluorescence microscopy images. *Journal of Computational Interdisciplinary Sciences*, 3(1-2):99–106, 2012.

[190] Florian Fäßler, Bettina Zens, Robert Hauschild, and Florian KM Schur. 3d printed cell culture grid holders for improved cellular specimen preparation in cryo-electron microscopy. *Journal of Structural Biology*, 212(3):107633, 2020.

[191] Jonathan Bouvette, Hsuan-Fu Liu, Xiaochen Du, Ye Zhou, Andrew P Sikkema, Juliana da Fonseca Rezende e Mello, Bradley P Klemm, Rick Huang, Roel M Schaaper, Mario J Borgnia, et al. Beam image-shift accelerated data acquisition for near-atomic resolution single-particle cryo-electron tomography. *Nature communications*, 12(1):1–11, 2021.

[192] David N Mastronarde and Susannah R Held. Automated tilt series alignment and tomographic reconstruction in imod. *Journal of structural biology*, 197(2):102–113, 2017.

[193] Boris Hinz, Wolfgang Alt, Christa Johnen, Volker Herzog, and Hans-Wilhelm Kaiser. Quantifying lamella dynamics of cultured cells by saced, a new computer-assisted motion analysis. *Experimental cell research*, 251(1):234–243, 1999.

[194] Deborah Wessels and DR Soll. Computer-assisted characterization of the behavioral defects of cytoskeletal mutants of dictyostelium discoideum. *Motion analysis of living cells*, pages 101–140, 1998.

[195] Daniel Zicha, Ian M Dobbie, Mark R Holt, James Monypenny, Daniel YH Soong, Colin Gray, and Graham A Dunn. Rapid actin transport during cell protrusion. *Science*, 300(5616):142–145, 2003.

[196] Mousumi Ghosh, Xiaoyan Song, Ghassan Mouneimne, Mazen Sidani, David S Lawrence, and John S Condeelis. Cofilin promotes actin polymerization and defines the direction of cell motility. *Science*, 304(5671):743–746, 2004.

[197] Charles W Wolgemuth and Mark Zajac. The moving boundary node method: A level set-based, finite volume algorithm with applications to cell motility. *Journal of computational physics*, 229(19):7287–7308, 2010.

[198] Daniel Schindler, Ted Moldenhawer, Maike Stange, Valentino Lepro, Carsten Beta, Matthias Holschneider, and Wilhelm Huisinga. Analysis of protrusion dynamics in amoeboid cell motility by means of regularized contour flows. *PLoS computational biology*, 17(8):e1009268, 2021.

[199] Bodo Borm, Robert P. Requardt, Volker Herzog, and Gregor Kirfel. Membrane ruffles in cell migration: indicators of inefficient lamellipodia adhesion and compartments of actin filament reorganization. *Experimental Cell Research*, 302(1):83–95, 2005. ISSN 0014-4827. doi: http://dx.doi.org/10.1016/j.yexcr.2004.08.034. URL http://www.sciencedirect.com/science/article/pii/S0014482704005142.

[200] Matthew J. Footer, Jacob W. J. Kerssemakers, Julie A. Theriot, and Marileen Dogterom. Direct measurement of force generation by actin filament polymerization using an optical trap. *Proc Nat Acad Sci USA*, 104(7):2181–2186, 2007. doi: 10.1073/pnas.0607052104.

[201] Israil Solomonowitsch Gradstein and Jossif Moissejewitsch Ryschik. *Table of Integrals, Series, and Products*. Academic Press, 8 edition, 2014. ISBN 0-12-384933-0.

[202] Keith Burridge and Christophe Guilluy. Focal adhesions, stress fibers and mechanical tension. *Experimental Cell Research*, 343(1):14 – 20, 2016.

[203] Pirta Hotulainen and Pekka Lappalainen. Stress fibers are generated by two distinct actin assembly mechanisms in motile cells . *Journal of Cell Biology*, 173(3):383–394, 05 2006. ISSN 0021-9525. doi: 10.1083/jcb.200511093. URL https://doi.org/10.1083/jcb.200511093.

[204] Corina Ciobanasu, Bruno Faivre, and Christophe Le Clainche. Actin dynamics associated with focal adhesions. *International Journal of Cell Biology*, 2012:941292, 2012.

[205] Stephanie Stahnke, Hermann Döring, Charly Kusch, David J.J. de Gorter, Sebastian Dütting, Aleks Guledani, Irina Pleines, Michael Schnoor, Michael Sixt, Robert Geffers, Manfred Rohde, Mathias Müsken, Frieda Kage, Anika Steffen, Jan Faix, Bernhard Nieswandt, Klemens Rottner, and T.E.B. Stradal. Loss of Hem1 disrupts macrophage function and impacts on migration, phagocytosis and integrin-mediated adhesion. *bioRxiv*, 2020. doi: 10.1101/2020.03.24.005835. URL https://www.biorxiv.org/content/early/2020/03/25/2020.03.24.005835.

[206] Marlene Vinzenz, Maria Nemethova, Florian Schur, Jan Mueller, Akihiro Narita, Edit Urban, Christoph Winkler, Christian Schmeiser, Stefan A. Koestler, Klemens Rottner, Guenter P. Resch, Yuichiro Maeda, and J. Victor Small. Actin branching in the initiation and maintenance of lamellipodia. *J Cell Sci*, 125(11):2775–2785, 2012. doi: 10.1242/jcs.107623.

[207] W.H. Press, S.A Teukolsky, W.T. Vetterling, and B.P. Flannery. *Numerical recipes in C++*. Cambridge University Press, Cambridge, 3rd edition, 2007.

[208] Ivan V. Maly and Gary G. Borisy. Self-organization of a propulsive actin network as an evolutionary process. *Proceedings of the National Academy of Sciences*, 98 (20):11324–11329, 2001. doi: 10.1073/pnas.181338798.

[209] Alexander B. Verkhovsky, Oleg Y. Chaga, Sebastien Schaub, Tatyana M. Svitkina, Jean-Jacques Meister, and Gary G. Borisy. Orientational Order of the Lamellipodial Actin Network as Demonstrated in Living Motile Cells. *Mol Biol Cell*, 14(11): 4667–4675, 2003. doi: 10.1091/mbc.E02-10-0630.

[210] Julian Weichsel, Edit Urban, J. Victor Small, and Ulrich S. Schwarz. Reconstructing the orientation distribution of actin filaments in the lamellipodium of migrating keratocytes from electron microscopy tomography data. *Cytometry Part A*, 81A(6):496–507, 2012. ISSN 1552-4930. doi: 10.1002/cyto.a.22050. URL http://dx.doi.org/10.1002/cyto.a.22050.

[211] Marcus Prass, Ken Jacobson, Alex Mogilner, and Manfred Radmacher. Direct measurement of the lamellipodial protrusive force in a migrating cell. *J Cell Biol*, 174(6):767–772, 2006. doi: 10.1083/jcb.200601159.

[212] Fabian Heinemann, Holger Doschke, and Manfred Radmacher. Keratocyte lamellipodial protrusion is characterized by a concave force-velocity relation. *Biophys J*, 100(6):1420 – 1427, 2011. ISSN 0006-3495. doi: DOI:10.1016/j.bpj.2011.01.063.

[213] Yonatan Schweitzer, Arnon D. Lieber, Kinneret Keren, and Michael M. Kozlov. Theoretical analysis of membrane tension in moving cells. *Biophysical Journal*, 106(1):84 – 92, 2014. ISSN 0006-3495. doi: https://doi.org/10.1016/j.bpj.2013.11.009. URL http://www.sciencedirect.com/science/article/pii/S000634951301237X.

[214] Kurt I. Anderson and Rob Cross. Contact dynamics during keratocyte motility. *Current Biology*, 10(5):253 – 260, 2000.

[215] Christoph Möhl, Norbert Kirchgessner, Claudia Schäfer, Bernd Hoffmann, and Rudolf Merkel. Quantitative mapping of averaged focal adhesion dynamics in migrating cells by shape normalization. *Journal of Cell Science*, 125(1):155–165, 2012.

[216] Sawako Yamashiro, Soichiro Tanaka, Laura M. McMillen, Daisuke Taniguchi, Dimitrios Vavylonis, and Naoki Watanabe. Myosin-dependent actin stabilization as revealed by single-molecule imaging of actin turnover. *Molecular Biology of the Cell*, 29(16):1941–1947, 2018.

[217] Antonina Y. Alexandrova, Katya Arnold, Sébastien Schaub, Jury M. Vasiliev, Jean-Jacques Meister, Alexander D. Bershadsky, and Alexander B. Verkhovsky. Comparative dynamics of retrograde actin flow and focal adhesions: Formation of nascent adhesions triggers transition from fast to slow flow. *PLoS ONE*, 3(9): e3234, 09 2008. doi: 10.1371/journal.pone.0003234. URL http://dx.doi.org/10.1371%2Fjournal.pone.0003234.

[218] Tim Mitchison and Marc Kirschner. Cytoskeletal dynamics and nerve growth. *Neuron*, 1(9):761 – 772, 1988.

[219] M Chrzanowska-Wodnicka and K Burridge. Rho-stimulated contractility drives the formation of stress fibers and focal adhesions. *Journal of Cell Biology*, 133(6): 1403–1415, 06 1996. ISSN 0021-9525.

[220] Daniel G. Jay. The clutch hypothesis revisited: Ascribing the roles of actin-associated proteins in filopodial protrusion in the nerve growth cone. *Journal of Neurobiology*, 44(2):114–125, 2000. doi: 10.1002/1097-4695(200008)44:2⟨114::AID-NEU3⟩3.0.CO;2-8. URL https://onlinelibrary.wiley.com/doi/abs/10.1002/1097-4695%28200008%2944%3A2%3C114%3A%3AAID-NEU3%3E3.0.CO%3B2-8.

[221] Armando del Rio, Raul Perez-Jimenez, Ruchuan Liu, Pere Roca-Cusachs, Julio M. Fernandez, and Michael P. Sheetz. Stretching single talin rod molecules activates vinculin binding. *Science*, 323(5914):638–641, 2009. ISSN 0036-8075. doi: 10.1126/science.1162912. URL https://science.sciencemag.org/content/323/5914/638.

[222] Yvonne Aratyn-Schaus, Patrick W. Oakes, and Margaret L. Gardel. Dynamic and structural signatures of lamellar actomyosin force generation. *Mol Biol Cell*, 22 (8):1330–1339, 2011. doi: 10.1091/mbc.E10-11-0891.

[223] Fang Kong, Andrés J. García, A. Paul Mould, Martin J. Humphries, and Cheng Zhu. Demonstration of catch bonds between an integrin and its ligand. *Journal of Cell Biology*, 185(7):1275–1284, 06 2009. ISSN 0021-9525. doi: 10.1083/jcb.200810002. URL https://doi.org/10.1083/jcb.200810002.

[224] Derek L. Huang, Nicolas A. Bax, Craig D. Buckley, William I. Weis, and Alexander R. Dunn. Vinculin forms a directionally asymmetric catch bond with f-actin. *Science*, 357(6352):703–706, 2017. ISSN 0036-8075. doi: 10.1126/science.aan2556. URL https://science.sciencemag.org/content/357/6352/703.

[225] Maxime F. Fournier, Roger Sauser, Davide Ambrosi, Jean-Jacques Meister, and Alexander B. Verkhovsky. Force transmission in migrating cells. *The Journal of Cell Biology*, 188(2):287–297, 2010. doi: 10.1083/jcb.200906139.

[226] Tim Oliver, Micah Dembo, and Ken Jacobson. Separation of Propulsive and Adhesive Traction Stresses in Locomoting Keratocytes . *Journal of Cell Biology*, 145(3):589–604, 05 1999. ISSN 0021-9525. doi: 10.1083/jcb.145.3.589. URL https://doi.org/10.1083/jcb.145.3.589.

[227] Igor L. Novak, Boris M. Slepchenko, and Alex Mogilner. Quantitative Analysis of G-Actin Transport in Motile Cells. *Biophys J*, 95(4):1627–1638, 2008. doi: 10.1529/biophysj.108.130096.

[228] Pascal Vallotton, Gaudenz Danuser, Sophie Bohnet, Jean-Jacques Meister, and Alexander B. Verkhovsky. Tracking Retrograde Flow in Keratocytes: News from the Front. *Mol Biol Cell*, 16(3):1223–1231, 2005.

[229] Chi-Li Chiu, Michelle A Digman, and Enrico Gratton. Measuring actin flow in 3d cell protrusions. *Biophysical journal*, 105(8):1746–1755, 2013.

[230] Thomas Fuhs, Michael Goegler, Claudia A. Brunner, Charles W. Wolgemuth, and Josef A. Kaes. Causes of retrograde flow in fish keratocytes. *Cytoskeleton*, 71(1): 24–35, 2014. ISSN 1949-3592.

[231] Erin M Craig, Jonathan Stricker, Margaret Gardel, and Alex Mogilner. Model for adhesion clutch explains biphasic relationship between actin flow and traction at the cell leading edge. *Physical biology*, 12(3):035002, 2015.

[232] Francois Bordeleau, Wenjun Wang, Alysha Simmons, Marc A Antonyak, Richard A Cerione, and Cynthia A Reinhart-King. Tissue transglutaminase 2 regulates tumor cell tensional homeostasis by increasing contractility. *Journal of cell science*, 133(1):jcs231134, 2020.

[233] Arnon D Lieber, Shlomit Yehudai-Resheff, Erin L Barnhart, Julie A Theriot, and Kinneret Keren. Membrane tension in rapidly moving cells is determined by cytoskeletal forces. *Current biology*, 23(15):1409–1417, 2013.

[234] Jeffrey R Kuhn and Thomas D Pollard. Real-time measurements of actin filament polymerization by total internal reflection fluorescence microscopy. *Biophysical journal*, 88(2):1387–1402, 2005.

[235] Marie-France Carlier and Dominique Pantaloni. Control of actin dynamics in cell motility. *Journal of molecular biology*, 269(4):459–467, 1997.

[236] Stefan A. Koestler, Klemens Rottner, Frank Lai, Jennifer Block, Marlene Vinzenz, and J. Victor Small. F- and g-actin concentrations in lamellipodia of moving cells. *PLoS ONE*, 4(3):e4810, 03 2009. doi: 10.1371/journal.pone.0004810.

[237] Naoki Watanabe and Timothy J Mitchison. Single-molecule speckle analysis of actin filament turnover in lamellipodia. *Science*, 295(5557):1083–1086, 2002.

[238] Kinneret Keren, Zachary Pincus, Greg M. Allen, Erin L. Barnhart, Gerard Marriott, Alex Mogilner, and Julie A. Theriot. Mechanism of shape determination in motile cells. *Nature*, 453(7194):475–480, 2008.

[239] Danying Shao, Herbert Levine, and Wouter-Jan Rappel. Coupling actin flow, adhesion, and morphology in a computational cell motility model. *Proc Nat Acad Sci USA*, 109(18):6851–6856, 2012. doi: 10.1073/pnas.1203252109.

[240] The Physical Sciences-Oncology Centers Network, David B Agus, Jenolyn F Alexander, Wadih Arap, Shashanka Ashili, Joseph E Aslan, Robert H Austin, Vadim Backman, Kelly J Bethel, Richard Bonneau, et al. A physical sciences network characterization of non-tumorigenic and metastatic cells. *Scientific reports*, 3:1449, 2013.

[241] Ning Wang, Iva Marija Tolic-Nørrelykke, Jianxin Chen, Srboljub M Mijailovich, James P Butler, Jeffrey J Fredberg, and Dimitrije Stamenovic. Cell prestress. I. Stiffness and prestress are closely associated in adherent contractile cells. *American Journal of Physiology-Cell Physiology*, 282(3):C606–C616, 2002.

[242] Ning Wang, Keiji Naruse, Dimitrije Stamenović, Jeffrey J Fredberg, Srboljub M Mijailovich, Iva Marija Tolić-Nørrelykke, Thomas Polte, Robert Mannix, and Donald E Ingber. Mechanical behavior in living cells consistent with the tensegrity model. *Proceedings of the National Academy of Sciences*, 98(14):7765–7770, 2001.

[243] Valérie M Laurent, Sylvie Hénon, Emmanuelle Planus, Redouane Fodil, Martial Balland, Daniel Isabey, and Francc ois Gallet. Assessment of mechanical properties of adherent living cells by bead micromanipulation: comparison of magnetic twisting cytometry vs optical tweezers. *J. Biomech. Eng.*, 124(4):408–421, 2002.

[244] Falk Wottawah, Stefan Schinkinger, Bryan Lincoln, Revathi Ananthakrishnan, Maren Romeyke, Jochen Guck, and Josef Käs. Optical rheology of biological cells. *Physical review letters*, 94(9):098103, 2005.

[245] T. R. Kießling, M. Herrera, K. D. Nnetu, E. M. Balzer, M. Girvan, A. W. Fritsch, S. S. Martin, J. A. Käs, and W. Losert. Analysis of multiple physical parameters for mechanical phenotyping of living cells. *European Biophysical Journal*, 42(5): 383–394, 2013.

[246] Micah Dembo and Yu-Li Wang. Stresses at the cell-to-substrate interface during locomotion of fibroblasts. *Biophysical Journal*, 76(4):2307 – 2316, 1999. ISSN 0006-3495.

[247] Viola Vogel and Michael Sheetz. Local force and geometry sensing regulate cell functions. *Nature Reviews Molecular Cell Biology*, 7(4):265–275, 2006.

[248] Lee A. Smith, Helim Aranda-Espinoza, Jered B. Haun, Micah Dembo, and Daniel A. Hammer. Neutrophil traction stresses are concentrated in the uropod during migration. *Biophys J*, 92(7):L58 – L60, 2007. ISSN 0006-3495. doi: 10.1529/biophysj.106.102822.

[249] Ulrich S. Schwarz and Jérôme R.D. Soiné. Traction force microscopy on soft elastic substrates: A guide to recent computational advances. *Biochimica et Biophysica Acta (BBA) - Molecular Cell Research*, 1853(11, Part B):3095 – 3104, 2015. ISSN 0167-4889. Mechanobiology.

[250] Risata A. Jannat, Micah Dembo, and Daniela A. Hammer. Traction forces of neutrophils migrating on compliant substrates. *Biophys J*, 101(3):575 – 584, 2011. ISSN 0006-3495. doi: 10.1016/j.bpj.2011.05.040.

[251] Arpita Upadhyaya, Jeffrey R. Chabot, Albina Andreeva, Azadeh Samadani, and Alexander van Oudenaarden. Probing polymerization forces by using actin-propelled lipid vesicles. *PNAS*, 100(8):4521–4526, 2003. doi: 10.1073/pnas.0837027100.

[252] Carlos Jurado, John R. Haserick, and Juliet Lee. Slipping or Gripping? Fluorescent Speckle Microscopy in Fish Keratocytes Reveals Two Different Mechanisms for Generating a Retrograde Flow of Actin. *Mol Biol Cell*, 16(2):507–518, 2005. doi: 10.1091/mbc.E04-10-0860.

[253] Chi-Hung Lin and Paul Forscher. Growth cone advance is inversely proportional to retrograde f-actin flow. *Neuron*, 14(4):763 – 771, 1995. ISSN 0896-6273. doi: 10.1016/0896-6273(95)90220-1.

[254] Karen A. Beningo, Kozue Hamao, Micah Dembo, Yu li Wang, and Hiroshi Hosoya. Traction forces of fibroblasts are regulated by the rho-dependent kinase but not by the myosin light chain kinase. *Archives of Biochemistry and Biophysics*, 456 (2):224–231, 2006. Highlight Issue on Contractile Proteins.

[255] Patricia T. Yam, Cyrus A. Wilson, Lin Ji, Benedict Hebert, Erin L. Barnhart, Natalie A. Dye, Paul W. Wiseman, Gaudenz Danuser, and Julie A. Theriot. Actin–myosin network reorganization breaks symmetry at the cell rear to spontaneously initiate polarized cell motility . *Journal of Cell Biology*, 178(7):1207–1221, 09 2007.

[256] Marc Herant and Micah Dembo. Form and function in cell motility: From fibroblasts to keratocytes. *Biophysical Journal*, 98(8):1408 – 1417, 2010.

[257] Sharona Even-Ram, Andrew D. Doyle, Mary Anne Conti, Kazue Matsumoto, Robert S. Adelstein, and Kenneth M. Yamada. Myosin iia regulates cell motility and actomyosin–microtubule crosstalk. *Nature Cell Biology*, 9(3):299–309, 2007.

[258] Miguel Vicente-Manzanares, Jessica Zareno, Leanna Whitmore, Colin K. Choi, and Alan F. Horwitz. Regulation of protrusion, adhesion dynamics, and polarity by myosins IIA and IIB in migrating cells. *Journal of Cell Biology*, 176(5):573–580, 02 2007.

[259] Aaron F. Straight, Amy Cheung, John Limouze, Irene Chen, Nick J. Westwood, James R. Sellers, and Timothy J. Mitchison. Dissecting Temporal and Spatial Control of Cytokinesis with a Myosin II Inhibitor. *Science*, 299(5613):1743–1747, 2003. doi: 10.1126/science.1081412.

[260] Sébastien Schaub, Sophie Bohnet, Valérie M. Laurent, Jean-Jacques Meister, and Alexander B. Verkhovsky. Comparative maps of motion and assembly of filamentous actin and myosin ii in migrating cells. *Molecular Biology of the Cell*, 18(10): 3723–3732, 2007.

[261] Marie Chupeau, Olivier Bénichou, and Raphaël Voituriez. Cover times of random searches. *Nature Physics*, 11:844, 2015.

[262] Behnam Amiri, Johannes Clemens Julius Heyn, Christoph Schreiber, Joachim O. Rädler, and Martin Falcke. On multistability and constitutive relations of cell

motion on fibronectin lanes. *bioRxiv*, 2022. doi: 10.1101/2022.08.30.505377. URL https://www.biorxiv.org/content/early/2022/08/31/2022.08.30.505377.

[263] C. E. Morris and U. Homann. Cell surface area regulation and membrane tension. *The Journal of Membrane Biology*, 179(2):79–102, 2001. ISSN 1432-1424. doi: 10.1007/s002320010040. URL https://doi.org/10.1007/s002320010040.

[264] Arnon D. Lieber, Shlomit Yehudai-Resheff, Erin L. Barnhart, Julie A. Theriot, and Kinneret Keren. Membrane tension in rapidly moving cells is determined by cytoskeletal forces. *Current Biology*, 23(15):1409–1417, 2013. ISSN 0960-9822. doi: https://doi.org/10.1016/j.cub.2013.05.063. URL https://www.sciencedirect.com/science/article/pii/S096098221300688X.

[265] Pierre Sens and Julie Plastino. Membrane tension and cytoskeleton organization in cell motility. *Journal of Physics: Condensed Matter*, 27(27):273103, jun 2015. doi: 10.1088/0953-8984/27/27/273103. URL https://doi.org/10.1088/0953-8984/27/27/273103.

[266] Jörg Renkawitz, Kathrin Schumann, Michele Weber, Tim Lämmermann, Holger Pflicke, Matthieu Piel, Julien Polleux, Joachim P. Spatz, and Michael Sixt. Adaptive force transmission in amoeboid cell migration. *Nature Cell Biology*, 11(12): 1438–1443, 2009.

[267] Y. Aratyn-Schaus and M. L. Gardel. Transient frictional slip between integrin and the ecm in focal adhesions under myosin ii tension. *Current Biology*, 20 (13):1145–1153, 2010. ISSN 0960-9822. doi: 10.1016/j.cub.2010.05.049. URL <GotoISI>://WOS:000280024300021.

[268] Ying Li, Prabhakar Bhimalapuram, and Aaron R Dinner. Model for how retrograde actin flow regulates adhesion traction stresses. *Journal of Physics: Condensed Matter*, 22(19):194113, apr 2010. doi: 10.1088/0953-8984/22/19/194113. URL https://doi.org/10.1088%2F0953-8984%2F22%2F19%2F194113.

[269] E. M. Craig, J. Stricker, M. Gardel, and A. Mogilner. Model for adhesion clutch explains biphasic relationship between actin flow and traction at the cell leading edge. *Physical Biology*, 12(3), 2015. ISSN 1478-3967. doi: Artn03500210.1088/1478-3975/12/3/035002. URL <GotoISI>://WOS:000361836300003.

[270] E. Evans. Probing the relation between force - lifetime - and chemistry in single molecular bonds. *Annual Review of Biophysics and Biomolecular Structure*, 30(1): 105–128, 2001.

[271] N.G. van Kampen. *Stochastic processes in physics and chemistry*. North-Holland, Amsterdam, 2001.

[272] E. M. Craig, J. Stricker, M. Gardel, and A. Mogilner. Model for adhesion clutch explains biphasic relationship between actin flow and traction at the cell leading edge. *Physical Biology*, 12(3), 2015. ISSN 1478-3967. doi: Artn03500210.1088/1478-3975/12/3/035002. URL <GotoISI>://WOS:000361836300003.

[273] David M. Rutkowski and Dimitrios Vavylonis. Discrete mechanical model of lamellipodial actin network implements molecular clutch mechanism and generates arcs and microspikes. *PLOS Computational Biology*, 17(10):1–32, 10 2021. doi: 10.1371/journal.pcbi.1009506. URL https://doi.org/10.1371/journal.pcbi.1009506.

[274] Murat Cirit, Matej Krajcovic, Colin K. Choi, Erik S. Welf, Alan F. Horwitz, and Jason M. Haugh. Stochastic model of integrin-mediated signaling and adhesion dynamics at the leading edges of migrating cells. *PLoS Comput Biol*, 6(2):e1000688, 02 2010. doi: 10.1371/journal.pcbi.1000688.

[275] Julian Weichsel and Ulrich S. Schwarz. Two competing orientation patterns explain experimentally observed anomalies in growing actin networks. *Proc Nat Acad Sci USA*, 107(14):6304–6309, 2010. doi: 10.1073/pnas.0913730107.

[276] Martine Coué, Stephen L Brenner, Ilan Spector, and Edward D Korn. Inhibition of actin polymerization by latrunculin a. *FEBS letters*, 213(2):316–318, 1987.

[277] Christoph Schreiber, Felix J. Segerer, Ernst Wagner, Andreas Roidl, and Joachim O. Rädler. Ring-shaped microlanes and chemical barriers as a platform for probing single-cell migration. *Scientific Reports*, 6(1):26858, 2016.

[278] Upinder S. Bhalla. Signaling in Small Subcellular Volumes. I. Stochastic and Diffusion Effects on Individual Pathways. *Biophys J*, 87(2):733–744, 2004. doi: 10.1529/biophysj.104.040469.

[279] William Bialek and Sima Setayeshgar. Physical limits to biochemical signaling. *Proc Nat Acad Sci USA*, 102(29):10040–10045, 2005. doi: 10.1073/pnas.0504321102.

[280] Lev S Tsimring. Noise in biology. *Reports on Progress in Physics*, 77(2):026601, jan 2014. doi: 10.1088/0034-4885/77/2/026601. URL https://doi.org/10.1088/0034-4885/77/2/026601.

[281] Martin Falcke. Life is change – dynamic modeling quantifies it. *Current Opinion in Systems Biology*, 3:iv – viii, 2017. ISSN 2452-3100. doi: https://doi.org/10.1016/j.coisb.2017.06.004. URL http://www.sciencedirect.com/science/article/pii/S2452310017301543.